QUANTITATIVE IMAGE ANALYSIS FOR SINGLE MOLECULE LOCALIZATION MICROSCOPY

QUANTITATIVE IMAGE ANALYSIS FOR SINGLE MOLECULE LOCALIZATION MICROSCOPY

Proefschrift

ter verkrijging van de graad van doctor
aan de Technische Universiteit Delft,
op gezag van de Rector Magnificus prof. ir. K. C. A. M. Luyben,
voorzitter van het College voor Promoties,
in het openbaar te verdedigen op dinsdag 12 januari 2016 om 15:00 uur

door

Robert Pieter Joachim NIEUWENHUIZEN

natuurkundig ingenieur
geboren te 's-Gravenhage.

Dit proefschrift is goedgekeurd door de promotor:

promotor:	Prof. dr. ir. L.J. Van Vliet
copromotors:	dr. S. Stallinga en dr. B. Rieger

Samenstelling promotiecommissie bestaat uit:

Rector Magnificus,	voorzitter
Prof. dr. ir. L. J. Van Vliet,	Technische Universiteit Delft
Dr. S. Stallinga,	Technische Universiteit Delft
Dr. B. Rieger,	Technische Universiteit Delft
Onafhankelijke leden:	
Prof. dr. C. Dekker,	Technische Universiteit Delft
Prof. dr. J. Enderlein,	Georg-August-Universität Göttingen, Duitsland
Prof. dr. I. F. Sbalzarini,	Technische Universität Dresden, Duitsland Max-Planck-Institut für molekulare Zellbiologie und Genetik
Dr. S. Cox,	King's College London, Verenigd Koninkrijk
Prof. dr. I. T. Young,	Technische Universiteit Delft, reservelid

This work was carried out in the Quantitative Imaging group at the faculty of Applied Sciences of Delft University of Technology and was supported by the Dutch Technology Foundation STW, which is part of the Netherlands Organisation for Scientific Research (NWO).

Printed by: Gildeprint, Enschede, The Netherlands.

Front cover: Tubulin and Vimentin filaments (data courtesy of Leila Nahidiazar).

Back cover: Nup160 proteins in the nuclear pore complex.

ISBN 978-94-6186-591-5

An electronic version of this dissertation is available at
http://repository.tudelft.nl/.

The first principle is that you must not fool yourself
– and you are the easiest person to fool.

Richard Feynman

CONTENTS

1

INTRODUCTION

Parts of this chapter have been published as Rieger, B., Nieuwenhuizen, R.P.J., Stallinga, S. *IEEE Signal Process. Mag.* **32**, 49–57 (2015). [1]

1.1. LOCALIZATION MICROSCOPY

Fluorescence microscopy is currently the most important tool for visualizing biological structures at the sub-cellular scale. The combination of fluorescence, which enables a high imaging contrast, and the possibility to apply molecular labeling, which allows for a high imaging specificity, makes it a powerful imaging modality. The use of fluorescence microscopy has risen tremendously, in particular since the introduction of the green fluorescent protein (GFP) in the mid 1990s and the possibility to genetically engineer cells to express these proteins. Fig. 1.1 shows the basic layout of a fluorescence microscope. Excitation light of a certain wavelength is reflected via a dichroic beamsplitter and projected onto the specimen via the objective lens of the microscope. The light is absorbed by the fluorescent labels and re-emitted, slightly Stokes-shifted by ~10-100 nm, at a larger wavelength, typically a few nanoseconds later. The emission light is captured by the objective lens and directed towards the camera via the dichroic beamsplitter.

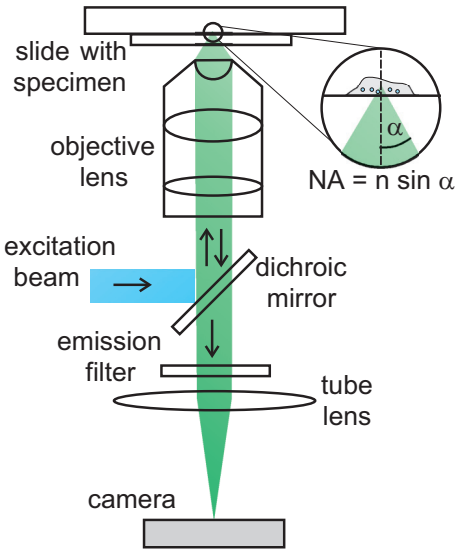

Figure 1.1: Schematics of an epi-fluorescence light microscope. The excitation light is focused onto the sample and the emission light is captured by the same lens and recorded on a camera. The dichroic mirror is chosen such that it reflects the excitation light but transmits the fluorescent emission light, which is of slightly larger wavelength. The objective is characterized by the numerical aperture NA, which combines the refractive index of the immersion medium n and the maximum angle α at which light is captured.

The resolution of a state-of-the-art microscope is limited by diffraction to a length scale $\lambda/2/\mathrm{NA}$, where λ is the emission wavelength and $\mathrm{NA} = n\sin(\alpha)$ is the so-called numerical aperture (NA) of the microscope, where n is the refractive index of the immersion medium n and α is the marginal ray angle of the collected beam (see Fig. 1.1). For visible light and high-NA immersion objectives this gives resolutions ~ 200 nm. While this is sufficient for imaging many sub-cellular structures, it is insufficient for

providing an image of the molecular machinery that underlies the functioning of the cell. Electron microscopy, however, can reveal image detail on the order of nanometers, but does not allow live-cell imaging nor efficient specific labeling.

Over the last decade a number of optical nanoscopy techniques have been proposed to bridge the resolution gap between electron and conventional light microscopy. Localization microscopy is one of these super-resolution techniques [2–5]. These techniques rely on the localization of single fluorescent molecules, which was already commonly done for example in the field of single particle tracking before the advent of localization microscopy [6]. In localization microscopy, the fluorescent labels are photo-chemically manipulated to switch on and off stochastically, such that at each instant in time only a sparse subset of all molecules is in the on-state in which they can fluoresce. By now there is a whole plethora of stochastic switching mechanisms and suitable fluorescent labels [5]. The required ratio of on/off times to see only single emitters in a region of size λ/NA depends on the labeling density, camera frame time, etc. but is typically less than 1/100. Recording many frames of blinking emitting molecules thus provides a sequence of images of different random subsets of all molecules. The active molecules appear as well separated spots that can be identified and processed to provide the position of the molecules. The localization precision is on the order of $\lambda/\mathrm{NA}/\sqrt{N_{\mathrm{ph}}} \approx 10$ nm with N_{ph} the number of detected photons (typically a few hundred to a few thousand). Assembling the localization data obtained from all frames into one visualization of the final super-resolution image reveals details on the length scale of 10-100 nm; this is about one order below the diffraction limit of conventional light microscopy.

The necessary technology for localization microscopy is not prohibitive: a state-of-the-art setup only requires a fluorescence microscope, powerful light sources and a camera with high quantum efficiency and low readout noise. Next to this hardware, software for image processing and analysis is essential for extracting the desired molecular locations in a robust, optimal and fast way.

1.2. IMAGE PROCESSING STEPS

This section details the image processing and workflow from raw camera frames to the visualization and quantitative analysis of the super-resolution image. Fig. 1.2 shows an overview of this workflow.

1.2.1. SEGMENTATION

The first step in processing the raw frames consists of identifying and segmenting regions of interest (ROIs) that contain the emissions of single fluorescent emitters. Usually this is done by thresholding the raw frames based on the pixel intensity relative to the (local) background noise level [2, 3]. Pixels in which the value is larger than a fixed threshold value or larger than a multiple of the background intensity b are taken as the center of ROIs that are used for localization of possible fluorophore positions in the next processing step.

Besides this basic thresholding approach, more advanced segmentation algorithms

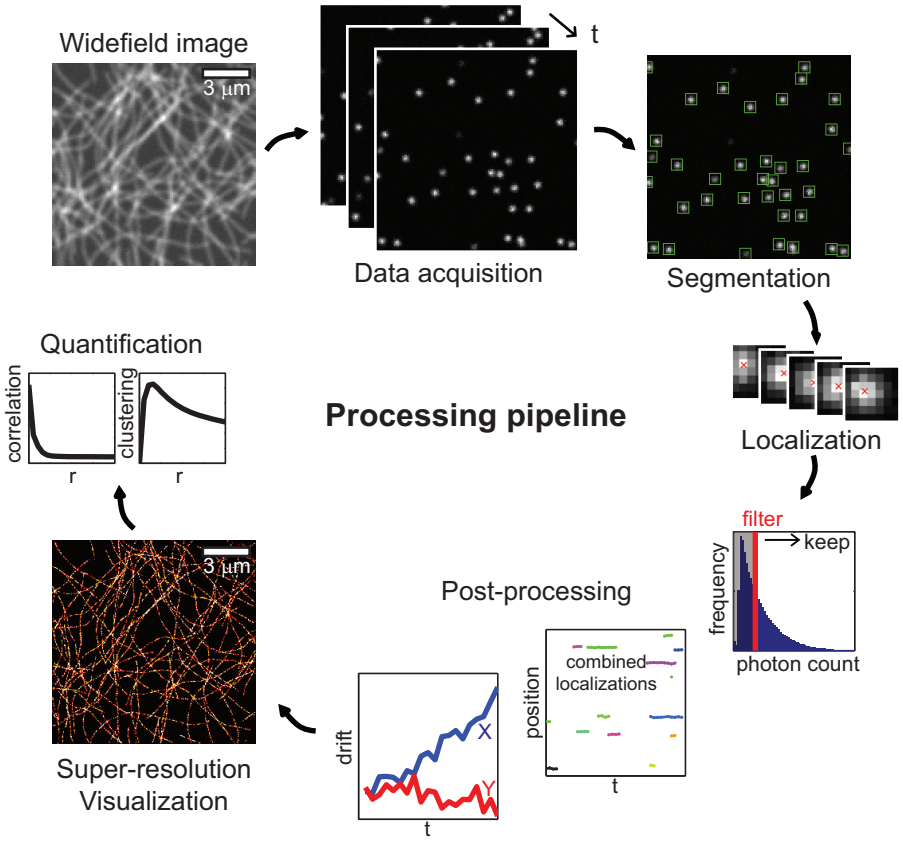

Figure 1.2: The complete pipeline for generating a two-dimensional super-resolution image based on raw frames of sparsely activated fluorophores. The consecutive steps in this pipeline are: acquisition of raw data, segmentation of regions of interest (ROIs), localization of potential fluorophores in the ROIs, post-processing of the localizations (e.g. filtering, frame connection, drift correction), and visualization of the localizations.

have also been proposed. In one proposed method, the raw images are first decomposed into wavelet maps to separate the fluorescence signal from blob-like sources from the background intensity and noise [7, 8]. Subsequently ROIs are identified using a watershed segmentation algorithm.

Another approach to identifying ROIs makes explicit use of local hypothesis testing against the null hypothesis that a pixel belongs to the local background. This is achieved by computing the P-value for each pixel under the assumption that it is drawn from a normal distribution with the local mean and standard deviation of pixel values as parameters [9]. A related method that was proposed for single particle tracking employs a likelihood ratio test in each pixel. In this test, the ratio is computed between the likelihoods of the null hypothesis and that of the hypothesis of having a single emission from a fluorophore in the center of the pixel, assuming that the noise per pixel is Gaussian [10] and the width of the PSF is constant. Under the null hypothesis this ratio follows a chi-squared distribution. Pixels are thus thresholded based on the P-value of the chi-squared distribution for the likelihood ratio value of that pixel. Finally, a recent method employed a likelihood ratio test between the likelihoods of PSF model fits with and without an emitter in each pixel[11]. False discovery rate control was then applied to simultaneously test the significance of all the likelihood ratios in all pixels and use the significant pixels to define ROIs for localization.

Segmentation algorithms typically assume a locally uniform background intensity. This is reasonable if the ROI is only a few pixels wide, unless there is a high degree of autofluorescence and the fluorophores themselves are relatively dim. For such cases, temporal median filtering has been proposed as a method for estimating the local background intensity [12].

1.2.2. SINGLE MOLECULE LOCALIZATION

Once ROIs in the raw data have been segmented, the next step is to estimate the positions of the emitting fluorescent molecules in these regions. The most common approaches for this are the center of mass algorithm (CM) and algorithms that fit a Point Spread Function (PSF) model to the data with a (weighted) least-squares estimator (LS) or a maximum likelihood estimator (MLE).

The CM algorithm computes the center of the intensity distribution. In the absence of any background intensity, this estimate corresponds well to the emitter's true location. However, for non-negligible background intensities this leads to a bias towards the center of mass of the background intensity, which is usually in the center of the ROI. Therefore the local background intensity needs to be estimated and subtracted before the center of mass can be computed.

LS and MLE algorithms attempt to fit a PSF model to the pixel intensities in a ROI. Typically the PSF model consists of a circularly symmetric Gaussian function for two-dimensional localization microscopy:

$$PSF\left(x,y\right) = \frac{1}{2\pi\sigma_g^2} e^{-\frac{(x-x_c)^2+(y-y_c)^2}{2\sigma_g^2}}. \tag{1.1}$$

Here the parameters x_c and y_c denote the position of the emitter in the x- and y-

direction and σ_g specifies the width of the PSF. The Gaussian PSF model is not derived from optical theory, but is instead chosen for its conceptual simplicity and computational efficiency. However, for typical imaging conditions, the Gaussian PSF approximates the theoretical PSF sufficiently well for accurate and precise localization [13, 14].

From the PSF model follows the expected intensity μ_k per pixel k that is fitted to the data:

$$\mu_k = I_0 \int_{A_k} PSF(u,v)\, du\, dv + b, \tag{1.2}$$

where I_0 denotes the sum intensity of the fluorophore, b the expected background photon count and the integration runs over the area A_k of the k-th pixel. The parameters that are to be estimated are thus x_c, y_c, I_0, b and possibly σ_g.

In addition to an optical model for μ_k, fitting the PSF model to the data also requires a noise model for the imaging system. LS algorithms implicitly assume a Gaussian noise model, whereas the slower but more precise MLE algorithms assume a Poissonian noise model. The latter algorithms can be implemented on a graphical processing unit (GPU) to estimate the positions of many emitters in parallel and so achieve real-time computation [15].

An important issue in localization microscopy is the precision with which single fluorophores can be localized [16–18]. This is often analyzed using the concept of the Cramer-Rao lower bound (CRLB), which expresses the lowest variance of any unbiased estimator of a fluorophore's position for a given noise model [19]. For a Poissonian noise model, a good analytical approximation for this bound is given by [20]:

$$\Delta {x_{loc}}^2 = \frac{\sigma_e^2}{N}\left(1 + 4\tau + \sqrt{\frac{2\tau}{1+4\tau}}\right). \tag{1.3}$$

Here N is the number of signal photons, $\sigma_e^2 = \sigma_g^2 + a^2/12$ with a^2 is the pixel area, and τ is a normalized dimensionless background parameter $\tau = 2\pi\sigma_g^2 b/\left(Na^2\right)$ with b the number of background photons per pixel.

The noise in the commonly used sCMOS and EMCCD cameras deviates from the Poisson noise model in two important ways. sCMOS cameras suffer from a small amount of (pixel dependent) Gaussian readout noise, which effectively acts as if b is increased with the variance of the readout noise [21]. EMCCD cameras suffer much less from readout noise due to the electron multiplication process. However, the stochasticity of this process also introduces so-called excess noise, which typically deteriorates the localization variance $\Delta {x_{loc}}^2$ by a factor of two [22]. Balancing the effects of readout noise and excess noise implies that sCMOS cameras are preferred over EMCCD cameras, except in extremely low light conditions that are not typically encountered in localization microscopy [21]. Other considerations in choosing between cameras are that EMCCD cameras have a better photosensitivity, and that sCMOS cameras typically have a smaller physical pixel size and faster frame rate. Finally, sCMOS cameras require a calibration of the gain and readout noise of each pixel for accurate localization, because they often vary substantially among different pixels on the same camera.

1.2.3. POST-PROCESSING

After all the segmented ROIs have been processed by the localization algorithm, post-processing of the raw localizations is needed.

In the first post-processing step raw localizations are usually filtered. The goal of this filtering is to remove localizations that do not represent accurate position estimates of single fluorescent molecules, for example because they are due to overlapping emissions of multiple fluorophores or due to autofluorescence or residual sample contaminations. The filtering is usually done based on information that is returned by the localization algorithm, such as the estimated intensity of the fluorophore, the localization precision, the width of the PSF, and based on the goodness of fit of the model to the data [2, 23]. The latter can be expressed as the (weighted) sum of squared errors between the fitted model and the data or as a ratio between the likelihoods of a fluorophore being present or absent.

In the second post-processing step, localizations originating from the same fluorophore in consecutive frames of the raw image sequence are combined. This is attempted by searching for localizations in subsequent frames that are also spatially proximate, typically within a few times the estimated localization precision. The rationale for this operation is that fluorophores are often visible in multiple consecutive frames before transitioning into a stable dark state or photobleached state, whereas it is unlikely that a nearby fluorophore starts emitting during this time. In practice, fluorophores will not always be localized in all frames before going into a stable dark state, either due to failures of the localization algorithm or due to short blinking events during which the fluorophores briefly stop emitting light. Therefore, spatially proximate localizations are usually still combined if they are only a few frames apart in time [24].

A third common post-processing operation is to correct for drift during the acquisition. Since localization microscopy experiments can last anywhere from a few minutes up to several hours, the sample often moves relative to the detector over distances larger than the localization precision of about 10 nm. This movement can be reduced with hardware solutions, for example by mechanically fixing the objective lens to the stage or by using a control system that actively controls the position of the sample in the image plane [25, 26]. Axial drift, causing the sample to drift out of focus, must be suppressed or controlled just as well as the lateral drift in the image plane.

One option is to add fiducial markers such as fluorescent microbeads to the sample that are visible during the entire acquisition [2]. These fiducial beads can then be localized and used to determine the position of the sample at each moment in time. Another option for drift correction is to estimate the shifts between images of the sample at different time points. This can be achieved by determining the maximum of the cross-correlation [25, 27, 28] between these images, which can either be raw camera images or super-resolution images that visualize the localizations from these frames. The latter, however, is preferred for precision due to the larger high-frequency content of the super-resolution image. The shift estimation should not be done between subsequent images only, as this leads to compounding of registration errors, but between image pairs further apart in time. The main benefit of this approach is that it does not require any changes on the experimental side.

1.2.4. VISUALIZATION

The final step in the processing pipeline from raw data to super-resolution image is the actual visualization of the data. For standard fluorescence microscopy acquisitions, this sampling occurs in the camera where the pixel positions along with the magnification determine the sampling of the image. In addition, the values per pixel are determined by the number of recorded photons per pixel bin that are translated into analog-to-digital units (ADU) with a linear amplification factor. Unlike these standard fluorescence microscopy techniques, localization microscopy does not sample an image at pixel locations but produces a list of coordinates that represent the estimated fluorophore locations. Several methods have been proposed for visualizing localizations in pixelated images that can be shown on a display device. Chapter 3 introduces the most common of these methods and compares them both qualitatively and quantitatively.

1.2.5. EXTENSIONS

Until now, the discussion focused in detail on the complete pipeline for generating a two-dimensional super-resolution image based on raw frames of sparsely activated fluorophores. Here we will address several extensions of this pipeline involving localization in three dimensions, multicolor localization and imaging with overlapping spots.

3D LOCALIZATION

One important extension of two-dimensional localization microscopy imaging is the localization of fluorophores in three dimensions. This requires that information about the axial position of the fluorophore is present and can be extracted from the recordings.

A first approach to this problem is to modify the optical setup such that the shape and/or size of the PSF can be uniquely related to the axial position of the fluorophore. The most common method to achieve this is to introduce astigmatism into the optical system [25]. This causes the minimum width of the PSF in the x and y-direction to occur at different axial positions. The position can then be determined based on the ellipticity of the PSF.

A second approach to obtain the axial position is to modify the setup such that multiple images of the fluorophores with different defocus are simultaneously acquired. This is usually accomplished with a beam splitter that splits the emission light into two channels with different optical path lengths to the camera, such that the two images of the fluorophores are defocused with respect to each other [29].

For both these approaches to 3D localization, the PSF model that is used in the basic 2D localization algorithm needs to be modified. The modified PSF model must provide a specification of the appearance of the fluorophore for the full range of axial positions under consideration and for all image channels on which it is observed. The PSF shapes for 3D localization techniques may be difficult to describe in an analytic formula such as the Gaussian PSF model. An example of this is the double-helix PSF, where a spot doublet rotates with the axial focus position [30]. In such cases, the

PSF can also be determined numerically or empirically. The latter approach then requires subsequent interpolation between the measured axial positions to provide a full specification of a fluorophore's appearance.

MULTICOLOR LOCALIZATION

Another important extension of the basic pipeline is the imaging of different labeled molecules in an experiment. A common method for doing this is to label these molecules with fluorophores with different emission spectra [31]. Wavelength dependent beam splitters are then inserted in the emission light path such that the light at different wavelengths ends up at different parts of the camera or at different cameras. The observed fluorophores can subsequently be classified into the different used species based on the fraction of the photons of each fluorophore ending up in the different color channels. Usually though, the beam splitters are optimally selected such that each color channel only shows a single fluorescent species.

An important problem that arises when imaging fluorophores in different color channels is the registration of the various channels with respect to each other. This needs to be done with an accuracy comparable to the localization precision, which is typically 10% of the camera pixel size or less. A common solution employs fiducial markers that are visible in all color channels. These markers are first imaged and localized, and subsequently a non-affine mapping function is computed which maps the positions of the markers in one color channel to their positions in the other channels [32].

An alternative approach to multicolor imaging is to use photoswitchable dye pairs with different activator dyes but identical reporter dyes [31]. In this way, the wavelength of the illumination can be used to determine which dye pairs are activated and therefore which labeled molecules are imaged. The emitted light of all reporter dyes can then be imaged in a single image on the camera, thus circumventing chromatic aberration problems and obviating the need for a registration procedure between different images.

Finally, approaches have recently been proposed for simultaneous measurement of fluorophores' emission wavelength and positions. One option to accomplish this is to introduce a diffraction grating in the emission light path[33]. This introduces satellite spots adjacent to the main spot. The emission wavelength of the fluorophore can then be estimated from the distances between the spots. A second option is to split the emission light in two paths and introduce a dispersing prism in one of the two paths, which makes it possible to measure the emission spectrum of each emitter in widefield[34].

HIGH DENSITY METHODS

A common problem when localizing fluorophores is that segmented regions of interest contain overlapping spots of multiple active fluorophores. This issue is particularly important when the density of active fluorophores is high. Several solutions have been proposed that attempt to fit a PSF model to each of the spots in the region of interest, either by fitting spots one by one [35] or by finding the model with the number of PSFs that best matches the data [36].

Several other methods for dealing with overlapping spots have been proposed that do not estimate fluorophore positions, but rather estimate the density of fluorophores instead. One such approach is to deconvolve the entire raw dataset [37]. This means that for each frame, a fluorophore density is estimated which has the highest likelihood of producing the experimentally recorded data after convolution with the PSF. To achieve sub-diffraction resolution, this density is sampled with a smaller pixel size than the experimental data. The estimation also incorporates a prior probability for the density per frame that promotes sparsity: because relatively few emitters are active in each frame, the solution should also have few pixels with nonzero density. A related approach to estimating the density is provided by compressive sensing [38, 39]. Unlike the deconvolution approach, an estimate $\rho(x,y)$ is made for each frame independently which minimizes the balanced sum between a data misfit term and sparsity promoting 'L1-norm' of the form $\sum_{x,y}\left|\rho(x,y)\right|$. A subtlety in these approaches is that, in principle, the final estimated density is a relative rather than an absolute estimation of the molecular density, as fluorophores can reappear in the on-state multiple times during the data acquisition.

The final approach to be mentioned here is called the Bayesian analysis of the blinking and bleaching (3B) method [40]. In this method, the on- and off-switching and bleaching behavior of each fluorophore is modeled as a Markov process. Using this model, many different estimates are made of the number of fluorophores, their positions and their activity in each frame. These estimates are then all used to create a probability map of the positions of the fluorophores. A major drawback of this method is its high computational cost.

1.3. MOTIVATION AND OUTLINE OF THIS THESIS

From the introduction above it becomes clear that localization microscopy produces radically different data than other fluorescence microscopy techniques. Although a pixelated image can be rendered, the data consist fundamentally of a list of localizations. Moreover, these data reveal information about biological structures at an order of magnitude smaller length scale than before. Therefore the major question that needs to be addressed is how to correctly interpret these data for maximum insight into the underlying biological structures and processes at the nanoscale. This presents both opportunities and challenges that can be addressed with new quantitative image analysis methods.

The evident opportunity with localization data is that biological structures can now be analyzed at a much smaller length scale. Structures that seem to overlap in diffraction limited images can be clearly distinguished using localization microscopy. Moreover, localizations provide information about individual molecules independent of neighboring molecules. New image analysis methods are therefore needed for quantitative measurements in these images to fully capture the available information. These measurements can then be used to condense this information into comprehensible quantities that facilitate the interpretation of the data, but also to craft and test models of the underlying biological structures and processes.

A substantial challenge with localization microscopy data is to prevent overinterpretation of the details that appear to be visible in the images. Localizations may appear as very determinate features in images because they relate very precisely to the molecules they are derived from. However, there is actually substantial stochasticity involved in the labeling, activation and localization of these molecules. Unlike degradation of images in other types of microscopy, caused for example by photon shot noise or blurring due to diffraction, this is not evident in the images in the same way. Thus new methods are needed to objectively determine what can be interpreted in these images when visual inspection of the images falls short. This prevents that misinterpretation of the data leads to incorrect biological conclusions.

A second major challenge with localization microscopy data is that the analysis methods need to be suitable for the nature of the data. On the one hand this implies the conceptual necessity that measurements must take into account that the data consist of a list of localizations. Therefore they cannot rely on image representations with set pixel sizes. On the other hand there is also a practical issue involved here: image analysis techniques usually assume that structures appear continuous in images and that noise sources operate independently in each pixel. Both of these assumptions are typically not met in localization microscopy. Therefore new image analysis techniques need to be developed specifically for localization microscopy.

This thesis describes several new image analysis techniques that have been developed specifically to address these challenges for a number of key applications. The remainder of this chapter provides an outline of this thesis and an overview the techniques that will be described.

1.3.1. THESIS OUTLINE

Chapter 2 is concerned with resolution measurement. The tremendous improvement in resolution is perhaps the most salient difference between diffraction limited microscopic images and localization microscopy images. This raises the question what the resolution is that is obtained. Chapter 2 introduces an image-resolution measure centered around Fourier Ring Correlation, which is commonly used for resolution-assessment in the field of cryo-electron microscopy[41–43]. We use the FRC resolution to analyze the trade-off between localization precision and labeling density. In addition, we discuss how the FRC can be corrected for spurious correlations that arise when molecules are localized multiple times to prevent biases in the computed resolution.

Chapter 3 is concerned with data visualization. Localization microscopy does not have a natural way of visualizing the data that are produced, although several visualization methods have been proposed. In chapter 3 we use the FRC resolution measurement to objectively compare these visualization methods with simulated data. In addition, we discuss how the different methods conform to users' expectations of the relation between the image and the sample, which have been formed for other fluorescence microscopy methods, such as widefield or confocal imaging.

Chapter 4 is concerned with a major application of localization microscopy which is the quantification of the molecular composition of biological structures. This re-

quires that numbers of localizations can be related to numbers of labeled molecules or binding sites. In chapter 2 we find that, surprisingly, spurious correlations in the FRC can be used to estimate the number of localizations per labeled molecule. Chapter 4 shows how this method is substantially refined by rigorously accounting for photobleaching of fluorophores and the stoichiometry of the number of fluorophores per molecule.

Although the method in chapter 4 enables accurate estimation of the number of localizations per labeled molecule, it is vulnerable to undercounting when not every molecule of interest is indeed labeled. Chapter 5 addresses this problem by extending the method from chapter 4 for well-defined macromolecular complexes such as the nuclear pore complex (NPC). We introduce a method to infer the number of protein copies per subunit in a complex, in which we combine the localizations from multiple NPCs in a single statistical analysis. We determine for which experimental conditions this approach is viable in a simulation study, and subsequently apply the analysis to experimental data of Nup160 and Seh1 molecules in NPCs.

Chapter 6 is concerned with the analysis of multicolor fluorescence images rather than single color images. These images are commonly probed for functional interactions between molecules in different channels using co-localization analysis. This chapter extends this basic co-localization analysis by including the orientations of the structures on which the molecules reside. The combination of co-localization and orientational alignment of structures will be referred to as co-orientation. The analysis is applied to experimental images of cytoskeletal filaments.

Finally, chapter 7 provides some concluding remarks about the work presented in this thesis as well as an outlook and recommendations for future research.

2

MEASURING IMAGE RESOLUTION IN OPTICAL NANOSCOPY

Resolution in optical nanoscopy (or super-resolution microscopy) depends on the localization uncertainty and density of single fluorescent labels and on the sample's spatial structure. Currently there is no integral, practical resolution measure that accounts for all factors. We introduce a measure based on Fourier ring correlation (FRC) that can be computed directly from an image. We demonstrate its validity and benefits on two-dimensional (2D) and 3D localization microscopy images of tubulin and actin filaments. Our FRC resolution method makes it possible to compare achieved resolutions in images taken with different nanoscopy methods, to optimize and rank different emitter localization and labeling strategies, to define a stopping criterion for data acquisition, to describe image anisotropy and heterogeneity, and even to estimate the average number of localizations per emitter. Our findings challenge the current focus on obtaining the best localization precision, showing instead how the best image resolution can be achieved as fast as possible.

Parts of this chapter have been published as: Nieuwenhuizen, RPJ., Lidke, K.A., Bates, M., Leyton Puig, D., Grünwald, D., Stallinga, S. & Rieger, B. *Nat. Methods* **10**, 557–562 (2013). [44]

2.1. INTRODUCTION

The first and foremost law of conventional optical imaging science is that resolution is limited to a value on the order of λ/NA, with λ equal to the wavelength of light and NA to the numerical aperture of the imaging lens. Rayleigh and Sparrow captured this law by empirical resolution criteria. These criteria were placed on solid foundations by Abbe and Nyquist, who defined resolution as the inverse of the spatial bandwidth of the imaging system. This diffraction limit, however, can be overcome by numerous optical nanoscopy techniques, notably stimulated emission depletion(STED[45]), reversible saturable optical fluorescence transitions (RESOLFT[46]), the family of localization microscopy techniques such as photoactivated localization microscopy (PALM), stochastic optical reconstruction microscopy (STORM), ground state depletion microscopy followed by individual molecule return (GSDIM), and direct STORM (*d*STORM) [2, 3, 47, 48] and statistical methods as blinking fluorescence localization and super-resolution optical fluctuation imaging (SOFI) [49, 50].

These revolutionary developments raise the question: what is resolution in diffraction-unlimited imaging. The resolving power of the instrument is often coupled to the uncertainty of localizing single emitters, that is, point sources. The closely related two-point resolution can be given a precise meaning in the context of localization microscopy[51], thus generalizing the Rayleigh criterion of conventional microscopy. These concepts characterize the resolution in images in which the structure of interest can be defined by a limited number of molecules – such as images of the nuclear pore complex[52] – or when investigating the relative position of different molecules[53]. However, if more-or-less continuous structures with a large number of potential labeling sites are imaged – for example, actin filaments or organelle membranes – then it is clear that the average density of localized fluorescent labels must also play a role. As early as the first demonstration of localization microscopy for cell imaging[2], it was noted that "both parameters – localization precision and the density of rendered molecules – are key to defining performance...". The effects of labeling density and photoswitching kinetics on resolution have since been investigated experimentally[54, 55]. Recently, an estimation-theoretic resolution concept was presented[56] that combines both labeling density and localization uncertainty using an a priori model of the sample. We conclude from all prior work that neither the average density of localized molecules needed for random Nyquist sampling nor the localization uncertainty alone is a suitable measure to characterize the resolution. In addition, the resolution depends on a multitude of other factors such as the link between the label and the structure, the underlying spatial structure of the sample itself, and the extensive data processing required to produce a final super-resolution image comprising, for example, single-emitter candidate selection and localization algorithms. Ultimately, only an integral, image-based resolution measure, not depending on any a-priori information, is suitable for determining what level of detail can be reliably discerned in a given image.

Here we propose an image-resolution measure that can be com¬puted directly from experimental data alone. It is centered on the FRC (or, equivalently, the spectral signal-to-noise ratio), which is commonly used in the field of cryo-electron mi-

croscopy (cryo-EM) to assess single-particle reconstructions of macromolecular complexes[41–43]. We have used the FRC resolution to analyze the trade-off between localization uncertainty and labeling density, and we have applied it to monitor resolution buildup during data acquisition and to compare different localization algorithms. Quantification of the spatial correlations in the image leading to this resolution measure also provides a means to estimate the average number of localizations per emitter contributing to the image.

2.2. RESULTS

To compute the FRC resolution, we divide the set of single-emitter localizations that constitute a super-resolution image into two statistically independent subsets, which yields two subimages $f_1(\vec{r})$ and $f_2(\vec{r})$, where $\vec{r}$ denotes the spatial coordinates. Subsequent statistical correlation of their Fourier transforms $\hat{f}_1(\vec{q})$ and $\hat{f}_2(\vec{q})$ over the pixels on the perimeter of circles of constant spatial frequency with magnitude $q = |\vec{q}|$ gives the FRC[42]

$$FRC(q) = \frac{\sum_{\vec{q}\in\text{circle}} \hat{f}_1(\vec{q})\,\hat{f}_2(\vec{q})^*}{\sqrt{\sum_{\vec{q}\in\text{circle}} \hat{f}_1(\vec{q})^2}\sqrt{\sum_{\vec{q}\in\text{circle}} \hat{f}_2(\vec{q})^2}}. \tag{2.1}$$

For low spatial frequencies, the FRC curve is close to unity; and for high spatial frequencies, noise dominates the data and the FRC decays to 0. The image resolution is defined as the inverse of the spatial frequency for which the FRC curve drops below a given threshold. We evaluated different threshold criteria used in the field of cryo-EM[41, 57–59] and found that the fixed threshold equal to $1/7 \approx 0.143$ [59] is most appropriate for localization microscopy images (see Appendix 2.A.1). The FRC resolution concept and the steps needed to compute it are illustrated in Fig. 2.1. FRC resolution describes the length scale below which the image lacks signal content; smaller details are not resolved in the image. Resolution values will always be larger than those based on localization uncertainty or labeling density alone.

2.2.1. THEORETICAL CONSIDERATIONS AND SIMULATIONS

FRC resolution allows predictions to be made about the impact of different imaging and sample parameters on the achievable resolution; these predictions are based on the expectation value of the FRC curve, which is given by

$$\langle FRC(q)\rangle = \frac{\sum_{\vec{q}\in\text{circle}} \left(Q + N\left|\hat{\psi}(\vec{q})\right|^2\right)\exp\left(-4\pi^2\sigma^2 q^2\right)}{\sum_{\vec{q}\in\text{circle}} \left[2 + \left(Q + N\left|\hat{\psi}(\vec{q})\right|^2\right)\exp\left(-4\pi^2\sigma^2 q^2\right)\right]}, \tag{2.2}$$

where N is the total number of localized emitters, σ is the average localization uncertainty and $\hat{\psi}(\vec{q})$ denotes the Fourier spectrum of the spatial distribution of the flu-

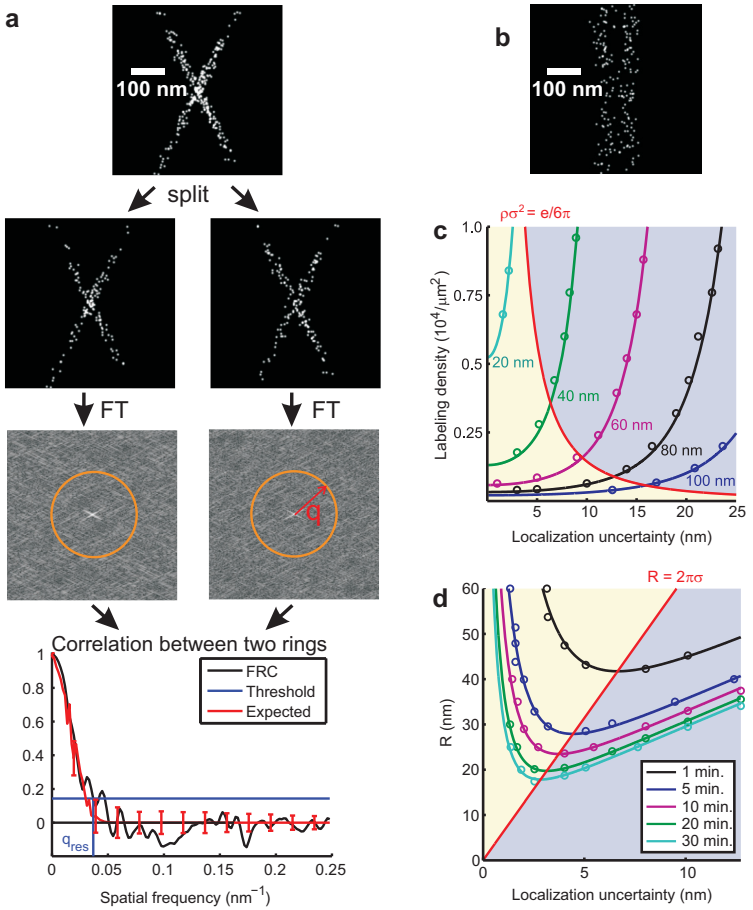

Figure 2.1: The FRC principle and trade-off between localization uncertainty and labeling density. (a) All localizations are divided into two halves, and the correlation between their Fourier transforms over the perimeter of the circle in Fourier space of radius q is calculated for each q, resulting in an FRC curve indicating the decay of the correlation with spatial frequency. The image resolution is the inverse of the spatial frequency for which the FRC curve drops below the threshold $1/7 \approx 0.143$, so a threshold value at $q = 0.04$ nm^{-1} is equivalent to a 25 nm resolution. Error bars indicate theoretically expected s.d. (Appendix 2.A.2). (b) Simulated localization microscopy image of a line pair with mean labeling density $\rho = 2.5 \times 10^3$ per μm^2 in the area occupied by the lines and localization uncertainty $\sigma = 7.6$ nm (line distance 70 nm, cosine-squared cross-section). (c) Constant resolution in theory (lines) and simulation data (circles) for line pairs as in b as a function of localization uncertainty and labeling density. Regions of localization uncertainty–limited resolution (blue) and labeling density–limited resolution (yellow) are separated by the red line $\rho\sigma^2 = e/(6\pi)$. (d) Simulation results for localization uncertainty versus image resolution for different fixed total measurement times. Camera frame rates were varied to match the on-times of the emitter. The minima of the curves fall on the line $R = 2\pi\sigma$ that separates the yellow region (not enough emitters localized) from the blue region (emitters not localized precisely enough).

orescent emitters (for a derivation, see Appendix 2.A.2). The parameter Q is a mea-

sure for spurious correlations due to, for example, repeated photoactivation of the same emitter. Each emitter contributing to the image is localized once for $Q = 0$ and in general $Q/(1-\exp(-Q))$ times on average, provided the emitter activation follows Poisson statistics. Careful analysis of the spatiotemporal correlations in the image and the emitter activation statistics (including effects of photobleaching) can provide a way to estimate Q and correct for its effect on image resolution as well as to estimate the number of fluorescent labels contributing to the image, as is discussed in section 2.2.3. Analytical expressions for the resolution can be derived for particular object types (such as line pairs) often used in resolution definitions (Appendix 2.A.3). The resolution R for an image consisting of two parallel lines with a cosine-squared cross-section and mean labeling density ρ in the area occupied by the lines is

$$R = \frac{2\pi\sigma}{\sqrt{W\left(6\pi\rho\sigma^2\right)}}, \tag{2.3}$$

where $W(x)$ is the Lambert W-function[60]. Two regimes can be identified in which changes in either labeling density or localization uncertainty have the most impact on improving the resolution. At the boundary between these regimes, the relative gains in resolution due to changes in either quantity are equally large. This trade-off occurs at $R = 2\pi\sigma$ (Appendix 2.A.4), which corresponds to

$$\rho\sigma^2 = \frac{e}{6\pi} \approx 0.14. \tag{2.4}$$

The region $\rho\sigma^2 < e/(6\pi)$ is labeling-density limited, whereas $\rho\sigma^2 > e/(6\pi)$ is localization-uncertainty limited (Fig. 2.1). The exact boundary between the two regimes depends on the underlying object, so the boundary value for the two-line example serves only as a rule of thumb (Appendix 2.A.4). For example, for M parallel lines, we obtain a value $e/(3\pi M)$. From this it may be inferred that the trade-off occurs for a value smaller than 0.14 for any intricate but irregular object structure.

The same trade-off as above may also manifest itself in the optimization of image resolution, given a fixed total acquisition time (Fig. 2.1b,d). Suppose that the photon count per localization is improved by increasing the on-times of the emitters while keeping the emitters' brightness and the number of simultaneously active emitters constant: this then also reduces the total number of labels that can be localized in a given acquisition time. Therefore, longer single-emitter events yield more accurate localizations, but at the expense of a lower recorded emitter density[2, 61]. Again, the optimum is $R = 2\pi\sigma$, independent of the object (Appendix 2.A.4). Tuning the on-times as described here may be done in the design phase of an experiment by the choice of label or buffer composition.

2.2.2. RESOLUTION BUILDUP DURING DATA ACQUISITION

To test and evaluate the FRC resolution measure, we imaged tubulin networks in fixed HeLa cells labeled with Alexa Fluor 647 using localization microscopy (Fig. 2.2a and section 2.4). The resolution improved with acquisition time (Fig. 2.2b–f), or, equiv-

alently, with the density of localized labels. The trade-off point between the localization density and uncertainty limited regimes lay at $R = 2\pi\sigma = 61$ nm. Therefore, the resolution values for Figs. 2.2b–e were labeling-density limited, and the trade-off point was just crossed at the end of the data acquisition. Real-time monitoring of the resolution buildup by real-time single-molecule fitting algorithms[62] provides a much needed stopping criterion for localization microscopy data acquisitions. The FRC resolution concept is also sensitive to differences in localization uncertainty (Fig. 2.2g–i). Maximum-likelihood estimation ($R = 58 \pm 1$ nm) is theoretically optimal[15] and is slightly better than least-squares fitting ($R = 60 \pm 1$ nm) and superior to centroid fitting ($R = 88 \pm 2$ nm). All specified uncertainties are computed from 20 FRC resolution estimates obtained from different random assignments of localizations to half data sets (s.e.m.). Because the effect of the parameter Q on the resolution for this data set was found to be negligible, it was not necessary to correct for it.

Sample drift is a common annoyance in optical nanoscopy, as motion has to be limited to a few nanometers over typical acquisition times of many minutes. We analyzed the drift in localization microscopy data of the actin cytoskeleton of a fixed HeLa cell labeled with phalloidin coupled to Alexa Fluor 647 (Fig. 2.2j) without the use of fiducial markers[27]. A drift of $\sim 70 - 100$ nm was found with this procedure and corrected for. Computed resolution values before drift correction (Fig. 2.2k,l; $R = 79 \pm 1$ nm) were much worse than those after drift correction (Fig. 2.2m,n; $R = 54 \pm 1$ nm), which is in agreement with the apparent detail in the images (Fig. 2.2k–n). For this data set also, the effect of Q was found to be negligible.

2.2.3. ESTIMATION OF THE NUMBER OF LOCALIZATIONS PER EMITTER

Multiple localizations per emitter due to, for example, repeated photoactivations lead to spurious correlations between the two image halves, resulting in overoptimistic resolution values. This is particularly problematic for cases involving large numbers of localizations per emitter, low localization uncertainties and low labeling densities.

The FRC can be corrected for this effect by estimating the spurious correlation parameter Q in Eq. 2.2. To that end, we divided the numerator of the FRC by the weighted average of the function $\exp(-4\pi^2\sigma^2 q^2)$ over the distribution of localization uncertainties. The parameter Q is proportional to the minimum of that curve, which takes the form of a broad plateau if $Q \gg 1$ (section 2.4). To test this method, we analyzed a two-color image of tubulin labeled with both Alexa Fluor 647 and Alexa Fluor 750 ([63]; Fig. 2.3a–c). The resolution values for Alexa Fluor 647 and Alexa Fluor 750 without correction (25 ± 1 nm and 34 ± 1 nm, respectively) were much lower than the resolution derived from the cross-channel, that is, when taking the two color images as data halves for the FRC (118 ± 2 nm). This difference was due to the multiple localizations per emitter, which affect the one-color FRC curves but not the cross-channel curve. The FRC curves and attendant resolution values were much more similar after correction. The remaining differences in the calculated resolution values reflected the differences in labeling density (the density of localizations was 4.0×10^3 μm^2 for Alexa Fluor 647 and 1.3×10^3 μm^2 for Alexa Fluor 750) and localization uncertainty (9.2 nm and 12 nm, respectively). We checked the data sets of Fig. 2.2a,j for spu-

rious correlations and found $Q = 0.28$ and $Q = 0.33$, respectively, which led to corrected resolution values equal to 62 ± 2 nm and 66 ± 1 nm, respectively. This means that neglecting to correct for spurious correlations gave rise to an underestimation of the resolution value by only several nanometers. These estimated values for Q are smaller than the values for the data set of Fig. 2.3 primarily because Q scales with the data acquisition time, which is much smaller in Fig. 2.2a,j than the 1.4×10^5 frames in 39 min and 3.0×10^4 frames in 25 min for Alexa Fluor 647 and Alexa Fluor 750, respectively (Fig. 2.3). Other reasons for the discrepancy of Q values may be found in differences in photobleaching behavior and preprocessing for candidate selection of single-emitter events (from false positives, for example). Finally, the density of localizations for Fig. 2.2 is close to 10^4 μm^2, 1–2 orders of magnitude larger than the density in other data sets. In the limit of high labeling density, the effects of spurious correlations are negligible compared to the intrinsic image correlations (sections 2.A.2 and 2.A.3). We point out that the correction method appears to be quite sensitive to (the distribution of) the localization uncertainty, and to any residual effects of drift, and must therefore be applied with care.

The estimation of the average number of localizations per emitter from the spurious correlation parameter Q also makes it possible to count the actual number of fluorescent labels that contribute to the overall image. Although such counting has been demonstrated for irreversibly photoactivatable fluorophores[64, 65], only a few studies have investigated the possibility of counting with reversibly photoswitchable dyes[66, 67]. One approach is based on pair correlation functions[65, 66], but unlike our method, it requires a model for the correlations in the spatial distribution of the fluorescent labels. Neither do we require a calibration experiment, in contrast to cluster kymography analysis, for example[67]. A potential complication for our method is that deviations from Poisson statistics of emitter activations due to photobleaching may lead to overestimation and in some cases underestimation ($Q < 1$) of the number of localizations per emitter (Appendix 2.A.2). The same caveat applies to alternative approaches[66, 67]. Chapter 4 will discuss how these deviations from Poisson statistics may be overcome. Calibration experiments on sparsely distributed labeled antibodies on a glass surface indicated that Q values for the data (Fig. 2.3) overestimated the true number of localizations per emitter by a factor of 1.5 for Alexa Fluor 647 and 1.7 for Alexa Fluor 750, even though the Q parameter was estimated much more accurately. Taking into account all factors leads to an estimated number of localizations per molecule equal to 7 for Alexa Fluor 647 and 11 for Alexa Fluor 750, which is in qualitative agreement with values reported earlier[68]. We found the labeling densities to be 6.0×10^4 μm^2 (Alexa Fluor 647) and 1.2×10^2 μm^2 (Alexa Fluor 750).

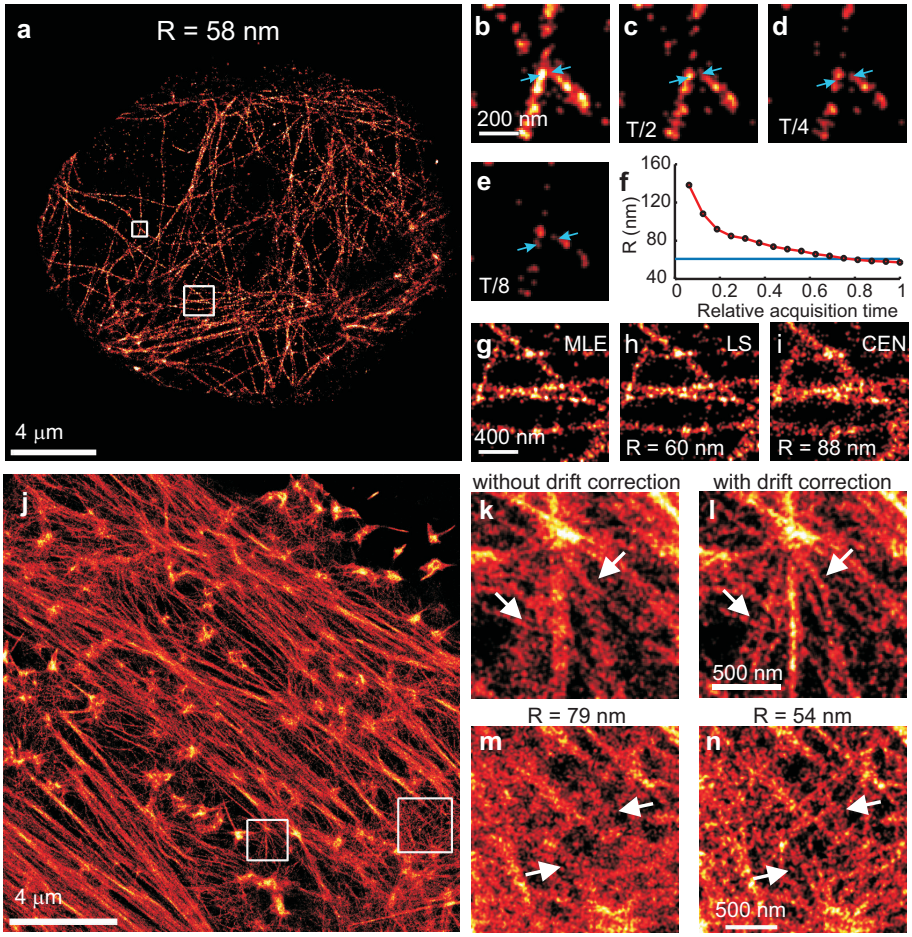

Figure 2.2: The effect of localization density and data processing on resolution. (a) Localization microscopy image of tubulin labeled with Alexa Fluor 647 in a HeLa cell ($R = 58 \pm 1$ nm for the whole image, where uncertainty reflects s.e.m. of 20 random repeats of FRC resolution calculation). Acquisition time was $T = 12$ min within 1.4×10^4 frames, the localization uncertainty was $\sigma = 9.7$ nm after merging nearby localizations in subsequent frames (2.4) and the density of localizations was $\rho = 6.0 \times 10^2$ per μm^2. (b–e) Magnified insets of two crossing filaments (upper boxed region in a) constructed from fewer time frames showing poorer resolution (indicated by the distance between the blue arrows). (f) Resolution (R) buildup during acquisition, with $R = 2\pi\sigma$ plotted in blue, showing a transition from density-limited to precision-limited resolution. (g–i) Reconstructions of lower boxed region in a by different localization algorithms showing maximum-likelihood estimation (g; MLE, $R = 58 \pm 1$ nm), least squares fitting (h; LS, $R = 60 \pm 1$ nm) and centroid fitting (i; CEN, $R = 88 \pm 1$ nm). (j) Localization microscopy image of the actin cytoskeleton (F-actin) of a fixed HeLa cell labeled with phalloidin coupled to Alexa Fluor 647 after correction for sample drift of ~ 70–100 nm during acquisition. The image was obtained from 5.0×10^4 frames in 8 min ($\sigma = 8.0$ nm, $\rho = 8.2 \times 10^3$ μm^{-2}, $\rho\sigma^2 = 0.52$, $2\pi\sigma = 50$ nm). (k–n) Magnified insets of reconstructions before (k,l; left boxed region in j) and after drift correction (m,n; right boxed region in j). Resolutions before and after drift correction were $R = 79 \pm 2$ nm and $R = 54 \pm 1$ nm, respectively. The arrows indicate regions of sharper detail after drift correction.

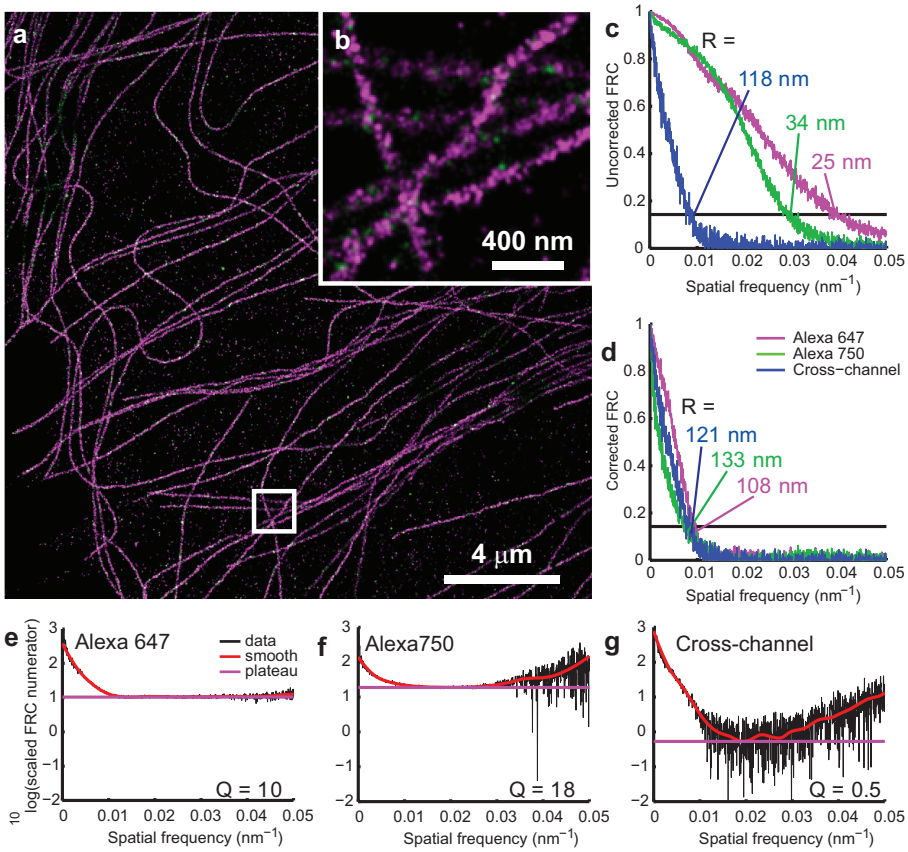

Figure 2.3: Spurious correlations from a two-color localization microscopy image. (a) Overview image of a tubulin network labeled with both Alexa Fluor 647 (magenta) and Alexa Fluor 750 (green). The inset shows the quality of registration. (b) Uncorrected FRC curves for the magenta and green channels are higher than that for the cross-channel because of spurious correlations from repeated photoactivations of individual emitters, which result in overly optimistic resolution values ($R = 25 \pm 1$ nm and $R = 34 \pm 1$ nm, respectively, compared to 118 ± 2 nm for the cross-channel). Uncertainty reflects s.e.m. of 20 random repeats of the FRC resolution calculation. (c) FRC curves corrected for spurious correlations all yield similar resolution values (108 ± 1 nm for Alexa Fluor 647, 133 ± 2 nm for Alexa Fluor 750, 121 ± 2 nm for the cross-channel). (d–f) Scaled FRC numerator curves showing a plateau for intermediate spatial frequencies, which is used to estimate the correction term and Q parameter. For this correction (2.4) we used a mean and width of the distribution of localization uncertainties equal to 9.2 nm and 2.8 nm for Alexa Fluor 647 and 12 nm and 2.0 nm for Alexa Fluor 750.

2.2.4. RESOLUTION IN 3D, ANISOTROPIC AND HETEROGENEOUS CONTENT

The FRC resolution concept can be generalized and extended in several ways. The first way addresses image anisotropy, which may arise, for example, from line-like features in the image or from differences between the axial and lateral resolving power in 3D imaging[69]. Anisotropic image resolution can be described similarly to FRC by correlating the two data halves in Fourier space over a line in 2D (Fourier line correlation, FLC) or plane in 3D (Fourier plane correlation, FPC) perpendicular to spatial frequency vectors $\vec{q}$. Spatial frequencies for which the FLC or FPC is above the threshold in the image are resolved. The FPC for a 3D image of a tubulin network labeled with Alexa Fluor 647 (Fig. 2.4) using the bifocal method[70] shows clear anisotropy with filaments oriented mostly in the xy plane along the x direction. Therefore, the FPC is highest in the y direction, orthogonal to the filaments, and worst in the z direction. Another way in which the FRC resolution concept can be generalized targets

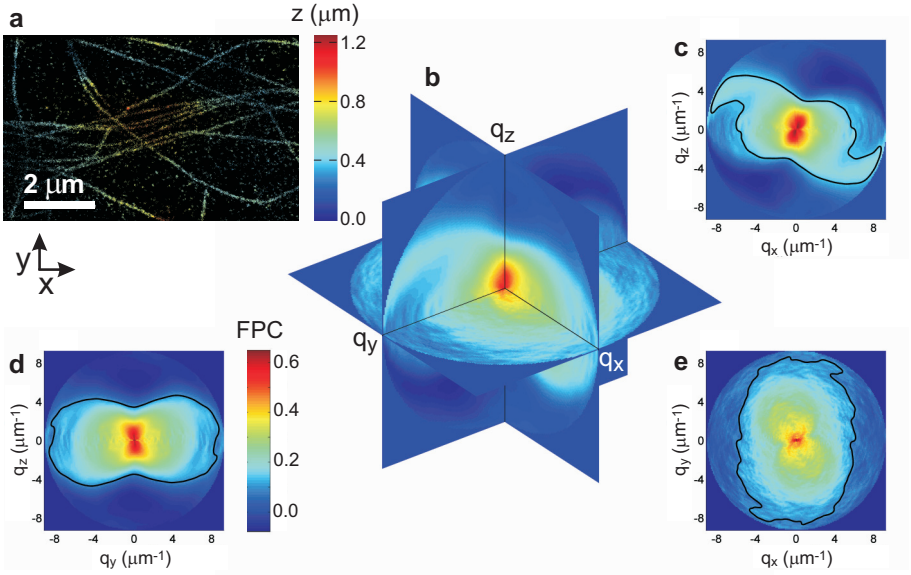

Figure 2.4: Spurious correlations from a two-color localization microscopy image. (a) Representation of a 3D localization microscopy image of a tubulin network, with the axial coordinate in false color. (b) Orthogonal slices of the Fourier plane correlation (FPC). (c–e) Cross-sections of the FPC for this data set in the $q_x q_z$ plane (c), $q_y q_z$ plane (d) and $q_x q_y$ plane (e), with added threshold contours for $FPC = 1/7$ (black lines). The FPC clearly shows the anisotropy of image content resulting from the line-like structure of the filaments (the highest image resolution is perpendicular to the filaments) as well as from the anisotropy in localization uncertainty (the lowest resolution is in the axial direction).

local variations in the density of the sample's spatial structure. Local image resolution can be obtained from resolution values of overlapping subimage patches.

2.3. DISCUSSION

The FRC resolution concept can be naturally extended to STED, imaging with an extended diffraction limit such as structured illumination microscopy[71], and conventional confocal and widefield imaging. It is possible not only to conceptually extend the FRC method but also to measure the resolution directly from experimental data. This stands in contrast to recently introduced unified resolution concepts[56], which provide only a rigorous theoretical framework. The FRC resolution is most easily computed from two images of the same scene that differ only in noise content. The resolution then depends on the signal-to-noise ratio, spectral image content and (effective) optical transfer function. The width of the effective point-spread function replaces the role of the localization uncertainty. In the limit of infinitely high signal-to-noise ratio, the FRC resolution reduces to Abbe's diffraction limit (for the conventional fluorescence imaging modalities) or to the limit that has been proposed for STED[72] (Appendix 2.A.5). For any extension of the FRC concept, systematic dependencies between image halves due to, for example, fixed-pattern noise or common alignment references must be prevented. Alignment references have caused particular problems for the application of the FRC concept in the field of single-particle cryo-EM[73].

We envision that FRC resolution may be used for characterizing and optimizing fluorescence labeling and data processing strategies in general. The FRC resolution may be used to rate different approaches for faster super-resolution image buildup that deal with high densities of simultaneously active emitters[35, 36, 38]. Access to the number of molecules in a multimolecular complex, such as the spliceosome or transcription machinery, without the need to make assumptions about their spatial structure adds a new dimension to the application of optical nanoscopy with reversibly switchable fluorescent dyes. Most notably, a resolution measure as proposed here is indispensable for advancing the blooming field of optical nanoscopy because it provides a quantitative guide for reliable interpretation of data, thus enabling sound biological conclusions.

2.4. MATERIALS AND METHODS

2.4.1. COMPUTATION OF FRC AND FRC RESOLUTION

COMPUTATION

The starting point for the computation of the FRC resolution is a set of estimated fluorophore locations along with the numbers of the frames from which they originate. In order to calculate the resolution from a set of localizations $\{\vec{r}_i\}$, the following steps were followed for experimental data:

1. The set of N localizations was divided into two half sets N_1 and N_2 of size $N/2$ by splitting the timeseries into blocks of 500 frames and assigning an equal number of blocks randomly to each half set. Alternatively, half sets could also have been obtained by simply assigning localizations randomly to half sets or by splitting the timeseries in two parts.

2. The localizations from each half set were binned into images f_1 and f_2. For the experimental data, the bin sizes (i.e. the superresolution pixel sizes) were taken to be p times smaller than the camera pixel size, typically $p = 10$ (10 nm backprojected pixel size). See Appendix 2.A.3 for a further discussion about the choice of pixel size.

3. An intensity mask $M(\vec{r})$ was applied to the binned images to taper the edges. For this work, a Tukey window[74] was used which has the form $M(\vec{r}) = m(x)\, m(y)$ where:

$$m(x) = \begin{cases} \sin^2(4\pi x/L) & \text{if } x < L/8 \text{ and } x > 7L/8 \\ 1 & \text{if } x \geq L/8 \text{ and } x \leq 7L/8 \end{cases} \tag{2.5}$$

   Here L denotes the size of the field of view.

4. Both binned images were Fourier transformed.

5. The FRC was obtained for spatial frequencies $q = 1/L, 2/L, \ldots$ by calculating:

$$FRC(q) = \frac{\sum\limits_{\vec{q} \in \text{ring}} \hat{f}_1(\vec{q})\, \hat{f}_2(\vec{q})^*}{\sqrt{\sum\limits_{\vec{q} \in \text{ring}} \hat{f}_1(\vec{q})^2} \sqrt{\sum\limits_{\vec{q} \in \text{ring}} \hat{f}_2(\vec{q})^2}}, \tag{2.6}$$

   where $\vec{q} \in \text{ring} \equiv \{\vec{q} \mid q \leq |\vec{q}| < q + \delta q\}$ where $\delta q = 1/L = l$ is the pixel size in Fourier space.

6. Since the FRC curve is often quite noisy, it was smoothed with a LOESS (locally estimated scatterplot smoothing) method[75] with a second order polynomial and tri-cube weight function around each q over a span $\Delta q = 1/(20l)$, where l is the pixel size.

7. The first intersection q_{res} between the resulting smoothed FRC curve and the threshold was used to finally calculate the resolution $R = 1/q_{\text{res}}$.

Please note, that the term $\sum_{\vec{q} \in \text{ring}} \hat{f}_1(\vec{q}) \hat{f}_2(\vec{q})^*$ is real, if $f_1(\vec{r})$ and $f_2(\vec{r})$ are real, because then it holds that $\hat{f}(\vec{q}) = \hat{f}(-\vec{q})^*$ and in each term $f(\vec{q}) + f(-\vec{q})$ the complex part cancel out. Note that we assume square sized images $f_1(\vec{r})$ and $f_2(\vec{r})$ for ease of computation. If the images are non-square the images must be extended through zero padding or the ring averaging must be replaced by averaging over ellipses as the pixel size in Fourier space depends on the linear size of the image. The uncertainty of the FRC resolution value is found by evaluating the resolution for typically 20 different random splittings of the entire dataset. The resulting mean and standard deviation are the reported numbers.

BRIGHT SPOTS

Localization microscopy images sometimes contain clusters of localizations with a diameter of a few times the localization precision σ where the density of localizations is very high. These clusters may for example be due to anomalous fluorescent molecules that are active during a large part of the total measurement time. However, the localizations in these clusters can represent a substantial fraction of all localizations and are very close together. This close spatial proximity translates into large correlations in the high spatial frequency components of the images that are not representative of the other parts of the image. Therefore these clusters are considered to be artifacts. Thus it is often necessary to suppress the influence of these clusters. One approach that we adopted to this end was to mask out these clusters if they were not on the main structures. Remaining bright spots were suppressed by the procedure to merge nearby localizations in time, which is further outlined below, and by limiting the number of binned localizations per superresolution pixel to a maximum of 5. For the data of Fig. 2.2a all these approaches were adopted: most bright spots were removed by segmenting the cell in the widefield image and deleting all localizations outside the cell. For the data in Fig. 2.2j, no masking of regions outside the cell was applied since the entire field of view is filled. For the other experimental datasets only the merging of nearby localizations was used to reduce the influence of bright spots.

SPURIOUS CORRELATIONS

Multiple localizations of the same emitter result in substantial correlations at all spatial frequencies. The result is that the numerator of the FRC contains a term $(2\pi qL)\,NQ\exp\left(-4\pi^2q^2\sigma^2\right)$ (or the weighted average of this quantity over the distribution of localization uncertainties) that belongs to the denominator of the FRC. Here L is the size of the field of view. Correction for this effect then requires that this spurious term is estimated and corrected for. The first step in estimating the spurious correlations consisted of calculating the numerator of the FRC and dividing by the number of pixels in the Fourier ring resulting in a function $v\left(q\right)$:

$$v\left(q\right) = \frac{1}{2\pi qL}\sum_{\vec{q}\,\in\,\text{ring}} \hat{f}_1\left(\vec{q}\right)\hat{f}_2\left(\vec{q}\right)^*. \tag{2.7}$$

Subsequently, $v\left(q\right)$ was divided by $H\left(q\right)\text{sinc}\left(\pi qL\right)^2$, where $H\left(q\right)$ is the factor in the correlation averages related to the localization uncertainties which depends on the mean σ_m and width $\Delta\sigma$ of the distribution of localization uncertainties, which is taken to be Gaussian (see Appendix 2.A.2):

$$H\left(q\right) = \frac{1}{\sqrt{1+8\pi^2\Delta\sigma^2q^2}}\exp\left(-\frac{4\pi^2\sigma_\text{m}^2q^2}{1+8\pi^2\Delta\sigma^2q^2}\right). \tag{2.8}$$

Also the low pass filtering effect of the localization uncertainty and finite pixel size was removed through division. Therefore the result should have an expectation value $\frac{1}{4}N\left(Q+NS\left(q\right)\right)$. Here $S(q)$ is defined formally in Eq. (S.23), as the ring average of the spectral signal content of the image. In order to estimate $NQ/4$ in a robust manner,

the logarithm of $\left|v(q)/H(q)/\mathrm{sinc}(\pi qL)^2\right|$ was taken and smoothed and $\log(NQ/4)$ was then estimated as the minimum of this smoothed logarithm. The smoothing was accomplished through robust LOESS (locally estimated scatterplot smoothing)[75] with a second order polynomial and tri-cube weight function around each q over a span $\Delta q = 1/(10l)$.

The logarithm of $\left|v(q)/H(q)/\mathrm{sinc}(\pi qL)^2\right|$ typically looks like a function that initially decreases, then levels off to a constant plateau value and finally increases again. The mean and width of the assumed Gaussian distribution of localization uncertainties are adjusted to get a horizontal plateau of the largest possible width. This procedure, though manually executed, can be used to estimate these parameters with an accuracy of typically one to two nanometer. A plateau results when $Q \gg NS(q)$, so that $\left|v(q)/H(q)/\mathrm{sinc}(\pi qL)^2\right| \approx NQ/4$. For large q, the noise on the absolute value of $v(q)$, which has an expected value of about $N/\sqrt{32\pi qL}$, is blown up by the factor $1/H(q)/\mathrm{sinc}(\pi qL)^2$. Therefore the aforementioned procedure will also yield a narrow plateau and thus a finite estimate for Q even in the case where $Q \ll NS(q)$, i.e. when there is no plateau due to Q. In this case Q will be overestimated and therefore there will be an overcorrection for spurious correlations.

2

FLC AND FPC COMPUTATION

The Fourier Line Correlation (FLC, $n = 2$ dimensions) or Fourier Plane Correlation (FPC, $n = 3$ dimensions) are evaluated numerically as follows. The entire image is again split into two sub-images $f_1(\vec{r})$ and $f_2(\vec{r})$, with Fourier transforms $\hat{f}_1(\vec{q})$ and $\hat{f}_2(\vec{q})$. The FLC and FPC are defined similar to the FRC or FSC as:

$$\frac{G_{12}(\vec{q})}{\sqrt{G_{11}(\vec{q})\,G_{22}(\vec{q})}}, \tag{2.9}$$

where the correlation averages are now defined as averages over lines ($n = 2$) or planes ($n = 3$) perpendicular to $\vec{q}$:

$$G_{jl}(\vec{q}) = \sum_{\vec{q}'\in \text{line/plane}} \hat{f}_j(\vec{q}')\,\hat{f}_l(\vec{q}')^*, \quad j,l = \{1,2\}, \tag{2.10}$$

where the summation over the line/plane means $\vec{q}' \in \{\vec{q}' | (\vec{q}' \pm \vec{q})\vec{q} = 0\}$.

For $n = 2$ the implementation of a line average boils down to a Radon transform, executed with the MATLAB (The Mathworks) function 'radon'. For $n = 3$ the plane average is done by first rotating $\hat{f}_1(\vec{q})$ and $\hat{f}_2(\vec{q})$ to a grid with $\vec{q}$ oriented along the z-axis, executed with the function 'rotation3D' of the DipImage toolbox (www.diplib.org), and subsequent averaging over the x and y directions in the rotated frame. Averaging over lines/planes with an orientation that is not aligned with one of the coordinate axes is possible but computationally much more costly than the rotation procedure. In order to save computational time the 3D Fourier transforms to get $\hat{f}_1(\vec{q})$ and $\hat{f}_2(\vec{q})$ are done on the full data cube of $L \times L \times L$ super-resolution pixels, and all the rotations are done on a cropped $M \times M \times M$ cube where M is adjusted so that the FPC drops

below the threshold close to the edge of the cropped data cube. For the dataset of Fig. 2.4 we used $L = 1024$, $M = 191$ and 10 nm superresolution pixels.

Note that square/cubic image sizes are used for convenience. Only square/cubic images have isotropic pixel sizes in Fourier space if the pixel sizes in real space are isotropic. Further information on the computation of FRC and FRC resolution is provided in Appendix 2.A.1.

2.4.2. SIMULATIONS

GENERAL SETUP

Simulations were conducted in MATLAB with the use of the image processing toolbox DipImage and several c-language and CUDA codes that were compiled to MATLAB mex-files and run from within the MATLAB environment. Localization microscopy data without multiple localizations per emitter ($Q \ll 1$) were simulated as follows: Poisson noise is added to an object image serving as the 'ground truth' (which has pixel values larger than zero). The resulting value per pixel is taken to be the simulated number of emitters in that pixel, and a number of random points equal to this value is generated for each pixel. Each of these points is then displaced according to a zero-mean normal distribution with variance $Var(\Delta x) = Var(\Delta y) = \sigma^2$, in order to obtain the simulated data (i.e. localizations). Localization microscopy data with multiple localizations per emitter were simulated in a similar way. The only difference is that each of the simulated emitter positions is used to generate a binomially distributed number M_j of offspring points (i.e. localizations) instead of one. All of these offspring points are then displaced with a zero-mean normal distribution with variance $Var(\Delta x) = Var(\Delta y) = \sigma^2$.

FIGURE 2.1B

The result in Fig. 2.1b was obtained by simulating measurements without multiple localizations per emitter (i.e. $Q \ll 1$) for 'ground truth' images of the form:

$$o(\vec{r}) = \begin{cases} \rho\,(1 - \cos(2\pi x/d)) & \text{if } |x| < d \text{ and } \left|y\right| < \frac{a}{2} \\ 0 & \text{otherwise} \end{cases} \tag{2.11}$$

This was done for $d = 20, 40, \ldots, 100$ nm and $\sigma = 1, 2, \ldots, 30$ nm, with a pixel size of 1 nm and $n_{\text{ph}} = 500$. For each d and σ, 400 simulations were carried out for a density of localizations $\rho = 2 \times 10^4\ \mu\text{m}^{-2}$. The value of ρ for which the resolution was calculated was varied in these simulations by taking $2\%, 4\%, \ldots 100\%$ of the simulated localizations at $\rho = 2 \times 10^4\ \mu\text{m}^{-2}$. However, the resolution could not be obtained by calculating where the FRC curve falls below the threshold because the FRC is not approximately monotonically decreasing for this object. Instead, contour lines in the $\rho\sigma$-plane were generated for each d where $FRC(1/d) = 1/7$. These contour lines are equivalent to lines of constant resolution $R = d$.

FIGURE 2.1C

The result in Fig. 2.1c was obtained in a similar way as the result in Fig. 2.1b. However, in the simulations for Fig. 2.1b, ρ and σ are used as independent variables,

whereas for Fig. 2.1c ρ is determined by both T_{total} and σ: $\sigma = \sigma_0/\sqrt{\phi_{\text{ph}} T_{\text{frame}}}$ and $\rho = M_{\text{sim}} T_{\text{total}}/T_{\text{frame}}$. Here $\sigma_0 = 90$ nm, $\phi_{\text{ph}} = 5.0 \cdot 10^4$ s^{-1} is the number of collected photons per emitter per unit time and $M_{\text{sim}} = 0.2$ μm^{-2} is the number of simultaneously active emitters[76]. Localized emitter localizations were simulated for this figure 100 times for $T_{\text{total}} = 30$ minutes, $T_{\text{frame}} = 10^{-3}, 10^{-2.8}, \ldots, 10^{-1}$ sec. and $d = 10, 15, \ldots, 60$ nm. The FRC curve was calculated by taking the localizations up to 1, 5, 10, 20 and 30 minutes out of these sets of localizations of 30 minutes to vary T_{total}. Lines of constant measurement time T_{total} were then calculated by taking the contour lines in the σR-plane where $FRC\left(q = 1/R\right) = 1/7$.

2.4.3. EXPERIMENTAL SETUP AND METHODS

FIG. 2.2A: IMAGING OF TUBULIN FILAMENTS

The first samples that were used for experimental validation of the results from the simulations were tubulin structures in human epithelial cervical cancer (HeLa) cells. These cells were plated on aminosilane coverslips in Labtex 8-well chambers (Nunc). Cells were fixed for 10 minutes in 4% paraformaldehyde in cytoskeleton buffer (10 mM MES pH 6.1, 138 mM KCl, 2 mM EGTA, 0.32 M sucrose, and 3 mM $MgCl_2$), and afterwards put in 50 mM Ammonium Chloride in phosphate buffered saline (PBS) to quench the fixation process. Subsequently, the cells were washed 3 times in PBS and permeabilized (0.5%v/v Triton X-100) for 2 minutes with 0.2% fish skin gelatin added to reduce non-specific binding. Cells were then washed 3 times in PBS again and subsequently labeled with anti-beta tubulin antibodies (9F3 rabbit monoclonal) conjugated to Alexa Fluor 647 dye molecules (Cell Signaling Technology Inc.) in PBS at a concentration of approximately 1.0 μg/ml in the presence of 0.2% fish skin gelatin, after which they were washed thrice in PBS. Before imaging the cells, a sparse dilution of 1:10^5 of fluorescent beads (0.1 μm TetraSpeck microspheres, Invitrogen Inc.) was put in solution for 3 minutes to enable drift correction. Next, the cells were immersed in an oxygen scavenging buffer solution consisting mainly of glucose oxidase and catalyze in PBS in the presence of glucose and 80 mM mercapto-ethylamine (MEA) as a reducing agent.

Imaging of the samples was carried out in an epi-fluorescence microscope setup. This setup consisted of the following components: an inverted microscope (IX71, Olympus), a 1.45 NA TIRF objective (U-APO 150x NA 1.45, Olympus), 635 nm diode laser (Radius 635, Coherent Inc.), 561 nm diode-pumped solid state laser (Crystalaser) and an EMCCD camera (iXon 897, Andor) with EM gain set to 25. The epi-fluorescence filter setup consisted of a dichroic mirror (650 nm, Semrock) and an emission filter (692/40, Semrock). The samples were mounted in a 3D piezo stage (Nano-LPS100, Mad City Labs). Images were taken in a TIRF configuration at 20 frames per second for 14,000 frames, giving a total measurement time of about 4 min. Drift correction was accomplished by moving the field of view to a preselected fluorescent bead and imaging it with the 561 nm laser after every 1,000 frames of acquisition with the 635 nm laser on. Position estimates of the beads were then used to move the sample back to its initial position at the beginning of the experiment.

FIG. 2.2J: IMAGING OF ACTIN FILAMENTS

HeLa cells were cultured on #1.5 coverslips. After 24 hours cells were washed briefly with PBS and fixed in 2 steps: A first incubation step in 0.3% Glutaraldehyde + 0.25% Triton in cytoskeleton buffer (10 mM MES pH 6.1, 150 mM NaCl, 5 mM EGTA, 5 mM glucose, and 5 mM $MgCl_2$) for 2 minutes at room temperature and a second step with 0.5% glutaraldehyde in the same buffer for 10 minutes at room temperature. The sample was treated with 0.1% $NaBH_4$ in PBS (freshly prepared) for 7 minutes at room temperature to reduce background fluorescence[77]. Samples were extensively washed with PBS and blocked with 5% BSA for 30 minutes at room temperature. Staining with phalloidin (Invitrogen Inc.) diluted in 5% BSA in PBS to a final concentration of 0.25 M was made overnight at a temperature of 4^{o}C. Cells were washed using first 0.1% Tween-20 in PBS and then PBS.
Imaging of the samples was carried out on a Leica SR-GSD microscope. This setup consisted of the following components: an inverted microscope (DMI6000 B, Leica Microsystems GmbH), a 1.47 NA TIRF objective (HCX PL APO 100.0x NA1.47), a tube lens providing an extra factor 1.6x in magnification, 532 nm fiber laser (2RU-VFL-P-1000-532-B1R, MBP communications Inc.), 642 nm fiber laser (2RU-VFL-P-1000-642-B1R, MBP communications Inc.) and an electron EMCCD camera (Ixon DU-897, Andor) with an effective EM gain of 50.6. The epi-fluorescence filter cube (642HP-T) for imaging with the 642 nm laser consisted of an excitation filter (zet405/642x), a dichroic mirror (t405/642rpc) and emission filters (et710 100lp and ET650LP). Images were taken in TIRF mode at 100 frames per second for 50,000 time frames, giving a total measurement time of about 8 min. The epi-fluorescence filter cube (532HP-T) for imaging with the 532 nm laser consisted of an excitation filter (zet405/532x), a dichroic mirror (t405/532rpc) and emission filters (et600/100m and ET550LP).

LOCALIZATION AND IMAGE RENDERING ALGORITHMS FIG. 2.2:

The recorded movies were processed by estimating the emitters' positions, as well as the Cramer-Rao-lower-Bounds (CRLBs) for those events, using a fast algorithm[15] on a Quadro 5000 GPU (NVidia). The method for finding candidate regions of interest for position estimation has been documented in the literature[36]. Since the fitting algorithm is expected to perform close to the CRLB for each fit, these CRLBs were taken as estimates of the localization precision of the fits. The resulting events were filtered in order to reduce the number of false positive localizations. The parameters used for filtering were the estimated number of signal photons n_{ph} of the event (at least 250), the estimated localization precision σ (at most 30 nm for Fig. 2.2a and 35 nm for Fig. 2.2j), the standard deviation of the Gaussian PSF model σ_{PSF} (101 − 161 nm for Fig. 2.2a and 100 − 150 nm for Fig. 2.2j) and the information divergence between the PSF model and the data in the fitted regions of interest (at least -120).
Fig. 2.2 shows a comparison between the maximum likelihood estimation algorithm, least squares estimation and a centroid estimation scheme for the same localization events[78, 79]. This means that the centroids were estimated for the same regions of interest (ROI) in the raw data that contributed to the localizations in the maximum likelihood image. For this estimation, the background was subtracted from the ROI

image, negative pixel values were set to zero, and subsequently the center of mass was calculated. The background value is the average of 24 edge pixels: the 32 edge pixels of the 9×9 pixel ROI excluding the 4 highest and 4 lowest values.
Least squares fitting was done by minimizing the mean square error between the observed ROI images and a Gaussian spot (integrated over the finite pixels), characterized by the emitter position, spot width, signal photon count and a constant background. The mean square error function was minimized using a standard Levenberg-Marquardt optimization routine, programmed in MATLAB.

The filtered localizations in Fig. 2.2j were corrected for stage drift using frame-by-frame cross-correlation algorithm[27]. Time series were split into M (typically $M = 20$) equal parts. For each of these parts a superresolution image was made by binning the localizations into bins, typically of size 10 nm. Subsequently the displacement of each image with respect to the first image was calculated and from this displacement the drift was calculated for the time points at the boundaries of each time block. Finally the average drift per time block was computed from the two drift estimates at the boundaries of those time blocks and these were integrated in order to come to an estimate of the sample's trajectory over time which was subtracted from the estimated fluorophore locations.

The N_{raw} drift corrected localizations were condensed into $N < N_{\text{raw}}$ localization events by grouping spatially nearby localizations that are less than Δ image frames apart into single localization events, where $\Delta = 5$ for the data in Fig. 2.2. 'Nearby' is defined here as having a distance less than three times the sum of the localization uncertainty of the two to-be merged localization events. For the single grouped localization, the position was taken to be equal to the weighted average of the localizations with the inverse of the variances as weights. Also, for each grouped localization the sum of the photon counts and background photon counts of the single localizations were stored, and the estimated variance of the grouped localization was taken to be the harmonic mean of the single localizations' variances. This procedure improves the localization uncertainty, as the average number of photons per localization event now scales with the fluorescent on-time τ_{on} rather than with the frame time T_{frame}.

FIG. 2.3: TWO COLOR IMAGING OF TUBULIN FILAMENTS

Green monkey kidney BS-C-1 cells were fixed with formaldehyde (3%) + glutaraldehyde (0.1%) at room temperature in PBS for 10 min. The fixing step was followed by quenching with sodium borohydride (0.1%) in PBS for 7 min. The fixed sample was permeabilized in blocking buffer (3% BSA, 0.5% Triton X-100 in PBS) for 10 minutes and stained with primary antibodies for 30 min in blocking buffer. The sample was rinsed with washing buffer (0.2% BSA, 0.1% Triton X-100 in PBS) three times for 10 minutes each. Secondary antibodies were added to the sample (diluted in blocking buffer) and left for 30 minutes at room temperature. The sample was then washed three times for 10 minutes each with washing buffer. The sample was post-fixed for 10 minutes at room temperature with formaldehyde (3%) + glutaraldehyde (0.1%), and then stored in PBS at 4 degrees C before imaging. For two-color imaging of microtubules labeled with both Alexa Fluor 647 and Alexa Fluor 750, the primary

antibody was rat anti-tubulin (Abcam ab6160, 1:100 dilution). The secondary antibody was donkey anti-rat (Jackson Immunoresearch, 712-005-153). Two separate labeled samples of secondary antibodies were prepared: one labeled with both Cy2 and Alexa Fluor 647, and the other labeled with Cy2 and Alexa Fluor 750, as described previously[63]. These two samples of secondary antibody were mixed in equal portions and used for labeling at a concentration of ~2.5 μg/ml.
The microscope setup used for localization imaging has been described in detail previously[80]. Briefly, an inverted fluorescence microscope (Olympus IX71) was equipped with a 100X oil immersion objective lens (Olympus, UPLANSAPO100XO) and an EMCCD camera (Andor DU-897) which enabled efficient detection of single fluorophores. A custom built focus lock system was used to maintain sample focus during all measurements. For imaging, photo-switchable Alexa Fluor 647 or Alexa Fluor 750 were excited using 642 nm light or 752 nm light, respectively. Laser light at 642 nm was generated using a fiber laser (MBP Communications, 2RU-VFL-P-1500-642), and laser light at 752 nm was generated using a Krypton gas laser (Coherent, In nova I300C). Additionally, the microscope was capable of laser illumination at 488 nm, generated using an Argon-Krypton laser (Coherent, Innova I-70), and 561 nm, generated using a solid state laser (Cobalt, Jive). For detection of Alexa Fluor 647 fluorescence, a dichroic mirror (Chroma, Z660DCXRU) was used to split excitation light from emitted fluorescence, and a bandpass emission filter (Chroma, ET700/75) was used to filter the emitted signal. Fluorescence detection of Alexa Fluor 750 also used a dichroic mirror (Chroma, Q770DCXR) and a bandpass emission filter (Chroma, HQ800/60). The data was reconstructed from 138,749 frames at 60 frames per second, giving a total measurement time of about 39 min (Alexa Fluor 647), and from 30,087 frames at 20 frames per second, giving a total measurement time of about 25 min (Alexa Fluor 750).

Imaging of tubulin labeled with both Alexa Fluor 647 and Alexa Fluor 750 was carried out in two sequential steps. First, a dataset was obtained for the Alexa Fluor 750 channel, followed by a second dataset for the Alexa Fluor 647 channel. Fiducial markers were used to register the two images, creating the final two-color image[80]. Fluorescent beads (Invitrogen Inc., F8810) were bound to the sample and used as fiducial markers for drift correction and image registration. Prior to imaging, the sample was incubated with a solution of beads (2% solids stock solution diluted 1:50,000 in PBS), which were allowed to bind to the sample for 1 minute. The sample was then rinsed and incubated with PBS + 50mM MgCl2, which caused the beads to stick to the surface of the coverglass. The buffer was then exchanged to imaging buffer, and the dataset was collected.

The imaging medium consisted of a pH-buffer with an enzymatic oxygen scavenging system consisting of glucose, glucose oxidase, and catalyze to reduce photobleaching, and a thiol to facilitate photoswitching. The specific composition of the imaging buffer was Tris (50 mM pH 8.0), NaCl (10 mM), glucose (10% w/v), β-mercaptoethanol (143 mM), and the enzymatic oxygen scavenging system (1% v/v). The enzymatic oxygen scavenging system stock solution (GLOX) was prepared by mixing glucose oxidase powder (10 mg, Sigma, G2133) with catalyze (50 μl, Sigma,

C100), in PBS (200 μl), and centrifuging the mixture at 13,000 rpm for 1 minute. The data analysis used for localization microscopy and the nanoscale image registration procedure, based on the positions of the fiducial marks, has been described in detail previously[63].

FIG. 2.4: 3D IMAGING OF TUBULIN FILAMENTS

Swiss 3T3 cells were plated in 8 well chambers (Lab-Tek II, Nunc) overnight in standard DMEM phenol free media. Samples were washed twice with room temperature PBS and then fixed with 4% PFA in cytoskeleton buffer (10 mM MES, 138 mM KCl, 3 mM MgCl, 2 mM EGTA, 0.32 M sucrose) for 30 minutes at room temperature. The sample was then incubated twice for 5 minutes in 10 mM Tris in PBS. The sample was permeabilized with a 1% BSA 0.1% triton solution in PBS for 15 minutes. During the permeabilization the primary antibodies were added to an aliquot of the previously mentioned blocking/permeabilizing buffer at a concentration of 12μg/mL. After permeabilization, the sample was incubated with the primary antibody (Sigma T8328 anti-B tubulin) at 12 μg/mL in permeabilization buffer for 1 hour at room temperature on an orbital shaker operating at a slow speed. The sample was then washed 3 times for 5 minutes with 1% BSA 0.1% triton solution. Secondary antibody labeling was performed using an anti-mouse antibody (Jackson Immuno 715-005-150 anti-mouse IgG) labeled with an average of two Alexa Fluor 647 dyes per protein. Labeling was performed at concentration of 15 μg/mL in permeabilization buffer for 30 minutes at room temperature on an orbital shaker. The sample was again washed 3 times for 5 minutes in PBS and post fixed for 10 minutes in 4% PFA, and stored in 0.05% PFA in PBS solution until the time of imaging. Before imaging, samples were washed 2 times with 10 mM Tris for 5 minutes.

3D imaging was performed using a dual focal plane setup. To define the imaging area, an adjustable slit was placed at the primary image position of the microscope (Olympus IX71), followed by a relay lens system (f = 75 mm, f = 50 mm) to create 1.5 magnification to a secondary image position. From there, a lens (f = 125 mm) was used to collimate the beam and a 50/50 beam splitter used to split the beam into two, equal length optical paths. In one pathway an additional lens (f = 1 m) was used to create the second focal plane, giving an approximately 330 nm defocused imaged compared to the unaltered beam path. The two optical paths were redirected by mirrors (two in each path), so that they both pass through an imaging lens (f = 125 mm) and image side by side onto the same EMCCD camera (Andor iXon 860). An emission filter (FF01-692/40-25, Semrock) was placed after the f = 125 mm collimation lens. Excitation light was provided by a 637 nm diode laser (ThorLabs HL63133DG). Samples were imaged in an oxygen scavenging buffer consisting of 10% (w/v) glucose, 50 mM Tris, 10 mM NaCl, pH 8.5, glucose oxidase, catalyze, and 20 mM MEA. Excitation at 637 nm (ThorLabs HL63133DG) was 1 kW/cm^2. 50,000 images were acquired at a 100 Hz frame rate. A 405 nm laser (DL405-010-O, CrystaLaser) was used to recover Alexa Fluor 647 from the dark state and the power was adjusted by hand to provide control over the active state duty cycle.

Position estimations were performed by maximum likelihood estimation using a Pois-

son noise model and PSF models calculated from phase retrieved pupil functions[81]. Pupil function were retrieved for each focal plane independently. The parameters position x, y, z, intensity I and background values bg_1, bg_2 were estimated simultaneously using both focal planes where x, y positions in each plane were connected by a pre-determined transform matrix, the z position was connected by a plane separation that was found in the phase retrieving process, and the intensity I was related with a pre-measured ratio factor.

2.A. APPENDIX

2.A.1. COMPUTATIONAL CONSIDERATIONS

DATA SPLITTING

For this work, half data sets were obtained by splitting the timeseries into blocks of 500 frames and assigning an equal number of blocks randomly to each half set. Alternatively, localizations could also have been assigned randomly to the half sets or the timeseries could have been split into two parts to obtain two sets with half the localizations. Both these methods have some issues though. Random assignment may cause spurious correlations due to localizations of a single emitter activation event being assigned to both half sets. This will also happen if the block size for splitting the data is too short compared with the on-time τ_{on} of the emitters.

Splitting the timeseries in two parts may cause the half sets to be overly dissimilar due to systematic differences between the halves of the timeseries. Next to drift, for example, photobleaching may occur and then the localizations in the second half set arise from fewer emitters or from more photostable emitters. On the other hand, photobleaching may also reduce spurious correlations due to reactivation of previously active emitters in the second half set for this splitting method. We have nevertheless chosen for splitting the experimental timeseries in smaller blocks because it only has the problem of spurious correlations and because it is more accurate in the absence thereof.

DISCRETIZATION

Two issues regarding the discrete computation of the FRC curve require some further discussion here. The first issue is the masking of the binned images. This masking is needed to suppress high frequency components in the Fourier transforms that may result from the edges of the binned images. It is a common technique in signal processing [82] to suppress edge artifacts resulting from the digital Fourier transformation which cannot be avoided otherwise. If an object which is imaged extends up to the edge of an image and no mask is applied, then the finite extent of the image acts as a rectangular window $M(\vec{r})$ which is 1 inside the field of view and 0 outside. In the frequency domain this has the effect on the images $\hat{f}(\vec{q})$ that:

$$\hat{f}(\vec{q}) \rightarrow \hat{f}(\vec{q}) * \hat{M}(\vec{q}) = \hat{f}(\vec{q}) * L^2 \text{sinc}(\pi q_x L) \text{sinc}(\pi q_y L) . \tag{2.12}$$

Here $\text{sinc}(x) \equiv \sin(x)/x$ and $*$ is the convolution operation. The window extends the highly correlating low spatial frequency components into the higher spatial frequencies due to the finite width and oscillating tails of the sinc functions. Therefore it increases the FRC at those frequencies and leads to a higher threshold frequency q_{res}. In order to reduce this effect, a mask $M(\vec{r})$ with a smooth drop-off to 0 at the edges has to be applied which is narrower in the frequency domain. Note that q_{res} will then still be slightly overestimated, proportional to the finite width of $\hat{M}(\vec{q})$.

A second issue worth mentioning here is the effect of the pixel size in the binned images (i.e. the superresolution pixel size) on the FRC. As a first consideration, pixel sizes larger than $R/2$ will result in aliasing at spatial frequencies around q_{res}. This will

appear as additional correlation in the FRC and may therefore artificially increase the estimated resolution. Furthermore, the pixel binning also acts as a low pass filter. If l is the pixel size then the effect is approximately as if the exponential in Eq. 2.2 is replaced by:

$$\exp\left(-4\pi^2\sigma^2q^2\right) \rightarrow \operatorname{sinc}\left(\pi q l\right)^2 \exp\left(-4\pi^2\sigma^2q^2\right). \tag{2.13}$$

At $q = q_{\text{res}}$ this is the same as replacing σ in Eq. 2.2 by:

$$\sigma^2 \rightarrow \sigma_{\text{eff}}^2 = \sigma^2 - \frac{\log\left(\operatorname{sinc}\left(\pi q l\right)^2\right)}{4\pi^2q^2}. \tag{2.14}$$

If we assume that $R \approx 2\pi\sigma$ and we require that the loss in the resolution from having a finite pixel size should not be greater than 10%, the this leads to the requirement that

$$\Delta R = 2\pi\left(\sigma_{\text{eff}} - \sigma\right) < 0.1R = 0.1 \cdot 2\pi\sigma, \tag{2.15}$$

which implies that

$$4\pi^2\sigma_{\text{eff}}^2q_{\text{res}}^2 - 4\pi^2\sigma^2q_{\text{res}}^2 = -\log\left(\operatorname{sinc}\left(\pi q_{\text{res}} l\right)^2\right) < 0.21, \tag{2.16}$$

from which it can be deduced that

$$l < \frac{0.25}{q_{\text{res}}} = \frac{R}{4}. \tag{2.17}$$

The recommendation is therefore to keep the superresolution pixel size smaller than $R/4$.

THRESHOLDS

In the field of single-particle electron microscopy, there is no general consensus on what threshold $\theta\left(q\right)$ should be used for the FRC or FSC. Three main kinds of thresholds are used: The first is fixed thresholds (e.g. $\theta\left(q\right) = 1/7 \approx 0.143$ [59] or $\theta\left(q\right) = 0.5$ [57, 58]). The second kind is sigma factor curves ($\theta\left(q\right) \propto 1/\sqrt{qL}$ [41, 83]), which require the FRC to be larger than some multiple of the standard deviation of the FRC for white noise (for which $\langle FRC\rangle = 0$), with L the field-of-view. The third kind is information level curves[84]. The curves were derived based on the RMS value of the numerator and denominator of the FRC curve which leads to the following approximation:

$$FRC\left(q\right) \approx \frac{SNR\left(q\right) + \left(2/SNR\left(q\right) + 1\right)/\sqrt{qL}}{SNR\left(q\right) + \left(2/SNR\left(q\right)\right)/\sqrt{qL} + 1}. \tag{2.18}$$

The requirement that the information content per pixel $\log_2\left(1 + SNR\right)$ is larger than a certain number of bits (e.g. 0.5 or 1) results in the desired curves. Note here that for 0.5 bits of information per pixel and large L, the threshold rapidly converges to $\theta\left(q\right) = 0.1716$, which is close to the 1/7 threshold. The sigma factor and information level curves are conceptually conservative: they are chosen such that even if due to noise $FRC\left(q\right)$ is larger than its expected value, the image should still be resolved

if it is above the threshold. However, since the FRC gives a single resolution figure for an entire image, it should be seen as giving the length scale at which details are resolved *on average* rather than *with certainty*. Moreover, these curves do not take into account that the noise on $FRC(q)$ is heavily suppressed by means of smoothing. Therefore these conservative thresholds are inappropriate. The most commonly used fixed threshold is 0.5 [85]. However, recent work [73] suggests that this threshold appears to give a realistic resolution estimate because the FSC in single-particle electron microscopy is often overoptimistic due to spurious correlations. In the absence of spurious correlations the threshold of $1/7 \approx 0.143$ was found to be more adequate. Ultimately though, the correct threshold is determined empirically: it is the one that corresponds best with what intuitively appears to be resolved in actual images. From the results in Fig. 2.5 we conclude that the 1/7 threshold is the most appropriate choice of threshold.

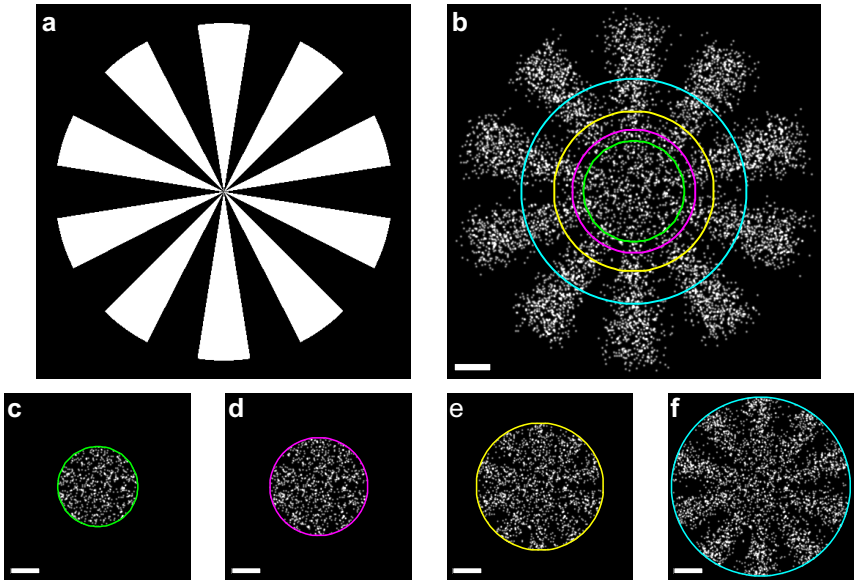

Figure 2.5: **Evaluation of resolution threshold criteria.** Simulations without multiple localizations per emitter (i.e. $Q \ll 1$) (b) for a Siemens star shaped object (a), for a density of localizations $\rho = 2 \times 10^3$ μm^{-2} and a localization uncertainty $\sigma = 20$ nm. A circle denotes where the arms of the star can just be distinguished according to the resolution computed with the most common threshold criteria: 1/7 threshold (83 ± 3 nm, green), half-bit threshold (100 ± 5 nm, magenta), 1/2 threshold (130 ± 7 nm, yellow), and 3σ threshold (186 ± 9 nm, cyan). White scalebar: 100 nm. For the correct threshold, the arms of the star should be distinguishable outside the corresponding circle and not distinguishable inside the circle. (c-f) show the regions of (b) within the different circles of the top right image. They are shown to illustrate the separability of the star arms in the absence of the visual aid from the regions outside the circles. Clearly, the 1/7 threshold is most appropriate in these images.

2.A.2. AVERAGE AND VARIANCE OF FRC

IMAGING MODEL

The object to be imaged, the 'ground truth' $o(\vec{r})$, is labeled with fluorescent probes. The distribution of fluorescent labels is described by the labeling density function:

$$\psi(\vec{r}) = \sum_{j=1}^{K} \delta\left(\vec{r} - \vec{r}_j^{\,em}\right), \tag{2.19}$$

and depends on the set of positions $\left\{\vec{r}_j^{\,\mathrm{em}} | j = 1,\ldots,K\right\}$ of the K labels.

Label j is activated and localized M_j times giving a total number of:

$$N = \sum_{j=1}^{K} M_j, \tag{2.20}$$

localizations, at the set of positions $\{\vec{r}_j \mid j = 1,\ldots,N\}$. It is assumed that localizations of the same emitter in subsequent image frames have been grouped into a single localization event such that there is only a single position estimate of an emitter each time it is activated. The probability density for localization of an emitter at position $\vec{r}$ is given by:

$$P_{\mathrm{loc}}(\vec{r}) = \frac{1}{K}\int d^n r'\, h\left(\vec{r} - \vec{r}\,'\right)\psi\left(\vec{r}\,'\right), \tag{2.21}$$

where $h(\vec{r})$ is the localization Probability Distribution Function (PDF), which is taken to be a Gaussian:

$$h(\vec{r}) = \frac{1}{2\pi\sigma^2}\exp\left(-|\vec{r}|^2/2\sigma^2\right), \tag{2.22}$$

where the width satisfies $\sigma^2 = \sigma_0^2/n_{\mathrm{ph}}$ in the absence of background. Here σ_0 is a measure for the width of the PSF of the optical system and n_{ph} is the number of photons per emitter.

The usual way to argue that the localization PDF must be a Gaussian with variance decreasing as $1/n_{\mathrm{ph}}$ is that a measurement with only one photon gives the PSF as localization PDF, with variance σ_0^2, so by repeating the measurement n_{ph} times the localization PDF must be a Gaussian with variance given by $\sigma_0^2/n_{\mathrm{ph}}$. However, this argument does not apply because the actual PSF has infinite variance as the integral $\int dxdy\, PSF(x,y)\left(x^2+y^2\right)$ diverges (the PSF decays with the second power of the coordinates times an oscillating function). A different argument is related to the asymptotic normality of the MLE-estimation of location. In case the number of signal photons is large the statistical error in the position estimation is small. Then we may approximate the log-likelihood with a parabolic function centered on the optimum. This means that the likelihood function (which is equal to the localization PDF) may be approximated with a Gaussian. In case of a non-zero background the same conclusion may be drawn, albeit with a different dependence of the localization uncertainty than the simple $1/\sqrt{n_{\mathrm{ph}}}$ relation, and provided that the number of signal photons is sufficiently large. We have used numerical analysis and the Kolmogorov-Smirnov (KS)

test for finding out the similarity between the actual localization PDF and the Gaussian distribution. We have performed numerical tests using fully vectorial modeling of the PSF of a freely rotating dipole emitter with zero aberrations and zero background, and 500 signal photons [14], and the MLE localization routine implemented on GPU for speed [15]. The KS-statistic (maximum difference between the CDF and the Gaussian CDF) is typically $5-10\times10^{-3}$ for 5,000 localizations. The statistical significance of this residual deviation is characterized by the p-value, which takes values between 40% and 100% for the 5,000 sample runs. The validity of the scaling of the localization uncertainty with the inverse square root of the photon count follows from the fact that the variance of the localization error for MLE-estimation follows the CRLB for a Gaussian ground truth PSF over a wide range of photon counts [15]. It is noted that the Gaussian nature of the localization PDF would imply an infinite spatial frequency content (no cut-off, as opposed to the PSF). However, extrapolating to spatial frequencies corresponding to the sub-nm scale is not physically meaningful, but down to that length scale the Gaussian provides an excellent description of the localization PDF, provided of course the emitter is not too dim.

AVERAGE FRC

Each localization event is assigned to one of two groups with probability 1/2, leading to a split $N = N_1 + N_2$ that is governed by the binomial distribution. The M_j localizations of emitter j are also split into two parts $M_j = M_{1j} + M_{2j}$ according to the binomial distribution. The two sub-images are described by the image functions:

$$f_m(\vec{r}) = \sum_{j=1}^{N_m} \delta\left(\vec{r} - \vec{r}_j\right), \tag{2.23}$$

for $m = 1,2$. The statistical averages of the two sub-images are simply:

$$\left\langle f_m(\vec{r}) \right\rangle = \frac{N}{2} P_{loc}(\vec{r}), \tag{2.24}$$

In the Fourier domain these relations are:

$$\left\langle \hat{f}_m(\vec{q}) \right\rangle = \frac{N}{2K} \hat{h}(\vec{q})\, \hat{\psi}(\vec{q}), \tag{2.25}$$

with:

$$\hat{h}(\vec{q}) = \exp\left(-4\pi^2\sigma^2 \left|\vec{q}\right|^2\right). \tag{2.26}$$

The definition for the FRC-curve in Eq. 2.1 was given by:

$$FRC(q) = \frac{\sum\limits_{\vec{q}\in\text{ring}} \hat{f}_1(\vec{q})\, \hat{f}_2(\vec{q})^*}{\sqrt{\sum\limits_{\vec{q}\in\text{ring}} \hat{f}_1(\vec{q})^2} \sqrt{\sum\limits_{\vec{q}\in\text{ring}} \hat{f}_2(\vec{q})^2}}.$$

Consequently, to obtain the average FRC-curve we need to calculate the 2×2-correlation matrix elements:

$$\left\langle \hat{f}_m\left(\vec{q}\right)\hat{f}_n^*\left(\vec{q}\right)\right\rangle = \left\langle \sum_{j=1}^{N_m}\sum_{l=1}^{N_n}\exp\left(-2\pi i\,\vec{q}\cdot\left(\vec{r}_j-\vec{r}_l\right)\right)\right\rangle, \tag{2.27}$$

for $m,n=1,2$. In order to evaluate these averages we must consider pairs of localization events r_j and r_l. The N_m^2 pairs appearing in the diagonal correlation matrix elements can be divided in three distinct groups. These are the N_m pairs of identical localization events, the $\sum_{j=1}^{K} M_{m,j}\left(M_{m,j}-1\right)$ pairs of different localization events of the same emitter, and the $N_m\left(N_m-1\right)-\sum_{j=1}^{K} M_{m,j}\left(M_{m,j}-1\right)$ pairs of different localization events of different emitters. A similar division can be made for the N_mN_n pairs in the off-diagonal correlation matrix elements. The N_mN_n pairs are necessarily all from different localization events, namely $\sum_{j=1}^{K} M_{m,j}M_{n,j}$ from the same emitter and $N_mN_n-\sum_{j=1}^{K} M_{m,j}M_{n,j}$ from different emitters. The probability density for two localizations of the same emitter is:

$$P_{\mathrm{loc,S}}\left(\vec{r}_1,\vec{r}_2\right)=\frac{1}{K}\int d^2r\,h\left(\vec{r}_1-\vec{r}\right)h\left(\vec{r}_2-\vec{r}\right)\psi\left(\vec{r}\right), \tag{2.28}$$

and the probability density for localizations from different emitters is:

$$P_{\mathrm{loc,D}}\left(\vec{r}_1,\vec{r}_2\right)=\frac{1}{K^2}\int d^2r\,d^2r'\,h\left(\vec{r}_1-\vec{r}\right)h\left(\vec{r}_2-\vec{r}\right)\psi\left(\vec{r}\right)\psi\left(\vec{r}\,'\right), \tag{2.29}$$

The Fourier transforms of these probability distributions are needed further on, and are given by:

$$\begin{aligned}\hat{P}_{\mathrm{loc,S}}\left(\vec{q}_1,\vec{q}_2\right) &= \int d^2r_1\,d^2r_2\,P_{loc,S}\left(\vec{r}_1,\vec{r}_2\right)\exp\left(-2\pi i\,\vec{q}\cdot\left(\vec{r}_1-\vec{r}_2\right)\right)\\ &= \frac{1}{K}\hat{h}\left(\vec{q}_1\right)\hat{h}\left(\vec{q}_2\right)^*\hat{\psi}\left(\vec{q}_1-\vec{q}_2\right), \qquad (2.30)\\ \hat{P}_{\mathrm{loc,D}}\left(\vec{q}_1,\vec{q}_2\right) &= \int d^2r_1\,d^2r_2\,P_{loc,D}\left(\vec{r}_1,\vec{r}_2\right)\exp\left(-2\pi i\,\vec{q}\cdot\left(\vec{r}_1-\vec{r}_2\right)\right)\\ &= \frac{1}{K^2}\hat{h}\left(\vec{q}_1\right)\hat{h}\left(\vec{q}_2\right)^*\hat{\psi}\left(\vec{q}_1\right)\hat{\psi}\left(\vec{q}_2\right)^*. \qquad (2.31)\end{aligned}$$

Combining all these ingredients gives:

$$\begin{aligned}\left\langle\left|\hat{f}_m\left(\vec{q}\right)\right|^2\right\rangle &= \langle N_m\rangle+\left\langle\sum_{j=1}^{K}M_{m,j}\left(M_{m,j}-1\right)\right\rangle\hat{P}_{\mathrm{loc,S}}\left(\vec{q},\vec{q}\right)\\ &\quad+\left\langle N_m\left(N_m-1\right)-\sum_{j=1}^{K}M_{m,j}\left(M_{m,j}-1\right)\right\rangle\hat{P}_{\mathrm{loc,D}}\left(\vec{q},\vec{q}\right), \qquad (2.32)\\ \left\langle\hat{f}_m\left(\vec{q}\right)\hat{f}_n^*\left(\vec{q}\right)\right\rangle &= \left\langle\sum_{j=1}^{K}M_{m,j}M_{n,j}\right\rangle\hat{P}_{\mathrm{loc,S}}\left(\vec{q},\vec{q}\right)\\ &\quad+\left\langle N_mN_n-\sum_{j=1}^{K}M_{m,j}M_{n,j}\right\rangle\hat{P}_{\mathrm{loc,D}}\left(\vec{q},\vec{q}\right). \qquad (2.33)\end{aligned}$$

Evaluating the averages over the binomial distribution of the localizations over the two sub-images gives:

$$\begin{aligned}\left\langle \hat{f}_m(\vec{q})\,\hat{f}_n^*(\vec{q})\right\rangle &= \frac{N}{2}\delta_{mn}+\frac{1}{4}\left\langle \sum_{j=1}^{K} M_j\left(M_j-1\right)\right\rangle \hat{P}_{\mathrm{loc,S}}(\vec{q},\vec{q}) \\ &\quad +\frac{1}{4}\left[N(N-1)-\left\langle \sum_{j=1}^{K} M_j\left(M_j-1\right)\right\rangle\right]\hat{P}_{\mathrm{loc,D}}(\vec{q},\vec{q}). \quad (2.34)\end{aligned}$$

In case each emitter is localized only once it holds that:

$$\sum_{j=1}^{K} M_j\left(M_j-1\right)=0, \quad (2.35)$$

and as a result this term drops from the correlation averages. When emitters can be localized more than once this term will be non-zero. This term represents the *spurious correlations* between the two image halves, since having localizations from the same emitters in both halves violates the assumption that they are independent.

In order to find an expression for the ensemble average of $M_j\left(M_j-1\right)$ a statistical model for on-off switching is needed. It appears that the number of activation cycles M_j for each emitter j is a Poisson distributed variable in case the on-off switching statistics is described by a first order process and provided the ratio of the transition rates between the on and off-states is very different from one. This can be proven in the framework of the so-called asymmetric Random Telegraph Signal (RTS) model [86]. Also in a STORM acquisition where activator-reporter dye pairs are switched on with the same probability over many switching cycles, M_j would be Poisson distributed. In practice, the switching kinetics are much more subtle and the approximation as a Poisson process is merely a working assumption. Suppose now that there is a reservoir of K_r emitters and the average number of activation cycles is given by Q. Then a total of $K=\left(1-\exp(-Q)\right)K_\mathrm{r}$ emitters is localized at least once and a total of $N=QK_\mathrm{r}$ localizations is generated. The average number of localizations per emitter for the group of emitters that has been localized at least once is:

$$Q_\mathrm{loc}=\frac{N}{K}=\frac{Q}{1-\exp(-Q)}. \quad (2.36)$$

Clearly, if the Poisson-rate Q goes to zero then the average number of localizations per emitter (restricted to the group of emitters that has been localized at least once) goes to one. It now follows that:

$$\left\langle \sum_{j=1}^{K} M_j\left(M_j-1\right)\right\rangle = K_\mathrm{r}Q^2=NQ. \quad (2.37)$$

For a more general distribution of M_j, this is modified to:

$$\left\langle \sum_{j=1}^{K} M_j\left(M_j-1\right)\right\rangle = N\left(\left\langle M_j\right\rangle+\frac{Var(M_j)}{\left\langle M_j\right\rangle}-1\right) \quad (2.38)$$

Consequently, M_j may be overestimated or underestimated if $Var(M_j) \neq \langle M_j \rangle$. For example, if almost all emitters have been localized and the dominant cause of variation of M_j is photobleaching, then M_j becomes geometrically distributed which implies that $Q \approx 2\langle M_j \rangle - 2$. This means that $\langle M_j \rangle$ would be underestimated for $\langle M_j \rangle < 2$. For $\langle M_j \rangle > 2$, $\langle M_j \rangle$ is overestimated up to 100%. In general, photobleaching will lead to a distribution of M_j that is in between the Poisson distribution and the geometrical distribution and will therefore also lead to an overestimation of up to 100%.

We may now further develop the expressions for the correlation averages using that $N \gg 1$ and $K \gg 1$ and filling in the expressions for the localization pair distribution functions:

$$\langle \hat{f}_m(\vec{q})\, \hat{f}_n^*(\vec{q}) \rangle = \frac{N}{2}\delta_{mn} + \frac{N}{4}\left[Q + \frac{N}{K^2} |\hat{\psi}(\vec{q})|^2 \right] |\hat{h}(\vec{q})|^2 . \tag{2.39}$$

These statistical averages must next be integrated over Fourier space with the Fourier ring weight function:

$$\int d^2q'\, D(|\vec{q}'| - q) \langle \hat{f}_m(\vec{q}')\, \hat{f}_n^*(\vec{q}') \rangle = \frac{N}{2}\delta_{mn} + \frac{N}{4}\left[Q + NS(q) \right] \exp\left(-4\pi^2\sigma^2 q^2\right), \tag{2.40}$$

with:

$$S(q) = \frac{1}{K^2} \int d^2q'\, D(|\vec{q}'| - q) |\hat{\psi}(\vec{q}')|^2 , \tag{2.41}$$

and where the isotropy and explicit form of the Gaussian localization PDF is used. The Fourier ring weight function may be expressed as:

$$D(|\vec{q}'| - q) = \frac{\delta(|\vec{q}'| - q)}{2\pi q}, \tag{2.42}$$

Recalling the definition of the FRC in this notation as:

$$\langle FRC \rangle = \frac{\int d^2q'\, D(|\vec{q}'| - q) \langle \hat{f}_1(\vec{q}')\, \hat{f}_2^*(\vec{q}') \rangle}{\left(\int d^2q'\, D(|\vec{q}'| - q) \langle \hat{f}_1(\vec{q}')\, \hat{f}_1^*(\vec{q}') \rangle \right)^{1/2} \left(\int d^2q'\, D(|\vec{q}'| - q) \langle \hat{f}_2(\vec{q}')\, \hat{f}_2^*(\vec{q}') \rangle \right)^{1/2}} \tag{2.43}$$

This results in the final expression for the statistical average of the FRC:

$$\langle FRC \rangle = \frac{\left(Q + NS(q)\right) \exp\left(-4\pi^2\sigma^2 q^2\right)}{2 + \left(Q + NS(q)\right) \exp\left(-4\pi^2\sigma^2 q^2\right)}, \tag{2.44}$$

The ratio of the terms in the FRC nominator representing the genuine intrinsic image correlations and the spurious correlations at the resolution threshold is $NS(q_{\text{res}})/Q = KS(q_{\text{res}})$. It follows that the spurious correlations may be neglected provided the number of emitters K is sufficiently high and the sample has spectral signal content at q_{res}. Solving the resolution threshold $\langle FRC \rangle = 1/7$ then gives an apparent resolution:

$$R = \frac{2\pi\sigma}{\sqrt{\log(3Q)}}. \tag{2.45}$$

Clearly, the apparent resolution is simply a linear factor times the localization uncertainty.

A possible way to correct for the spurious correlations and come to a more realistic image resolution follows from a hypothetical division of the entire group of localization events such that all localizations of an emitter appear in either the first or the second data halve, but not mixed. Such a procedure results in a modified average FRC:

$$\langle FRC' \rangle = \frac{NS(q)\exp\left(-4\pi^2\sigma^2 q^2\right)}{2+\left(2Q+NS(q)\right)\exp\left(-4\pi^2\sigma^2 q^2\right)}. \tag{2.46}$$

This modified FRC can also be produced if the average residual correlation $\sim Q\exp\left(-4\pi^2\sigma^2 q^2\right)$ is estimated from the data and then subtracted from the FRC nominator and added to the FRC denominator. This procedure for estimating the spurious correlation parameter Q is outlined in section 2.4. Note that an effect of the parameter Q is still present in Eq. 2.46, but now represents the trade-off between the number of localizations per emitter and the total number of localized emitters at constant total number of localization events. In this trade-off it is more favorable to localize more emitters a fewer number of times.

The current model may be expanded by taking a distribution of localization uncertainties into account instead of a unimodal value. The correlation averages $\langle \hat{f}_m(\vec{q})\,\hat{f}_n^*(\vec{q})\rangle$ for a single value of the localization uncertainty must then be convolved with the distribution function of the localization uncertainty. Taking that distribution to be Gaussian with mean σ_m and width $\Delta\sigma$ we must replace the localization PDF factor $H(q) = \exp\left(-4\pi^2\sigma^2 q^2\right)$ by:

$$\begin{aligned} H(q) &= \int d\sigma\, \frac{1}{\sqrt{2\pi}\Delta\sigma}\exp\left(-\frac{(\sigma-\sigma_\mathrm{m})^2}{2\Delta\sigma^2}\right)\exp\left(-4\pi^2\sigma^2 q^2\right) \\ &= \frac{1}{\sqrt{1+8\pi^2\Delta\sigma^2 q^2}}\exp\left(-\frac{4\pi^2\sigma_\mathrm{m}^2 q^2}{1+8\pi^2\Delta\sigma^2 q^2}\right), \end{aligned} \tag{2.47}$$

in all expressions for the expectation value of the FRC.

VARIANCE OF THE FRC

The variance of the FRC curve can be computed by using the following formula for the variance of the correlation coefficient $C = \vec{v}_1 \cdot \vec{v}_2 / \sqrt{|\vec{v}_1|^2\,|\vec{v}_2|^2}$ between two random vectors $\vec{v}_1$ and $\vec{v}_2$ with the same mean [87]:

$$Var(C) = \frac{\left(2\alpha^2+1\right)\left(\alpha^2+1\right)^2 - \alpha^4\left(2\alpha^2+3\right)}{n\left(\alpha^2+1\right)^4}. \tag{2.48}$$

Here n is the dimension of the vectors and α^2 is defined as:

$$\alpha^2 \equiv \frac{\sum_{i=1}^n \langle v_{1,i}\rangle^2}{\sum_{i=1}^n Var\left(v_{1,i}\right)} = \frac{\sum_{i=1}^n \langle v_{2,i}\rangle^2}{\sum_{i=1}^n Var\left(v_{2,i}\right)}. \tag{2.49}$$

This equation holds under the conditions that n is large and that the components of $\vec{v}_1$ and $\vec{v}_2$ are independent. If $\vec{v}_1$ and $\vec{v}_2$ are associated with the real and imaginary parts of the frequency components $\hat{f}_1(\vec{q})$ and $\hat{f}_2(\vec{q})$ in the Fourier rings, then it appears that:

$$\begin{aligned}\langle FRC\rangle &= \left\langle \frac{\sum\limits_{\vec{q}\in\text{ring}} \hat{f}_1(\vec{q})\,\hat{f}_2(\vec{q})^*}{\sqrt{\sum\limits_{\vec{q}\in\text{ring}} \hat{f}_1(\vec{q})^2}\sqrt{\sum\limits_{\vec{q}\in\text{ring}} \hat{f}_2(\vec{q})^2}} \right\rangle \approx \frac{\sum\limits_{\vec{q}\in\text{ring}} \left|\langle \hat{f}_1(\vec{q})\rangle\right|^2}{\sum\limits_{\vec{q}\in\text{ring}} \left|\hat{f}_1(\vec{q})\right|^2} \\ &= \frac{\alpha^2}{1+\alpha^2}, \end{aligned} \tag{2.50}$$

so that:

$$\alpha^2 = \frac{\langle FRC\rangle}{1-\langle FRC\rangle}. \tag{2.51}$$

The quantity α^2 can be interpreted here as the signal-to-noise ratio of a half data image in the Fourier ring, (i.e. half the SNR of the total dataset). Substituting this into Eq. 2.48 then gives:

$$Var(FRC) = \frac{1}{n}(1-\langle FRC\rangle)^2\left(1+2\langle FRC\rangle - \langle FRC\rangle^2\right), \tag{2.52}$$

where n is the number of pixels in a Fourier ring. Since the width of a Fourier pixel is $1/L$, where L is the linear size of the field of view, $n = 2\pi qL$ and therefore one gets finally:

$$Var(FRC) = \frac{1}{2\pi qL}(1-\langle FRC\rangle)^2\left(1+2\langle FRC\rangle - \langle FRC\rangle^2\right). \tag{2.53}$$

The careful reader may notice that this equation suggests that increasing L through zero padding of the superresolution images would decrease the variance. However, because neighboring Fourier pixels are actually slightly correlated, increasing L through zero padding will increase the sampling in Fourier space but also leads to stronger correlations among neighboring pixels. Therefore, the effective number of independent pixels in a Fourier ring remains the same and the variance is not affected by zero padding.

2.A.3. ANALYTICAL EXPRESSIONS FOR PERIODIC OBJECT MODELS

In this section we will work out explicit expressions for the FRC resolution for periodic structures (gratings) with different cross-sections. In all cases we assume that the Q-parameter is small, so $Q \ll 1$. Under this condition, setting the right-hand side of Eq. 2.44 equal to the 1/7 threshold criterion leads to the following equality:

$$NS(q_{\text{res}})\exp\left(-4\pi^2\sigma^2 q_{\text{res}}^2\right) = \frac{1}{3}. \tag{2.54}$$

This expression now needs to be solved to obtain an explicit expression for the FRC resolution.

GRATING WITH A COSINE CROSS-SECTION

Consider a periodic structure consisting of $M \geq 1$ periods with period d and length L, and with an average density of localized labels ρ. The total number of localized labels is then $K = M\rho dL$. The labeling density function is given by:

$$\psi(\vec{r}) = \begin{cases} \rho\,[1-\cos(2\pi x/d)] & \text{if } |x| < Md/2 \text{ and } |y| < L/2 \\ 0 & \text{otherwise} \end{cases} \tag{2.55}$$

Fourier transforming results in:

$$\begin{aligned} \hat{\psi}(\vec{q}) \quad = \quad & K\left[\operatorname{sinc}(\pi M q_x d) + \frac{1}{2}\operatorname{sinc}(\pi M d\,(q_x - 1/d))\right. \\ & \left. + \frac{1}{2}\operatorname{sinc}(\pi M d\,(q_x + 1/d))\right] \operatorname{sinc}(\pi q_y L). \end{aligned} \tag{2.56}$$

If L is sufficiently large, this gives the following expression for $S(q)$ at $q = 1/d$:

$$S(q) = \frac{1}{2\pi K^2}\int_0^{2\pi} d\varphi_k \left|\hat{\psi}_{em}(\vec{q})\right|^2 \approx \frac{d}{\pi K^2}\int_{-\infty}^{+\infty} dq_y \left|\hat{\psi}_{em}(\vec{q})\right|^2, \tag{2.57}$$

where the last integral is evaluated at $q_x = q = 1/d$, and so:

$$S(q) \approx \frac{d}{4\pi}\int_{-\infty}^{+\infty} dq_y \operatorname{sinc}^2(\pi q_y L) = \frac{d}{4\pi L}. \tag{2.58}$$

The resolution $R = 1/q_{\text{res}}$ follows from solving the threshold criterion Eq. 2.54. If the grating can just be resolved, then $R = d$. It follows that an expression may be derived for the required density of localized labels ρ for achieving a resolution $R = d$, given the localization uncertainty σ:

$$\rho = \frac{4\pi}{3MR^2}\exp\left(4\pi^2\sigma^2/R^2\right). \tag{2.59}$$

The dependence on the ratio σ/R is rather steep. For example, when $\sigma/R = 1$ the exponential factor is already on the order 10^{17}! Realistic minimum labeling densities arise when σ/R is less than approximately $1/4$. So, even though the resolution is not determined solely by the localization uncertainty, the necessity of having practically achievable labeling densities does imply that the minimum resolution is of the order of the localization uncertainty. Eq. 2.59 can also be solved for the resolution R as a function of the density of localized labels and the localization uncertainty:

$$R = \frac{2\pi\sigma}{\sqrt{W\left(3\pi M\rho\sigma^2\right)}}, \tag{2.60}$$

where $W(\cdot)$ is the Lambert W-function [88], which is the inverse of $y = x\exp(x)$. A useful analytical approximation for the Lambert W-function is $W(y) \approx \ln(2y) - \ln(\ln(1+2y))$ [60].

It appears that an increase in M leads to a better resolution. This implies that adding grating lines to the global image improves the ability to distinguish neighboring lines. The underlying reason for this is that a grating is a perfectly periodic structure. Therefore, if M increases then the contributions of the different lines add up in Fourier space and the SNR increases.

GRATING WITH A SQUARE CROSS-SECTION

In a similar way as above, it is also possible to derive the resolution for a grating object consisting of $M \geq 1$ lines of width a, length L and separation $d > a$. The density of localised labels is ρ and the total number of labels is $K = M\rho aL$. For such an object, the Fourier transform of the labeling density function $\psi(\vec{r})$ reads:

$$\hat{\psi}(\vec{q}) = \rho aL \frac{\sin(\pi M q_x d)}{\sin(\pi q_x d)} \operatorname{sinc}(\pi q_x a) \operatorname{sinc}(\pi q_y L). \tag{2.61}$$

The ring average of the spectral density is found for sufficiently large line length L as:

$$S(q) = \frac{1}{2\pi K^2} \int_0^{2\pi} d\psi \left|\hat{\psi}(\vec{q})\right|^2 \approx \frac{1}{\pi q K^2} \int_{-\infty}^{+\infty} dq_y \left|\hat{\psi}(\vec{q})\right|^2, \tag{2.62}$$

where the last integral is evaluated at $q_x = q$, and so:

$$\begin{aligned} S(q) &\approx \frac{\operatorname{sinc}^2(\pi q a)}{\pi q} \left[\frac{\sin(\pi M q d)}{M \sin(\pi q d)}\right]^2 \int_{-\infty}^{+\infty} dq_y \operatorname{sinc}^2(\pi q_y L) \\ &= \frac{\operatorname{sinc}^2(\pi q a)}{\pi q L} \left[\frac{\sin(\pi M q d)}{M \sin(\pi q d)}\right]^2. \end{aligned} \tag{2.63}$$

The equation for solving the resolution is:

$$\frac{3M\rho a}{\pi q_{\text{res}}} \operatorname{sinc}^2(\pi q_{\text{res}} a) \left[\frac{\sin(\pi M q_{\text{res}} d)}{M \sin(\pi q_{\text{res}} d)}\right]^2 \exp\left(-4\pi^2 \sigma^2 q_{\text{res}}^2\right) = 1. \tag{2.64}$$

The grating can just be resolved ($q_{\text{res}} = 1/d$) if the density of localized labels satisfies:

$$\rho = \frac{\pi}{3MaR} \frac{\exp\left(4\pi^2\sigma^2/R^2\right)}{\operatorname{sinc}^2(\pi a/R)}. \tag{2.65}$$

In the limit of thin lines ($a \ll d$) this may be inverted to give a resolution:

$$R = 2\pi\sigma \sqrt{\frac{2}{W\left(72M^2\rho_{\text{lin}}^2\sigma^2\right)}}, \tag{2.66}$$

where $\rho_{lin} = \rho a$. For a single line ($M = 1$) the equation for solving the resolution simplifies to:

$$\frac{3\rho a}{\pi q_{\text{res}}} \operatorname{sinc}^2(\pi q_{\text{res}} a) \exp\left(-4\pi^2\sigma^2 q_{\text{res}}^2\right) = 1. \tag{2.67}$$

In the limit of large density of localized labels ($\rho a^2 \gg 1$) and small localization uncertainty ($\sigma \ll a$) this equation may be solved to give $R = a$, i.e. the resolution is equal to the line width. This may seem counter-intuitive, but it reflects the fact that no details smaller than the line width are present in the object itself. The predicted resolution from M grating lines might be tested if super-resolution data is obtained for a sample with a very sophisticatedly engineered ground truth [89].

EFFECT OF SPURIOUS CORRELATIONS

The preceding analysis provides some quantitative insights into the relevance of the spurious correlations between the two sub-images for techniques with multiple localizations per emitter. The equation for the resolution for a grating with the cosine cross-section for a non-zero Q-parameter is:

$$\left[Q + \frac{M \rho_{\mathrm{loc}} R^2}{4\pi} \right] = \exp\left(4\pi^2 \sigma^2 / R^2\right), \tag{2.68}$$

where $\rho_{\mathrm{loc}} = \rho Q / \left(1 - \exp(-Q)\right)$ is the density of localizations, proportional to the labeling density and the average number of localizations per emitter (Appendix 2.A.2). The effects of spurious correlations on resolution may be neglected provided the ratio of the second and first term on the l.h.s. of Eq. 2.68 is sufficiently large. This happens when ρ_{loc} satisfies:

$$\rho_{\mathrm{loc}} \gg \frac{\pi Q}{M} \left(\frac{2}{R} \right)^2. \tag{2.69}$$

This regime is typically found when the resolution is much worse than the Nyquist resolution following from the density of localized labels ρ, i.e. $R \gg 2/\sqrt{\rho}$. Eq. 2.69 can be used as a self-consistency test for the need to correct for spurious correlations. The resolution found without Q-correction and the estimated value of Q can be confronted given the experimentally found density of localizations. If the inequality is satisfied for, say $M = 2$, then there is probably no need to recompute the resolution with Q-correction, as the magnitude of the correction does not outweigh the added uncertainties of the additional processing steps.

RELATION TO NYQUIST SAMPLING

Consider Eq. 2.60 in the limit where $\sigma \to 0$. The resolution becomes:

$$R = \sqrt{\frac{4\pi}{3M\rho}}, \tag{2.70}$$

which is nearly equal to the Nyquist resolution $R_{\mathrm{Nyquist}} = 2/\sqrt{\rho}$:

$$R = \sqrt{\frac{\pi}{3M}} R_{\mathrm{Nyquist}} \approx R_{\mathrm{Nyquist}} \quad \text{for } M = 1, \tag{2.71}$$

The FRC resolution is not exactly equal to the Nyquist resolution in this limit, because it is conceptually different: it describes for which spatial frequency q there is

a sufficiently high signal-to-noise ratio rather than an absence of aliasing due to undersampling. However, the Nyquist sampling theorem does not strictly apply since localizations do not constitute samples of a bandwidth limited function. Therefore it is not surprising that these two concepts give slightly different values for the resolution.

2.A.4. LABELING-LOCALIZATION TRADE-OFF

TRADE-OFF FOR A PERIODIC OBJECT MODEL

The expression in Eq. 2.60 can be used to analyze the impact of improvement in the density of localized labels ρ and the localization uncertainty σ on the resolution. Clearly obtaining infinitely many localizations yields $R = 0$, whereas perfect localization at $\sigma = 0$ was shown in the preceding section to result in a finite resolution value. This is the consequence of the imaging model, in which structures can have infinitely many labels attached to them. Localizing all these labels yields a blurry image without counting noise due to finite localization densities, which implies that the signal-to-noise ratio is infinite for all spatial frequencies.

Alternatively one could ask whether marginal improvements in ρ or σ yield greater improvements in resolution. The trade-off point in which both improvements are equivalent is found by requiring that the relative change in resolution for a given relative change in Nyquist area $\sim 1/\rho$ is equal to a relative change in resolution for a given relative change in localization uncertainty area σ^2, i.e. if we change either quantity with a given percentage, the resulting percentile change in resolution must be the same:

$$\frac{\sigma^2}{R}\frac{\partial R}{\partial \sigma^2} = -\frac{\rho}{R}\frac{\partial R}{\partial \rho}. \tag{2.72}$$

Evaluating the derivatives results in:

$$\frac{\sigma^2}{R}\frac{\partial R}{\partial \sigma^2} = \frac{W\left(3\pi M\rho\sigma^2\right)}{2\left(1+W\left(3\pi M\rho\sigma^2\right)\right)}, \tag{2.73}$$

$$\frac{\rho}{R}\frac{\partial R}{\partial \rho} = -\frac{1}{2\left(1+W\left(3\pi M\rho\sigma^2\right)\right)}. \tag{2.74}$$

It follows that:

$$W\left(3\pi M\rho\sigma^2\right) = 1, \tag{2.75}$$

implying that the resolution must be:

$$R = 2\pi\sigma, \tag{2.76}$$

and that the optimum trade-off occurs for:

$$\rho\sigma^2 = \frac{e}{3\pi M}. \tag{2.77}$$

For a two-line object ($M = 2$) this corresponds to $\rho\sigma^2 = e/6\pi \approx 0.144$. For M parallel lines we obtain a lower value, from which it may be inferred that for any intricate

but irregular object structure the trade-off occurs for a value smaller than 0.144. For that reason the value $s\rho\sigma^2 = e/6\pi \approx 0.144$ should be considered in practice only as a rule-of-thumb.

TRADE-OFF IN GENERAL

The preceding analysis of marginal improvements in ρ and σ can be generalized by not assuming a specific object model. For this analysis it is useful to revisit Eq. 2.46. At $q = q_{\text{res}}$, the expected FRC curve drops below the threshold, which means that at this point $q_{\text{res}} = 1/R$ is an increasing function of:

$$A\left(q_{\text{res}}\right) = N \exp\left(-4\pi^2\sigma^2 q_{\text{res}}^2\right). \tag{2.78}$$

Therefore R has its minimum whenever $A\left(q\right)$ has its maximum. Consider now the relative changes in A due to changes in N and n_{ph}:

$$\frac{N}{A}\frac{dA}{dN} = 1, \tag{2.79}$$

$$\frac{n_{\text{ph}}}{A}\frac{dA}{dn_{\text{ph}}} = -4\pi^2 n_{\text{ph}} q_{\text{res}}^2 \frac{d\sigma^2}{dn_{\text{ph}}}. \tag{2.80}$$

If $\sigma^2 \propto 1/n_{\text{ph}}$ then these expressions are equal if $2\pi\sigma q_{\text{res}} = 1$ so that $R = 2\pi\sigma$. This is therefore the point where obtaining 1% more localizations has about the same effect on A (and R) as obtaining 1% higher photon counts per localization. Hence $R = 2\pi\sigma$ marks the boundary between the regime $R > 2\pi\sigma$ where the resolution is limited by the number of localizations (labeling density) and the regime $R < 2\pi\sigma$ where the resolution is limited by localization uncertainty.

If a limited amount of time is available, then $R = 2\pi\sigma$ also marks the value of σ for which R is optimal. The localization uncertainty can be improved by increasing n_{ph}. However, when this is accomplished by increasing the on-time of the fluorophores, this also reduces the total number of labels that can be localized in a given acquisition time. This is implied by the requirement of having a sufficiently large distance between individual activated emitters at any point in time [61]. The decrease of σ thus has a positive effect on resolution, whereas the decrease of N has a negative effect on resolution, implying that an optimum can be found by balancing the two effects. This trade-off was already identified in the first publication on localization microscopy [2], where it was noted that 'Including fewer, but brighter, molecules results in higher localization and crisper images, but at a reduced molecular density giving less complete information about the spatial distribution of the target protein'.

This argument can be made quantitative by setting $N \propto \tau_{\text{on}}^{-1}$ and $n_{\text{ph}} \propto \tau_{\text{on}}$ and subsequently considering the following equation:

$$\begin{aligned}\frac{\tau_{\text{on}}}{A}\frac{dA}{d\tau_{\text{on}}} &= \frac{\tau_{\text{on}}}{A}\frac{dA}{dn_{\text{ph}}}\frac{dn_{\text{ph}}}{d\tau_{\text{on}}} + \frac{\tau_{\text{on}}}{A}\frac{dA}{dN}\frac{dN}{d\tau_{\text{on}}} \\ &= \frac{n_{\text{ph}}}{A}\frac{dA}{dn_{\text{ph}}} - \frac{N}{A}\frac{dA}{dN}.\end{aligned} \tag{2.81}$$

This derivative is equal to zero when $R = 2\pi\sigma$, which means that this expression marks the point where the best resolution has been obtained for the given amount of time available. Since the resolution is assumed to always increase as more time becomes available, this also implies that $R = 2\pi\sigma$ marks when the resolution R was obtained in the shortest possible amount of time.

The tuning of the switching kinetics of emitters outlined above is typically not a very important issue yet for localization microscopy experiments. Often the choice of fluorescent labels is constrained by the biological context, and under these constraints it is possible that some labels provide more photons in a shorter on-time than other labels. Moreover, imaging does not always take place at the optimal density of simultaneously active emitters, which means that increasing the on-time does not require that fewer emitters are simultaneously active. However, with the rapid developments of new fluorescent dyes and proteins, this trade-off described above will become more important in the future. Tuning may then be done by the choice of the fluorescent label or buffer composition. Tuning of emitter switching kinetics independent of brightness was demonstrated for example for oxazine dyes using the concentrations of the reducing and oxidizing agents in the imaging buffer [90]. Alternatively, if PALM imaging is combined with a triplet state relaxation scheme [91], the bleaching rate could be decoupled from the excitation intensity, giving the bleaching rate as tuning parameter. Then, in a fixed total time fewer but brighter single emitter events yield more accurate localizations but at the expense of a lower recorded emitter density [2].

MINIMAL TIME TO RESOLUTION

The rule $R = 2\pi\sigma$ indicates for which σ the resolution R is obtained as quickly as possible. This is the conjugate of the result of Fig. 2.1c where it is shown that $R = 2\pi\sigma$ indicates when the highest possible resolution is obtained for a fixed total measurement time. To support this insight, the simulations results from Fig. 2.1c were taken, but this time lines of constant resolution R were calculated by taking the contour lines in the σT_{total}-plane where $FRC\left(q = 1/R\right) = 1/7$. The resulting graph is shown in Fig. 2.6. As in Fig. 2.1c, the lines from the simulated data show good agreement with the theoretically predicted lines. Moreover, Fig. 2.6 shows that the red curve corresponding to $R = 2\pi\sigma$ does indeed seem to go through the points where the measurement time T_{total} is minimal for each resolution in the simulations.

2.A.5. FRC RESOLUTION FOR OTHER IMAGING MODALITIES

The FRC resolution concept can be applied to imaging modalities for which the image formation theory may be centered around the conventional concept of the Point Spread Function (PSF). This applies to both diffraction-limited modalities such as confocal or widefield fluorescence imaging, as well as to diffraction-unlimited modalities such as STED. There the resolving power of the imaging system is given by a modification of Abbe's formula[72]

$$d = \frac{\lambda}{2NA\sqrt{1 + I_{\text{STED}}/I_0}}, \tag{2.82}$$

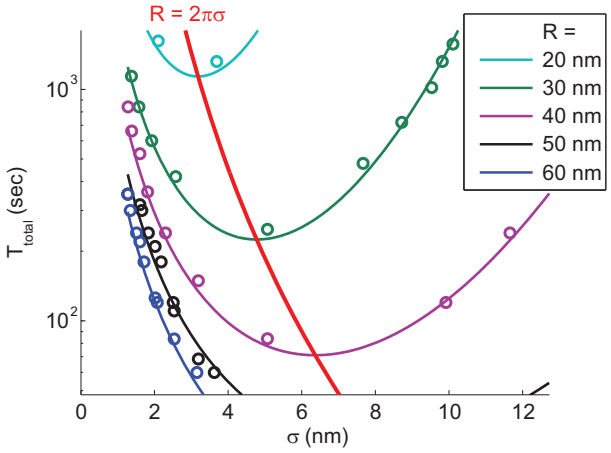

Figure 2.6: Solid lines indicate constant resolution as a function of the total measurement time T_{total} and localization precision σ as predicted by Eq. 2.3 for two lines. The circles represent simulations averaged over 100 realizations. The red separation line $R = 2\pi\sigma$ goes through the shortest measurement time for each resolution in theoretical and simulated data. Left of the separation not enough emitters are collected, whereas to the right the emitters have not been localized precisely enough.

where the crucial parameter is now the ratio of the intensity of the STED beam I_{STED} to the saturation intensity I_0. This measure characterizes optics, properties of the fluorophore and imaging conditions, but does not take the sample structure into account. We demonstrate here that the FRC resolution depends on the Optical Transfer Function (OTF), the spatial frequency content of the sample and the noise level. The resolution is always inferior to the spatial cut-off frequency for which the optical transfer goes to zero. This maximum resolution is only reached in the limit of high signal-to-noise ratio (SNR). So, for diffraction-limited modalities the FRC resolution coincides with the Abbe-resolution in the limited of high SNR. For the STED case it coincides with the formula of Eq. 2.82 in the limit of dense spatial frequency content of the sample.

Starting point of the proof is the labeling density function for an object consisting of fluorescent labels located at positions $\vec{r}_j^{\,em}$ for $j = 1,2,\ldots K$:

$$\psi(\vec{r}) = \sum_{j=1}^{K} \delta\left(\vec{r} - \vec{r}_j^{\,em}\right). \tag{2.83}$$

We assume that the on average n_{ph} photons are detected per emitter. Then the signal part of the image is given by:

$$s(\vec{r}) = n_{\text{ph}} \int d^2 r'\, h\left(\vec{r} - \vec{r}\,'\right) \psi(\vec{r}), \tag{2.84}$$

with $h(\vec{r})$ the PSF, which is normalized such that:

$$\int d^2 r\, h(\vec{r}) = 1. \tag{2.85}$$

In the Fourier domain the relation between the signal and the labeling density function is:

$$\hat{s}(\vec{q}) = n_{\mathrm{ph}} \hat{h}(\vec{q}) \hat{\psi}(\vec{q}). \tag{2.86}$$

The FRC requires two measured images:

$$f_j(\vec{r}) = s(\vec{r}) + n_j(\vec{r}), \tag{2.87}$$

for $j = 1,2$ where $n_j(\vec{r})$ is the noise. In order to simplify the analysis we assume that the only noise source is shot noise from photon statistics. In that case the correlation function for the two images is:

$$\langle f_j(\vec{r}) f_l(\vec{r}\,')\rangle = s(\vec{r}) s(\vec{r}\,') + s(\vec{r}) \delta(\vec{r} - \vec{r}\,') \delta_{jl}, \tag{2.88}$$

which gives after Fourier transformation:

$$\langle \hat{f}_j(\vec{q}) \hat{f}_l(\vec{q}\,')^*\rangle = \hat{s}(\vec{q}) \hat{s}(\vec{q}\,')^* + \hat{s}(\vec{q} - \vec{q}\,') \delta_{jl}. \tag{2.89}$$

If $\vec{q} = \vec{q}\,'$ then:

$$\begin{aligned} \langle \hat{f}_j(\vec{q}) \hat{f}_l(\vec{q})^*\rangle &= |\hat{s}(\vec{q})|^2 + \hat{s}(0)\delta_{jl} \\ &= n_{\mathrm{ph}}^2 |\hat{h}(\vec{q})|^2 |\hat{\psi}(\vec{q})|^2 + K n_{\mathrm{ph}} \delta_{jl}. \end{aligned} \tag{2.90}$$

Taking the average over rings in Fourier space, using the assumption that the OTF is rotationally symmetric, and defining (identical to the case of localization microscopy, Eq. 2.41):

$$S(q) = \frac{1}{K^2} \int d^2 q'\, D(|\vec{q}\,'| - q) |\hat{\psi}(\vec{q}\,')|^2, \tag{2.91}$$

with

$$D(|\vec{q}\,'| - q) = \frac{\delta(|\vec{q}\,'| - q)}{2\pi q}, \tag{2.92}$$

the Fourier ring weight function, we obtain an expression for the expected value of the FRC:

$$\langle FRC\rangle = \frac{K^2 n_{\mathrm{ph}}^2 |\hat{h}(\vec{q})|^2 S(q)}{K^2 n_{\mathrm{ph}}^2 |\hat{h}(\vec{q})|^2 S(q) + K n_{\mathrm{ph}}}. \tag{2.93}$$

Clearly, the FRC decays to zero for large $\vec{q}$ as the OTF $\hat{h}(q)$ also goes to zero for large $\vec{q}$ and is zero for $|\vec{q}| \geq q_{cut}$. The FRC resolution for the sum image is obtained by setting the FRC equal to the threshold value of 1/7. This results in the implicit equation for q_{res}:

$$6 K n_{\mathrm{ph}} |\hat{h}(q_{\mathrm{res}})|^2 S(q_{\mathrm{res}}) = 1. \tag{2.94}$$

So, in general, the FRC resolution depends on the OTF $\hat{H}(q)$, the spatial frequency content of the object $S(q)$, and the level of noise (photon count). In the limit of infinite SNR the resolution resulting from this analysis is given by:

$$\hat{h}(q_{\mathrm{res}}) = 0, \tag{2.95}$$

which corresponds to the Abbe-resolution for diffraction-limited imaging systems. It is stressed that the conclusions described here are not altered by obvious generalizations of the model, e.g. effects of finite pixel size and additional noise sources such as readout noise.

The analysis for diffraction-limited systems can be readily extended to diffraction-unlimited methods such as STED, taking the effective transfer at a given I_{STED} for the OTF-function in Eq. 2.94. Interestingly, previous theoretical analyses of STED[72] have shown before that the sample structure ultimately influences the resolution in the case of finite intensities. For STED as well as for fluorescence nanoscopy techniques it should be noted that this conclusion is contingent on the assumption made here that the labels on the sample are the relevant signal source. If the labeled structure rather than the labels themselves is considered to be the signal source, then the labeling process becomes a source of noise as well. Repeating the above analysis with the labeling process included as a noise source then results in an extra term $2Kn_{\mathrm{ph}}^2\left|\hat{h}\left(\vec{q}\right)\right|^2$ in the denominator of Eq. 2.93. From this it can be concluded that the labeling density, rather than the OTF, may become the limiting factor to resolution for high photon counts in e.g. STED.

3

VISUALIZATION IN LOCALIZATION MICROSCOPY

Localization microscopy lacks a natural way of visualizing the data that are produced, which consist instead of sets of estimated fluorophore positions and possibly additional parameters per position estimate. Therefore an important issue that remains is how the data should be visualized. In literature a few methods are used on an ad-hoc basis, i.e. histogram binning, Gaussian rendering, jittering, Delaunay triangulation, and quadtree visualization. We show that rendering localizations as Gaussian blobs with the same size as the localization error distribution is superior to the other visualization techniques in terms of the FRC resolution of the rendered images. Since this method is also linear in the density of localizations and conveys information about the localization precision, we conclude that it is the visualization method of choice. However, the histogram binning method provides a similar resolution in a shorter computation time and is therefore a good alternative method.

Parts of this chapter have been published as: Nieuwenhuizen, R., Stallinga, S. & Rieger, B. *Cell Membrane Nanodomains: from Biochemistry to Nanoscopy*, chap. Visualization and Resolution in Localization Microscopy, 409–430 (Taylor and Francis, 2014). [92]

3.1. OVERVIEW OF VISUALIZATION METHODS

Localization microscopy has no natural way to display the recordings. It does not sample the image at pixel locations as in standard widefield microscopy. In widefield microscopy images are typically recorded on a CCD camera. The pixels of the camera together with the magnification of the objective lens naturally define the way how an image is sampled. The back projected pixel size is chosen such that it fulfills Nyquist sampling, i.e. a pixel should be smaller than half the diffraction limit $d \leq \lambda/(4NA)$, with λ the wavelength of light and NA the numerical aperture of the imaging system. The emission photons recorded per CCD pixel bin are translated into analog-to-digital units (ADU) with a linear amplification factor (gain). These ADU are typically discretized into 8,12 or 16-bit integers and they represent the intensity or count values. The recorded sample is therefore visualized as a pixelated image where the discrete intensity scale is about linearly proportional to the recorded number of photons and thus the density of fluorescent molecules. The same natural visualization is shared by confocal microscopy, where the CCD pixel is replaced by a point detection device such as a photomultiplier tube or an avalanche photodiode. The stepping of the scan mirror naturally defines the pixel size. Please note that it is common to have a regular (square) sampling grid of pixels and/or scan positions, but that is not strictly necessary. Especially to avoid phototoxicity adaptive schemes of illuminating and recording have been proposed [93, 94].

As localization microscopy lacks any of the above natural ways of visualization, it is an important issue how data should be visualized. Basically the positions of single fluorescent emitters are estimated from the asynchronous recordings of blinking emitters. To this end different localization schemes are employed that estimate the positions (i.e. a list of 2D or 3D coordinates), as well as the estimated fluorophore intensities, background intensities, localization precisions and possibly other parameters depending on the localization method [15, 19, 62, 95]. Thus localization microscopy produces datasets but no images initially. To make these data comprehensible, these localization data need to be translated into a visual representation in the form of an image. Subsequently this image needs to be translated into brightness values of the pixels in the display device. Reconstruction (in the Nyquist sense) of the fluorophore distribution of the underlying imaged object from the set of localizations is not considered to be a part of the visualization process.

This chapter is concerned with the choice of the visualization method for translating localization data into an image. Several methods have been proposed in the literature which will be discussed here: scattergram plots [3], histogram binning [96], Gaussian rendering [2], jittered histogram binning [23], Delaunay triangulation [97], and quad-tree visualization [97]. Fig. 3.1 shows an illustration of the different visualization methods, except the scattergram method. First we will describe and illustrate of each of these visualization methods before moving on to the next sections which discuss the merits and implications of using these methods.

Scattergram: each coordinate is plotted as a symbol, typically a cross or plus, in a Cartesian coordinate system [3].

Histogram binning: the field of view is divided into a complete set of square pixel

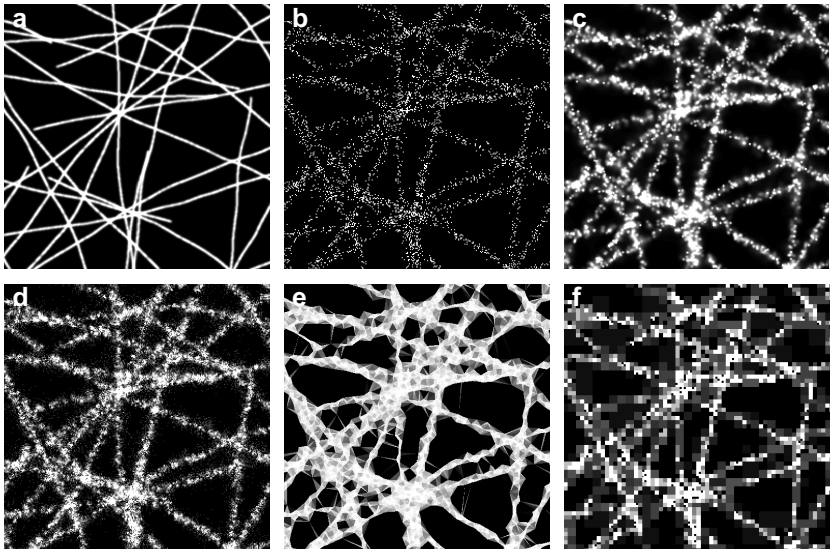

Figure 3.1: Illustration of different visualization methods. The images show the different visualization methods applied to simulated localization data of filaments for a density of localizations $\rho = 2.0 \cdot 10^3 \mu m^{-2}$ and localization precision $\sigma = 10$ nm. Panels: (a) The ground truth structure, (b) histogram binning, (c) Gaussian rendering, (d) jittering, (e) Delaunay triangulation, (f) quad-tree visualization. Images are individually 95 percentile stretched for better visibility on paper.

bins and the number of localizations that falls in each bin is counted and used to assign intensity values to bins [96]. The size of the pixel bins should generally not exceed one quarter of the image resolution in order not to deteriorate the resolution [44]. Histogram images often appear rather noisy due to the low signal-to-noise-ratio per pixel, which can be resolved by post-blurring the histogram images. This blurring also prevents problems with aliasing if the sampling density of the display device is too low. If a radially symmetric kernel is used for blurring then the image resolution remains unchanged for reasonably isotropic structures [44].

Gaussian rendering: an image is rendered where localizations are represented with Gaussian blobs with a width proportional to the estimated localization precision in the respective axial and lateral dimensions [2]. Thus the resulting image conveys information on the localization precision of each localization. It should be noted that effects such as imperfect correction for stage drift effectively lead to an additional localization error that is not taken into account in the estimated localization precision. Therefore the rendered Gaussian blobs cannot always be interpreted to be likelihood functions for the positions of the fluorophores.

Jittered histogram binning: each localization gives rise to a fixed number of offspring points (typically 10 or 20) that are randomly displaced (i.e. jittered) with a zero-mean normal distribution whose standard deviation is equal to the estimated localization precision [23]. Thus for very large numbers of offspring points, this visu-

alization method gives the same result as Gaussian rendering.

Delaunay triangulation: a tiling is created in the image plane using triangles whose vertices correspond to the estimated emitter locations [97]. The triangles are rendered with a grayscale intensity inversely proportional to the area of the triangle such that higher local densities of emitters result in higher intensities. The size of the triangles emphasizes the local density of localizations.

Quad-tree visualization: an image is formed using square pixels whose size depends on the local density of localizations [97]. Initially the image plane is divided into four pixels. Each pixel that contains more than a fixed threshold number of localizations is subsequently split into four subpixels. This process is repeated for the subpixels, until each pixel contains fewer localizations than the threshold value.

3.2. QUALITATIVE COMPARISON OF VISUALIZATION METHODS

With the multitude of available visualization methods, the question arises which method is best for representing experimental data. A number of relevant considerations in choosing a visualization method were discussed by Baddeley *et al.* [97]. Here we will focus on the most important of those: the extent to which images produced with a visualization method can be intuitively interpreted and the image resolution of these images.

Intuitive interpretation of localization microscopy images requires that the images conform to users' expectations based on other fluorescence microscopy methods, such as widefield or confocal imaging. In these microscopy techniques, the local intensity in the image can be described by a convolution of the fluorophore density in the sample with the effective point spread function. Hence the image intensity values are linear in the density of imaged molecules and typically vary smoothly due to the effective blurring by the point spread function. This linearity is also inherent in super-resolution imaging techniques such as STED [45, 98], structured illumination [71, 99] and image scanning microscopy [100, 101].

The expected linearity of intensity values argues against the use of the scattergram visualization method: at a high localization density the symbols in the scattergram overlap and lead to a saturated image. The Delaunay triangulation and quad-tree methods are also not linear in the density of localized molecules, but these do not provided saturated images.

Linearity is more generally an issue for localization microscopy because the acquisitions are nonlinear in the density of labeled molecules. Some molecules are not localized in an experiment and do not contribute to the final image. Additionally, fluorophore activation events are sometimes not recognized or rejected by the localization software. This could happen for example if fluorophores are too dim to be picked up by the algorithm that selects candidates for fitting or too dim to pass the threshold for the allowed localization precision. Also if nearby fluorophores are simultaneously active such that their emissions overlap in the image plane then the localization algorithm results in a position intermediate between the two simulta-

neously active molecules. Although currently methods towards multi-fluorophore fitting [35, 36, 38] are proposed, the application of these methods to non-ideal acquisitions outside TIRF imaging remains a challenge. In the worst case, overlapping emissions may result in unnoticed missing structures. Hence the final images are always nonlinear in the density of labeled molecules. None of the above visualization methods, however, shows activation events missed by the preprocessing software for candidate selection.

The smooth, blurry appearance of images produced with conventional fluorescence microscopy methods normally conveys a sense of the resolution of the imaging system. Therefore, the Gaussian rendering and jittered binning methods vary the apparent width of localizations in images to indicate how well the corresponding fluorophores can be distinguished from nearby molecules. The ability, however, to resolve structures in localization microscopy depends not only on the localization precision, but also for example on the labeling density [44]. Therefore the apparent size of localizations in Gaussian rendering and jittered binning methods does not indicate the actual image resolution. Delaunay triangulation and quad-tree visualization emphasize local variations in the image resolution by adjusting the triangle sizes or subpixel sizes to the labeling density. Unfortunately, these sizes do not correspond to the image resolution that would be determined with the FRC method.

3.3. QUANTITATIVE COMPARISON OF VISUALIZATION METHODS

The second consideration for choosing a visualization method that merits attention, next to intuitive interpretation, is the actual image resolution in the image that is produced. This issue will be addressed by studying the resolution of images produces with different visualization methods for simulation data. By using simulation data where the underlying imaged structure is known, it is possible to identify if the FRC between images of two halves of the simulated data is biased. Such a bias could result in inaccurate resolution determination for experimental data.

SIMULATION SETUP

Localization microscopy acquisitions of filaments were simulated where both the chosen average localization precision σ and density of localizations ρ were varied. For these simulations, the ground truth structure consisted of 100 filaments generated with a worm-like chain model [102–104] for a persistence length of 15 μm (i.e. approximately the persistence length of F-actin [105]). Each filament had a random starting position and starting orientation inside the field of view of 5.12 μm by 5.12 μm. All filaments were then Gaussian blurred with a standard deviation of 5 nm to provide the filaments with a finite width. Subsequently, they were rendered in an image with a pixel size of 2.5 nm.

For this ground truth structure, 100 acquisitions were simulated for each combination of densities ρ and localization uncertainties σ. For each acquisition, a Poisson distributed number of points was generated with a density proportional to the

ground truth structure and average density equal to ρ. These points were then randomly displaced with a Gaussian probability density with variance $d^2 + \sigma_0^2/n_{photons}$ to simulate the finite label size and localization error. Here d represents the finite size of fluorescent labels and had a value $d = 5$ nm. For each point σ_0 was randomly drawn from a normal distribution with a mean specified by $\langle\sigma_0\rangle = 450$ nm and standard deviation of $0.1\langle\sigma_0\rangle$. The parameter $n_{photons}$ was randomly drawn from a geometric distribution, which is the distribution for the photon counts of a photon source whose duration has an exponential distribution. These values give a localization uncertainty of 10 nm at 2000 photons.

The simulated localization data were used to compute the resolutions of the images generated by the various visualization methods. For each acquisition, the localizations were split into two half sets to obtain two images per visualization methods. All images had pixel sizes of 5 nm, except the images obtained with Delaunay triangulation which were rendered using the PALM Siever software [106] with a pixel size of 2.5 nm. For the quad-tree visualization, the threshold number of localization per pixel for splitting into subpixels was 6. Subsequently, the resolution was obtained with these images by computing the FRC and finding the spatial frequency for which the FRC dropped below the threshold of $1/7$. To investigate potential biases in the computed FRC curves, additional images were made with all localizations of each acquisition. These were then used to compute the FRC between those images and the ground truth structure. The spatial frequency at which this full data FRC crosses a threshold of $1/2$ should give the same result as before for unbiased resolution estimation [59].

RESULTS

The results of the simulations are summarized in Figs. 3.2 and 3.3. Fig. 3.2 shows the resolution between the full data images and the ground truth structure for the various visualization methods. From this figure it becomes clear that generally histogram binning, jittering, and Gaussian rendering result in more or less the same resolution. Gaussian rendering provides the best resolution, especially when the mean localization error σ is large and strongly affects the image resolution. This result will be discussed in more detail in the next paragraph. Delaunay triangulation and quad-tree visualization result in substantially deteriorated resolutions when the density ρ is not very high. For Delaunay triangulation this deterioration is attributed to the hard edges that are introduced. For the quad-tree method the deterioration is attributed to the lack of shift invariance of the pixel splitting.

Fig. 3.3 shows that Delaunay triangulation and quad-tree visualization bias the resolution estimation with two half data sets for small ρ and small σ. The bias is also evident in Fig. 3.4 where the FRC curves between two half data sets are compared with the expected FRC curves based on the FRC between the full data and the ground truth images for these visualization methods. The irregular bias in the quad-tree FRC curve for two half data sets also explains the irregularity in the resolution bias as a function of ρ and σ for that method. All this implies that these visualization methods should not be used to compute and assess the resolution for experimental data.

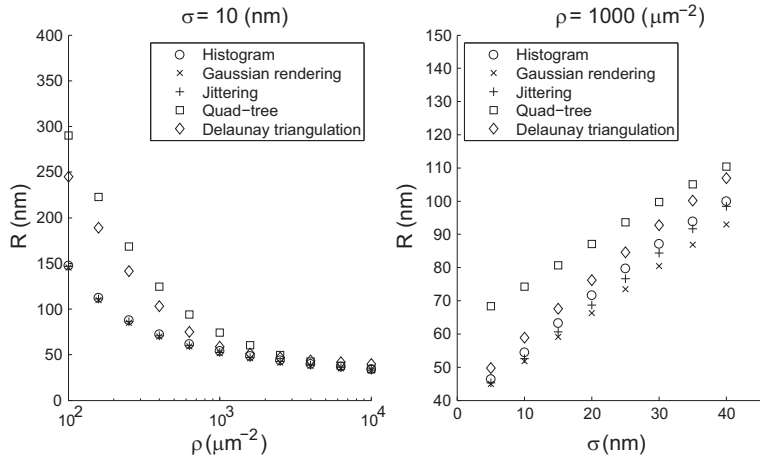

Figure 3.2: Resolution for the different visualization methods as a function of the density of localizations ρ and localization precision σ. The resolution is computed from the FRC between images of the full data sets and the ground truth structure. The standard error of the mean is smaller than the marker sizes in this plot.

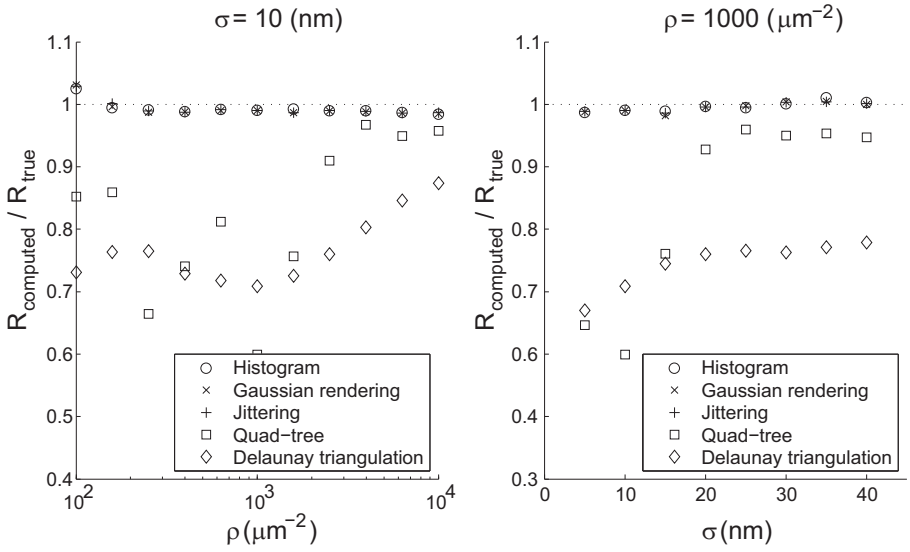

Figure 3.3: Bias in resolution estimation for the different visualization methods as a function of the density of localizations ρ and localization precision σ. R_{true} is the resolution obtained from the FRC between images of the full data sets and the ground truth structure, whereas $R_{computed}$ is the resolution obtained from the FRC between two images of half data sets. The standard error of the mean is smaller than the marker sizes in this plot.

THEORETICAL CONSIDERATIONS

This paragraph provides a theoretical explanation for why Gaussian rendering performs better than histogram binning. To this end, the expected FRC will be derived

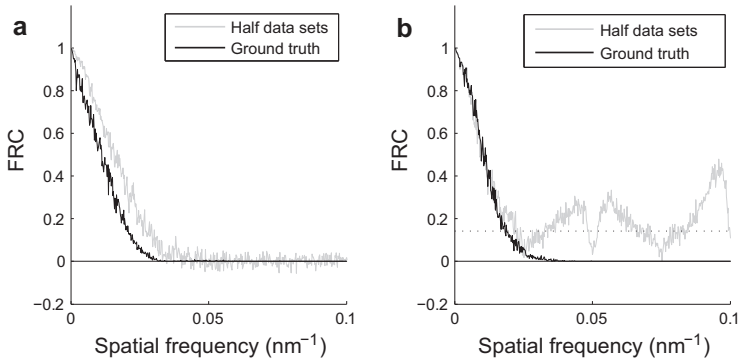

Figure 3.4: FRC curves for (a) Delaunay triangulation and (b) quad-tree visualization. The FRC between two images of half data sets is compared here with the curve that would be expected based on the FRC between images of the full data sets and the ground truth structure.

for the case where the localization precision σ is not constant for both the Gaussian rendering method and the histogram binning method. Consistent with the simulations above, it will be assumed for simplicity that all fluorophores on the structure at hand are localized exactly once.

Before deriving the expected FRCs, we provide a few definitions. Firstly, the ground truth object for this derivations is given by:

$$\psi(\vec{r}) = \sum_{j=1}^{N} \delta\left(\vec{r} - \vec{r}_j^{\,em}\right), \tag{3.1}$$

where δ is the Dirac delta function. The object depends on the set of positions $\left\{\vec{r}_j^{\,\mathrm{em}} | j = 1,\ldots,N\right\}$ of the N fluorophores or labels. These labels are localized at positions $\{\vec{r}_j | j = 1,\ldots,N\}$ with probability $P(\vec{r}_j) = (2\pi\sigma_j^2)^{-1}\exp(-\left\|\vec{r}_j - \vec{r}_j^{\,em}\right\|^2/2\sigma_j^2)$. In the following we assume no specific dimensionality, but typically $\vec{r}_j \in \mathbb{R}^2$ or $\vec{r}_j \in \mathbb{R}^3$. For the three-dimensional case, the localization uncertainty is typically 2-3 times worse in the axial direction than in the lateral direction [70, 107, 108], except for very specific experimental setups [69, 109]. For the sake of compactness, two-dimensional acquisitions with isotropic localization uncertainties will be assumed, although the conclusions derived here are also valid for anisotropic localization uncertainties.

The set of localizations is split into two subsets of size N_1 and N_2 to produce two images $f_1(\vec{r})$ and $f_2(\vec{r})$, with $N_1 + N_2 = N$ and $N_1 \approx N_2$. The FRC between such images is defined as given by Eq. 2.1. The expected value of the numerator of the FRC when emitters are localized is

$$\left\langle \sum_{\vec{q}\in\mathrm{circle}} \hat{f}_1(\vec{q})\,\hat{f}_2(\vec{q})^* \right\rangle = \sum_{\vec{q}\in\mathrm{circle}} \langle \hat{f}_1(\vec{q})\rangle \langle \hat{f}_2(\vec{q})^*\rangle, \tag{3.2}$$

where $\langle f(\vec{r})\rangle \equiv \int d\vec{r}_1 \ldots d\vec{r}_N f(\vec{r}) P(\{\vec{r}_j\})$. For Gaussian rendering, the images are denoted by $g_m(\vec{r})$ with $m = \{1,2\}$, and equal to

$$g_m(\vec{r}) = \sum_{j=1}^{N_m} \frac{1}{2\pi\sigma_j^2} e^{-||\vec{r}-\vec{r}_j||^2/2\sigma_j^2}, \tag{3.3}$$

with Fourier transformation

$$\hat{g}_m(\vec{q}) = \sum_{j=1}^{N_m} e^{-2\pi^2 q^2 \sigma_j^2} e^{-i2\pi\vec{q}\cdot\vec{r}_j}. \tag{3.4}$$

For the case of constant $\sigma_j \equiv \sigma \,\forall\, j$, this expression simply describes a convolution of the found positions r_j with a Gaussian kernel of size σ. Assuming that σ_j is given (i.e. not a stochastic variable), the expected value of $f_m(\vec{q})$ becomes:

$$\langle \hat{g}_m(\vec{q})\rangle = \int d\vec{r}_j \sum_{j=1}^{N_m} e^{-2\pi^2 q^2\sigma_j^2} e^{-i2\pi\vec{q}\cdot\vec{r}_j} P(\{\vec{r}_j\}) \tag{3.5}$$

$$= \sum_{j=1}^{N_m} e^{-2\pi^2 q^2\sigma_j^2} \int d\vec{r}_j\, e^{-i2\pi\vec{q}\cdot\vec{r}_j} P(\{\vec{r}_j\}) \tag{3.6}$$

$$= \sum_{j=1}^{N_m} e^{-4\pi^2 q^2\sigma_j^2} e^{-i2\pi\vec{q}\cdot\vec{r}_j^{em}} \approx \frac{1}{N}\hat{\psi}(\vec{q}) \sum_{j=1}^{N_m} e^{-4\pi^2 q^2\sigma_j^2}. \tag{3.7}$$

If the effect of low pass filtering due to finite pixel size is neglected, $f_m(\vec{r})$ for histogram binning is equal to

$$f_m(\vec{r}) = \sum_{j=1}^{N_m} \delta(\vec{r} - \vec{r}_j), \tag{3.8}$$

which leads to

$$\langle \hat{f}_m(\vec{q})|\sigma_j\rangle \approx \frac{1}{N}\hat{\psi}(\vec{q}) \sum_{j=1}^{N_m} e^{-2\pi^2 q^2\sigma_j^2}. \tag{3.9}$$

The difference between the two visualization methods already becomes apparent here. Comparing Eq. 3.7 and Eq. 3.9 shows that an extra factor 2 appears in the exponent due to the extra blurring of the Gaussian rendering. For the expected value of the denominator of the FRC, the expected value of $|f_m(\vec{q})|^2$ needs to be evaluated.

For Gaussian rendering this goes as follows:

$$\left\langle \left|\hat{g}_m(\vec{q})\right|^2 \right\rangle = \left\langle \sum_{j=1}^{N_m}\sum_{k=1}^{N_m} e^{-2\pi^2 q^2\sigma_j^2} e^{-2\pi^2 q^2\sigma_k^2} e^{-i2\pi\vec{q}\cdot(\vec{r}_k-\vec{r}_j)} \right\rangle \tag{3.10}$$

$$= \left\langle \sum_{j=1}^{N_m}\sum_{k\neq j} e^{-2\pi^2 q^2\left(\sigma_j^2+\sigma_k^2\right)} e^{-i2\pi\vec{q}\cdot(\vec{r}_k-\vec{r}_j)} \right\rangle + \left\langle \sum_{j=1}^{N_m} e^{-4\pi^2 q^2\sigma_j^2} \right\rangle \tag{3.11}$$

$$\approx \left| \left\langle \sum_{j=1}^{N_m} e^{-2\pi^2 q^2\sigma_j^2} e^{-i2\pi\vec{q}\cdot\vec{r}_j} \right\rangle \right|^2 + \left\langle \sum_{j=1}^{N_m} e^{-4\pi^2 q^2\sigma_j^2} \right\rangle \tag{3.12}$$

$$= \left|\left\langle \hat{g}_m(\vec{q})\right\rangle\right|^2 + \left\langle \sum_{j=1}^{N_m} e^{-4\pi^2 q^2\sigma_j^2} \right\rangle. \tag{3.13}$$

Thus, if the average spectrum of the object over rings of constant spatial frequency is defined as $S(q) = \frac{1}{N^2}\int d^2q' \frac{\delta(|\vec{q}'|-q)}{2\pi q}\left|\hat{\psi}(\vec{q}')\right|^2$, the expected FRC becomes

$$\langle FRC\rangle = \frac{NS(q)\left\langle \exp\left(-4\pi^2\sigma^2q^2\right)\right\rangle^2}{2\left\langle \exp\left(-4\pi^2\sigma^2q^2\right)\right\rangle + NS(q)\left\langle \exp\left(-4\pi^2\sigma^2q^2\right)\right\rangle^2} \tag{3.14}$$

$$= \frac{NS(q)\left\langle \exp\left(-4\pi^2\sigma^2q^2\right)\right\rangle}{2+NS(q)\left\langle \exp\left(-4\pi^2\sigma^2q^2\right)\right\rangle}. \tag{3.15}$$

Similarly, for histogram binning the expected value of $\left|f_m(\vec{q})\right|^2$ is

$$\left\langle \left|\hat{f}_m(\vec{q})\right|^2 \right\rangle = \left\langle \sum_{j=1}^{N_m}\sum_{k=1}^{N_m} e^{-i2\pi\vec{q}\cdot(\vec{r}_k-\vec{r}_j)} \right\rangle \approx \left|\left\langle \hat{f}_m(\vec{q})\right\rangle\right|^2 + N_m, \tag{3.16}$$

which leads to the following expected FRC

$$\langle FRC\rangle = \frac{NS(q)\left\langle \exp\left(-2\pi^2\sigma^2q^2\right)\right\rangle^2}{2+NS(q)\left\langle \exp\left(-2\pi^2\sigma^2q^2\right)\right\rangle^2}. \tag{3.17}$$

The superiority of the Gaussian rendering over histogram binning now follows from comparing Eq. 3.15 and Eq. 3.17 and observing that

$$\left\langle e^{-4\pi^2\sigma^2q^2}\right\rangle - \left\langle e^{-2\pi^2\sigma^2q^2}\right\rangle^2 = \left\langle \left(e^{-2\pi^2\sigma^2q^2} - \left\langle e^{-2\pi^2\sigma^2q^2}\right\rangle\right)^2 \right\rangle \geq 0. \tag{3.18}$$

The explanation for this general superiority following from the equations above is that Gaussian rendering effectively weights the contribution of localizations to spatial frequency components depending on their localization precision. This weighting was already obvious from the comparison of Eq. 3.7 and Eq. 3.9 which showed that Gaussian rendering introduces an extra factor 2 in the exponent. This causes the exponentials corresponding to imprecise localizations to decrease faster and therefore those localizations contribute less to high frequency components. This leads to

higher correlations at those frequencies. For a constant localization uncertainty for all localizations, i.e. $\sigma_j \equiv \sigma \; \forall j$, both visualization methods are equivalent as the difference in Eq. 3.18 is then equal to zero.

This derivation did not include the effects of finite pixel size and multiple localizations per emitter. Low pass filtering due to finite pixel sizes introduces an extra damping of $S(q)$ which is the same for histogram binning and Gaussian rendering. For very large pixel sizes, the damping due to finite pixel size will be stronger than damping due to the localization error, thus negating the benefits of Gaussian rendering. For multiple localizations per emitter, the impact of Gaussian rendering on the FRC is more subtle and dependent on the statistics of the localization uncertainties σ_j.

3.4. DISCUSSION & CONCLUSION

The above results lead to the conclusion that the Gaussian rendering method provides the best resolution of the evaluated visualization methods. Please note that this is only true if the Gaussian blobs reflect the localization uncertainty of each single fluorophore and not if one applies one global Gaussian kernel to all localizations. Since this method is also linear in the density of localizations and conveys information about the localization precision it seems to be the visualization method of choice. However, the histogram binning method provides a similar resolution in a shorter computation time and is therefore a good alternative method. In particular, the reduced computation time make histogram binning the preferred method for fast and unbiased resolution determination. When this method is used for visualization, it is recommended to post-blur the image, for example with a Gaussian kernel with a standard deviation equal to the average localization precision. This reduces the noise in the image without reducing the resolution. The jittering method provides a compromise between the histogram binning and Gaussian rendering methods, with a better resolution than histogram binning and typically a shorter computation time than Gaussian rendering. Quad-tree visualization and Delaunay triangulation lead to resolution deterioration and biased resolution estimation and are therefore not recommended.

A significant limitation of this simulation study is that the ground truth structure and the Delaunay triangulation results had to be pixelated to compute their Fourier transforms, even though they contain infinitely high spatial frequency components. In principle this could lead to changes in frequency contents due to aliasing and the effective low-pass filtering due to the finite pixel size. The resolutions, however, in these simulations were typically more than twenty times the pixel size of these images. Therefore these problems should not play a role at the spatial frequencies where the FRC drops below the threshold and should not affect the computed resolution.

4

QUANTITATIVE LOCALIZATION MICROSCOPY

Quantification in localization microscopy with reversibly switchable fluorophores is severely hampered by the unknown number of switching cycles a fluorophore undergoes and the unknown stoichiometry of fluorophores on a marker such as an antibody. We overcome this problem by measuring the average number of localizations per fluorophore, or generally per fluorescently labeled site from the build-up of spatial image correlation during acquisition. To this end we employ a model for the interplay between the statistics of activation, bleaching, and labeling stoichiometry. We validated our method using single fluorophore labeled DNA oligomers and multiple-labeled neutravidin tetramers where we find a counting error of less than 17% without any calibration of transition rates. Furthermore, we demonstrated our quantification method on nanobody- and antibody-labeled biological specimens.

Parts of this chapter have been published as: Nieuwenhuizen, R.P.J., Bates, M., Szymborska, A., Lidke, K.A., Rieger, B. & Stallinga, S. *PLoS ONE* **10**, e0127989 (2015).

4.1. INTRODUCTION

Localization microscopy (e.g. PALM/STORM) is a powerful tool for imaging biological structures on the nanoscale[2–4, 47, 48]. In order to yield information about the molecular composition of the sample, localization microscopy images must be quantifiable in terms of the density of fluorescently labeled molecules or of binding sites. The relationship between these desired densities and the actual measured density of localizations is non-trivial however, since the (average) number of localizations per fluorophore and the labeling stoichiometry are unknown.

The use of photo-activatable fluorescent proteins (FPs)[2, 4, 64] offers a relatively direct approach to counting and thus to obtaining the desired densities, provided they switch off irreversibly after a non-interrupted on-state. In practice, however, there are several factors that can either lead to overcounting or undercounting of molecules[110]. Overcounting occurs when molecules are localized several times, either due to short-term blinking during the on-state or due to long lived dark states that effectively lead to reversible switching of FPs[67, 111]. In addition, overexpression of fluorescent fusion proteins, which is needed to substitute the native protein, may also lead to overestimation of protein numbers relative to endogenous expression levels. Undercounting occurs when the weak signals from FPs are missed by the localization algorithm or when FPs are not functional due to protein misfolding or incomplete maturation[112–114].

Another method of labeling employs organic fluorophores, which typically have a higher brightness and photostability than FPs, and thus have a higher probability to be successfully detected and then to be localized more accurately[68]. Organic fluorophores have not been widely used for quantification studies, however, as quantification is complicated by undercounting problems due to incomplete labeling of potential binding sites, and by overcounting problems due to reversible switching of the fluorophores and unknown stoichiometry of the fluorescent labels on the marker (e.g. antibody). These undercounting problems can only be solved in general by new advances in biochemical labeling techniques that result in a higher labeling efficiency. Instead, we focus here on addressing the overcounting problems with computational methods.

Efforts have been made in the past towards resolving the issue of overcounting with reversibly switchable fluorophores. For example, in kymograph analysis samples are prepared with sparsely distributed fluorescent markers to calibrate the fluorophore switching kinetics[67]. Similarly, a titration method was recently proposed where the concentration of markers during labeling was titrated to calibrate the number of localizations per marker[115, 116]. However, both methods are susceptible to differences in the local chemical environment in the calibration conditions that affect the switching kinetics and thus render the calibration inaccurate. Alternatively, pair correlation analysis[65, 66] does not require a separate calibration experiment, but relies on an over-simplified physical model (e.g. neglecting the effects of photobleaching). Methods addressing the short-term blinking of fluorescent proteins (e.g. [64, 67, 111]) rely on spatiotemporal clustering of localizations of the same fluorophore. This does not work for reversibly switching fluorophores as the lifetime of

the long-lived dark states is much longer than the timescale on which other nearby fluorophores are activated.

In chapter 2 we have proposed the use of spatial frequency correlations in the reconstructed super-resolution image to estimate the average number of localizations per marker. However, in that chapter bleaching effects were treated in an ad hoc manner and labeling stoichiometry was not considered. Here, we present a study of how both effects can be accounted for to provide accurate quantification of localization microscopy data in terms of the number of localizations per fluorescently labeled site. Our method requires only limited calibration of the labeling stoichiometry and is applicable to common labeling techniques (e.g. antibodies).

4.2. RESULTS

4.2.1. QUANTIFICATION WITH A SINGLE FLUOROPHORE PER SITE

The starting point of our analysis is a three-state switching model[117, 118] for a fluorophore consisting of an on-state, off-state and a bleached state. The on-off switching is characterized by a switching rate $k_{sw} = k_{on}k_{off}/(k_{on} + k_{off})$ and the photobleaching by an effective bleaching rate k_{bl}. Bleaching from the on-state, as well as from the off-state, is taken into account. Therefore the effective bleaching rate k_{bl} depends on the rates of both bleaching channels. This model (see Appendix 4.A.2 for a derivation) gives rise to an average number of activations per fluorophore:

$$\langle M(t)\rangle = M_\infty \left(1 - \exp\left(-k_{bl}\, t\right)\right) \tag{4.1}$$

where $M_\infty = k_{sw}/k_{bl}$ is the average number of switching cycles the fluorophore undergoes before photobleaching. For small times ($k_{bl}\, t \ll 1$) the statistics of on-off switching dominates the number of localizations of a single emitter, which then follows a Poisson distribution with expectation value $k_{sw}\, t$. For longer times ($k_{bl}\, t \gg 1$) bleaching is more important and the number of localizations follows a geometric distribution with expectation value M_∞.

Measurement of the bleaching rate k_{bl} from the cumulative number of localizations as a function of time is straightforward. Determination of the switching rate k_{sw}, or equivalently the asymptotic number of localizations per emitter M_∞, requires an additional measurement. Spatial correlation analysis with Fourier Ring Correlation[44] enables the measurement of the correlation parameter
$Q(t) = \langle M(M-1)\rangle / \langle M\rangle$. This correlation parameter is related to the variance in M by $Var(M) = \langle M\rangle (Q - \langle M\rangle + 1)$. It depends on the parameters of the three-state switching model as:

$$Q(t) = 2\,(M_\infty - 1)\left(1 - \frac{k_{bl}\, t}{\exp\left(k_{bl}\, t\right) - 1}\right). \tag{4.2}$$

Measurement of $Q(t)$ enables the determination of M_∞, as k_{bl} is already known from the fit to the cumulative number of localizations. The average number of localizations per emitter $\langle M(t)\rangle$ can be directly found from k_{bl} and M_∞ using Eq. 4.1. The desired density of emitters then follows from the measured density of localizations by dividing with $\langle M(t)\rangle$ at the final time point of the data acquisition.

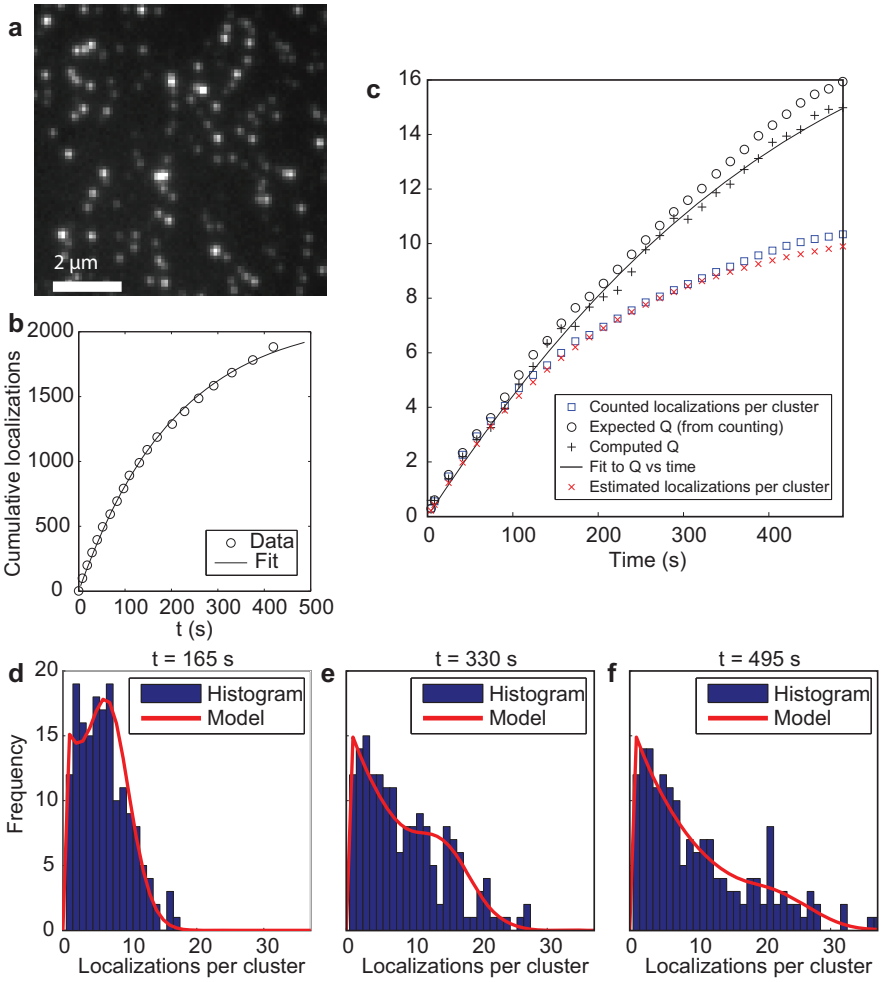

Figure 4.1: Quantitative localization microscopy with a single fluorophore per labeled site. (a) Three state model with rates. (b) Cutout of total image of sparsely distributed DNA oligomers on glass labeled with single Alexa Fluor 647 dyes showing well-isolated clusters of localizations. (c) Cumulative number of localizations and single-exponential fit. (d) Correlation parameter Q determined from the spatial image correlations and fit with switching model shows agreement with the ground truth value determined from the cluster analysis. The estimated value for the average number of localizations $\langle M(t) \rangle$ shows agreement with the ground truth value determined from the cluster statistics. (e-g) Histograms of the number of localizations accumulated per cluster and model prediction at three time points during the image acquisition.

The three-state switching model for individual fluorophores has been validated by experiments on isolated DNA oligomers labeled with single Alexa Fluor 647 dyes on a glass substrate (Fig. 4.1a). Clearly recognizable isolated clusters of localizations provide a ground truth for the distribution of localizations per emitter. First order switching kinetics are confirmed by the observation of exponential on and off-time

distributions (Fig. 4.2) giving $\tau_{on} = 26.6 \pm 0.5$ ms and $\tau_{off} = 18.0 \pm 0.4$ s. Fits of the cumulative number of localizations (Fig. 4.1b) and the correlation parameter yield $k_{bl} = (4.7 \pm 0.1) \times 10^{-3}$/s and $M_\infty = 11.0 \pm 0.1$. Both the correlation parameter $Q(t)$ and the predicted number of localizations per emitter $\langle M(t) \rangle$, which is found with the estimated values of k_{bl} and M_∞, agree with less than 10% error with the ground truth values obtained from the cluster analysis (Fig. 4.1c).

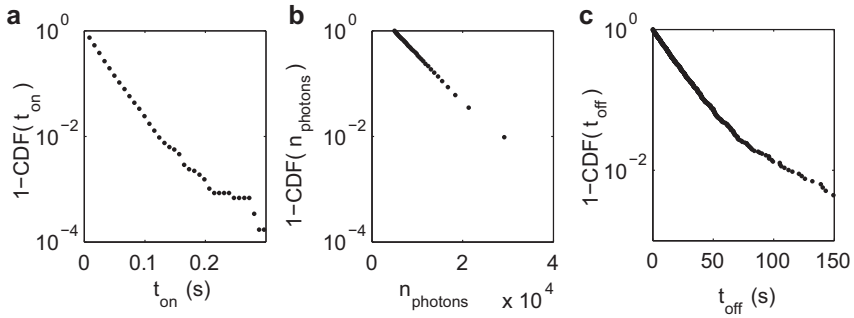

Figure 4.2: Linearity of switching kinetics. (a) Empirical distributions of the on- and off-times, respectively t_{on} and t_{off}, of individual fluorophores were obtained for the data of DNA oligomers labeled with single Alexa Fluor 647 dyes on a glass substrate shown in Fig. 4.1. t_{on} was determined by finding all localizations belonging to the same activation event and determining the time between the first and last localization. (b) The sum of estimated signal photons $n_{photons}$ from the combined localizations shows a single exponential distribution. (c) t_{off} was determined as the time interval between subsequent localizations of the same fluorophore as determined by cluster analysis. The distribution of t_{on} is mono-exponential, the distribution of t_{off} is reasonably described with a single exponential distribution but possibly also by a bi-exponential distribution, which can possibly be attributed to residual effects of sample contaminations.

Neglecting effects of photobleaching would lead to the estimate $\langle M(t) \rangle = Q(t)$ which results here in an error of up to 47%. Note that the use of pair-correlation functions for counting also comes down to an alternative procedure for estimating the quantity $Q(t)$ [66], and would thus suffer from a comparable error when photobleaching is neglected. The measured on and off-times of the clustered localizations lead to a switching rate $k_{sw} = (5.6 \pm 0.1) \times 10^{-2}$/s, in reasonable agreement with the value $k_{bl} M_\infty = (5.2 \pm 0.2) \times 10^{-2}$/s obtained from the fit parameters above. Finally, the distribution of the number of localizations per emitter as a function of time (Fig. 4.1d-f) corresponds well to theory for the estimated values of k_{bl} and M_∞: p = 0.67, 0.91, and 0.71, in one-sample two-sided discrete Kolmogorov-Smirnov tests at times t = 122, 243 and 365 s respectively, so no significant difference was found at a 0.05 significance level.

We applied our method to images of the Seh1 protein, a component of the Nuclear Pore Complex (NPC)[119] tagged with mEGFP and labeled with anti-GFP nanobodies (NBs) conjugated to Alexa Fluor 647 fluorophores. The degree of labeling (DOL) and average brightness of the NBs were characterized with absorption spectroscopy and Fluorescence Correlation Spectroscopy (FCS), respectively. This revealed that only one emitter per NB contributes to fluorescence imaging due to quenching effects

(Fig. 4.3a), implying that counting the number of fluorophores is equivalent to counting the number of NBs. The resulting quantitative localization microscopy image is shown in Fig. 4.3b. We found that the estimated number of NBs bound per NPC varies between 3 and 17 (Fig. 4.3c). This indicates that the labeling efficiency was relatively low, given the eightfold symmetry of the NPC and given that recent stoichiometry data point to up to 32 Seh1 copies per NPC[120, 121].

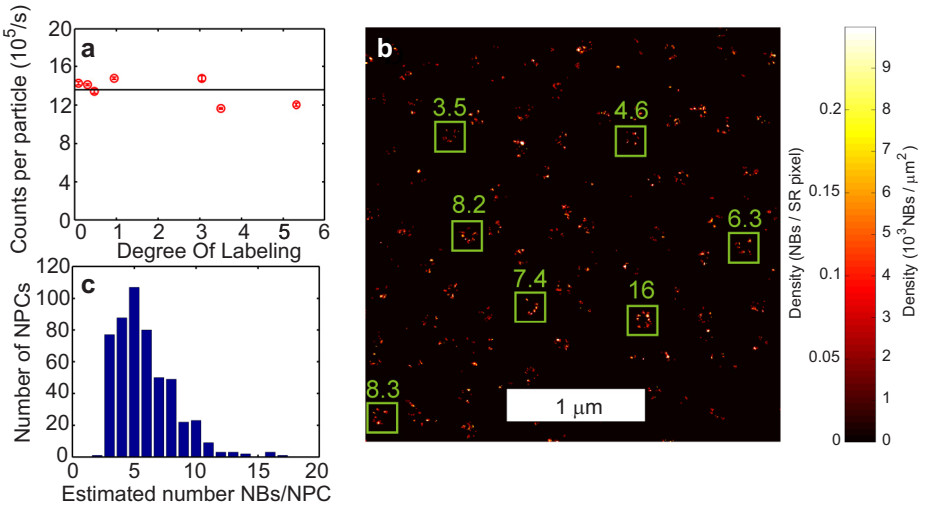

Figure 4.3: Quantitative localization microscopy of NB-labeled Seh1 in the NPC. (a) FCS-analysis of NB stoichiometry indicating there is a single fluorophore per NB. (b) Cutout of quantitative localization microscopy image of NB-labeled Seh1 in the NPC ($k_{bl} = 4.8 \times 10^{-3}$/s and $M_\infty = 5.0$). The numbers at the green boxes indicate the estimated number of NBs within the box. (c) Histogram of the estimated number of NBs per NPC.

4

4.2.2. QUANTIFICATION WITH MULTIPLE FLUOROPHORES PER SITE

In commonly used antibody labeling schemes there are $S > 1$ fluorescent molecules per labeled site (e.g. antibody). The three-state switching model can be expanded to incorporate this labeling stoichiometry (see Appendix 4.A.3) from which we obtain an average number of activations per labeled site $\langle M \rangle$ and a correlation parameter Q:

$$\langle M(t) \rangle = \langle S \rangle M_\infty \left(1 - \exp\left(-k_{bl}\, t\right)\right), \tag{4.3}$$

$$Q(t) = 2\left(M_\infty - 1\right)\left(1 - \frac{k_{bl}\, t}{\exp\left(k_{bl}\, t\right) - 1}\right) + \mu M_\infty \left(1 - \exp\left(-k_{bl}\, t\right)\right), \tag{4.4}$$

where the average number of emitters per site $\langle S \rangle$ and the stoichiometry parameter $\mu = \langle S(S-1) \rangle / \langle S \rangle$ are novel parameters entering the description. The averages here are understood to be averages over the distribution of labeled sites (sites with $S \geq$

1). When each labeled site has only one emitter we have $\langle S \rangle = 1$ and $\mu = 0$, and we retrieve the previously considered case of Eqs. 4.1 and 4.2. Expressions for the average number of emitters per site $\langle S \rangle$ and the stoichiometry parameter μ can be derived from models for the labeling stoichiometry (Appendix 4.A.3).

Primary antibody labeling may be described by Poisson statistics for weakly interacting fluorophores. Then the DOL revealed by absorption spectroscopy corresponds to the Poisson rate of the labeling process. It follows that the average number of emitters per site $\langle S \rangle = \mathrm{DOL}/\left[1-\exp(-\mathrm{DOL})\right]$ and the stoichiometry parameter $\mu = \mathrm{DOL}$. Quenching (usually attributed to dye aggregation[122–124]), invalidates the assumption of weakly interacting fluorophores for larger DOL values[115] and a separate calibration of both the average number of emitters per site $\langle S \rangle$ and the stoichiometry parameter μ (but not of the switching and bleaching rates k_{sw} and k_{bl}) is then necessary. The case of secondary antibody labeling is even more complicated as now the stoichiometry of secondary to primary antibodies is relevant in addition to the stoichiometry of emitters on the secondary antibodies (Appendix 4.A.3). Generally, prior knowledge on the labeling via a calibration of the average number of emitters per site $\langle S \rangle$ and the stoichiometry parameter μ is needed to compute the average number of localizations per labeled site $\langle M(t) \rangle$ from the cumulative number of localizations and the correlation parameter $Q(t)$.

We validated the approach for estimating the number of localizations per site with multiple fluorophores per site using a control sample of sparsely distributed neutravidin tetramers on glass labeled with varying numbers of Alexa Fluor 647 fluorophores. The labeling stoichiometry parameters were determined from FCS brightness measurements and from the brightness statistics of single neutravidin tetramers in the first frames of the sparse control samples (Fig. 4.4a and b). The values obtained with the latter method were applied to estimate the number of localizations per neutravidin tetramer with a Root Mean Square Error (RMSE) of 17% of the ground truth number, which was established by cluster analysis (Fig. 4.5a). This result appears to be robust against errors in the calibration of the stoichiometry parameter μ, as variations in this parameter on the order of unity change the result by 10% or less.

The estimated switching model parameters M_∞ and k_{bl} do not vary significantly with DOL (Fig. 4.5f), suggesting independent switching and bleaching of the detected, non-quenched emitters (see also Fig. 4.4c). The remaining quenched emitters that do contribute to the measured DOL in absorption spectroscopy do not appear to contribute to the localizations (Fig. 4.4a and d).

Next, we applied our counting method to images of Immunoglobulin E (IgE) receptors in fixed Rat Basophilic Leukemia (RBL) cells labeled with IgE conjugated to Alexa Fluor 647 (Fig. 4.5c). The data were analyzed assuming a stoichiometry parameter $\mu = \mathrm{DOL}$ and an average number of emitters per site $\langle S \rangle = \mathrm{DOL}/\left[1-\exp(-\mathrm{DOL})\right]$, where the measured DOL = 1.5 was low enough to neglect possible quenching effects. The density of receptors on the membrane was estimated as $81\,\mu\mathrm{m}^{-2}$. This is on the same order as e.g. Espinoza et al.[125], where on average $64 \pm 32\,\mu\mathrm{m}^{-2}$ were obtained in TEM images (252 ± 123 receptors per field of view of $(2266\ \mathrm{nm})^2$ with a labeling efficiency of 0.8 ± 0.1). Densities may vary substantially with cell incubation times and

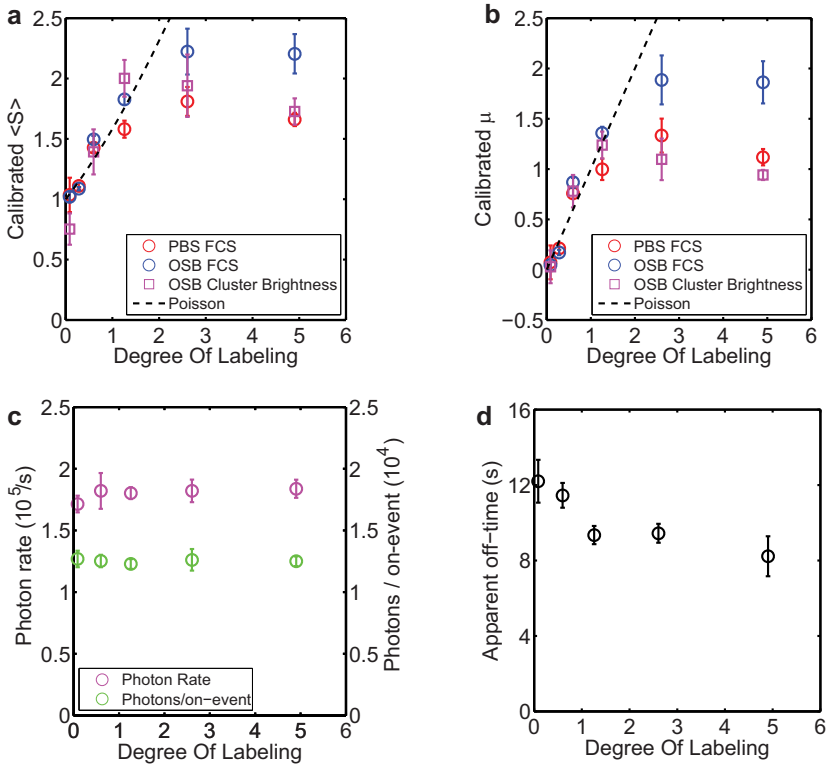

Figure 4.4: Stoichiometry calibration and characterization of neutravidin tetramers labeled with multiple Alexa Fluor 647 labels. (a) Average number of labels per neutravidin tetramer and (b) stoichiometry parameter μ as a function of DOL calibrated from cluster brightness statistics and FCS measurements for Phosphate Buffered Saline (PBS) and Oxygen Scavenging Buffer (OSB). Both indicate labeling according to Poisson statistics for DOL values below about 2 and significant quenching effects for higher DOL values. (c) The photon rate during on-events and the photon count per on-event (i.e. localization) do not depend on DOL. This indicates that single emitters are observed in the detected on-events and the brightness and off-switching of these emitters are not affected by nearby emitters on the same tetramer. (d) The time between localizations of the same neutravidin tetramer decreases with DOL indicating that multiple fluorescent labels are observed per tetramer for higher DOL.

between cell types though, implying that more precise values cannot be specified.

4.2.3. HIGH DENSITY SAMPLES

Care must be taken when applying our analysis to samples that have markers with mutual distances well below the localization precision due to high labeling densities or clustering. Effectively these markers would be seen as a single labeled site by the current correlation analysis algorithm, which causes overestimation of the number of localizations per marker. Appendix 4.A.4 provides estimates for the labeling densities above which problems are to be expected. As a rule of thumb, problems ar expected

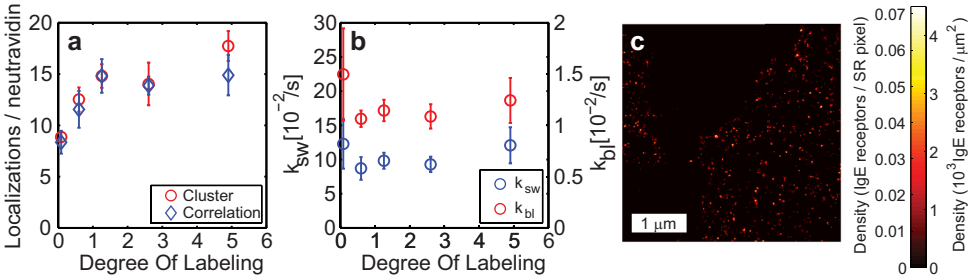

Figure 4.5: Quantitative localization microscopy with multiple emitters per labeled site. (a) Number of localizations per neutravidin tetramer as a function of DOL as estimated from the image correlations and the ground truth values from cluster analysis, showing good agreement. (b) Fitted bleach rate k_{bl} and switching rate $k_{sw} = M_\infty k_{bl}$ as a function of DOL values for the same data, indicating independent activation and bleaching per label. Error bars indicate the standard deviation among samples at the same DOL. (c) Image of IgE receptors on the membrane of RBL cells labeled with primary antibodies with a DOL of 1.5 ($k_{bl} = 9.1 \times 10^{-3}$/s and $M_\infty = 2.3$).

when the density is higher than $1/\sigma_m$ (for filaments) or $1/2\sigma_m^2$ (for punctate clusters), where σ_m is the average localization precision.

An experimental approach to verify that counting results are not affected by high density artefacts is to compare them with the results that are obtained by computing the correlation parameter $Q(t)$ in regions of relatively low labeling density. We have analyzed an image of secondary antibody-Alexa Fluor 647 labeled Nup153 protein of the NPC in this way (Fig. 4.6). The densely labeled region with NPCs inside the nuclear membrane gives rise to a correlation parameter $Q(t)$ that is about 2.4 times higher than for the region with non-specifically bound antibodies outside the nuclear membrane. This shows that the clustered antibodies inside the nucleus appear as a single site for the estimation of $Q(t)$. However, the relative rate with which localizations are accumulated is similar, indicating similar bleaching behavior and identical fluorophores in both regions. A fit to the correlation parameter $Q(t)$ for the outside region gives $k_{bl} = 3.8 \times 10^{-3}$/s and $M_\infty = 5.5$, under the assumption that the outside region labeling entities are secondary antibodies, and using the calibrated fluorophore to secondary antibody DOL equal to 1.2. Applying these values in a fit of the correlation parameter $Q(t)$ for the region inside the nuclear membrane gives approximately 2.7 secondary antibodies per NPC on average, which agrees with the ratio of 2.4 between the localizations per NPC and the localizations per non-specifically bound antibody outside the nucleus. The NPCs are likely to have multiple primary antibodies, because this would explain the difference in the spread of localizations of NPCs (16 nm) and localizations of the non-specifically bound antibodies outside the nuclear membrane region (11 nm).

We also verified that the counting results in Fig. 4.3 are not affected by high density artefacts by computing the correlation parameter $Q(t)$ in a region outside the nucleus with similar bleaching behavior. A fit to $Q(t)$ returned $k_{bl} = 5.3 \times 10^{-3}$/s and $M_\infty = 4.5$ (compared with $k_{bl} = 5.3 \times 10^{-3}$/s and $M_\infty = 5.0$ inside the nucleus), which

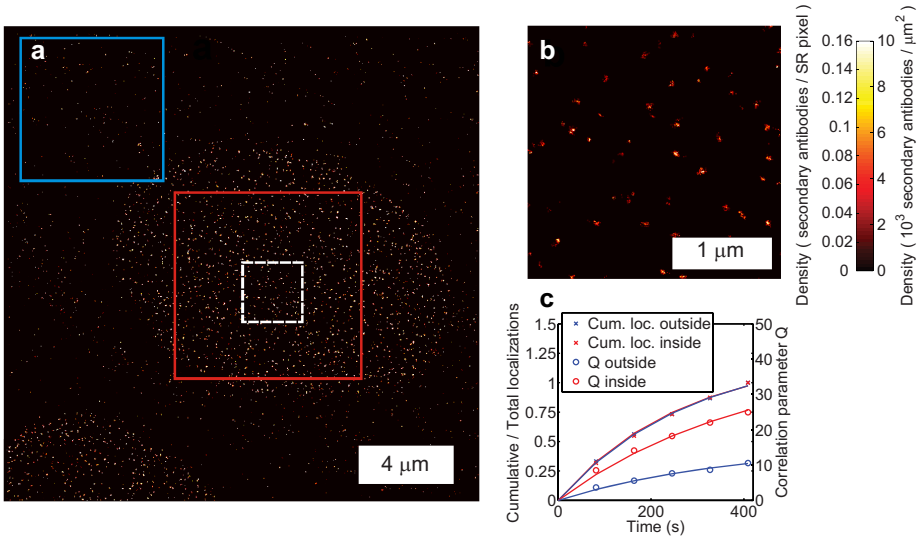

Figure 4.6: Quantitative localization microscopy with heterogeneous labeling density. (a) Overview image (pixel size 10 nm, clipped for visibility) and (b) zoomed inset (pixel size 4 nm) of the dashed white box in (a) of secondary antibody-Alexa Fluor 647 labeled Nup153 protein of the NPC in the nuclear membrane with non-specifically bound (secondary) antibodies outside the nuclear membrane region. (c) The correlation parameter Q for the region inside the nuclear membrane (red box) is higher than outside (blue box) due to the tight clustering of the secondary antibodies labeling the Nup153 proteins. The relative number of accumulated localizations at each time point is similar, indicating that the bleaching behavior is similar and the sources of the localizations are identical in both regions.

4

showed that the estimation of $Q(t)$ was not substantially affected by clustering of Seh1 in these data.

4.3. DISCUSSION

The switching model assumes constant and uniform rates. Accordingly, all data was acquired under conditions where the excitation and activation light intensities did not vary spatially across the sample, nor change as a function of time during the experiment. To adapt the method for experiments in which the switching rate is varied, the illumination intensities should be recorded over time and included in a generalization of the switching model that includes time dependent switching rates. The method has been demonstrated on Alexa Fluor 647 dyes, but applies to any fluorophore that can effectively be described by the three-state switching model. Such a description becomes problematic for the existence of multiple long lived dark states with lifetimes on the same order of magnitude[118]. This would require a more substantial modification of the theory, in which the three-state model is expanded with one or more additional states and two or more additional rates between the states. Subsequently, the average number of localizations per labeled site $\langle M(t) \rangle$ needs to be derived and expressed in a form that only depends on parameters that can be

obtained from fits to the cumulative number of localizations and to the correlation parameter $Q(t)$. Finally we note that fluorophore activation events that are missed by the localization algorithm, so-called false negative localizations, do not affect the accuracy of the method by more than 5 to 10% (see Appendix 4.A.3).

The analyses for the data presented in Figs. 4.1 and 4.5a showed that overcounting errors on the order of 50% occur when neglecting reversible switching of the fluorophores and unknown stoichiometry of the fluorescent labels, as is typically done for example in pair-correlation analysis[66]. As we noted before, the latter represents an alternative approach for estimating the spurious correlation parameter $Q(t)$, and could therefore be corrected for overcounting similar to how we treat the estimate for $Q(t)$ from the FRC. However, the pair-correlation analysis does require a parametric model for the correlations in the spatial distribution of the labeled sites, unlike the FRC approach. In-vitro calibration of fluorophore switching and bleaching rates for counting purposes may be susceptible to differences in the chemical environment of the fluorophores. Comparing the estimated rates for Neutravidin on a glass slide (Fig. 4.5) and inside cells indicates that differences in these rates of a factor 2 to 3 may occur, which would result in similar differences in the estimated number of localizations per site.

In summary, we have developed a method for estimating the number of localizations per fluorescently labeled site in order to resolve overcounting problems with reversibly switchable emitters. For labeling entities with single fluorophores the method can be used directly on the localization data. Otherwise the method requires only a one-time calibration of the number of fluorophores per label as an additional input, which can be used for all subsequent uses of that label. With spatial resolution approaching the molecular scale, this will expand the possibilities of researchers to address questions about the molecular stoichiometry and spatial organization of protein complexes. This is essential to establish localization microscopy as a method which may be used to not just observe the nanoscale "shape" of biological structures, but also to obtain quantitative information about their composition.

4.4. MATERIALS AND METHODS

4.4.1. EXPERIMENTAL MATERIALS AND METHODS

PREPARATION OF FLUORESCENT DNA OLIGONUCLEOTIDES

To characterize the on-off switching kinetics of single reversibly switchable fluorescent molecules, a single Alexa Fluor 647 fluorophore was conjugated to the end of a double stranded DNA (dsDNA) construct, and the construct was immobilized on a glass surface for single-molecule imaging. DNA constructs were labeled as previously described [31, 117]. Briefly, PAGE purified DNA oligos (30 base pairs in length) with biotin and/or amine modifications at the ends were obtained from Eurofins Operon. Amine-modified oligos were labeled post-synthesis with amine reactive Alexa Fluor 647 (Life Technologies, A20006) following the manufacturer's protocol. Dye-labeled oligos were purified using reverse-phase HPLC. Complimentary strands of DNA, one with a biotin label and the other with a fluorescent label, were annealed to form fluo-

rescent biotinylated dsDNA. Annealing was carried out by mixing equimolar amounts of the two complimentary strands in 10mM Tris-Cl (pH 7.5), 50mM NaCl, heating for 60s at 90°C, and cooling to room temperature during ~1 hr.

PREPARATION OF FLUORESCENT SECONDARY ANTIBODIES, NANOBODIES, AND NEUTRAVIDIN

Donkey anti-mouse secondary antibodies (Jackson ImmunoResearch # 715-005-150), anti-GFP camelid antibody fragments (a.k.a. "Nanobodies", Chromotek, GT-250), and Neutravidin tetramers (Life Technologies, A2666) were labeled with amine-reactive Alexa Fluor 647 according to the manufacturer's protocol. Briefly, unlabeled antibodies, nanobodies, or neutravidin were mixed with amine reactive dye in a sodium bicarbonate buffer (0.1 M, pH 8.5), and the labeling reaction was left to proceed at room temperature for 30 min. The labeled product was separated from unreacted dye by running the reaction mixture over a gel filtration column (Illustra NAP-5 column, GE Healthcare), and eluting in PBS. The labeled product was stored at 4°C in PBS. The degree of labeling (DOL) of the antibodies, nanobodies, or neutravidin was measured using a UV/Vis spectrophotometer. The DOL was adjusted by varying the amount of dye that was added to the reaction.

FCS CHARACTERIZATION OF FLUORESCENT NANOBODIES, NEUTRAVIDIN, AND SECONDARY ANTIBODIES

The fluorescence lifetime and brightness per particle of fluorescent antibodies, nanobodies, and neutravidin were measured using a commercial FCS spectrometer (Evotec FCS plus spectrometer, Evotec Technologies, Hamburg, Germany). This instrument has been described in detail previously[126]. Samples were diluted in PBS or in MEA imaging buffer (see below) and loaded into 96-well plates. The sample was illuminated with a pulsed 633nm laser diode (Picoquant) and imaged using an Olympus 60X 1.2NA water immersion objective and a confocal detection scheme. Fluorescence intensity traces were recorded and analyzed using the Evotec FCS++ analysis software. This yielded measurements of fluorescence brightness per particle and fluorescence lifetime for each sample.

SINGLE MOLECULE IMAGING OF IMMOBILIZED DNA AND NEUTRAVIDIN

The labeled dsDNA was immobilized on glass coverslips via a biotin-streptavidin linkage. A biotinylated BSA solution (1.0 mg/mL, Sigma Aldrich) was first added to the coverslip, followed by 0.25 mg/mL streptavidin (Life Technologies), and finally the DNA sample at a low concentration (~30 pM) in order to obtain a low surface density of DNA molecules such that individual molecules were well separated and optically resolvable from each other. The surface was rinsed with 10mM Tris-Cl (pH 7.5), 50mM NaCl solution prior to the addition of each reagent. MEA imaging buffer, described below, was added to the sample prior to imaging. Single molecule Neutravidin samples were prepared in a similar way. A biotinylated BSA solution was first added to the coverslip, followed by rinsing with Tris buffer, and then the neutravidin sample was added at a low concentration (~50 pM). Following a second rinsing step,

the surface density of labeled neutravidin molecules was low enough such that individual molecules were well separated and optically resolvable from each other. MEA imaging buffer, described below, was added to the sample prior to imaging.

IMAGING BUFFER

All imaging experiments, including measurements of single molecule switching and STORM imaging, were carried out in MEA imaging buffer as previously described[31, 117]. The imaging buffer consists of 50mM Tris-Cl (pH 8.0), 10mM NaCl, 10% Glucose (w/v), 10mM β-mercaptoethylamine (pH 8.5, Sigma, 30070), and 1% of an enzymatic oxygen scavenger system stock solution. The oxygen scavenging system was added to the buffer immediately before use. The oxygen scavenger stock solution was prepared by mixing glucose oxidase powder (10 mg, Sigma, G2133) with catalase (50 μL, 20 mg/mL, Sigma, C30) in PBS (200 μL), and centrifuging the mixture at 13.000 rpm for 1 minute.

FLUORESCENT STAINING OF CULTURED CELLS

For experiments involving actin imaging, Vero cells were plated on coverslips and fixed in 4% paraformaldehyde for 10 minutes at room temperature. The cells were permeabilized in 0.1% triton in PBS for 5 minutes, and then washed 3 times with blocking buffer (2% BSA in PBS) for 5 minutes. Cells were then labeled with biotin-xx phalloidin (Life Technologies, B7474) at 1:50 dilution in blocking buffer for 1 hour. Cells were rinsed with PBS 3 times for 5 minutes, and then labeled with fluorescent neutravidin (DOL 1.28) at a high dilution in blocking buffer for 1 hour. The cells were rinsed in PBS before mounting in imaging buffer and imaging.

For experiments involving tubulin imaging, Ptk2 cells were fixed with ice-cold methanol for 4 minutes, before washing 3 times for 5 minutes in blocking buffer. Cells were labeled with mouse anti-tubulin primary antibodies (Sigma T6074) at 1:100 dilution in PBS for 1 hour at room temperature, followed by 3 washes for 5 minutes in blocking buffer. The secondary antibody was added at a high dilution in blocking buffer for 1 hour. The sample was rinsed in PBS before mounting in imaging buffer and imaging.

For fluorescent imaging of Nup153, Vero cells were fixed, permeabilized, and blocked as described above for the case of actin imaging. Cells were labeled with mouse anti-Nup153 primary antibodies (Abcam ab24700) at 1:100 dilution in PBS for 1 hour at room temperature, followed by 3 washes for 5 minutes in blocking buffer. The sample was inclubated with the secondary antibody in blocking buffer for 1 hour. The sample was rinsed in PBS before mounting in imaging buffer and imaging.

For the NPC staining of Seh1, a Hela Kyoto cell line stably expressing an siRNA-resistant version of the human Seh1 transcript tagged with mEGFP was established by selection of cells transfected with pmEGFP-Seh1-s37879res[127] with 1 mg/mL Geneticin (Life Technologies). To increase the degree of replacement of the endogenous protein with the mEGFP-tagged version, the cells were repeatedly transfected every 48 hours over the course of 12 days with Silencer Select siRNA s37879 against Seh1 (Life Technologies) by solid phase transfection on siRNA-coated 24-well plates (for

details on the coating procedure see Szymborska et al.[127]). After knock down, the cells were transferred onto cover slips, allowed to attach and processed for staining with Alexa Fluor 647-coupled anti-GFP nanobody as described before[127]. For imaging we chose cells with low cytoplasmic GFP signal and excluded cells with aberrant nuclear shape.

MICROSCOPE

All imaging measurements were performed using a custom built inverted fluorescence microscope, similar to that described previously[63]. To summarize, an inverted fluorescence microscope stand (Olympus IX71) was fitted with a 100X oil-immersion objective lens (Olympus, UPLANSAPO100XO) which enabled efficient detection of single fluorophores. A custom-built focus lock system based on the reflection of an infra-red laser from the sample was used to maintain sample focus during all measurements. For STORM imaging, photo-switchable Alexa Fluor 647 was excited using 642 nm light, and in some measurements the sample was also exposed to 405 nm light to increase the activation rate of switching. A solid-state diode laser (Oxxius) was used to generate 405 nm light, and a fiber laser (MPB Communications, 2RU-VFL-P-1500-642) was used to generate 642 nm light. The laser illumination was configured such that the illumination angle could be varied between an epi-illumination geometry and a total internal reflection (TIRF) illumination mode. For STORM data acquisition, the sample was illuminated with oblique illumination (not TIRF) for reduced background signal. Fluorescence emission of Alexa Fluor 647 was filtered using a dichroic mirror (Chroma, Z660DCXRU) and a bandpass emission filter (Chroma, ET700/75). Fluorescence was detected using an EMCCD camera (Andor Technology, Ixon DU897).

IMAGING OF IGE

RBL cells were seeded on aminosilane coverslips in Lab-Tek eight-well chambers (Nunc). The cells were then incubated for 60 min. at 37°C with 1 μg/mL Alexa Fluor 647-conjugated IgE with a dye/antibody ratio of 1.5. Subsequently, cells were rinsed thrice for 5 min. in Phosphate Buffered Saline (PBS). Then, the cells were fixed in 4.0% (wt/vol) paraformaldehyde and 0.2% glutaraldehyde in phosphate-buffered saline (PBS) for 60 min at room temperature, after which they were rinsed twice for 5 min. with 10 mM Tris and stored in PBS for imaging. Right before imaging, the cells were immersed in an imaging buffer consisting of 450 μL 10% (w/v) glucose in 50 mM Tris, 10 mM NaCl, pH 8.5; 50 μL oxygen scavenger buffer [14040U catalase (C9322-1G, Sigma Aldrich), 1688U glucose oxidase (G2133-50KU, Sigma Aldrich) in 50 mM Tris, 10 mM NaCl, pH 8.5; 5 μL 1M mercaptoethylamine (MEA), pH 8.5. The IgE samples were imaged with an epifluorescence microscope setup, consisting of an inverted microscope (IX71, Olympus), a 1.45-NA TIRF objective (U-APO 150X NA 1.45, Olympus), a 637-nm diode laser (HL63133DG, ThorLabs, with home built collimation optics) and an EMCCD camera (iXon 897, Andor) with EM gain set to 200. Samples were mounted into a 3D piezo stage (Nano-LPS100, Mad City Labs). For sample illumination and emission, a quad-band dichroic and emission filter set was used

(FF01-446/523/600/677-25, Semrock). Images were taken in a TIRF configuration at 57 frames per second for 33,000 frames.

4.4.2. DATA ANALYSIS METHODS

LOCALIZATION ANALYSIS

Identification of regions of interest and estimation of the fluorophores' position followed established methods[15, 31, 36]. Localizations corresponding to the same activation event were subsequently combined by grouping spatially nearby localizations in subsequent frames

into single localization events. 'Nearby' is defined here as having a distance less than five times the sum of the localization uncertainty of the two to-be merged localization events. The tolerance in the distances was chosen relatively high because the risk of accidentally combining localizations from different nearby molecules was low in view of the sparsity of the image. The center position of the grouped localizations was determined as the weighted average of the localizations with the inverse of the localization variances as weights. Localizations were filtered based on the photon count per localization before and after combining localizations per activation event, photons per activation event, activation event duration and fitted PSF full width at half maximum. An overview of filter values is shown in Table 4.1. Photon count thresholds were chosen relatively high to filter out localizations due to sample contaminations for obtaining accurate results in the cluster analyses. Localizations were finally corrected for lateral stage drift using frame-by-frame cross-correlation, as documented elsewhere[27, 31].

Table 4.1: **Parameters used for filtering localization events.** Localizations were filtered for the minimum number of photons per event before grouping, minimum number of photons per event after grouping, the maximum duration of the event after grouping, and the maximum width (FWHM) of the Gaussian fitted to the spot.

Dataset	Photons before	Photons after	Duration (frames)	Width (nm)
DNA oligomers	500	5,000	100	377
Nuclear Pore Complex	1,200	2,000	20	283
Neutravidin	1,200	3,000	20	283
Tubulin	500	5,000	100	377

ESTIMATING THE CORRELATION PARAMETER Q

The first step towards estimating the number of localizations per marker consists of estimating the spurious correlation parameter Q at various points in time; typically 30 time points were used. The first steps of this estimation of Q were the same as done in chapter 2 and culminate in the determination of the numerator $v\left(q\right)$ of the Fourier Ring Correlation (FRC) for spatial frequencies $q = 1/L, 2/L, \ldots$ (L is the size of the field of view). Briefly, the full set of estimated fluorophore positions is divided into two independent subsets. This yields two sub-images $f_1(\vec{r})$ and $f_2(\vec{r})$, where $\vec{r}$ denotes the

spatial coordinates. Subsequently the Fourier transforms of those images, $\hat{f}_1(\vec{q})$ and $\hat{f}_2(\vec{q})$ respectively, are computed. The statistical correlation between those Fourier transforms is then evaluated over pixels on the perimeter of circles in Fourier space with radius q:

$$\nu(q) = \frac{1}{2\pi q L} \sum_{\vec{q} \in \text{circle}} \hat{f}_1(\vec{q})\, \hat{f}_2(\vec{q})^*, \tag{4.5}$$

At high spatial frequencies q, $\nu(q)$ is dominated by spurious correlations due to multiple localizations of the same site. Thus, the spurious correlation parameter Q is computed by fitting $\nu(q)$ with the following model function:

$$H(q;\sigma_m,\Delta\sigma) = \frac{1}{\sqrt{1+8\pi^2\Delta\sigma^2 q^2}} \exp\left(\frac{4\pi^2\sigma_m^2 q^2}{1+8\pi^2\Delta\sigma^2 q^2}\right) \text{sinc}(q)^2. \tag{4.6}$$

This function describes the theoretical decay of the spurious correlations, assuming that the uncertainties σ of localizations follow a normal distributed with unknown mean σ_m and standard deviation $\Delta\sigma$.

The actual fit to $\nu(q)$ is obtained using a novel method which involves the minimization of the cost function:

$$C_\nu(Q,\sigma_m,\Delta\sigma) = -\sum_q \exp\left(-\frac{\left(\nu(q) - QH(q;\sigma_m,\Delta\sigma)\right)^2}{d^2 Q^2 H(q;\sigma_m,\Delta\sigma)^2}\right) \tag{4.7}$$

where d was chosen to be 0.1. The rationale behind this cost function is that it promotes parameters for which $\nu(q)/H(q)$ is constant for a large range of spatial frequencies. This objective was used in chapter 2 as a requirement for the manually provided parameters σ_m and $\Delta\sigma$. The search for parameters Q, σ_m and $\Delta\sigma$ that minimize C_ν was done with the Nelder-Mead simplex algorithm. This algorithm was initialized two times, where the starting values for the second optimization were randomly perturbed with respect to the first.

For each time t, this procedure of dividing localizations into subsets, computing $\nu(q)$ and fitting it to obtain values for Q, σ_m and $\Delta\sigma$ was repeated five or ten times with randomly perturbed initial values for σ_m and $\Delta\sigma$. The median of the different estimates of $Q(t)$ at each time t was then taken to obtain a robust estimation result for $Q(t)$.

ESTIMATING THE NUMBER OF LOCALIZATIONS PER LABELED SITE

After the correlation parameter $Q(t)$ is obtained at various time points t, the next step in estimating the number of localizations per labeled site M involves a simultaneous model fit to $Q(t)$ and the cumulative number of localizations $N(t)$. This is achieved by minimizing the cost function:

$$C_Q(M_\infty, k_{bl}, N_\infty) = \sum_t \left\{ \frac{(N(t) - N_{model}(t))^2}{N_{model}(t) N_{model}(t_{end})} - \frac{(Q(t) - Q_{model}(t))^2}{Q_{model}(t_{end})^2} \right\} \tag{4.8}$$

where the sum runs over all times t for which the spurious correlation parameter was estimated, t_{end} is the total acquisition time, and:

$$N_{model}(t) = N_\infty\left(1-\exp\left(-k_{bl}\,t\right)\right) \tag{4.9}$$

$$Q_{model}(t) = 2\left(M_\infty-1\right)\left(1-\frac{k_{bl}\,t}{\exp\left(k_{bl}\,t\right)-1}\right)+\mu M_\infty\left(1-\exp\left(-k_{bl}\,t\right)\right). \tag{4.10}$$

Optimizing C_Q was again performed using the Nelder-Mead simplex algorithm. The parameter μ was a separate manual input for the optimization for the purpose of this work, obtained from a calibration detailed below. The fitted values M_∞ and k_{bl} are used to obtain the final estimate:

$$M(t) = \langle S\rangle\, M_\infty\left(1-\exp\left(-k_{bl}\,t\right)\right) \tag{4.11}$$

where the average number of emitters per labeled site $\langle S\rangle$ was obtained from the same calibration as μ. Potentially, μ could be obtained from a fit of $Q(t)$, completely eliminating the need for calibration experiments. It turned out, however, that for the datasets we considered this could not be done reliably, possibly due to residual errors in extracting $Q(t)$ from the data or flaws in the switching model.

CALIBRATION OF THE LABELING STOICHIOMETRY

The stoichiometry parameter μ was calibrated for the Neutravidin data as follows. The localizations obtained for the datasets of Neutravidin on glass were clustered as described below. Subsequently, clusters were discarded if there was another cluster within a square region of 7 CCD pixels around each of them. For the remaining clusters, the site was localized in the first frame of the raw sequence to accurately determine the number of signal photons B of the site in that frame. If we assume that each fluorophore is active during the entire first frame, then computing the average and variance of the brightness over the found clusters provides the following equalities:

$$\langle B\rangle = \left\langle B_{single}\right\rangle\langle S\rangle \tag{4.12}$$

$$\frac{\left\langle B^2\right\rangle}{\langle B\rangle} = \frac{\left\langle B^2_{single}\right\rangle}{\left\langle B_{single}\right\rangle}+\left\langle B_{single}\right\rangle\mu \tag{4.13}$$

Here, B_{single} is the brightness of a single emitter. For small DOL values it is assumed that the labeling is described by Poisson statistics giving $\mu \approx$ DOL and $\langle S\rangle \approx$ DOL$/(1-\exp(-\text{DOL}))$. A linear fit on the data points for $\langle B\rangle$ with DOL < 2 gives values for $\left\langle B_{single}\right\rangle$, which are subsequently used to find values for $\langle S\rangle$ for all for all DOL-values. Similarly, a linear fit on the data points for $\left\langle B^2\right\rangle / \langle B\rangle$ for DOL < 2 is used to find the parameters needed to compute μ for all DOL-values. It appears that the value for $\left\langle B_{single}\right\rangle$ fitted from Eq. 4.13 is a factor 1.4 higher than the value fitted from Eq. 4.12, possibly due to a bias in the clustering procedure or due to a breakdown of the Poisson assumption. Bleaching in the initial switching-off phase of the data acquisition may introduce a small bias in the calibration procedure towards higher values of $\langle S\rangle$ and μ (relative error at most about $1/M_\infty$).

In an alternative calibration approach, the markers were analyzed in solution with Fluorescence Correlation Spectroscopy (FCS). The brightness per marker can be analyzed to find values for $\langle S \rangle$ just as done for the cluster brightness analysis. Values for the stoichiometry parameter μ are found by inverting the Poisson relation $\langle S \rangle = \mu/((1-\exp(-\mu)))$, which gives rise to biases in the quenching regime DOL > 2.

CLUSTER ANALYSIS

The ground truth for the distribution of the number of emitters per labeled site for the data of Fig. 4.1c (DNA oligomers) and Fig. 4.5a (neutravidin tetramers) was established from the following steps. First, an image was created in which each localization was rendered as a Gaussian blob with a maximum of 1 and a standard deviation equal to the localization uncertainty obtained from the localization algorithm. The pixel size in these images was 8 nm. Subsequently, these images were thresholded at a value of 10^{-3}, 8-connected regions of nonzero pixels were identified and the localizations in these regions were assigned to clusters. For each cluster, the center position was determined using weighted-least squares estimation. The sum of squared Mahalanobis distances from the localizations to their cluster centers was then computed and clusters where this sum was significantly larger than expected for a sum of Gaussian localization errors (at statistical significance level of 10^{-3}) were discarded for further analysis. Finally, clusters without localizations before a specified time threshold were discarded on the suspicion that they were due to sample contaminations rather than fluorophores; for the DNA oligomer data the threshold was at 10,000 frames, for the Neutravidin data at the 95 percentile value of the times between localizations in clusters. The remaining clusters of localizations were considered to be localizations of the same labeled site.

For the somewhat denser tubulin samples a different clustering method was found more suitable, based on nearest-neighbor linking. Localization events are considered as belonging to the same cluster if their relative distance $|\vec{r}| < R \approx 2\sigma$, with σ the localization uncertainty. The likelihood of localizing an emitter at position $\vec{r}$ from the true emitter position is a Gaussian in x and y with standard deviation σ. Therefore the likelihood of two localizations of the same emitters at relative position $\vec{r}$ is a Gaussian in x and y with standard deviation $\sqrt{2}\sigma$, as follows by convolution of the two individual Gaussian likelihood functions. It follows then that the likelihood of two localizations of the same emitters at relative distance $|\vec{r}| < R$ is:

$$P(|\vec{r}| < R) = 1 - \exp\left(-R^2/4\sigma^2\right) \tag{4.14}$$

so, for $R = 2\sigma$ we find a likelihood for correctly linking two localizations of the same emitter $P(|\vec{r}| < R) = 1 - 1/e = 0.63$. As typically each cluster consists of ~ 10 localizations most clusters will be correctly detected. After initial nearest-neighbor linking clusters with less than 2 or more than 50 localizations are filtered out. Subsequently, the distribution of localization uncertainties of the detected clusters is evaluated. Clusters with a localization uncertainty $\sigma > \sigma_m + 2\Delta\sigma$, with σ_m and $\Delta\sigma$ the mean and standard deviation of the distribution of localization uncertainties, are removed. Next, the correlation Q values were evaluated on the filtered set of localizations and

compared to the Q values from the found clusters. The value of R was chosen to optimize the correspondence between the two sets of Q values, and was found to be $R = 12$ nm for the datasets at hand. The distribution of cluster based localization uncertainties for this value of R turned out to have an average and standard deviation with $\sigma_m = 5.1$ nm and $\Delta\sigma = 1.9$ nm, i.e. close to $R = 2\sigma$. This value is somewhat higher than the precision of 3.0 nm found from the localization procedure, probably due to residual drift correction errors.

4.A. APPENDIX

4.A.1. THREE-STATE ACTIVATION-BLEACHING MODEL FOR SINGLE FLUOROPHORES

We consider switching between three states, the on-state, the off-state, and the bleached state. The switching between the on and off-states is modelled with the Poisson distribution; i.e. in the absence of photobleaching the number of transitions from the off-state to the on-state P_m^{sw} satisfies:

$$P_m^{\mathrm{sw}} = \frac{r^m}{m!} \exp(-r), \tag{4.15}$$

where $r = k_{\mathrm{sw}} t$ with t the time and k_{sw} the switching rate, which is related to the lifetimes of the on and off-states by $1/k_{\mathrm{sw}} = \tau_{\mathrm{on}} + \tau_{\mathrm{off}}$. The bleaching is governed by the geometrical distribution, namely the probability for bleaching at the m-th switching cycle is:

$$P_m^{\mathrm{bl}} = b(1-b)^{m-1}. \tag{4.16}$$

where $b = k_{\mathrm{bl}}/k_{\mathrm{sw}}$ is the probability for bleaching during one cycle, with k_{bl} the effective bleaching rate. Intuitively, for small time scales the statistics will be close to the activation dominated Poisson-model, whereas for large times it will be close to the bleaching dominated geometric distribution. For intermediate times t the probability for m activation cycles is the sum of two terms. The first is the product of the probability P_m^{sw} of having m switching cycles and the probability $(1-b)^m$ that the emitter has not bleached in the m switching cycles. The second term is the product of the probability P_m^{bl} of bleaching during the m-th switching cycle and the probability of having at least m switching cycles. In mathematical terms (for $m \geq 1$):

$$P_m = (1-b)^m \frac{r^m}{m!} \exp(-r) + b(1-b)^{m-1} \sum_{n=m}^{\infty} \frac{r^n}{n!} \exp(-r). \tag{4.17}$$

For $m = 0$ bleaching does not play a role, so the probability is then given by the Poisson term only:

$$P_0 = \exp(-r). \tag{4.18}$$

It may be verified that

$$\sum_{m=0}^{\infty} P_m = 1, \tag{4.19}$$

so that conservation of probability is satisfied. A rigorous derivation of these expressions for P_m is presented in the next subsection.

Interestingly, the probability distribution of the number of activation cycles m is equivalent to the distribution of the minimum of two random variables m_{Poisson} and $m_{\mathrm{geometric}}$, where m_{Poisson} is Poisson distributed with expectation value r and $m_{\mathrm{geometric}}$ follows a geometric distribution with expectation value $1/b$.

The moments of this probability distribution can be calculated from the moment generating function:

$$\begin{aligned} G(a) &= \sum_{m=0}^{\infty} P_m \exp(am) \\ &= \exp(-r) + \sum_{m=1}^{\infty} \left((1-b)\exp(a)\right)^m \frac{r^m}{m!} \exp(-r) \\ &\quad + b\exp(a) \sum_{m=1}^{\infty} \left((1-b)\exp(a)\right)^{m-1} \sum_{n=m}^{\infty} \frac{r^n}{n!} \exp(-r) \\ &= \exp\left(r(1-b)\exp(a) - r\right) \\ &\quad + b\exp(a) \sum_{n=1}^{\infty} \frac{1-\left((1-b)\exp(a)\right)^n}{1-(1-b)\exp(a)} \frac{r^n}{n!} \exp(-r) \\ &= \frac{b\exp(a) + \left(1-\exp(a)\right)\exp\left(r(1-b)\exp(a) - r\right)}{1-(1-b)\exp(a)}. \end{aligned} \tag{4.20}$$

The moments follow from the derivatives of this function at $a = 0$:

$$\begin{aligned} M_1(t) &= \sum_{m=1}^{\infty} m P_m = \left.\frac{dG(a)}{da}\right|_{a=0} \\ &= \frac{1}{b}\left[1-\exp(-rb)\right], \end{aligned} \tag{4.21}$$

$$\begin{aligned} M_2(t) &= \sum_{m=1}^{\infty} m^2 P_m = \left.\frac{d^2G(a)}{da^2}\right|_{a=0} \\ &= \frac{1}{b}\left[1-\exp(-rb)\right] + \frac{2(1-b)}{b^2}\left[1-\exp(-rb) - rb\exp(-rb)\right], \end{aligned} \tag{4.22}$$

giving a correlation parameter Q as:

$$\begin{aligned} Q(t) &= \frac{M_2(t) - M_1(t)}{M_1(t)} \\ &= \frac{2(1-b)}{b}\left[1 - \frac{rb}{\exp(rb)-1}\right]. \end{aligned} \tag{4.23}$$

If we define the asymptotic value $M_\infty = \lim_{t\to\infty} M_1(t) = 1/b$ then the results for the average number of activations and for the correlation parameter Q may be written as:

$$M_1(t) = M_\infty\left[1-\exp(-k_{\rm bl}t)\right], \tag{4.24}$$

$$Q(t) = 2(M_\infty - 1)\left[1 - \frac{k_{\rm bl}t}{\exp(k_{\rm bl}t)-1}\right].. \tag{4.25}$$

For $k_{\rm bl}t \ll 1$ we find:

$$M_1(t) \approx k_{\rm sw}t, \tag{4.26}$$

$$M_2(t) - M_1(t) \approx \left(1 - \frac{1}{M_\infty}\right)(k_{\rm sw}t)^2, \tag{4.27}$$

which is consistent with Poisson statistics provided that $k_{bl} \ll k_{sw}$. For $k_{bl}t \gg 1$ we find constant values:

$$M_1(t) \approx M_\infty, \tag{4.28}$$

$$M_2(t) - M_1(t) \approx 2M_\infty(M_\infty - 1), \tag{4.29}$$

consistent with a geometrical distribution with bleaching probability $1/M_\infty = k_{bl}/k_{sw}$ per activation cycle. These limiting cases fit with the a priori expectations.

4.A.2. DERIVATION OF MIXED POISSON-GEOMETRIC PROBABILITY DISTRIBUTION

This subsection presents a derivation of the mixed Poisson-geometric probability distribution in Eq. 4.17.

The treatment is based on a generalization of the asymmetric Random Telegraph Signal (RTS) model [86], which describes switching between two states. Here a third state is introduced, representing the bleached state, which can in principle be reached from both the on-state and the off-state of the emitter. So, the starting point is the three-state model with state 0 ('off-state'), state 1 ('on state'), and state 2 (bleached state) with four transition rates k_{01} ($0 \to 1$), k_{10} ($1 \to 0$), k_{02} ($0 \to 2$), and k_{12} ($1 \to 2$). The total decay rate of state 0 is thus $k_0 = k_{01} + k_{02}$, and the decay rate of state 1 is thus $k_1 = k_{10} + k_{12}$. The lifetimes of the on and off states are thus $\tau_{on} = 1/k_1$ and $\tau_{off} = 1/k_0$, generally $\tau_{off} \gg \tau_{on}$. Suppose the system starts out in state 0 at time $t = 0$. The probability that the emitter remains in state 0 and never is activated is:

$$g_0(t) = \exp(-k_0 t), \tag{4.30}$$

for $t \geq 0$. The probability that the system makes a single jump to state 1 in this time interval is:

$$g_1(t) = \int_0^t dt'\, g_0(t')\, k_{01} \exp\left(-k_1\left(t - t'\right)\right), \tag{4.31}$$

the probability that the system makes two jumps and returns to state 0 is:

$$g_2(t) = \int_0^t dt'\, g_1(t')\, k_{10} \exp\left(-k_0\left(t - t'\right)\right). \tag{4.32}$$

The probability that the emitter bleaches directly to state 2 is:

$$h_1(t) = \int_0^t dt'\, g_0(t')\, k_{02}, \tag{4.33}$$

and the probability it bleaches to state 2 after one transition to state 1 is:

$$h_1(t) = \int_0^t dt'\, g_1(t')\, k_{12}. \tag{4.34}$$

Clearly, these probabilities can be calculated by iteration. This is accomplished most easily by application of a Laplace transform:

$$\hat{g}_n(s) = \int_0^\infty dt\, g_n(t) \exp(-st). \tag{4.35}$$

If so desired, a transition to the Fourier domain can be made by the substitution $s \to \varepsilon + i\omega$ and taking the limit $\varepsilon \to 0$ after the inverse (Fourier) transform. We find that for $n = 2m$ even and $n = 2m+1$ odd different relations hold:

$$\hat{g}_{2m}(s) = \frac{k_{10}}{k_0 + s}\hat{g}_{2m-1}(s), \tag{4.36}$$

$$\hat{g}_{2m+1}(s) = \frac{k_{01}}{k_1 + s}\hat{g}_{2m}(s), \tag{4.37}$$

$$\hat{h}_{2m}(s) = \frac{k_{02}}{s}\hat{g}_{2m}(s), \tag{4.38}$$

$$\hat{h}_{2m+1}(s) = \frac{k_{12}}{s}\hat{g}_{2m+1}(s). \tag{4.39}$$

Starting from $\hat{g}_0(s) = 1/(k_0 + s)$ this leads to the solutions:

$$\hat{g}_{2m}(s) = \frac{\beta^m}{k_0 + s}, \tag{4.40}$$

$$\hat{g}_{2m+1}(s) = \frac{\beta^{m+1}}{k_{10}}, \tag{4.41}$$

$$\hat{h}_{2m}(s) = \frac{k_{02}\beta^m}{(k_0 + s)s}, \tag{4.42}$$

$$\hat{h}_{2m+1}(s) = \frac{k_{12}\beta^{m+1}}{k_{10}s}, \tag{4.43}$$

with:

$$\beta = \frac{k_{01}k_{10}}{(k_0 + s)(k_1 + s)}. \tag{4.44}$$

The Laplace transform of the probability that the molecule is activated m times during the time interval t now follows as:

$$\begin{aligned}\hat{q}_m(s) &= \hat{g}_{2m-1}(s) + \hat{g}_{2m}(s) + \hat{h}_{2m-1}(s) + \hat{h}_{2m}(s)\\ &= \frac{k_{10}(k_{02} + s) + (k_{12} + s)(k_0 + s)}{k_{10}(k_0 + s)s}\beta^m\\ &= \frac{(k_0 + s)(k_1 + s) - k_{01}k_{10}}{k_{10}(k_0 + s)s}\beta^m\\ &= \frac{k_1 + s}{k_{10}s}(1 - \beta)\beta^m,\end{aligned} \tag{4.45}$$

and:

$$\hat{q}_0(s) = \hat{g}_0(s) + \hat{h}_0(s) = \frac{k_{02} + s}{(k_0 + s)s}. \tag{4.46}$$

It may be checked that the sum satisfies:

$$\sum_{m=0}^{\infty} \hat{q}_m(s) = \frac{1}{s}, \tag{4.47}$$

giving that:

$$\sum_{m=0}^{\infty} q_m(t) = \theta(t), \tag{4.48}$$

implying that conservation of probability applies.

Only the subset of molecules that is activated at least once is accessible to analysis. It follows that we need the renormalized probability distribution:

$$P_m(t) = \frac{q_m(t)}{1 - q_0(\infty)}, \tag{4.49}$$

for $m \geq 1$ and $P_0(t) = 0$. Here $q_0(t)$ can be found via an inverse Laplace transform:

$$q_0(t) = \frac{k_{02}}{k_0} + \left(1 - \frac{k_{02}}{k_0}\right) \exp(-k_0 t), \tag{4.50}$$

giving $q_0(\infty) = k_{02}/k_0$ and a normalization factor $1/\left(1 - q_0(\infty)\right) = k_0/k_{01}$ leading to a probability distribution (in the Laplace domain):

$$\hat{P}_m(s) = \frac{k_0(k_1 + s)}{k_{01} k_{10} s}\left(1 - \beta\right)\beta^m, \tag{4.51}$$

for $m \geq 1$.

An important simplification can be made for times t much larger than $1/k_1 = \tau_{\text{on}}$. In that case we may use the approximation:

$$\hat{P}_m(s) = \frac{k_0 k_1}{k_{01} k_{10} s}\left(1 - \beta\right)\beta^m, \tag{4.52}$$

with:

$$\beta = \frac{k_{01} k_{10}}{k_0 k_1 + (k_0 + k_1)\, s}, \tag{4.53}$$

$$1 - \beta = \frac{k_0 k_1 - k_{01} k_{01} + (k_0 + k_1)\, s}{k_0 k_1 + (k_0 + k_1)\, s}. \tag{4.54}$$

At this point it is convenient to introduce the two physically relevant rates/time scales, namely the activation and bleaching rates, defined by:

$$k_{\text{sw}} = \frac{k_0 k_1}{k_0 + k_1}, \tag{4.55}$$

$$k_{\text{bl}} = \frac{k_0 k_1 - k_{01} k_{10}}{k_0 + k_1} = \frac{k_{01} k_{12} + k_{10} k_{02} + k_{02} k_{12}}{k_0 + k_1}. \tag{4.56}$$

The activation time constant is simply $\tau_{\text{sw}} = 1/k_{\text{sw}} = \tau_{\text{on}} + \tau_{\text{off}}$. We also find that $k_{01} k_{10}/k_0 k_1 = 1 - k_{\text{bl}}/k_{\text{sw}}$. Now the probability distribution can be written as:

$$\hat{P}_m(s) = \frac{k_{\text{sw}}(k_{\text{sw}} - k_{\text{bl}})^{m-1}(k_{\text{bl}} + s)}{s(k_{\text{sw}} + s)^{m+1}}, \tag{4.57}$$

This expression may be rewritten in a form that is more amenable to inverse Laplace transform:

$$\begin{aligned}\hat{P}_m(s) &= \left(1-\frac{k_{\rm bl}}{k_{\rm sw}}\right)^{m-1}\frac{k_{\rm sw}^m}{(k_{\rm sw}+s)^{m+1}}+\frac{k_{\rm bl}}{k_{\rm sw}}\left(1-\frac{k_{\rm bl}}{k_{\rm sw}}\right)^{m-1}\frac{k_{\rm sw}^{m+1}}{s(k_{\rm sw}+s)^{m+1}}\\ &= \left(1-\frac{k_{\rm bl}}{k_{\rm sw}}\right)^{m-1}\frac{k_{\rm sw}^m}{(k_{\rm sw}+s)^{m+1}}\\ &\quad+\frac{k_{\rm bl}}{k_{\rm sw}}\left(1-\frac{k_{\rm bl}}{k_{\rm sw}}\right)^{m-1}\left[\frac{1}{s}-\sum_{n=1}^{m}\frac{k_{\rm sw}^n}{(k_{\rm sw}+s)^{n+1}}\right],\end{aligned} \tag{4.58}$$

The inverse Laplace transform now gives:

$$\begin{aligned}P_m(t) &= \left(1-\frac{k_{\rm bl}}{k_{\rm sw}}\right)^{m-1}\frac{(k_{\rm sw}t)^m}{m!}\exp(-k_{\rm sw}t)\\ &\quad+\frac{k_{\rm bl}}{k_{\rm sw}}\left(1-\frac{k_{\rm bl}}{k_{\rm sw}}\right)^{m-1}\left[1-\sum_{n=0}^{m}\frac{(k_{\rm sw}t)^n}{n!}\exp(-k_{\rm sw}t)\right]\\ &= \left(1-\frac{k_{\rm bl}}{k_{\rm sw}}\right)^{m}\frac{(k_{\rm sw}t)^m}{m!}\exp(-k_{\rm sw}t)\\ &\quad+\frac{k_{\rm bl}}{k_{\rm sw}}\left(1-\frac{k_{\rm bl}}{k_{\rm sw}}\right)^{m-1}\sum_{n=m}^{\infty}\frac{(k_{\rm sw}t)^n}{n!}\exp(-k_{\rm sw}t),\end{aligned} \tag{4.59}$$

in agreement with the results of the previous subsection.

4.A.3. EFFECT OF LABELING STOICHIOMETRY

Suppose there are K labeling sites with S_i ($i=1,2\ldots K$) fluorescent emitters per site which have M_{ij} activations ($j=1,2\ldots S_i$). The number of activations per site is then:

$$M_i=\sum_{j=1}^{S_i}M_{ij}. \tag{4.60}$$

Suppose the statistics of the number of emitters per site is independent of the site and has moments $\langle S\rangle$ and $\langle S^2\rangle$. Suppose furthermore that the statistics of the number of activations of each emitter is independent of emitter and site and gives rise to moments according to the three-state model:

$$\langle M_{ij}\rangle = M_\infty\left[1-\exp(-k_{\rm bl}t)\right], \tag{4.61}$$

$$\langle M_{ij}^2-M_{ij}\rangle = 2M_\infty(M_\infty-1)\left[1-\exp(-k_{\rm bl}t)-k_{\rm bl}t\exp(-k_{\rm bl}t)\right], \tag{4.62}$$

for all i and j and with $M_\infty=k_{\rm sw}/k_{\rm bl}$. The Q-parameter determined from the spatial correlation analysis is given by:

$$Q=\frac{\langle {M_i}^2-M_i\rangle}{\langle M_i\rangle}, \tag{4.63}$$

with:

$$\langle M_i \rangle = \langle S \rangle \langle M_{ij} \rangle, \tag{4.64}$$

and:

$$\langle {M_i}^2 \rangle = \langle S(S-1) \rangle \langle M_{ij} \rangle^2 + \langle S \rangle \langle {M_{ij}}^2 \rangle.$$

Combining all results gives:

$$Q = 2(M_\infty - 1)\left[1 - \frac{k_{\mathrm{bl}} t}{\exp(k_{\mathrm{bl}} t) - 1}\right] + \mu M_\infty \left[1 - \exp(-k_{\mathrm{bl}} t)\right], \tag{4.65}$$

with:

$$\mu = \frac{\langle S^2 \rangle - \langle S \rangle}{\langle S \rangle}, \tag{4.66}$$

a number characterizing the statistics of the number of emitter per site. The second term on the r.h.s. is new compared to the previous analysis of the statistics per emitter. Clearly, there are now three parameters that determine Q as a function of t, the effective bleaching rate k_{bl}, the asymptotic value of the number of activations per emitter M_∞ and the labeling stoichiometry parameter μ. The expected total number of activations is:

$$\begin{aligned} \langle N \rangle &= \sum_{i=1}^{K} \sum_{j=1}^{S_i} M_{ij} = K \langle S \rangle \langle M_{ij} \rangle \\ &= K \langle S \rangle M_\infty \left[1 - \exp(-k_{\mathrm{bl}} t)\right]. \end{aligned} \tag{4.67}$$

All that is lacking then to determine the number of labeling sites K is a connection between $\langle S \rangle$ and μ. We consider now three examples in which there is a connection between the mean and the variance of the statistical distribution of the number of emitter per site.

The first example refers to having a monomer/dimer on each site with probabilities $P_1 = 1 - \beta$ and $P_2 = \beta$. It follows that then $\langle S \rangle = 1 + \beta$ and $\langle S^2 \rangle = 1 + 3\beta$ so that $\mu = 2\beta/(1+\beta)$. Measurement of μ from Q thus gives a value for $\beta = \mu/(2-\mu)$ and hence for $\langle S \rangle = 2/(2-\mu)$. So, the average degree of monomerization/dimerization can potentially be measured in this way, in addition to the total number of labeling sites.

The second example is for a Poisson distributed number of emitters per site. This is a model for primary antibody labeling where multiple fluorophores are attached to the antibody, under the condition that there is no significant fluorescence quenching. The averages are over the subset of sites with at least one emitter. This gives $\langle S \rangle = \eta/(1 - \exp(-\eta))$ and $\langle S^2 - S \rangle = \eta^2/(1 - \exp(-\eta))$ with η the Poisson rate, so that $\mu = \eta$. Possibly, the Poisson-rate can thus be measured directly from the fit of the measured Q as a function of t to the model. In case η is large compared to unity then we simply have $\langle S \rangle = \mu = \eta$.

The third example is a model for secondary antibody labeling, where multiple secondaries can bind to a single primary, and where multiple emitters are attached

to each secondary, i.e. now $S = \sum_{i=1}^{n} T_i$ with n the number of secondaries and the T_i the number of emitters per secondary. We will analyze the case where the n are Poisson distributed with rate μ_1 and the T_i with rate μ_2. The probability distribution of S is given by:

$$P(S) = \sum_{n=0}^{\infty} P(S|n)\, P_1(n), \tag{4.68}$$

$$P(S|n) = \sum_{T_1=0}^{\infty} \dots \sum_{T_n=0}^{\infty} P_2(T_1) \dots P_2(T_n)\, \delta\left(S - \sum_{i=1}^{n} T_i\right), \tag{4.69}$$

$$P_1(n) = \frac{\mu_1^n \exp(-\mu_1)}{n!}, \tag{4.70}$$

$$P_2(T) = \frac{\mu_2^T \exp(-\mu_2)}{T!}. \tag{4.71}$$

We find that the probability of observing zero fluorophores is:

$$\begin{aligned} P(0) &= \sum_{n=0}^{\infty} P(0|n)\, P_1(n) = \sum_{n=0}^{\infty} \frac{\mu_1^n \exp(-\mu_1)}{n!} \exp(-n\mu_2) \\ &= \exp\left(-\mu_1\left(1 - \exp(-\mu_2)\right)\right). \end{aligned} \tag{4.72}$$

Restricting to the observed cases $S > 0$ implies we have to normalize the probability distribution by a factor $1/(1 - P(0))$ and sum only over values $S > 0$. This leads to:

$$\langle S \rangle = \frac{1}{1 - P(0)} \langle n \rangle \langle T \rangle, \tag{4.73}$$

$$\left\langle S^2 \right\rangle = \frac{1}{1 - P(0)} \left[\langle n \rangle \langle T^2 \rangle + \langle n(n-1) \rangle \langle T \rangle^2 \right], \tag{4.74}$$

giving:

$$\mu = \frac{\langle T^2 \rangle}{\langle T \rangle} - 1 + \langle T \rangle \left[\frac{\langle n^2 \rangle}{\langle n \rangle} - 1 \right]. \tag{4.75}$$

Here, the angular brackets indicate averaging over the individual probability distributions for n and for the T_i. For the Poisson-distribution at hand this gives:

$$\langle S \rangle = \frac{\mu_1 \mu_2}{1 - \exp\left(-\mu_1\left(1 - \exp(-\mu_2)\right)\right)}, \tag{4.76}$$

$$\mu = \mu_2\left(\mu_1 + 1\right). \tag{4.77}$$

Generally prior knowledge on the distribution of secondaries per primary and the distribution of fluorophores per secondary is needed to proceed. It appears that the final counting result is not very sensitive to details of the secondary to primary labeling stoichiometry, i.e. errors in the value of μ_1 are largely compensated by opposite errors in the estimated M_∞, giving a relatively robust estimate for the number of localizations per primary antibody. This can be understood semi-quantitatively as follows. In case there is little bleaching the fitting of M_∞ is dominated to a large extent

by the switching regime $k_{\mathrm{bl}}t \ll 1$. Then it holds that:

$$\langle M \rangle \approx \langle S \rangle M_\infty k_{\mathrm{bl}} t, \tag{4.78}$$

$$Q \approx \left(\mu + 1\right) M_\infty k_{\mathrm{bl}} t. \tag{4.79}$$

So, given the measured correlation parameter Q as a function of time and bleach rate k_{bl}, the product $A = \left(\mu+1\right) M_\infty$ is fixed for all values of μ. It then follows that the estimate for the number of localizations per primary antibody is:

$$\langle M \rangle \approx \frac{\langle S \rangle}{\mu + 1} A k_{\mathrm{bl}} t, \tag{4.80}$$

so that the stoichiometry only affects the final counting estimate via the ratio:

$$\zeta = \frac{\langle S \rangle}{\mu + 1} = \frac{\langle S \rangle^2}{\left\langle S^2 \right\rangle}. \tag{4.81}$$

It turns out that the functional dependence of ζ on μ_2 hardly changes with μ_1 for the range of values $1 < \mu_1 < 5$, with relative variations on the order of 10%. In fact, the dependence of ζ on μ_2 in the range of values $1 < \mu_2 < 5$ is also rather weak. It should be noted that the current analysis neglects quenching, but in case that can be safely neglected, it does show that the counting analysis is robust against errors in the stoichiometry calibration.

4.A.4. ESTIMATION OF CORRELATION PARAMETER AT HIGH LABELING DENSITY

In samples with high labeling densities or with tightly clustered labeled molecules, the Q-estimation may be prone to overestimation because it mistakes correlations due to the sample's spatial structure for correlations from repeated localization of the same labeling site. Here we will analyze under which conditions this problem is expected to occur.

The Q-estimation algorithm attempts to fit a model function $H(q)$ to the FRC numerator, which describes the decay in spatial correlations due to localizations of the same labeling site. $H(q)$ depends on the unknown spread of localizations of a single labeling site (i.e. effective localization error) due to localization error, errors in the correction for stage drift and the finite size of the labels, and is parameterized in Eq. 6 as:

$$H\left(q; \sigma_m, \Delta\sigma\right) = \frac{1}{\sqrt{1 + 8\pi^2 \Delta\sigma^2 q^2}} \exp\left(-\frac{4\pi^2 \sigma_{\mathrm{m}}^2 q^2}{1 + 8\pi^2 \Delta\sigma^2 q^2}\right), \tag{4.82}$$

where σ_m is the mean of the effective localization error and $\Delta\sigma$ it's standard deviation.

The FRC's numerator $\nu(q)$ can be expressed as:

$$\nu\left(q\right) \propto \left(NS(q) + Q\right) H(q), \tag{4.83}$$

where the term $S(q)$ relating to the sample's spatial structure is equal to:

$$S\left(q\right) = \frac{1}{K^2} \int d^2 q' \left|\hat{\psi}\left(\vec{q}\,'\right)\right|^2 \frac{\delta\left(\left|\vec{q}\,'\right| - q\right)}{2\pi q}, \tag{4.84}$$

with K the number of labeling sites and $\hat{\psi}(\vec{q})$ the Fourier transform of the normalized density of labeling.

The algorithm will have difficulties estimating σ_m and $\Delta\sigma$ when the decay of $S(q)H(q)$ and $QH(q)$ cannot be distinguished very well. This would occur if the decay of $S(q)$ is still larger than Q at the spatial frequency $q = 1/2\pi\sigma_m$ where $QH(q)$ starts to decay appreciably. Thus, we have the criterion:

$$NS(1/2\pi\sigma_m) < Q. \tag{4.85}$$

If we take as an example structure a line of length L and Gaussian cross-section with full width at half maximum w, then we have [44]:

$$S(q) \approx \frac{1}{\pi qL} \exp\left(-\frac{\pi^2 q^2 w^2}{2\log(2)}\right), \tag{4.86}$$

leading to the criterion for the linear density of labeled sites:

$$\rho_{lin} = \frac{K}{L} < \frac{1}{\sigma_m}\left(\frac{Q}{2M}\exp\left(\frac{w^2}{8\log(2)\sigma_m^2}\right)\right). \tag{4.87}$$

If the width of the filaments is on the same order as the width of the localization error distribution and $Q \approx M$, it follows that there should be fewer than one site per $2\sigma_m/e \approx 0.74\sigma_m$. In a more typical scenario $Q \approx 1.5M$ and thus the criterion becomes less than one per $0.5\sigma_m$.

Similarly, for a line with a rectangular cross-section and width w we would have [44]:

$$S(q) \approx \frac{1}{\pi qL}\left(\frac{\sin(\pi qw)}{\pi qw}\right)^2, \tag{4.88}$$

and thus we get the criterion:

$$\rho_{lin} < \frac{1}{\sigma_m}\left(\frac{Q}{2M}\right)\left(\frac{\sin(w/2\sigma_m)}{w/2\sigma_m}\right)^{-2}, \tag{4.89}$$

or if w equals the full width at half maximum of the localization error distribution that ρ_{lin} should be less than one site per $1.23\sigma_m$ (pessimistic case) or one per $0.82\sigma_m$ (typical case).

Thirdly, if we have a bell-shaped structure that can be described by a Gaussian with standard deviation a, then the number of sites K in the structure should satisfy:

$$K < \frac{Q}{M}\exp(a^2/\sigma_m^2). \tag{4.90}$$

Finally, if we have a circular structure with a radius a and K sites, then

$$S(q) = \left(2\frac{J_1(2\pi qa)}{2\pi qa}\right)^2, \tag{4.91}$$

and therefore we obtain the criterion

$$K < \frac{Q}{M}\left(2\frac{J_1(a/\sigma_m)}{a/\sigma_m}\right)^{-2}. \tag{4.92}$$

For $a \approx \sigma_m$ this gives $K < 1.3$ (pessimistic case) or $K < 1.9$ (typical case). For $a \approx 2\sigma_m$ this becomes $K < 3$ (pessimistic case) or $K < 4.5$ (typical case).

4.A.5. EFFECT OF FALSE NEGATIVE LOCALIZATIONS

False negative localizations refer to events where a fluorophore is activated during an acquisition but this fluorescence does not lead to a successful localization by the reconstruction algorithm. This may happen for example if nearby fluorophores are simultaneously active or if the fluorophore is very dim or the event is very short. The consequence of false negative localizations is that the number of localizations per fluorophore does not correspond anymore to the number of activation events. Below we will analyze the consequences assuming that the probabilities for activation events to result in a successful localization P_{loc} are independent and the same for all events.

Firstly, let us consider what happens to the expected number of *localizations* per fluorophore M_{loc}:

$$\langle M_{loc}\rangle = \langle\langle M_{loc}|M\rangle\rangle = \langle MP_{loc}\rangle = P_{loc}\langle M\rangle. \tag{4.93}$$

Here, M denotes the number of *activations* per fluorophore. Similarly, we find that:

$$\left\langle M_{loc}^2\right\rangle = \left\langle\left\langle M_{loc}^2|M\right\rangle\right\rangle = P_{loc}(1-P_{loc})\langle M\rangle + P_{loc}^2\left\langle M^2\right\rangle, \tag{4.94}$$

from which it follows that

$$Q \to \frac{\left\langle M_{loc}^2 - M_{loc}\right\rangle}{\langle M_{loc}\rangle} = \frac{P_{loc}^2\left\langle M^2 - M\right\rangle}{P_{loc}\langle M\rangle} = P_{loc}Q. \tag{4.95}$$

Another important consequence of false negative localizations is that a fraction P_0 of all fluorophores is never localized. This fraction is given by:

$$P_0 = \sum_{m=1}^{\infty} b(1-b)^{m-1}(1-P_{loc})^m = \frac{b(1-P_{loc})}{1-(1-b)(1-P_{loc})} \tag{4.96}$$

Finally, it can be shown that the probability distribution for the number of localizations per fluorophore is given by the same expression as in Eq. 4.17, if the following substitutions are made:

$$r \quad \to \quad r(P_{loc} + b(1-P_{loc})) \tag{4.97}$$

$$b \quad \to \quad \frac{b}{1-(1-b)(1-P_{loc})} = \frac{b}{P_{loc}+b(1-P_{loc})} \tag{4.98}$$

If $b = 1/M_\infty$ is not too large, then effectively only M_∞ appears to be reduced by a factor P_{loc}. However, because M becomes smaller by the same amount, the accuracy of the estimate for M does not deteriorate much. For example, if $P_{loc} = 80\%$ and $M_\infty = 5$ then the estimate for M would be off by 5%.

5

DATA FUSION OF IDENTICAL PARTICLES FOR STOICHIOMETRY INFERENCE

The previous chapter introduced a method to overcome overcounting problems with reversibly switchable fluorophores. However, undercounting problems due to incomplete labeling of the sample were not addressed. Here we examine how undercounting problems can possibly be overcome when many identical copies of well-defined macromolecular complexes are available. A data fusion approach is adopted to align different complexes and count the number of localizations per subunit of each complex. This allows us to infer the number of protein copies in each subunit, using the distribution of localizations per fluorophore from our method in chapter 4. The required conditions for accurate inference are investigated in a simulation study. We tested our method on the Nup160 and Seh1 proteins in the nuclear pore complex (NPC). Although prior evidence points to 32 copies of these proteins being present in the NPC, our method assigns the highest probability to an hypothesis of 40 copies per NPC. We therefore conclude that the given experimental conditions did not allow for the accurate application of our method.

A manuscript for a research article based on this chapter is in preparation. Authors: Nieuwenhuizen, R.P.J., Bates, M., Rieger, B. & Stallinga, S.

5.1. INTRODUCTION

The quantification method in chapter 4 was used to overcome overcounting problems with reversibly switchable fluorophores. However, that method could not account for undercounting due to incomplete labeling of binding sites. Because the fraction of successfully labeled binding sites is unknown and hard to calibrate, this limits the counting precision that can be achieved in practice.

Undercounting due to incomplete labeling does not only pose a problem for our quantification method. Other methods for reversibly switchable fluorophores based for example on kymograph analysis[67] or pair-correlation analysis[65, 66] are similarly capable only of estimating the number of localizations per labeled site. Only methods based on titration of marker concentrations during labeling have been used to overcome undercounting problems due to unlabeled molecules[115, 116]. However, as we noted in chapter 4, this method is susceptible to differences in the local chemical environment in the calibration experiments.

Quantification methods for fluorescent proteins (FPs) suffer from related undercounting problems. Not all FPs will be functional in an experiment due to protein misfolding or incomplete maturation. Therefore a calibration experiment is often performed to quantify the fraction of non-functional FPs[112–114]. However, some undercounting remains as some of the FPs are missed by the localization algorithm due to their weak signals.

Here we present a new approach to overcome undercounting problems for well-defined macromolecular complexes. If many identical copies of these complexes are available, then the data of these complexes can be combined into one single reconstruction. This approach was previously developed in the field of cryo electron microscopy (EM) single particle analysis (SPA)[128–130]. In this field many thousands of two-dimensional projections of macromolecular complexes are imaged and combined into a single three-dimensional reconstruction. Recently this particle alignment approach was extended to localization microscopy data.

In a first application, Löschberger and coworkers aligned localizations of thousands of identical copies of the nuclear pore complex (NPC) to create a reconstruction with a high signal-to-noise ratio (SNR)[52]. The NPC controls the transport of molecules between the cytoplasm and the nucleus in cells. It consists of several hundred proteins and has an eightfold rotation symmetry. Subsequently, similar approaches were used to elucidate the structure of the NPC[127], the Herpes Simplex virus[131], and HIV particles in three dimensions[132].

In this chapter, we will use a similar data fusion approach to infer the number of protein copies per subunit of a macromolecular complex using localization microscopy with reversibly switchable fluorophores. In particular we will consider the NPC here as a model system. In line with the terminology used in cryo EM, we will refer to such complexes as particles. Alignment of the particles is used to determine to which subunit of the complex each localization belongs. The number of counted localizations per subunit is then used to infer the number of protein copies in each subunit, using the distribution of localizations per fluorophore from our method in chapter 4. Fig. 5.1 provides a schematic overview of the method.

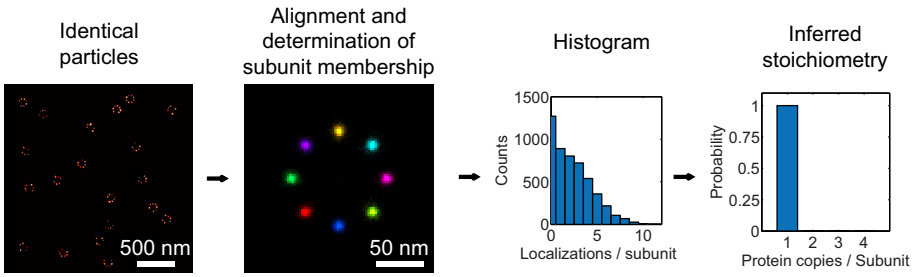

Figure 5.1: **Schematic overview of the stoichiometry inference method.** Localization microscopy data are obtained of a large number of structurally identical but incompletely labeled particles. These particles are segmented from the images and aligned. Subsequently, the subunit membership of each localization is determined, which is depicted here with different colors. The counted number of localizations per subunit is used to infer the stoichiometry of the number of protein copies in a subunit of the particle.

5.2. THEORY

5.2.1. PROBABILITY FOR THE NUMBER OF LOCALIZATIONS PER SUBUNIT

The starting point for the analysis is the probability distribution for the number of localizations M of a single fluorophore from Eq. 4.17:

$$P_m = (1-b)^m \frac{r^m}{m!} \exp(-r) + b(1-b)^{m-1} \sum_{n=m}^{\infty} \frac{r^n}{n!} \exp(-r) \tag{5.1}$$

where $r = k_{sw}t$ and $b = k_{bl}/k_{sw}$. If we now consider a subunit of a macromolecular complex labeled with $S = 2$ emitters each labeled with one fluorophore, then the probability $P(M|S=2)$ that the sum of localizations equals M is given by convolving P_m with itself. In general the probability $P(M|S)$ is found by convolving P_m in total $S-1$ times with itself.

In practice the number of emitters per subunit is not fixed. Instead, there is a probability $P(S_i)$ that a subunit i has S_i emitters. We will assume that each subunit has S_{max} labeling sites with a probability η of being labeled, which implies that S_i follows a binomial distribution. This gives the following distribution for the number of localizations per subunit M_i:

$$P\left(M_i|S_{max},\eta\right) = \sum_{S_i=0}^{S_{max}} P\left(M_i|S_i\right) \frac{S_{max}!}{S_i!(S_{max}-Si)!} \eta^{S_i} (1-\eta)^{S_{max}-S_i}. \tag{5.2}$$

As the labeling efficiency η is not known, we will assume a uniform prior probability. Consequently, $P\left(M_i|S_{max}\right)$ is found by integrating $P\left(M_i|S_{max},\eta\right)$ over the possible values for η.

If we now have a set $\{M_i\}$ of numbers of localizations of K identical subunits, then the total probability of obtaining that set is simply:

$$P\left(\{M_i\}|S_{max}\right) = \prod_{i=1}^{K} P\left(M_i|S_{max}\right). \tag{5.3}$$

In the absence of any statistical dependencies between the sites, different outcomes $\{M_i\}$ are indistinguishable under changes in the ordering of the sites. However, accounting for this indistinguishability only introduces a constant prefactor in the probability $P(\{M_i\})$, which will be irrelevant for our comparative analysis.

5.2.2. INFERENCE OF THE NUMBER OF MOLECULES PER SUBUNIT

Our goal is to determine the number of protein copies per subunit based on the counted number of localizations per subunit $\{M_i\}$. This number of protein copies is equal to S_{max} when each of these proteins corresponds to a single labeling site. We will therefore compute the posterior probability that S_{max} molecules per subunit are present, given the probability model in Eq. 5.3 and the available simulated or experimental data. In this computation we will assume that the localization precision and particle alignment are sufficiently accurate to unambiguously establish the subunit membership of localizations.

Assume now that a limited set of competing hypotheses $H_1, H_2, \ldots$ is available for the number of molecules S_{max} per subunit. The posterior probability that hypothesis H_l is correct can then be computed using Bayes' rule:

$$P(H_l|\{M_i\}) = \frac{P(\{M_i\}|H_l)\,P(H_l)}{\sum_k P(\{M_i\}|H_k)\,P(H_k)} \tag{5.4}$$

where $P(H_l)$ is the *prior* probability that H_l is true. For simplicity, we will assume throughout this chapter that these probabilities are equal for all competing hypotheses. If each hypothesis H_l simply corresponds to $S_{max} = l$, then $P(\{M_i\}|H_l) = P(\{M_i\}|S_{max} = l)$. Thus, if the switching rates in Eq. 5.1 can be measured, then the counted numbers of localizations per subunit M_i can be used to infer number of molecules per subunit with Eq.5.4. If multiple datasets are available, then Eq. 5.4 has to be used as an update rule: with each new dataset the probability $P(\{M_i\}|H_l)$ from the previous dataset becomes the prior probability $P(H_l)$ for the new dataset.

5

5.3. MATERIALS AND METHODS

5.3.1. SIMULATION METHODS

In our simulations we modeled the nuclear complex as a structure consisting of eight points evenly distributed on a circle with a diameter of 100 nm. Each of these points constitutes a subunit of the corresponding simulated structure. The structures were randomly rotated and positioned in a field of view of size 10 μm by 10 μm. Structures with a randomly drawn center position within 120 nm of another structure were discarded for the subsequent simulation.

Next, a set of simulated localizations was obtained for each structure. For each subunit, the S fluorophores were randomly drawn from a binomial distribution assuming S_{max} trials with success probability η (default value: $\eta = 0.4$). The positions of these fluorophores were then displaced with a Gaussian probability density with FWHM = 5 nm to account for the size of the antibodies linked to the fluorophores.

Each fluorophore was then assigned a random number of localizations M. In line with the results in chapter 4, M was obtained from the minimum of two quantities: $M_{poisson}$ and M_{geo} drawn from a Poisson distribution with an expected value of $k_{sw}t_{end}$ and a geometric distribution with an expected value of k_{sw}/k_{bl} respectively (default values: $k_{bl} = 2 \times 10^{-5}$ frame^{-1}, $t_{end} = 5 \times 10^4$ frames and $k_{sw}/k_{bl} = 7$. Localizations were then finally displaced with a Gaussian probability density with standard deviation σ, where a different value of σ was randomly generated for each localization based on the following expression[20, 133]:

$$\langle \sigma^2 \rangle = \frac{\sigma_a^2}{n_{ph}} \left(1 + 4\tau + \sqrt{\frac{2\tau}{1+4\tau}} \right) \tag{5.5}$$

where $\tau = 8\pi\sigma_a^2 b/(n_{ph}a^2)$. Here we used the following values: the pixel size a = 100 nm, the number of signal photons per localization n_{ph} (drawn from a geometric distribution with a default expected value of 5400), background photons b (average of 9×9 Poisson distributed values with expected value of 20), and the PSF width σ_a (Gaussian distributed with mean $0.3 \times \lambda/NA = 0.3 \times 670\text{nm}/1.45 \approx 138$ nm and standard deviation of 2% of the mean; this is roughly the distribution we obtain when fitting the PSF of Alexa Fluor 647 fluorophores and is in agreement with the range of previously suggested values[14]). Localizations with fewer than 2000 signal photons were discarded.

5.3.2. EXPERIMENTAL MATERIALS AND METHODS

PREPARATION OF FLUORESCENT NANOBODIES

Anti-GFP camelid antibody fragments (also known as "Nanobodies", Chromotek, GT-250) were labeled with amine-reactive Alexa Fluor 647 according to the manufacturer's protocol. Briefly, unlabeled nanobodies were mixed with amine reactive dye in a sodium bicarbonate buffer (0.1 M, pH 8.5), and the labeling reaction was left to proceed at room temperature for 30 min. The labeled product was separated from unreacted dye by running the reaction mixture over a gel filtration column (Illustra NAP-5 column, GE Healthcare), and eluting in PBS. The labeled product was stored at 4°C in PBS.

FLUORESCENT STAINING OF CULTURED CELLS

Hela Kyoto cell lines stably expressing siRNA-resistant versions of the human Nup160 and Seh1 transcripts tagged with mEGFP were established by selection of cells transfected with respectively pmEGFP-Nup160-s23466res and pmEGFP-Seh1-s37879res [127] with 1 mg/mL Geneticin (Life Technologies). To increase the degree of replacement of the endogenous protein with the mEGFP-tagged version, the cells were repeatedly transfected every 48 hours over the course of 12 days with respectively Silencer Select siRNA s23466 against Nup160 or s37879 against Seh1 (Life Technologies) by solid phase transfection on siRNA-coated 24-well plates (for details on the coating procedure see Szymborska et al.[127]). After knock down, the cells were transferred onto cover slips, allowed to attach and processed for staining with Alexa Fluor 647-coupled

anti-GFP nanobody as described before[127]. For imaging we selected cells with relatively flat nuclei exhibiting high Alexa Fluor 647 signals.

IMAGING BUFFER

The imaging buffer consisted of 50mM Tris-Cl (pH 8.0), 10mM NaCl, 10% Glucose (w/v), 10mM β-mercaptoethylamine (pH 8.5, Sigma, 30070), and 1% of an enzymatic oxygen scavenger system stock solution. The oxygen scavenging system was added to the buffer immediately before use. The oxygen scavenger stock solution was prepared by mixing pyranose oxidase powder (10 mg, Sigma, P4234) with catalase (50 μL, 20 mg/mL, Sigma, C30) in PBS (200 μL), and centrifuging the mixture at 13.000 rpm for 1 minute.

MICROSCOPE

Measurements were performed using the same custom built inverted fluorescence microscope as in 4, which was similar to that described previously[63]. To summarize, an inverted fluorescence microscope stand (Olympus IX71) was fitted with a 100X oil-immersion objective lens (Olympus, UPLANSAPO100XO, NA=1.4) which enabled efficient detection of single fluorophores. A custom-built focus lock system based on the reflection of an infra-red laser from the sample was used to maintain sample focus during all measurements. For STORM imaging, photo-switchable Alexa Fluor 647 was excited using 642 nm light, and in some measurements the sample was also exposed to 405 nm light to increase the activation rate of switching. A solid-state diode laser (Oxxius) was used to generate 405 nm light, and a fiber laser (MPB Communications, 2RU-VFL-P-1500-642) was used to generate 642 nm light. The laser illumination was configured such that the illumination angle could be varied between an epi-illumination geometry and a total internal reflection (TIRF) illumination mode. For STORM data acquisition, the sample was illuminated with TIRF illumination for reduced background signal. Fluorescence emission of Alexa Fluor 647 was filtered using a dichroic mirror (Chroma, Z660DCXRU) and a bandpass emission filter (Chroma, ET700/75). Fluorescence was detected using an EMCCD camera (Andor Technology, Ixon DU897).

5.3.3. PARTICLE ALIGNMENT

Structures were identified in images by cross-correlation with a template image consisting of a ring with inner diameter of 50 nm and outer diameter of 140 nm in a square region of 210 nm by 210 nm. Candidate regions that contained multiple NPCs or unspecifically bound nanobodies were manually discarded for the analysis. The position and orientation of each structure was then determined by alignment with a template consisting of 8 evenly distributed points on a circle, with the position, rotation and size as free parameters. In line with the approach we followed earlier[134], these parameters were determined by minimization using the fminsearch function in MATLAB of the following cost function:

$$D = -\sum_{i=1}^{8}\sum_{j}\exp\left(-\left|\vec{x}_{t,i}-\vec{x}_{s,j}\right|^2/4\sigma_j^2\right) \tag{5.6}$$

where $\vec{x}_{t,i}$ are the positions of the template points, $\vec{x}_{s,j}$ are the localizations belonging to structure j and σ_j are the corresponding localization precisions. Subsequently, the results were filtered by discarding structures with: a fitted size more than one standard deviation from the mean fitted size; a number of localizations of less than 75% or more than 400% of the average number of localizations per particle (in simulations) or of the number of localizations corresponding to a representative manually segmented structure (in experiments).

5.3.4. INFERENCE

The probability distribution for the number of localizations per fluorophore requires estimates of the spurious correlation parameter Q. For the experimental data we obtained 20 estimates of Q for each of 20 time points using localizations of sparse unspecifically bound nanobodies outside the nucleus, similar to how the data in Fig. 4.6 were processed. This provided an estimate for Q independent of the localizations of the NPCs themselves. For the simulated data, no unspecifically labeled markers were used but instead the ground truth Q at 20 time points was corrupted with normally distributed noise (default standard deviation 0.25). Values for the number of accumulated localizations N were obtained from the localizations in the NPCs.

To infer the number of target molecules per subunit, we first counted the number of localizations per subunit. The localizations were assigned to different subunits based on the nearest point in the template for each of them. Localizations were ignored for the counting if they were too close (e.g. closer than 25 nm) or too far (e.g. further than 70 nm) away from the fitted center position of the corresponding template.

In the subsequent inference step, a bootstrap sample of values for Q was used to estimate k_{bl} and k_{sw}. In this bootstrap sample, a set of 20 values for Q per time point were randomly drawn with replacement from the 20 original values at that time point. k_{bl} and k_{sw} were used next to compute the distribution of localizations per emitter P_m. This was then used to compute the conditional probability matrix $P(M_i|S)$ for the number of localizations per subunit M_i given a number of fluorophores per subunit S. Next, the log-likelihood was computed for each of 100 different values of the labeling efficiency η under each hypothesis H_l for the number of binding sites per subunit; in other words, we computed $\log\big(P\left(\{M_i\}|H_l,\eta\right)\big)$. This log-likelihood value was corrected for the filtering steps of the NPCs by subtracting $N_p \log P_f$, where N_p is the number of particles and P_f is the probability that the sum of eight independent values of M_i would fall in the range that was allowed in the filtering of the aligned particles. This procedure was repeated for 100 bootstrapped sets of values for Q. The log-likehood values for different sets of Q were averaged for each value of η.

The averaged conditional log-likelihood values $\log\big(P\left(\{M_i\}|H_l,\eta\right)\big)$ were converted into likelihood values by taking the exponent. These likelihoods were then multiplied with the (uniform) prior probability for the labeling efficiency η and numerically integrated to obtain the likelihood $P\left(\{M_i\}|H_l\right)$ of each model. These likelihood values were then used in Eq. 5.4 to compute the posterior probability of each model.

5.4. RESULTS

5.4.1. SIMULATION RESULTS

To test the method for inferring the number of molecules per subunit, we simulated localization microscopy datasets of structures consisting of eight equally spaced points on a circle. Each point contained $S_{max} = 1, 2, 3$ or 4 target molecules (i.e. labeling sites). Subsequently we tested our workflow for identifying and aligning the structures, classifying the localizations, and finally inferring the number of molecules per subunit (i.e. points on the circle). The inference considered the hypotheses that the number of molecules per site is either one, two, three, or four. We then computed in what fraction out of 100 simulated datasets the method assigned the highest probability to the correct hypothesis. We used the following default parameters in these simulations: 500 particles in the field of view, 40% labeling efficiency, 4 nm localization precision, 4.42 activations per fluorophore, and a fraction of non-bleached fluorophores of $1/e$ at the end of the acquisition (i.e. $k_{bl}\, t_{end} = 1$).

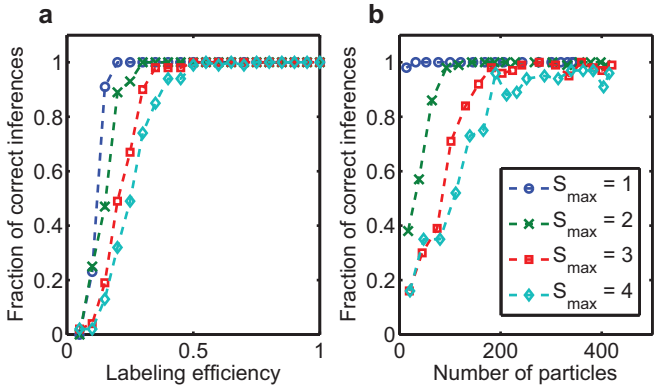

Figure 5.2: **Overcoming undercounting through data fusion in simulations.** (a) Accuracy of the inference method in simulations with varying labeling efficiencies η. For each value of η we show in which fraction out of 100 simulations the method assigned the highest posterior probability to the correct hypothesis for the number of molecules per subunit of a complex S_{max}. (b) The same as in (a), but instead of the labeling efficiency we varied the number of particles in the field of view in the simulations. The x-axis shows the number of detected particles in the field of view that were used in the inference.

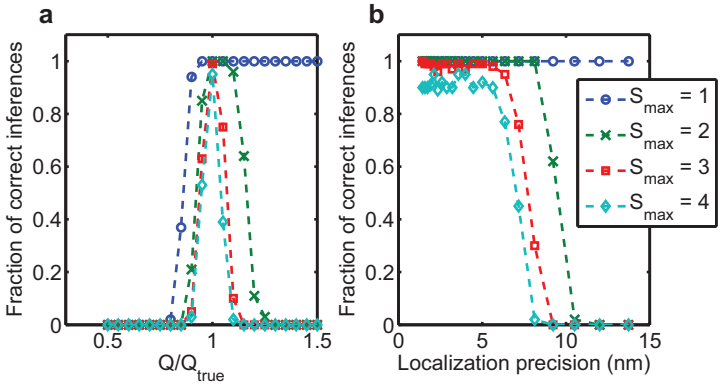

Figure 5.3: **Influence of Q-estimation and localization precision on the inference.** (a) Accuracy of the inference method in simulations as a function of the bias in the values for the parameter Q. The bias is expressed here as the fraction between the average Q per time point and the ground truth value Q_{true} at that time point. (b) Accuracy of the inference method in simulations as a function of the localization precision σ.

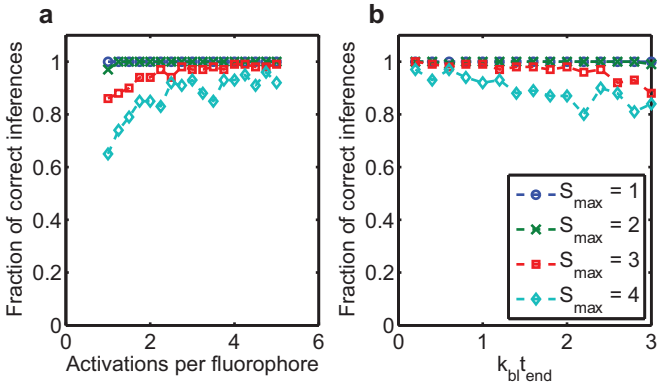

Figure 5.4: **Influence of switching kinetics on the inference.** (a) Accuracy of the inference method in simulations with varying numbers of on-events per fluorophore obtained by varying the switching rate k_{sw} in the simulations. (b) Accuracy of the inference method in simulations with various degrees of bleaching of the fluorophores, obtained by varying the effective bleaching rate k_{bl}. The total number of localizations per fluorophore remained constant in these simulations by varying k_{sw} as well.

Firstly, we investigated whether our method could indeed be used to overcome undercounting due to incomplete labeling. Therefore we tested the performance of the method on simulated data for different labeling efficiencies (i.e. the fraction of sites that were labeled). The results, which are shown in Fig. 5.2a, reveal that when the labeling efficiency is 40% or higher, the method does indeed correctly infer the right number of molecules per subunit in more than 90% of the cases. For lower labeling efficiencies, the fraction of correct inferences decreases because the method incorrectly returns higher probabilities for models with too low values of S_{max}. In other words, the method is biased towards lower numbers of proteins per subunit under these circumstances. This indicates that the estimated values of the posterior probability can be inaccurate, as the method does not consider possible biases in the counted number of localizations per site. Such biases could result for example from inaccurate alignment of the particles or from biases in the identification of particles.

Fig. 5.2b shows how the performance of the method depends on the number of particles used for inference. This reveals that the number of particles required for accurate inference is actually not very high: only about 200 particles suffice for accurate inference. For lower numbers of particles, the method incorrectly returns higher probabilities for models with too low values of S_{max}. Note that in other cases more particles will be needed for similar performance, because each particle has eight identical subunits in these simulations.

Next we investigated how the inference is affected by the accuracy of the estimation of the correlation parameter Q, which is used to quantify the fluorophore switching rates. To this end we introduced a bias in the Q-values used to compute the distribution of the number of localizations per fluorophore in the simulations. Fig. 5.3a shows the results obtained as a function of this bias. These results indicate that the analysis is quite sensitive to the accuracy with which the parameter Q is estimated: errors in the estimated Q on the order of 5 to 10% will already result in inaccurate inference. We also investigated the influence of the standard deviation in the values of Q per time point on the inference, but we found that the accuracy was not substantially affected for standard deviations in the tested range between 0 to 2, where $Q = 3.2$ at the end of the acquisition.

In addition to the accuracy of the Q-estimation, we also considered how the localization precision affects the inference. The expectation is that a worse localization precision results in less accurate particle alignment and consequently to errors in the counted number of localizations per subunit. To test this we performed simulations for different numbers of signal photons per localization. The threshold on the minimum photon count per localization was varied as well to keep the fraction of subthreshold localizations constant. This allowed us to assess the accuracy of the inference as a function of the localization precision. The results are shown in Fig. 5.3b. This shows that indeed the accuracy of the inference deteriorates as the localization precision becomes larger than 6 nm. This is about one sixth of the distance of 38 nm between neighboring points in the structure in this simulation. Worse localization precision causes the method to incorrectly return higher probabilities for models with too low values of S_{max}. In addition, the labeling efficiencies with the high-

est likelihood values increase for larger localization precisions. These observations are attributed to an effective redistribution of localizations from sites with relatively many molecules to sites with fewer molecules. In general, the required localization precision will depend on this characteristic distance between molecules in different subunits. Surprisingly, the accuracy of the inference also deteriorates here when the localization precision becomes less than 1 nm, due to a failure of the particle alignment algorithm to converge. This is possibly the result of the finite label size which effectively introduces a localization error larger than the fit precision. Modifying the localization precision in Eq. 5.6 may overcome this issue.

A final set of simulations was used to investigate how the switching kinetics of the fluorophores affect the accuracy of the inference. Therefore we simulated datasets for different values of the switching rate k_{sw}, while keeping the effective bleaching rate k_{bl} and the acquisition time constant. The result in Fig. 5.4a shows that the accuracy improves with increasing numbers of on-events per fluorophore as expected. Moreover, the results show that higher values of S_{max} require increasing numbers of activations per fluorophore for accurate inference. Note here that only 69% of the on-events actually result in a localization in our simulations, due to the filtering of localizations on photon counts. Therefore approximately 3 localizations per fluorophore seem to be sufficient for accurate inference under these conditions.

The fraction of bleached fluorophores was varied in the simulations by changing k_{bl}, while keeping the average number of localizations per fluorophore constant. Fig. 5.4b shows that in fact photobleaching of the fluorophores leads to a slightly worse performance of the method, especially for $S_{max} = 4$. This can be explained by the fact that a narrower distribution is obtained for the number of localizations per fluorophore when bleaching is absent (i.e. under Poisson statistics) than when all fluorophores have bleached (i.e. under geometric statistics). Therefore different numbers of fluorophores per subunit are more easily distinguished when bleaching is limited. Note though that shortening the acquisition time will not benefit the inference, as this also results in fewer localizations per fluorophore.

5.4.2. INFERENCE OF THE NUMBER OF PROTEIN COPIES IN THE NPC

In order to test if our method can provide accurate inference of numbers of protein copies, we applied it to images of Seh1 and Nup160 proteins in the human nuclear pore complex (NPC). Both of these proteins are members of the Y-shaped Nup170 subcomplex. Recent evidence from mass spectrometry and electron microscopy suggests that the human NPC contains 32 copies of this complex[120, 121]. These copies form two eightfold symmetric reticulated rings on the cytoplasmic and nucleoplasmic side of the nuclear membrane. As before, the proteins were tagged with mEGFP and labeled with anti-GFP nanobodies (NBs), each of which contained only one Alexa Fluor 647 fluorophore that contributed to the imaging.

Fig. 5.5a shows (part of) one of the resulting images for Seh1. This image does indeed show the eightfold symmetry of the structure. However, the localization precision is not high enough to distinguish between each Seh1 protein and its counterpart on the nearest Nup107 subcomplex on the same ring. Moreover, in this two dimen-

sional projection of the NPC, the proteins on different rings appear to be situated in the same lateral position. Therefore the images show eight distinguishable clusters of localizations. For the following analysis we will refer to these eight clusters as subunits. Moreover, we will assume that all eight subunits on the NPC are identical, such that they all contain the same average number of Seh1 and Nup160 copies.

To infer the number of Seh1 proteins per subunit for the dataset corresponding to Fig. 5.5a, we first aligned the localizations of different NPCs. Fig. 5.5b shows an image of the combined localizations from all the aligned NPCs. Subsequently we determined the switching rate k_{sw} and effective bleaching rate k_{bl} using a region outside the nucleus, which contained sparsely distributed unspecifically bound nanobodies. Fig. 5.5c shows that the number of accumulated localizations exhibits the same time dependence in this region and inside the nucleus, suggesting identical switching kinetics. Computation of the correlation parameter Q leads to the estimates $k_{bl} = 4.8 \times 10^{-3}$ s^{-1} and $M_\infty = k_{sw}/k_{bl} = 3.3$ for the dataset corresponding to Fig. 5.5a.

Next, the histogram of the counted number of localizations per subunit in Fig. 5.5e was used to compute the likelihood values in Fig. 5.5f for different values of the labeling efficiency for each hypothesis for the number of Seh1 copies per subunit. This reveals that the highest likelihood is obtained for the hypothesis of 4 copies per subunit for a labeling efficiency of 27%. Fig. 5.5e also shows the maximum likelihood prediction for the counted number of localizations under each hypothesis superimposed on the histogram. Finally, we used the computed likelihood values to compute the posterior probability for the different hypothesis for the copy number of Seh1 in Fig. 5.5g. For this particular dataset, the highest probability is assigned to the model with 4 copies per subunit. Although previous mass spectrometry data points to 3 Seh1 copies per subunit instead[120], 4 copies per subunit would be consistent with the structural evidence from electron microscopy[121].

When comparing the inference results in Fig. 5.6a for the different datasets that were acquired for Seh1, we observe substantial variation in the posterior probabilities assigned to different hypotheses. In fact, the most probability mass is assigned to the hypothesis with $S_{max} = 5$ copies per subunit (i.e. 40 copies per NPC), although including more models with $S_{max} > 5$ would introduce a further shift of probabilities to higher copy numbers per NPC. Similarly, Fig. 5.6b shows the results for the Nup160 protein. Also here high probability values are assigned to the hypothesis of 5 copies per subunit. However, both mass spectrometry and electron microscopy data have provided substantial evidence in favor of 32 copies of Nup160 per NPC, which corresponds to 4 copies per subunit. Therefore we conclude that in these experiments was not accurate enough to correctly infer the copy numbers of Seh1 and Nup160 in the human NPC. Instead, the method appears to have suffered from a bias towards higher copy numbers.

To analyze why the inference overestimates the number of protein copies per NPC, we compared the experimental conditions to the simulation results in Fig. 5.2, Fig. 5.3 and Fig. 5.4. Assuming that the ground truth for the number of Seh1 and Nup160 copies per subunit is indeed 4, we find that: the maximum likelihood label-

ing efficiency in these datasets ranged from 26% to 40% for Seh1 and 15% to 25% for Nup160; the number of NPCs used for the analysis ranged from 140 to 382 for Seh1 and 28 to 268 for Nup160; the typical localization precision was on the order of 2.5 nm in both cases; the estimated number of localizations per fluorophore ranged from 2.2 to 3.0 for Seh1 and 1.4 to 3.0 for Nup160. Therefore the labeling efficiency, the number of particles and the number of localizations per fluorophore were all in the range where accurate inference may just be possible based on the simulation results. However, insufficienct labeling efficiencies, particle numbers and localizations per fluorophore all led to biases to lower copy numbers per NPC in the simulations. Therefore these conditions cannot explain the observed results.

The comparison with the simulation results leaves two possible explanations that could account for the observed bias in the results. Firstly, it is possible that the correlation parameter Q is systematically underestimated. The magnitude of the correlation parameter Q in these experiments was on the order of 2 to 4. However, as we saw previously in chapter 4, the estimation of Q has a typical precision on the order of unity, which is on the order of 25% to 50% here. This is substantially worse than the 5% accuracy that was required in simulations to obtain accurate inference. Therefore, the low number of activations per fluorophore, which in turn results in a low value for Q, may well have been the limiting factor in these experiments.

An alternative explanation would be that the experiments deviate from the simulation model in some respect. For example, the simulations did not account for missed localizations due to overlapping PSFs from simultaneously active fluorophores. We found a possible indication for this in the azimuthal autocorrelation function of localizations on the same NPC. We observed that the correlation between adjacent subunits was reduced compared to the correlation between opposing subunits. Also, false positive localizations, and inhomogeneities in the fluorophore switching rates or correlations in the photoswitching of fluorophores on adjacent nanobodies within the same NPC could give rise to a discrepancy between the simulations and the experiments.

5.5. DISCUSSION

The simulation results in this chapter indicate how the inference is affected by variations in experimental conditions. The results cannot be used directly to derive the necessary conditions for successful application of the method. However, these results do show that better inference is obtained for higher labeling efficiencies, localization precision and accuracies in Q-estimation, more particles and localizations per fluorophore, and for lower levels of photobleaching. Moreover, the inference appears to be particularly sensitive to biases in the estimation of the Q-parameter.

For the application of our method it is very important to check the quality of the estimation of the Q-parameter, as well as the identification and alignment of particles. Possible biases in these steps can lead to inaccurate probability estimates in the inference. However, this inaccuracy will not always be reflected in the returned probability estimates. For example, if the Q-parameter is underestimated the infer-

ence may return a probability value close to unity for the hypothesis that two protein copies are present per subunit, when in fact only one protein copy is present. A possible test that may reveal if the Q-parameter was accurately determined is to compare the histogram of the counted localizations per subunit $\{M_i\}$ with the maximum likelihood prediction for the distribution of M_i. This could reveal discrepancies between the data and the model caused by inaccurate estimation of the Q-parameter.

The accuracy of the inference method could be improved by developing better algorithms for identifying and aligning particles. Moreover, the performance could also be enhanced by including timing information of the localizations[40]. At present, the inference only considers the set $\{M_i\}$ of numbers of localizations per subunit at the end of the acquisition. Instead the inference could also consider numbers of localizations per subunit at multiple time points $\{M_i(t)\}$. The probabilities of the sets $\{M_i(t)\}$ can be derived from the switching model in chapter 4. Including timing information in this manner also introduces the possibility to estimate the switching rates k_{sw} and k_{bl} from the counted localizations per subunit, thus obviating the need for the potentially inaccurate Q-estimation. Alternatively, the inference could also be defined with respect to the interval times between localizations in the same subunit[135].

The inference method was applied here to two-dimensional localization microscopy data of particles with eightfold rotational symmetry. However, the method can also be applied to three-dimensional data or asymmetric particles. This requires a different approach to identify and align the particles in those data[134], which does not necessarily require a template structure. The inference itself does not require any modification though, as long as the alignment accuracy and localization precision are good enough to determine to which subunit each localization belongs. The inference could even be applied to well-defined parts of otherwise heterogeneous structures, if the identical copies of those parts can be identified in the image and subsequently aligned. A similar approach was used in the field of cryo electron tomography, where sub-tomograms are averaged to obtain a higher resolution reconstruction[136]. Furthermore, the method could even be extended for labeling schemes with multi-fluorophore markers, such as primary antibody labeling. This would require a calibration of the distribution of the number of fluorophores per marker though, for example through counting based on photon antibunching effects[115].

Our method assumes that all labeling sites are equally likely to be labeled. However, in practice there may be differences in the accessibility of each site, for example if they are on opposite sides of a membrane. Moreover, a marker labeling one site may also reduce the accessibility of neighboring sites. This issue might be overcome by abandoning the assumption that $P(S)$ follows a binomial distribution. Instead, it is also possible to estimate all the parameters $P(S=0|S_{max})\dots P(S=S_{max}|S_{max})$. Comparing different hypotheses for S_{max} then requires a prior probability for S_{max} which accounts for the greater number of free parameters in the estimation with increasing S_{max}.

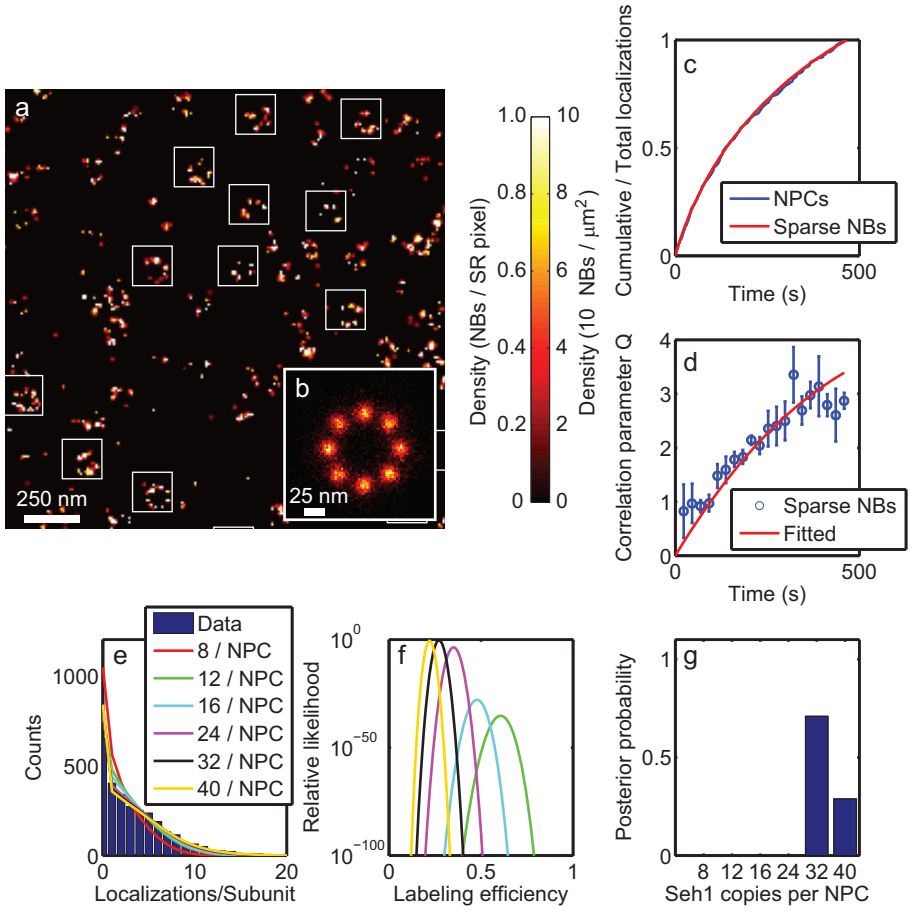

Figure 5.5: **Example inference of the number of Seh1 copies in the NPC.** (a) Cutout of a quantitative localization microscopy image of nanobody-labeled Seh1 in the NPC. (b) Image of the combined localizations after alignment. (c) Comparison of the relative number of accumulated localizations from NPCs and from unspecifically bound nanobodies (NBs) outside the nucleus, which were used to estimate the Q-parameter. (d) Median estimated values of the Q-parameter and corresponding model function for the fitted values of the switching rates k_{sw} and k_{bl}. Error bars indicate the standard deviation among estimated values per time point. (e) Histogram of the counted number of localizations per subunit of the NPC at the end of the acquisition of about 6.6 min. in the corresponding dataset. The plotted lines show the maximum likelihood predictions for the distribution under different hypotheses for the number of Seh1 copies per NPC. (f) The likelihood of the labeling efficiency in this sample under the different hypotheses, normalized to the highest likelihood. (g) Posterior probability for each hypothesis for the number of Seh1 copies per NPC.

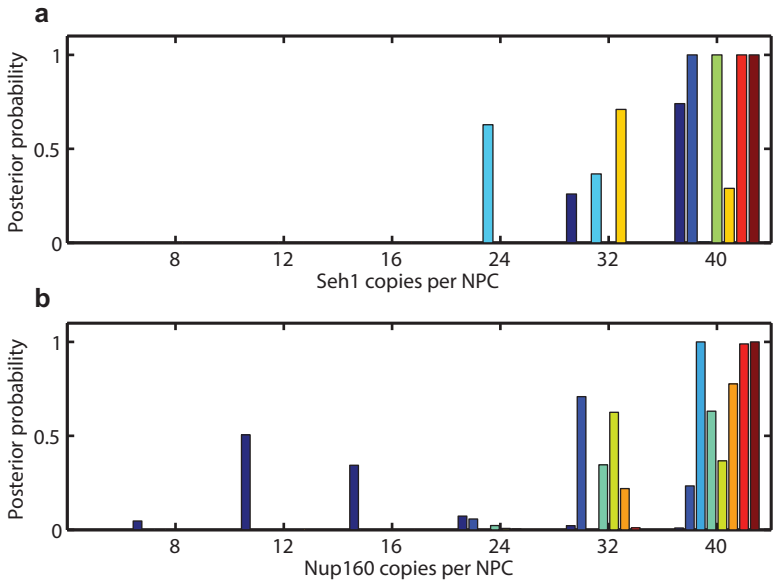

Figure 5.6: **Inference results for the number of Seh1 and Nup160 copies in the NPC** (a) Results of the application of our inference method to $n = 7$ datasets of the Seh1 protein, which were processed similarly to the dataset shown in Fig. 5.6, whose results are also included here. (b) Results of the applications of our inference method to $n = 8$ datasets of the Nup160 protein.

6

CO-ORIENTATION

Co-localization analysis is a widely used tool to seek evidence for functional interactions between molecules in different color channels in microscopic images. Here we extend the basic co-localization analysis by including the orientations of the structures on which the molecules reside. We refer to the combination of co-localization of molecules and orientational alignment of the structures on which they reside as co-orientation. Because the orientation varies with the length scale at which it is evaluated, we consider this scale as a separate informative dimension in the analysis. Additionally we introduce a data driven method for testing the statistical significance of the co-orientation and provide a method for visualizing the local co-orientation strength in images. We demonstrate our methods on simulated localization microscopy data of filamentous structures, as well as experimental images of similar structures acquired with localization microscopy in different color channels. We also show that in cultured primary HUVEC endothelial cells, filaments of the intermediate filament vimentin run close to and parallel with microtubuli. In contrast, no co-orientation was found between keratin and actin filaments. Co-orientation between vimentin and tubulin was also observed in an endothelial cell line, albeit to a lesser extent, but not in 3T3 fibroblasts. These data therefore suggest that microtubuli functionally interact with the vimentin network in a cell-type specific manner.

Parts of this chapter have been published as: Nieuwenhuizen, R.P.J., Nahidiazar, L., Manders, E.M.M., Jalink, K., Stallinga, S. & Rieger, B. *PLoS ONE* **10**, e0131756 (2015).

6.1. INTRODUCTION

Cytoskeletal protein networks serve a number of crucial roles in living cells. Traditionally, three types of cytoskeletal networks are discriminated[137]. First, thin filaments with a diameter of about 10 nm, which consist of actin polymers with associated cross-linking proteins and "muscle-like" myosins give stiffness to cells and play important roles in the generation of motile forces. Second, microtubules, which consist of hollow tubules of the protein tubulin with an outer diameter of approximately 23 nm. Microtubules run throughout the cell and play a dominant role as cellular highways for the transport of cargo, which can be moved either outwards from or inwards to the center of the cell by specific, ATP-consuming motor proteins. The third type of cytoskeleton are termed intermediate filaments due to their intermediate unit-filament diameter. Over 60 different proteins such as keratins, vimentin and lamins have been identified, most of which have a strict cell type-specific distribution. Whereas each of these filament systems, their subunits and methods of polymerization have been the subject of many thousands of studies, remarkably little is known on how the three principal filament systems may interact and collaborate to keep the cell alive and functioning. This is due in part because imaging with confocal fluorescence microscopy provides insufficient resolution to reliably discriminate individual filaments in most cases, whereas electron microscopy does provide ample resolution but is much less suited to routinely identify and track the different filaments. The recent advances in optical super-resolution microscopy, including localization microscopy [2–4, 47, 48] and STED microscopy[138] do provide sufficient resolution to distinguish individual fluorescently labeled filaments within the cell, and they can be routinely applied in a convenient manner.

The availability of superresolved multicolor images of filaments introduces the need for new quantitative tools to interrogate the organization of and mutual interrelations between the different cytoskeletal elements. Tools developed for diffraction limited fluorescence microscopy focused on the problem of co-localization analysis. This analysis asks whether images show evidence for possible interactions between the molecules imaged in both color channels. Typically the answer to this question is expressed in terms of: 1) the Pearson correlation coefficient between the intensities[139]; 2) the Manders coefficients, which are defined as the fraction of the total intensity per channel that occurs in co-localizing pixels[140], i.e. pixels whose values in both channels exceed certain thresholds; or 3) the overlap fractions of segmented objects in both color channels[141].

The different measures of co-localization cannot simply be applied to localization microscopy techniques; these techniques produce datasets consisting of coordinates of localized molecules instead of intensity values in pixels. This suggests that coordinate based analyses of distances between molecules should be used instead. Proposed measures include: the pair-correlation function between coordinates in two color channels[65]; a hypothetical potential energy function that is estimated from the distances from each localization to the nearest neighbor in the other color channel[142]; and the rank correlation between the distances from a localization to its neighbors in the same color channel on the one hand and distances to its neigh-

bors in the other channel on the other hand[143]. However, all these analyses only consider the spatial proximity of molecules in different color channels. They do not take into account that the molecules reside on extensive structures such as filaments that have additional geometric features such as size, orientation or curvature.

Here we report a rigorous quantitative framework for analyzing the simultaneous co-localization and similarity in orientation of structures in multicolor images. We will refer to the combination of co-localization and orientational alignment as co-orientation. We focus here on the orientation as a geometric feature as it presents a particularly salient property of cytoskeletal filament networks. Because the orientation varies with the length scale at which it is evaluated, we include this scale as a separate informative dimension for the analysis. We demonstrate our methods on simulated localization microscopy data of filament structures, as well as experimental images of filamentous structures acquired with localization microscopy in different color channels. Software for our co-orientation analysis is freely available in the form of Matlab code at http://www.diplib.org/add-ons/.

6.2. MATERIALS AND METHODS

6.2.1. ORIENTATION MEASUREMENT

The co-orientation analysis starts with the determination of the orientation in each color channel. The two images of two different molecular species imaged in color channels $l = 1,2$ will be denoted with $I_l(\vec{x})$. For now we will assume these to be two-dimensional and we will discuss the generalization to three-dimensional images below. In this work we will only apply our methods to localization microscopy data. The estimated fluorophore coordinates are converted into images by binning them into two-dimensional histogram with bin sizes of 10 nm. It should be noted here that although all subsequent operations are carried out on pixelated images, this is not problematic when the pixel size is smaller than 1.5 times the localization precision[44] because the information lost at small length scale is limited. For smaller pixel sizes we do not expect that the choice of pixel size affects any outcomes. Note also that in principle rendering localizations as Gaussian blobs the size of the localization error distribution provides a better data representation than the histogram binning applied here[92]. However, in practice this rendering is too slow due for the large number of required renderings for the significance tests that are discussed below.

The orientations of the filaments in the images are analyzed by considering orientation space representations $I_l(\vec{x},\phi)$ [144], which quantify for each position $\vec{x}$ how much evidence there is for the presence of structures with an orientation ϕ. By considering multiple orientations, it is possible to determine the orientations of several crossing filaments at the same location.

To compute $I_1(\vec{x},\phi)$ and $I_2(\vec{x},\phi)$, the images $I_1(\vec{x})$ and $I_2(\vec{x})$ are first filtered with a set of orientation selective filters $\Phi\left(\vec{x};\phi\right)$, which have an orientation ϕ between $-\pi/2$ and $\pi/2$ with respect to the x-axis. Applying these filters gives the orientation space

representation:

$$I_l\left(\vec{x},\phi\right) = I_l\left(\vec{x}\right) * \Phi\left(\vec{x};\phi\right), \tag{6.1}$$

where $*$ denotes the convolution operation, and the filters $\Phi\left(\vec{x};\phi\right)$ are defined by their Fourier transforms:

$$\hat{\Phi}\left(\vec{q};\phi\right) = \int_{-\infty}^{\infty} \Phi\left(\vec{x};\phi\right) \exp(-i2\pi\vec{q}\cdot\vec{x}) d^2 r, \tag{6.2}$$

as[145]:

$$\hat{\Phi}\left(\vec{q};\phi\right) \equiv 2\exp\left(-\frac{\left(\phi_q-\phi\right)^2}{2w_\phi^2}\right)\left(qs_o\right)^{w_q^2 s_o^2} \exp\left(-\frac{q^2 s_o^2 - 1}{2w_q^2 s_o^2}\right). \tag{6.3}$$

Here ϕ_q is the angle of $\vec{q}$ with respect to the x-axis, w_ϕ is the angular bandwidth of the filter, s_o is the length scale for which the orientation is evaluated and w_q is the bandwidth of the filter with respect to the spatial frequency magnitude $q = \left|\vec{q}\right|$. For this work we chose $w_q = 0.8/s_o$ and the orientation scale s_o was determined by selecting the smallest value that still had a good orientation selectivity upon visual inspection of the orientation space representation. Generally, the scale should be set such that the features of interest have a high contrast with respect to the local background and a high contrast with respect to the responses at the same location to filters with different orientations. However, it does not make sense to choose a scale smaller than the resolution of the images[44]. The width w_ϕ is derived from the number of independent orientations n_o that are analyzed via $w_\phi = \pi/n_o$. Here we used $n_o = 41$ for simulated datasets and for experimental datasets, which gives an angular resolution of about 77 mrad. This is on the same order as the angular extent of linelike structures with a width w at a scale s_o which is $w/s_o \sim 0.05$ (for $w \sim 10$ nm and $s_o = 200$ nm). Note that by definition $I_l\left(\vec{x},\phi+\pi\right) = I_l\left(\vec{x},\phi\right)$.

Next, we take the absolute value of the orientation space representation and subtract the minimum value per location $\vec{x}$. Subsequently we normalize the outcome such that the sum over ϕ in each location equals the number of localizations by computing:

$$\tilde{I}_l\left(\vec{x},\phi\right) = \left(\frac{\left|I_l\left(\vec{x},\phi\right)\right| - \min_\phi\left(\left|I_l\left(\vec{x},\phi\right)\right|\right)}{\int_{-\pi/2}^{\pi/2}\left|I_l\left(\vec{x},\phi'\right)\right| d\phi' - \pi\min_\phi\left(\left|I_l\left(\vec{x},\phi\right)\right|\right)}\right) I_l\left(\vec{x}\right). \tag{6.4}$$

$\tilde{I}_l\left(\vec{x},\phi\right)$ can be interpreted as the expected density of localizations in channel l at position $\vec{x}$ belonging to molecules in filaments with local orientation ϕ. The subtraction of the minimum corrects for the non-zero response given by the filters $\Phi\left(\vec{x};\phi\right)$ for orientations that do not correspond to the orientations of the filaments at $\vec{x}$.

For three-dimensional images, the three-dimensional orientation can be analyzed in a similar manner, see e.g. [146]. The generalization of the normalization in Eq. 6.4 for three-dimensional orientation space representation involves normalization over solid angles. However, the orientation difference can always be expressed as a single angle.

6.2.2. CO-ORIENTATION ANALYSIS

The next step in the analysis is to define a measure that quantifies both the co-localization and orientational alignment of structures in the two color channels. For this purpose we extend the concept of the cross-correlation function used in localization microscopy[65] to the generalized cross-correlation function:

$$c\left(\Delta\vec{x},\Delta\phi\right)=\pi\frac{\left\langle\tilde{I}_1\left(\vec{x},\phi\right)\tilde{I}_2\left(\vec{x}+\Delta\vec{x},\phi+\Delta\phi\right)\right\rangle}{\langle I_1\rangle\langle I_2\rangle}, \tag{6.5}$$

where $\langle.\rangle$ denotes the averaging operation over both $\vec{x}$ and ϕ. The averaging over the spatial coordinate $\vec{x}$ is restricted to the selected region of interest, which typically excludes regions outside cells. The multiplication with π gives $c\left(\Delta\vec{x},\Delta\phi\right)=1$ for statistically independent images. Often it will be convenient to compute the average of $c\left(\Delta\vec{x},\Delta\phi\right)$ over circles of constant distance $|\Delta\vec{x}|=r$, which we will denote with $c\left(r,\Delta\phi\right)$. An illustration of the steps needed to compute $c\left(\Delta\vec{x},\Delta\phi\right)$ from the superresolution images is shown in Fig. 6.1.

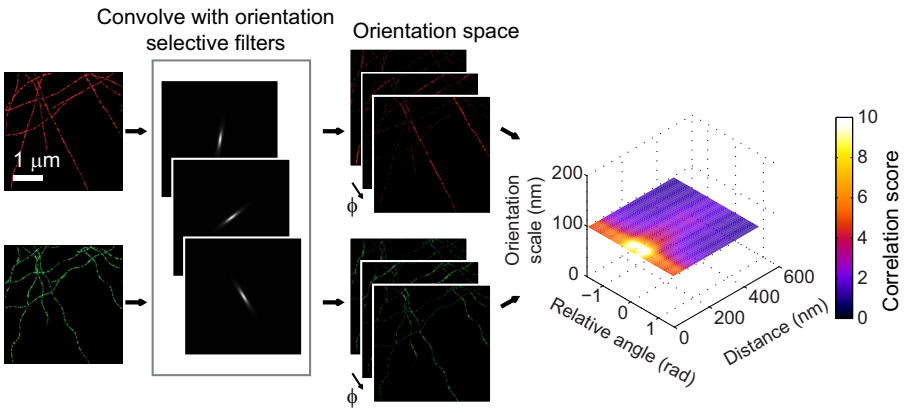

Figure 6.1: **Steps for obtaining the co-orientation plot.** To compute the co-orientation plot, the images in both color channels are first processed by a filter bank of orientation selective filters (shown here for an orientation scale of 100 nm). This provides orientation space representations of both channels with the evidence per orientation in each pixel. The cross-correlation between these representations then leads to the co-orientation plot showing the correlation c as a function of the distance between localizations and angle between the filaments they belong to.

The cross-correlation in $c\left(\Delta\vec{x},\Delta\phi\right)$ is efficiently computed using three-dimensional (x,y,ϕ) Fourier transformations:

$$c=\pi\frac{\mathrm{FT}^{-1}\left(\mathrm{FT}\left(\tilde{I}_1\right)\mathrm{FT}\left(\tilde{I}_2\right)^*\right)}{\langle I_1\rangle\langle I_2\rangle\,\mathrm{FT}^{-1}\left(|\mathrm{FT}\left(W\right)|^2\right)}, \tag{6.6}$$

where W is a two-dimensional binary mask image that has a value of 1 inside the selected region of interest and 0 outside.

The interpretation of $c(r,\Delta\phi)$ is as follows: for a typical point on a filament in one channel, it is the density of filaments in the other channel at a distance r with a relative orientation (i.e. angle with the first filament) of ϕ which is normalized by the density that would have been obtained if the filaments were statistically independent. Alternatively, it could also be interpreted as a normalized probability density for two randomly chosen points on two filaments in different color channels to have a separation r and an orientation difference ϕ between the filaments they belong to.

6.2.3. TESTING FOR STATISTICAL SIGNIFICANCE

A measure for the strength of the co-orientation in an image is given by the normalized anisotropic Ripley's K statistic $K_{\parallel}(R)$, which is computed as:

$$K_{\parallel}(R) = \frac{1}{\pi R^2}\frac{2}{\pi}\int_A\int_{-\pi/2}^{\pi/2} d^2\Delta x\, d\Delta\phi\, c\left(\Delta\vec{x},\Delta\phi\right)\cos\left(2\Delta\phi\right), \tag{6.7}$$

where A denotes a circular domain with radius R. The rationale for choosing a $\cos\left(2\Delta\phi\right)$ weight is the following: assuming that $c\left(\Delta\vec{x},\phi\right)$ is symmetric with respect to $\Delta\phi$, this weight returns the strength of the second nonzero term of a Fourier series expansion of $c\left(\Delta\vec{x},\phi\right)$. Therefore it expresses to first order the tendency of $c\left(\Delta\vec{x},\phi\right)$ to assume higher values for smaller angles $\Delta\phi$. Filaments with relative smaller angles contribute positively to $K_{\parallel}(R)$ whereas perpendicularly crossing filaments have a negative contribution. The first term in the same Fourier series expansion of $c\left(\Delta\vec{x},\phi\right)$ has a constant weight with respect to $\Delta\phi$ and thus gives a result that is proportional to Ripley's K statistic and expresses co-localization rather than co-orientation. The higher order terms in the Fourier series expansion could be used to describe more complicated relationships between the co-localization and orientations of filaments.

The anisotropic Ripley's K statistic $K_{\parallel}(R)$ was used to test the statistical significance of the co-orientation of individual images. The radius R is chosen beforehand by the experimenter and expresses the range of the co-orientation effect. In theory, all possible radii R could be relevant and could all be tested, while keeping in mind that tests at different radii are not statistically independent. However, in practice this is unnecessarily complicated and a single radius R can be set such that the main peak in the co-orientation plot at small distances r is captured in the significance test. Alternatively, prior expectations about the range of physically meaningful effects can also be used to determine a single value of R for testing.

The null hypothesis for the significance test is that the filaments in both color channels do not interact and are thus statistically independent, which implies that the expected value of $K_{\parallel}(R)$ is 0. The expected deviations from 0 under the null hypothesis are very difficult to treat analytically due to the statistical dependencies between the localizations in each color channel[147]. These dependencies arise firstly because the localized molecules are constrained in their positions because they reside in filaments and secondly because each molecule is localized multiple times. Therefore we assume as a working assumption that under the null hypothesis, $K_{\parallel}(R)$ is normally distributed with a mean value of 0 and variance σ_K^2, which was estimated as follows. Firstly, a circular region of interest is selected in the images. Next, the im-

age of the second color channel is rotated with respect to the image of the first color channel over equally spaced angles θ between 0 and 2π. Note that the ROI was chosen to be circular in order to ensure that the sum of pixel values in each channel does not change with the rotation. For each rotation we recomputed $K_{\parallel}(R)$, giving the co-orientation strength per rotation $K_{\parallel}(R;\theta)$. The variance σ_K^2 was then computed as:

$$\sigma_K^2 = \left(\frac{1}{n_\theta} \sum_\theta K_{\parallel}(R;\theta) \right)^2 + \frac{1}{2n_\theta} \sum_\theta \left(K_{\parallel}(R;\theta) - K_{\parallel}(R;-\theta) \right)^2, \tag{6.8}$$

where n_θ is the number of angles θ (see section 6.A.1 for a derivation). Given σ_K^2, the probability of having a value $K_{\parallel}(R)$ at $\theta = 0$ under the null hypothesis is given by

$$P = \frac{1}{2} \left(1 + \mathrm{erf}\left(\frac{K_{\parallel}(R)}{\sigma_K \sqrt{2}} \right) \right), \tag{6.9}$$

where erf(.) denotes the error function.

Note that our method resembles the approach of Van Steensel et al. [148] for qualitatively determining if the co-localization in diffraction limited fluorescence imaging may be significant. In this approach the image in one color channel is shifted instead of rotated. Furthermore, it is important to note that σ_K^2 does not accurately predict the uncertainty in $K_{\parallel}(R)$ if the null hypothesis does not hold. Therefore it cannot be used to test differences in co-orientation strength between images. Instead, sets of values for $K_{\parallel}(R)$ obtained from several datasets representing one biological condition can be compared with another set of values representing another condition using standard statistical tests such as the Mann-Whitney U test [149].

6.2.4. LOCAL CO-ORIENTATION

In order to detect which parts of a region of interest exhibit the strongest co-orientation, we developed a scheme for visualizing the local co-orientation strength. In this scheme we determine $K_{\parallel}(R)$ in square subregions of the image with a size of $3R$ which were displaced by multiples of R horizontally or vertically with respect to each other, i.e. two-thirds of the pixels in each region overlapped with two-thirds of the pixels in each adjacent region. For each subregion, we took the previously determined orientation space representations $\tilde{I}_l(\vec{x},\phi)$ and used it to compute $c(\Delta\vec{x},\Delta\phi)$, where the average densities $\langle I_l \rangle$ across the field of view were used in the denominator rather than the averages per subregion. $K_{\parallel}(R)$ then follows from $c(\Delta\vec{x},\Delta\phi)$ as before.

To ensure a smooth visualization, the values of $K_{\parallel}(R)$ were assigned to the center point of each subregion and linearly interpolated in between these points. A visualization of the local co-orientation was then obtained by applying a blue overlay to the image of the filaments, where the negative pixel values were set to 0, the brightest 3% of the pixels were clipped and the remaining pixels were linearly scaled between 0 and 255.

Note that in this visualization scheme, crossings of filaments lead to a low score for the local co-orientation strength which may be unintuitive in some cases. Instead, it is also possible to replace the $\cos(2\phi)$ weight in the computation of $K_{\parallel}(R)$ in Eq. 6.7

by a $\cos^2(\phi)$ weight. However, unlike with the $\cos(2\phi)$ weighting, the $\cos^2(\phi)$ weighting also makes the score sensitive to mere co-localization without orientational alignment. Therefore it is generally best to compare images with both kinds of weighting for identifying areas with strong co-orientation.

A somewhat computationally faster method to approximate the local co-orientation strength can be implemented using convolution operations. Specifically, the orientation space representation $\tilde{I}_1$ has to be convolved with a kernel $g(\vec{x},\phi) = \cos(2\phi)\, O(\vec{x}/R)$, subsequently multiplied by $\tilde{I}_2$ and summed over ϕ, followed by a smoothing with a kernel $O(\vec{x}/3R)$ and finally a multiplication by a normalization constant. Here the circular kernel $O(\vec{x}) = 1$ if $|\vec{x}| < 1$ and 0 otherwise.

6.2.5. SIMULATIONS OF TEST DATA

Simulated localization microscopy images in two color channels were obtained in two steps. Firstly, two-dimensional images of filaments were generated for both color channels. Secondly, positions of fluorescent molecules are generated and several localizations of each of these fluorophores were simulated.

The filaments in one color channel were generated according to the two-dimensional wormlike chain model of Kratky and Porod [102]: All filaments consisted of 10^4 connected segments of 1 nm. The position of the central segment was randomly positioned within a circular region with a radius of $FOV\sqrt{2} + L/2$, where $FOV = 4\,\mu$m is the size of the field of view for the final image and L is the length of the filament. This circular region was deliberately chosen to be large enough to ensure a homogeneous and anisotropic distribution of filaments within the field of view. The orientation of the central segments was chosen randomly between $-\pi$ and π. Angles between subsequent segments of the filament were taken from a normal distribution with standard deviation 1 nm$/\xi$, where ξ is the persistence length of the filament. The filaments in the second color channel were obtained in various manners: firstly by displacing each filament in the first channel over a fixed distance perpendicular to its orientation; secondly by independently simulating them in the same way as the filaments in the first channel but with a different persistence length; thirdly by displacing each segment perpendicular to their orientation with a sinusoidally modulated magnitude of the displacement such that the filaments in the second channel appeared to be twisted around those in the first channel. Finally, image representations of the filaments were made by counting the number of connecting points between segments in pixel bins of 5 nm in size, and convolving the resulting images with a Gaussian kernel with a full width at half maximum $FWHM = 5$ nm to account for the finite width of the filaments.

Subsequently, localization datasets were simulated from the images of the filaments. A Poisson distributed number of N fluorophores was obtained with a relative density proportional to the pixel values in the filament images. The positions of these fluorophores were then displaced with a Gaussian probability density with $FWHM = 5$ nm to account for the size of the antibodies linked to the fluorophores. Each fluorophore was then assigned a random number of localizations M defined as the minimum of two quantities: $M_{poisson}$ and M_{geo} drawn from a Poisson distribu-

tion with an expected value of 25 and a geometric distribution with an expected value of 11 respectively. Localizations were then finally displaced with a Gaussian probability density with standard deviation σ, where a different value of σ was randomly generated for each localization based on the expression in Equation 4 in Ref. [20, 133] and using the following values: the number of signal photons per localization n_{ph} (drawn from a geometric distribution with an expected value of 2000), background photons b (average of 9×9 Poisson distributed values with expected value of 1), and the PSF width σ_a (Gaussian distributed with mean $0.3 \times \lambda / NA = 0.3 \times 670/1.45 \approx 1.38$ and standard deviation of 2% of the mean; this is roughly the distribution we obtain when fitting the PSF of Alexa Fluor 647 fluorophores and is in agreement with the range of previously suggested values[14]). All images in which the simulated datasets are visualized were obtained by rendering visualizations as Gaussian blobs with a kernel size equal to σ.

6.2.6. ACQUISITION AND PROCESSING OF EXPERIMENTAL DATA

SAMPLE PREPARATION

Primary human umbilical vein endothelial cells (HUVECs) were purchased from Lonza and cultured on fibronectin (Sanquin)-coated dishes in EGM-2 medium, supplemented with SingleQuots (Lonza) at 37°C and under 5% CO_2 until passage 8. To stain vimentin and tubulin, HUVEC cells were grown for 24 hours on cleaned #1.5 coverslips in Medium 200 (Life technologies) with the addition of Low Serum Growth Supplement (LSGS) (Life technologies) at 5%.

Immortalized Human Vascular Endothelial Cells (EC-RF24)[150] were grown in a mixture of HUVEC cell medium, 25% DMEM and 25% RPMI. NIH-3T3 mouse fibroblasts were maintained in DMEM supplemented with 10% fetal calf serum (FCS) as previously described[151]. The cells then were fixed with 10% MeS buffer (100 mM MeS, pH 6.9, 1mM EGTA and 1mM $MgCl_2$) and 90% methanol for 5 minutes on ice. After blocking with 5% Bovine Serum Albumin (BSA) for 1 hour, HUVEC and EC-RF24 cells were incubated with rabbit anti-tubulin polyclonal antibodies (Abcam) and mouse anti-vimentin monoclonal antibodies (Clone V9-Dako) for 1 hour. NIH-3T3 mouse fibroblasts were stained with anti-tubulin antibody raised in mouse (Sigma-Aldrich) and rabbit monoclonal antibody against vimentin (GeneTex). Subsequently all the cells were incubated with goat anti-rabbit and goat anti-mouse antibodies (Alexa 488, Alexa 647, Invitrogen) for 30 minutes. All the fixation and staining steps were done at room temperature. Control experiments were also performed where the fluorophore types labeling the secondary antibodies were swapped to rule out color-related artefacts.

In the case of actin and keratin, primary keratinocytes isolated from newborn (1-3 day old) plectin deficient mice were kindly provided by Prof. Sonnenberg (NKI, Amsterdam, the Netherlands)[152]. Glutaraldehyde fixation was used to preserve both keratin and actin structure. Briefly, this fixation consisted of a first incubation step in 0.3% glutaraldehyde + 0.25% Triton in cytoskeleton buffer (10 mM MES pH 6.1, 150 mM NaCl, 5 mM EGTA, 5 mM glucose, and 5 mM $MgCl_2$) for 2 min. and a second step with 0.5% glutaraldehyde in the same buffer for 10 min. Subsequently, the sam-

ple was treated with freshly made 0.1% $NaBH_4$ in PBS. After fixation, samples were extensively washed with PBS and blocked with 5% BSA for 40 minutes. Staining was performed with rabbit anti-keratin 14 polyclonal antibody (Covance) and Phalloidin conjugated to Alexa Fluor 488 fluorophores (Invitrogen). Samples were incubated with a goat anti-rabbit secondary antibody labeled with Alexa Fluor 647 fluorophores (Invitrogen) afterwards. All the steps were performed at room temperature. Control experiments were also performed where the Phalloidin was labeled with Alexa Fluor 647 and the goat anti-rabbit antibodies with Alexa Fluor 488 to rule out color-related artefacts.

MICROSCOPE

Samples were imaged on a Leica SR-GSD microscope (Leica Microsystems, Wetzlar, Germany) equipped with 488 nm/300 mW, 532 nm/500 mW and 647 nm/500 mW lasers and an EMCCD camera (Ixon DU-897, Andor). A 160x oil immersion objective was used. Coverslips were mounted in a holder (Chamlide CMB, Korea) with 500 μL consisting of PBS, merceptoethylamine (MEA, 50 mM) and newly developed oxygen scavenging system consisting of Oxyrase (OXYRASE Inc, Mansfield, Ohio, U.S.A, 3%) and lactate (20%) in PBS. Details will be described elsewhere. Before imaging, a waiting time of 30 min. was observed to allow the sample to stabilize and avoid initial drift. Images were then taken in TIRF mode at 100 frames per second with image sizes of 180 × 180 or 400 × 400 pixels; the backprojected pixel size was 100 nm. For all datasets, images with 642 nm illumination were acquired first.

LOCALIZATION ANALYSIS OF EXPERIMENTAL DATA

The acquired movies were processed by estimating fluorophores' positions using a fast algorithm[15] on a Quadro 5000 GPU (NVIDIA). The method for finding candidate regions of interest for position estimation has been documented in the literature[36]. Localizations corresponding to the same activation event were subsequently combined by grouping spatially nearby localizations (i.e. less than three times the sum of the localizations' precisions apart) in subsequent frames into single localization events. The center position of the grouped localizations was determined as the weighted average of the localizations with the inverse of the squared localization precisions as weights. Localizations were then filtered based on the number of signal photons per localization event and the PSF width. Subsequently, localizations were corrected for lateral stage drift using frame-by-frame cross-correlation, as documented elsewhere[27, 31]. All images in which the experimentally obtained localizations are visualized were obtained by rendering visualizations as Gaussian blobs with a kernel size equal to the estimated localization precision. Pixels whose values were in the highest 2% (5% for Fig. 6.6e) of all non-zero pixels were clipped to obtain sufficient contrast for display, and subsequently all intensities were linearly stretched between 0 and 255.

Color channel registration Localizations of the Alexa Fluor 647 fluorophore (red) channel were mapped onto the Alexa Fluor 488 fluorophore (green) channel using

affine mapping. This mapping was estimated in a least squares estimation procedure with 8 different datasets of (in total 448) fluorescent beads visible in both color channels. Briefly, 100 nm TetraSpeck microspheres (T7284 blue green orange and dark red, Life Technologies) were diluted to a ratio of 1:100 and dried on ultraclean coverslip. The bead-dried coverslips were mounted on the microscope with 500 μL of MQ water and imaged on 8 different fields of view where beads were well separated. The beads were localized using the same algorithm as above. The target registration error of this mapping procedure was determined to be 16 nm (by leaving one of the recordings at a time out when computing the mapping so that it can be independently used to assess the error)[153].

6.3. RESULTS

6.3.1. SIMULATED DATASETS

To demonstrate the proposed co-orientation measurement method, we simulated two-color localization microscopy datasets of samples with filament networks in both channels with a well-defined relationship between them. As a first example, we used a sample with 200 filaments with a persistence length $\xi = 5$ μm in the red color channel, labeled with 10^4 fluorophores in total; each of these filaments was accompanied by a filament in the green color channel at a fixed distance of 50 nm. This resulted in the dataset shown in Fig. 6.2a, and the corresponding co-orientation plot of the generalized cross-correlation function $c(r, \Delta\phi)$ in Fig. 6.2b (for a scale s_o = 200 nm for the orientation analysis). The plot shows the distance r between the localizations in both color channels on the vertical axis and the orientation difference ϕ between the filaments to which those localizations belong on the horizontal axis. The plot shows a clear peak at distance of approximately 50 nm and an orientation difference close to 0, confirming that filaments are accompanied by another filament at a distance of 50 nm in the other color channel. The enhanced correlation for larger angles ϕ is caused by the finite size of the orientation selective filters: when filaments cross or come in close proximity to each other, the filters give a non-zero response for orientations other than those of the filaments themselves. For larger distances $r > 200$ nm, $c(r, \phi)$ decays to a value of 1, meaning that filaments at those distances apart appear statistically independent from each other.

As a second in-silico example, we used a sample in which there was no relationship between the filaments in both color channels. Unlike the previous example, the filaments in the green channel were now independently generated, but with a persistence length $\xi = 1$ μm. A representative example of a result under this condition (out of $n = 500$ simulations) is visualized in Fig. 6.2c and the corresponding co-orientation plot in Fig. 6.2d. Clearly, the values of $c(r, \phi)$ in Fig. 6.2d are no longer substantially larger than 1, and there is no longer a noticeable dependence of the co-localization on the relative orientation of the filaments.

The third simulation example serves to illustrate the importance of the scale of the orientation analysis. For this example, 50 filaments labeled with 5,000 fluorophores were simulated for the red channel as before. The filaments in the red channel were

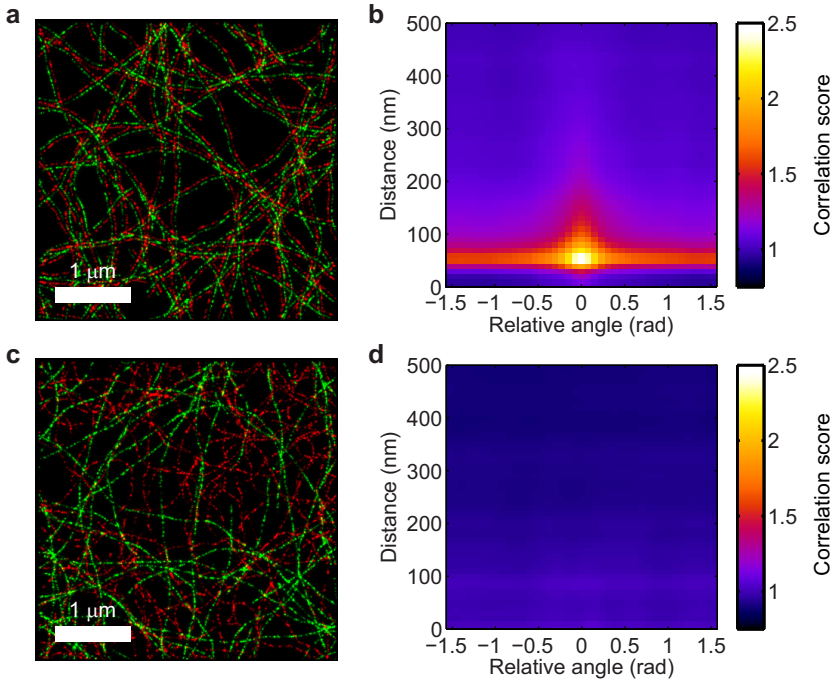

Figure 6.2: **Co-orientation plot of parallel and unrelated filaments.** (a) Simulated data of parallel filaments in two color channel channels and (b) the corresponding co-orientation plot, showing strong co-orientation at a distance of 50 nm between filaments. The co-orientation plot shows the cross-correlation between the color channels as a function of the distance between localizations in both channels (on the horizontal axis) and the difference in the orientations of the filaments those localizations belong to (on the vertical axis). (c) Simulated data of statistically independent filaments in two color channel channels and (d) the corresponding co-orientation plot, showing no substantial co-orientation.

twisted around the green filaments with a maximum separation of 50 nm and with a periodicity of one twist per 300 nm. The resulting dataset is visualized in Fig. 6.3a. Co-orientation plots for these data were computed for scales $s_o = 50$ nm and $s_o = 500$ nm for the orientation analysis, which are shown in Figs. 6.3b and 6.3c respectively. The plot for $s_o = 50$ nm shows two peaks at orientation differences of about $\pm 40°$, whereas the plot for $s_o = 500$ nm only has a single peak at $\pm 0°$. Thus these plots express how indeed the filaments in both channels display co-orientation at larger length scales, although at a shorter length scale there is a signature of the filaments crossing each other. This shows that the scale s_o of the orientation analysis can itself be used as a separate dimension for the analysis of co-orientation in an extensive co-orientation assay. The shortest length scale for which the orientation analysis could be meaningfully applied is determined by the resolution of the images[44]; at shorter length scales the data do not contain enough information about the filaments for an accurate analysis.

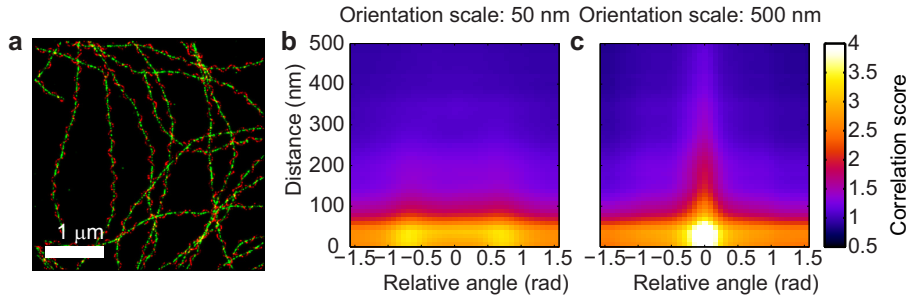

Figure 6.3: **Orientation scale as a dimension for analysis.** (a) Simulated data of filaments in the green color channel with filaments in the red channel twisted around them. (b) When the orientation is analyzed at a scale of 50 nm, the co-orientation plot shows two peaks at positive and negative angles between the filaments in both channels; (c) for a scale of 500 nm the peaks shift to the center of the plot indicating that the filaments in both channels appear to run in parallel at that scale. The smallest scale for the orientation analysis is determined by the FRC resolutions in both channels, are 34 nm (red) and 36 nm (green).

6.3.2. SIGNIFICANCE TESTING

The question that arises upon inspection of the co-orientation plots is for which values of $c\left(r,\Delta\phi\right)$ the co-orientation can be said to be statistically significant. To this end we computed the normalized anisotropic Ripley's K parameter $K_{\parallel}(R)$ with $R = 200$ nm for the simulated datasets in Fig. 6.2 to quantify the co-orientation strength. Subsequently, we applied the significance test outlined in the materials and methods section, which extracts the uncertainty in $K_{\parallel}(R)$ by rotating the image in the green channel with respect to the red channel over 49 equally spaced angles θ between 0 and 2π and recomputing $K_{\parallel}(R)$ for every rotation. The profiles of $K_{\parallel}(R)$ as a function of the rotation angle θ for the datasets in Fig. 6.2 are shown in Fig. 6.4. The dashed line in the plot indicates the minimum value of $K_{\parallel}(R)$ at $\theta = 0$ for which it would be significant at a significance level of 0.05. The value of $K_{\parallel}(R)$ for the parallel filaments in Fig. 6.2a turned out to be statistically significant ($p = 2.0 \times 10^{-37} \ll 10^{-3}$), whereas the value of $K_{\parallel}(R)$ for the unrelated filaments shown in Fig. 6.2c was not ($p = 0.079$).

We validated the proposed significance test by simulating 500 datasets where the filaments in both color channels were independent in the same manner as for the data shown in Fig. 6.2c. For each of these simulations we applied the proposed significance test and computed the p-value for the value of $K_{\parallel}(R)$ at $\theta = 0$ for $R = 200$ nm . We found that the p-values returned by the test were consistent with a uniform distribution between 0 and 1 (see Fig. 6.5): a one-sample two-sided Kolmogorov-Smirnov test revealed no significant difference at a 0.05 significance level ($p = 0.47$). This is exactly what is required, as the returned p-values should report the probability of obtaining values of $K_{\parallel}(R)$ larger than the one being tested if the null hypothesis is true. Additionally, the assumption that $K_{\parallel}(R)$ is normally distributed was not rejected in a Shapiro-Wilks test at a significance level 0.05 ($p = 0.42$). However, 38 of 500 the simulated datasets had a p-value smaller than 0.05, which is significantly more than the expected 25, indicating that the p-values obtained from the proposed significance test are not exact. This is attributed to the RMS error of 31% in the estimated stan-

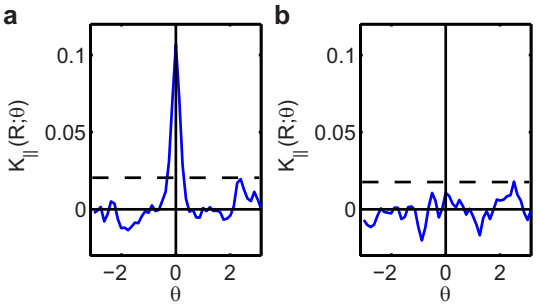

Figure 6.4: **Statistical significance test results on simulated data.** (a) The normalized anisotropic Ripley's K statistic $K_{\parallel}(R)$ quantifies the co-orientation strength. Rotation over an angle θ of the color channels in Fig. 6.2a relative to each other leads to a rapid decline of $K_{\parallel}(R)$; the residual fluctuations can be used to determine that the value $K_{\parallel}(R)$ at $\theta = 0$ exceeds the threshold for statistical significance at the 0.01 level (dashed line). (b) The same plot for the data show in Fig. 6.2c indicates that the co-orientation there is not significant for $\theta = 0$.

dard deviation of $K_{\parallel}(R)$, since the normality of $K_{\parallel}(R)$ itself was not rejected. The test can still be used though, provided that a somewhat more conservative threshold than 0.05 is chosen for the p-value.

6.3.3. APPLICATION TO EXPERIMENTAL DATA OF CYTOSKELETAL FILAMENTS

We applied the co-orientation analysis to experimental data of tubulin and vimentin and of actin and keratin. Multicolor localization microscopy images of tubulin and vimentin were obtained from primary human umbilical vein endothelial cells. Fig. 6.6a and c show two clear example results at stable cell edges, with tubulin in red and vimentin in green. The corresponding co-orientation plots in Fig. 6.6b and d confirm the strong co-orientation effect that appears to be present. The effect appears stronger in b than in d, due to the lower density of the filaments which leads to a stronger apparent bundling of the filaments. Correspondingly, the co-orientation strength parameter $K_{\parallel}(R)$ for the selected circular ROI in Fig. 6.6a is larger than that in the ROI in Fig. 6.6c, which are respectively 0.22 and 0.12 for $R = 500$ nm; in both ROIs the co-orientation is statistically significant ($p \ll 10^{-3}$). The value of $R = 500$ nm was chosen here such that the $K_{\parallel}(R)$ just incorporates the primary peak in the co-orientation plots in the analysis. The observed co-orientation could also just be seen when the co-orientation analysis was applied to the TIRF images of the cells shown in Fig. 6.6a and c. Generally though, the higher resolution of SR microscopy is much more suitable, and often will be necessary, to detect the co-orientation between these intricate filament networks. Note that the filament networks in these images show a clear preferential direction in these cells. Local deviations from these global trends could be investigated for example by filtering out the dominant filament orientations in the orientation space representations of the tubulin and vimentin images. Alternatively, the co-orientation plot could be normalized with respect to its average value at

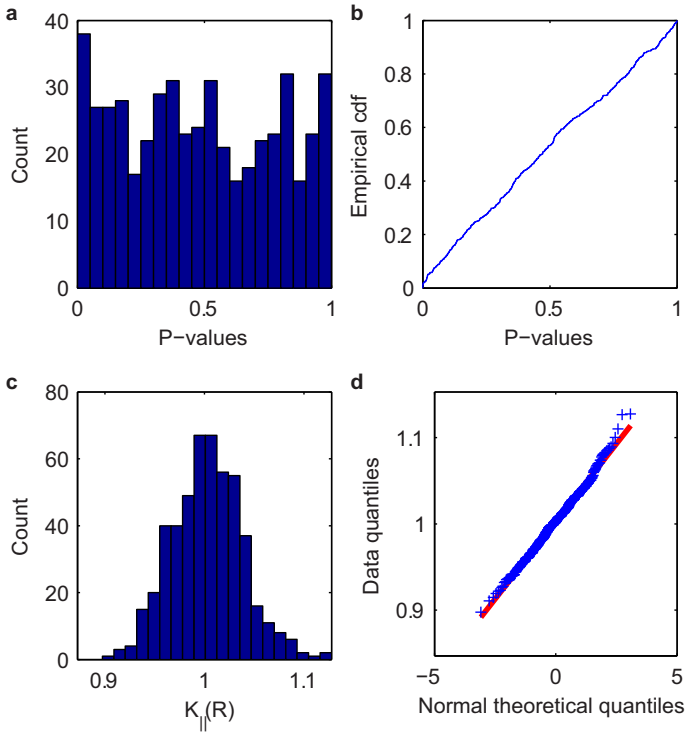

Figure 6.5: **Validation of the significance test.** Results are obtained for 500 simulated datasets generated in the same manner as Fig. 6.2c. Application of the significance test results in a uniform distribution of P-values, as evidenced by the histogram in (a) and empirical cumulative distribution function in (b). The values of $K_{\parallel}(R)$ exhibit a Gaussian distribution in the histogram in (c) and the quantile-quantile plot in (d).

each distance r in order to determine how the alignment changes with r independent of the co-localization.

The observed co-orientation between vimentin and tubulin is not a universal feature of any image showing two types of filaments. Consider for example Fig. 6.6e, which shows a localization microscopy image of actin (green) and keratin (red) obtained from plectin deficient keratinocytes. As opposed to the previous images of tubulin and vimentin, there is no apparent co-orientation between actin and keratin: the corresponding co-orientation plot in Fig. 6.6f does not exhibit a strongly peaked correlation score for small distances and small relative angles between the actin and keratin filaments. Indeed, no significant co-orientation ($p = 0.20$) was found in a statistical significance test for $R = 500$ nm ($p = 0.065$ for $R = 200$ nm).

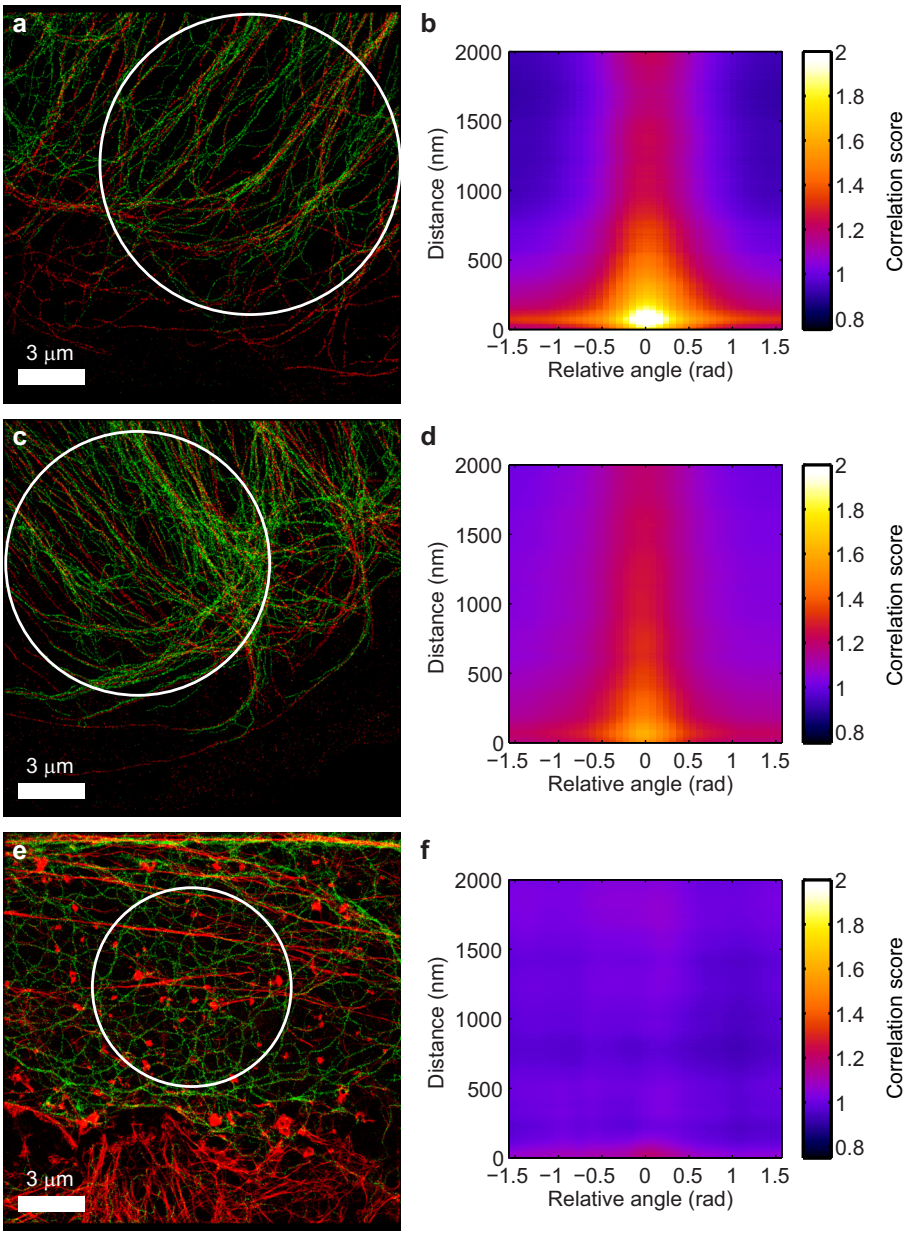

Figure 6.6: **Co-orientation analysis for experimental data of tubulin and vimentin and of actin and keratin.** (a) and (c) Localization microscopy images of tubulin (red) and vimentin (green) at stable cell edges. The co-orientation plots for the ROIs demarcated by the white circles are shown in (b) and (d), showing clear co-orientation at distances up to 500 nm (with a scale s_o = 200 nm for the orientation analysis). (e) Localization microscopy image of actin (red) and keratin (green). The co-orientation plot in (f) for the selected region of interest shows no significant co-orientation.

To visualize how the co-orientation between filaments varies across the image, we evaluated the local co-orientation strength $K_{\parallel}(R)$ in overlapping subregions of the image. The resulting values are then shown as an overlay in the blue color channel on top of the image of the filaments. Fig. 6.7 shows an example of tubulin and vimentin filaments with this overlay for different values of R, with subregion sizes equal to $3R$. The blue overlay effectively highlights regions with the strongest local co-orientation, where high densities of filaments with similar orientations are within a distance R from each other. Increasing R causes more filaments to positively contribute to $K_{\parallel}(R)$. However, it also leads to a less localized evaluation of the co-orientation strength. Regions in the image with crossing filaments exhibit lower values, because locally there is evidence both for and against orientational alignment of the tublin and vimentin. An alternative visualization method that does not give this low response with crossing filaments is demonstrated in Fig. 6.7d. In this method the $\cos(2\phi)$ weight in the computation of $K_{\parallel}(R)$ in Eq. 6.7 is replaced by a $\cos^2(\phi)$ weight. This leads to more connected regions with high values in the blue channel, but this visualization also highlights regions with mere co-localization where filaments are not aligned.

In larger images (i.e. of $18 \times 40\,\mu$m), it was apparent that co-orientation between vimentin and tubulin occurred predominantly in the periphery of the cells, whereas at the center, close to the nucleus, co-orientation appeared substantially less. When we compared the right and left half of Fig. 6.8a respectively, we found $K_{\parallel}(R) = 0.11$ ($p \ll 10^{-3}$) and $K_{\parallel}(R) = 2.9 \times 10^{-2}$ ($p \ll 10^{-3}$) respectively for $R = 200$ nm.

We next investigated whether co-orientation between tubulin and vimentin is a generic property of these filaments. We therefore compared data from HUVEC cells (Fig. 6.8b) to data obtained from NIH-3T3 fibroblasts (Fig. 6.8d), which also express both filament systems. Remarkably, little if any co-orientation was observed throughout the cell in these fibroblasts: for the ROI in Fig. 6.8d we found no statistically significant co-orientation ($K_{\parallel}(R) = 4.4 \times 10^{-2}$ and $p = 0.14$ for $R = 200$ nm). We also did not observe a difference between peripheral and more central parts of the cells. This may reflect lineage-dependency, i.e. a difference between endothelial cells and fibroblasts. We therefore also studied a cultured endothelial cell line, EC-RF24 (Fig. 6.8c). Indeed, we observed significant co-orientation ($K_{\parallel}(R) = 9.4 \times 10^{-2}$ and $p \ll 10^{-3}$ for $R = 200$ nm), but both strength and extent of colocalization appeared less than in HUVEC cell ($K_{\parallel}(R) = 0.24$ and $p \ll 10^{-3}$ for $R = 200$ nm).

These results show that our analysis methods makes it possible to quantitatively address biological co-orientation. Associations between different filament systems have recently attracted significant attention and may either indicate the existence of physical crosslinks between the filaments[154] or, perhaps, reflect deposition of intermediate filaments following their transport along microtubuli[155]. Our analysis tools will enable addressing such questions in an unbiased and quantitative manner.

6.4. DISCUSSION

In this work, we describe a framework for the quantitative analysis of co-orientation: the simultaneous co-localization and orientational alignment of structures in images.

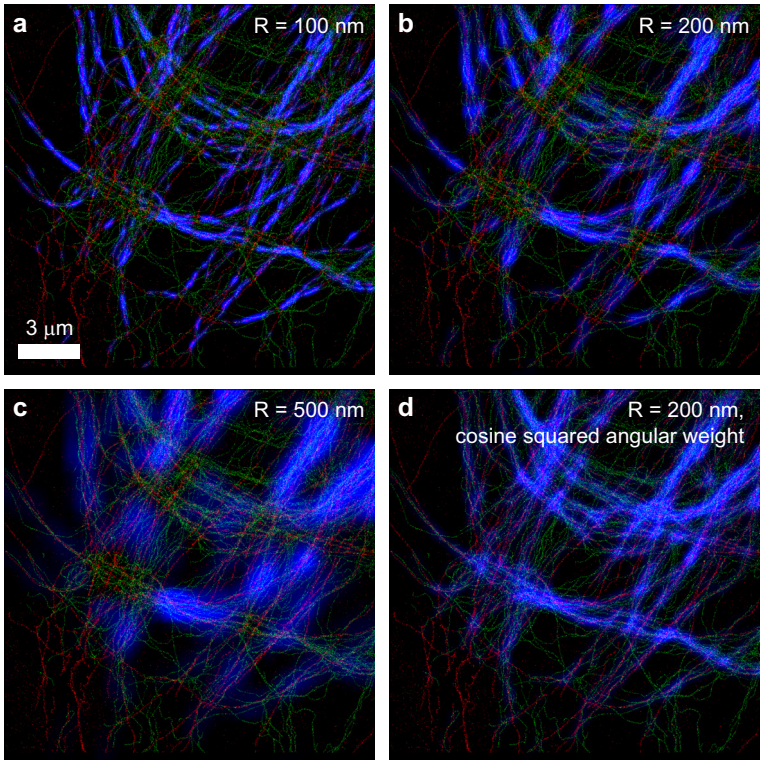

Figure 6.7: **Visualization of the local co-orientation strength.** (a-c) Localization microscopy images of tubulin (red) and vimentin (green). Blue overlays show the local co-orientation strength $K_{\parallel}(R)$ in order to highlight the regions with the strongest local co-orientation. Increasing R causes more filaments that are further apart from each other to contribute to $K_{\parallel}(R)$, but also causes $K_{\parallel}(R)$ to appear less localized. (d) The same image as (b), but with the $\cos(2\phi)$ weight in the computation of $K_{\parallel}(R)$ in Eq. 6.7 replaced by a $\cos^2(\phi)$ weight. This provides a visualization in which crossing filaments do not cancel the contributions to the local co-orientation strength of parallel filaments. However, this visualization is also sensitive to regions with mere co-localization where filaments are not aligned.

In this framework we consider generalized cross-correlation between color channels as a function of spatial separation and orientational difference of structures. Additionally we quantify the (local) co-orientation strength using an anisotropic Ripley's K parameter and use it to test the statistical significance of the co-orientation. Our co-orientation analysis sensitively and quantitatively describes spatial association between vimentin and microtubuli in HUVEC cells. Moreover, this association is cell-type specific and appears to occur predominantly in the cell periphery.

Although the results presented in this manuscript are obtained using simulated and experimental localization microscopy datasets, the methods proposed here can be analogously applied to data obtained with other superresolution microscopy techniques as well as widefield and confocal microscopy data if the resolving power is

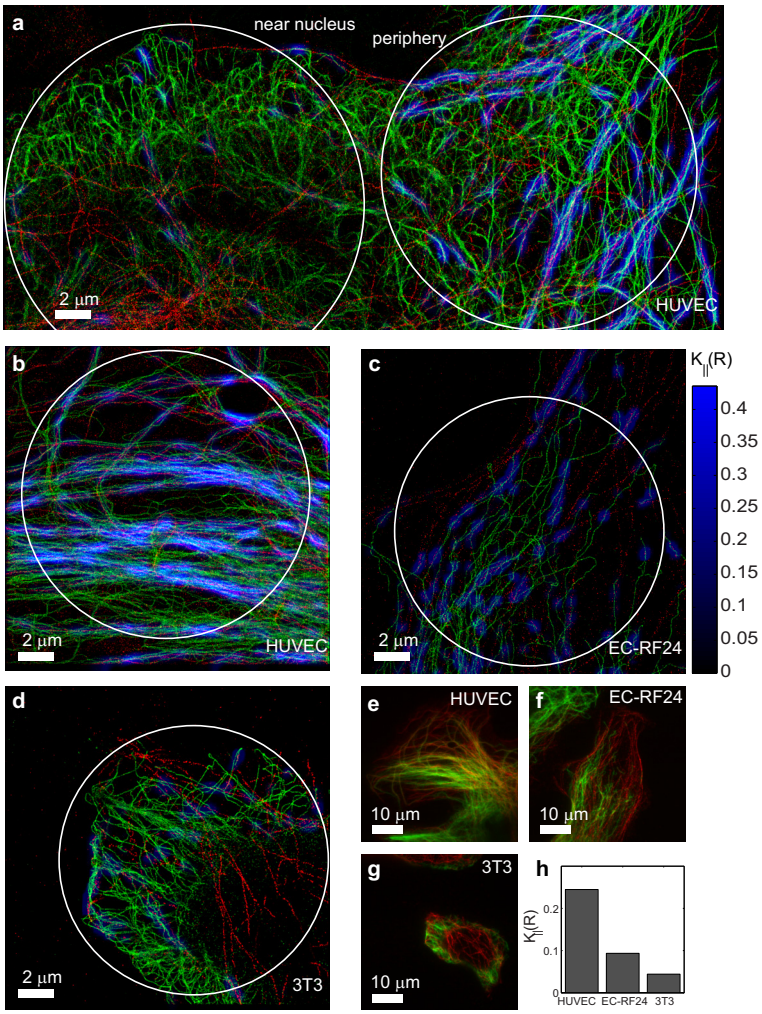

Figure 6.8: **Co-orientation strength in endothelial and fibroblast cells.** Localization microscopy images of tubulin (red) and vimentin (green) in various cell types. (a) Large SR image of a HUVEC cell, showing that co-orientation is predominantly observed in the peripheral parts (right), and not near the nucleus (left). (b-d) Higher magnifications of comparable peripheral parts of (b) a HUVEC cell showing extensive co-orientation, (c) a EC-RF24 endothelial cell with less, but still significant co-orientation, and (d) a NIH-3T3 fibroblast as an example of a cell-type with very little co-orientation. (e-g) TIRF images corresponding to b, c and d and (h) quantification of the co-orientation strength for the circular ROIs in these three examples for $R = 200$ nm.

appropriate for distinguishing the structures (e.g. filaments) in those images.

The co-orientation measurement is affected to some extent by experimental factors such as autofluorescence and background fluorescence from out-of-focus structures, apparent blurring of structures by the imaging system (e.g. due to diffraction

or localization error), cross-talk between color channels, noise, and stochasticity in the fluorescent labeling (see section 6.A.2 for a detailed discussion). Particularly the localization error in localization microscopy and analogously the point-spread function in other microscopy techniques may have substantial effects on the measurement outcomes. Firstly, they will lead to a change in the effective scale at which the orientation of filaments is assessed. Secondly, they smear out the generalized cross-correlation function $c\left(\Delta\vec{x},\Delta\phi\right)$, causing the peaks in the co-orientation plot to decrease in magnitude and shift to larger values of the distance between filaments.

There are several practical aspects that merit attention when interpreting the outcome of the orientation measurement and significance test. Firstly, it is important to note that the measured co-orientation strength $K_{\parallel}(R)$ may decrease if the density of co-oriented filaments in the field of view increases. This merits attention when comparing the measurement outcomes for different cells or cell lines if their filament densities are not similar. The co-orientation measurement could be made less sensitive by changing the average values per channel in the denominator of $c\left(\Delta\vec{x},\Delta\phi\right)$ into the root-mean-square values; however, this normalization has the important disadvantage of being sensitive to changes in noise levels, density of fluorescent labels on the filaments, or localization precision.

Secondly, the density of filaments also affects the validity of the significance testing method. Its derivation assumes a Gaussian distribution of $K_{\parallel}(R)$ under the null hypothesis, which may not hold if the number of filaments in the field of view is small. Furthermore, the accuracy with which the standard deviation of $K_{\parallel}(R)$ is estimated under the null hypothesis also depends on the number of filaments in the field of view. Therefore it is recommended to consider a more conservative significance level than 0.05 when testing for statistical significance. Also, care should be taken with strong co-localization in the absence of co-orientation, as it violates the assumption of rotation invariance under the null hypothesis that is built into the test.

Thirdly, if no statistically significant co-orientation is detected, this does not imply that no co-orientation effect is present. The likelihood of successfully detecting co-orientation depends on how different the co-orientation effect appears from random variations in the proximity and alignment of unrelated filaments. Stronger co-localization or alignment therefore increase the detection probability. In addition, the detection probability will be higher for larger numbers of filaments as random variations tend to average out more. Of course, imaging more samples will increase the probability of detection as well, provided that a suitable procedure for simultaneously performing multiple significance tests is used (e.g. false discovery rate control).

The visualization schemes that were proposed either underemphasize co-orientation in regions with crossing filaments or overemphasize regions where co-localization with little orientational alignment is present. These visualization schemes may be improved in several ways. Firstly, a method for detecting regions with crossing filaments in both color channels could identify where each scheme is most appropriate. This could be achieved by a crossing detector per color channel and then feeding the output into a co-localization measure. Secondly, higher order terms in the Fourier series expansion of $c\left(\Delta\vec{x},\Delta\phi\right)$ could be used to describe the local geometry in regions

with crossing filaments. For example, the term with $\cos(4\phi)$ rather than $\cos(2\phi)$ expresses co-orientation between a filament in one channel and one of two orthogonal filaments in the other channel.

Finally, the quantitative approach presented in this manuscript was specifically focused on the analysis of co-orientation, i.e. the combination of co-localization of filaments and the alignment in their orientations. However, the quantitative framework presented here can be applied more generally to the analysis of co-localization in conjunction with other geometric properties, such as the curvature or length of filaments or diameter of filament bundles. The analysis would then entail the computation of the cross-correlation between color channels as a function of these geometric properties, possibly at multiple measurement scales. Deriving a scalar metric for the magnitude of the observed effect similar to $K_{\parallel}(R)$ then allows for the assessment of the local effect size and testing of its statistical significance. Approaches such as these will be of great use for exploiting the wealth of information provided by super-resolution microscopy images for studying the spatial arrangements of cytoskeletal filaments and associated proteins relative to each other.

6.A. APPENDIX

6.A.1. DERIVATION OF THE PROPOSED SIGNIFICANCE TEST

In this subsection we provide a justification for the significance testing procedure described in the main text. The first assumption that is made is that $K_{\parallel}(R)$ follows a Gaussian distribution. This is an hypothesis based on the idea that the images I_1 and I_2 are actually sums of images of filaments. These filaments therefore all contribute to $K_{\parallel}(R)$ in an additive manner, if we assume that the average density per channel is more or less fixed. Assuming then that the contribution of each filament has a well-defined mean and variance and that positions and orientations of filaments that are far apart are only weakly correlated, we can invoke the central limit theorem which describes that the distribution of $K_{\parallel}(R)$ should tend towards a Gaussian distribution.

The task is then to estimate the variance of $K_{\parallel}(R)$, assuming that the null hypothesis that the filamens in both color channels are unrelated is true. This assumption can be used because the significance test determines the probability under the null hypothesis of finding an outcome for $K_{\parallel}(R)$ that is at least as extreme as the current value. Now suppose that we have measured $K_{\parallel}(R;\theta)$ for several equally spaced angles θ between 0 and 2π. We know that under the null hypothesis, the expected value for $K_{\parallel}(R)$ is 0.

The variance of $K_{\parallel}(R;\theta=0)$ can be expressed as:

$$\mathrm{Var}\left(K_{\parallel}(R;\theta=0)\right) = \frac{1}{n_\theta}\sum_\theta \mathrm{Var}\left(K_{\parallel}(R;\theta)\right) = \frac{1}{n_\theta}\sum_\theta \left\langle K_{\parallel}(R;\theta)^2\right\rangle, \tag{6.10}$$

since rotations of one color channel by an angle θ should not affect any expectation values under the null hypothesis: rotating one of the channels still leaves two independent images. Note that the notation $\langle . \rangle$ denotes the expected value here instead of the averaging operation. The discrete angle Fourier transform of $K_{\parallel}(R;\theta)$ is defined as:

$$\hat{K}_{\parallel}\left(R;q_\theta\right) \equiv \sum_\theta K_{\parallel}(R;\theta)\exp\left(-iq_\theta\theta\right) \tag{6.11}$$

By applying Parseval's theorem, we find that:

$$\left\langle K_{\parallel}(R;\theta=0)^2\right\rangle = \left\langle \frac{1}{n_\theta^2}\hat{K}_{\parallel}\left(R;q_\theta=0\right)^2\right\rangle + \left\langle \frac{1}{n_\theta^2}\sum_{q_\theta\neq 0}\mathrm{Re}\left(\hat{K}_{\parallel}\left(R;q_\theta\right)\right)^2 + \mathrm{Im}\left(\hat{K}_{\parallel}\left(R;q_\theta\right)\right)^2\right\rangle, \tag{6.12}$$

where Re(.) and Im(.) denote the real and imaginary part of a complex number respectively. By definition we have that,

$$\frac{1}{n_\theta}\hat{K}_{\parallel}\left(R;q_\theta=0\right) = \frac{1}{n_\theta}\sum_\theta K_{\parallel}(R;\theta). \tag{6.13}$$

The next step now to realize that because of the invariance of the statistics with respect to rotation of one channel by an angle $\Delta\theta$, we find that the distribution of $K_{\parallel}(R;\theta)$ is the same as that of $K_{\parallel}(R;\theta+\Delta\theta)$. This in turn implies that also $\hat{K}_{\parallel}\left(R;q_\theta\right)$

and $\hat{K}_{\parallel}\left(R;q_\theta\right)\exp\left(-i\Delta\theta\right)$ are identically distributed, and by extension also that $\mathrm{Re}\left(\hat{K}_{\parallel}\left(R;q_\theta\right)\right)$ and $\mathrm{Im}\left(\hat{K}_{\parallel}\left(R;q_\theta\right)\right)$ are identically distributed. Therefore:

$$\begin{aligned}\left\langle K_{\parallel}\left(R;\theta=0\right)^2\right\rangle &= \left\langle\left(\frac{1}{n_\theta}\sum_\theta K_{\parallel}\left(R;\theta\right)\right)^2\right\rangle + \left\langle\frac{2}{n_\theta^2}\sum_{q_\theta\neq 0}\mathrm{Im}\left(\hat{K}_{\parallel}\left(R;q_\theta\right)\right)^2\right\rangle \\ &= \left\langle\left(\frac{1}{n_\theta}\sum_\theta K_{\parallel}\left(R;\theta\right)-1\right)^2\right\rangle \\ &+ \left\langle\frac{1}{2n_\theta}\sum_\theta\left(\frac{1}{2}K_{\parallel}\left(R;\theta\right)-\frac{1}{2}K_{\parallel}\left(R;-\theta\right)\right)^2\right\rangle. \end{aligned} \tag{6.14}$$

This shows that σ_K^2 is an unbiased estimator of the variance of $K_{\parallel}\left(R;\theta=0\right)$ if it is defined as:

$$\sigma_K^2=\left(\frac{1}{n_\theta}\sum_\theta\left(K_{\parallel}\left(R;\theta\right)-1\right)\right)^2+\frac{1}{2n_\theta}\sum_\theta\left(K_{\parallel}\left(R;\theta\right)-K_{\parallel}\left(R;-\theta\right)\right)^2. \tag{6.15}$$

The rationale for looking only at the imaginary part of $\hat{K}_{\parallel}\left(R;q_\theta\right)$ is that true co-orientation effects are expected to be symmetric with respect to positive and negative rotation angles θ. Therefore, if the null hypothesis is false, this estimate of the variance will be lower and thus make rejection of the null hypothesis using this test more likely.

6.A.2. INFLUENCE OF EXPERIMENTAL FACTORS ON THE CO-ORIENTATION MEASUREMENT

The following sections provide a brief discussion of the most important experimental factors that affect the outcome of the co-orientation measurement. To make the discussion applicable, we will discuss both the effects that play a role in localization microscopy, as well as the analogous effects in microscopy methods that do not rely on stochastically activated or switching fluorophores. The latter will be referred to as deterministic microscopy techniques, and include among others widefield microscopy, confocal microscopy, stimulated emission depletion (STED)[45, 138], and structured illumination microscopy (SIM)[71, 156].

BACKGROUND

Background intensities in deterministic microscopy tend to result from out of focus structures and therefore typically do not possess much fine detail. Similarly, in localization microscopy the localizations due to this background do not show much small scale variation. Consequently, the effect of these on the orientation measurement will be limited as low spatial frequencies associated with large scale variations are suppressed by the orientation selective filters $\hat{\Phi}\left(\vec{q};\phi\right)$.

The primary effect of the background then is to increase the average values of the images I_1 and I_2. If we assume that the background is uncorrelated to the signal

intensities I_1 and I_2 and we denote the background intensities in channels 1 and 2 with b_1 and b_2 respectively, then we find that the result is that:

$$c\left(\Delta\vec{x},\Delta\phi\right) \rightarrow 1+\left(c\left(\Delta\vec{x},\Delta\phi\right)-1\right)\left(\frac{\langle I_1\rangle}{\langle b_1\rangle+\langle I_1\rangle}\right)\left(\frac{\langle I_2\rangle}{\langle b_2\rangle+\langle I_2\rangle}\right) \tag{6.16}$$

POINT SPREAD FUNCTION AND LOCALIZATION ERROR

The localization error, and analogously also the point spread function for deterministic microscopy, has a double effect when it comes to orientation analysis.

Firstly, the effective scale at which the orientation is analyzed changes. Suppose for a moment that the image I corresponds to an object ψ. If the point spread function $h\left(\vec{x}\right)$ is approximated with a two-dimensional Gaussian function with standard deviation σ, then the expected Fourier transform of the image I can be written as:

$$\left\langle \hat{I}\left(\vec{q}\right)\right\rangle = \hat{\psi}\left(\vec{q}\right)\hat{h}\left(\vec{q}\right) = \hat{\psi}\left(\vec{q}\right)\exp\left(-2\pi^2\sigma^2q^2\right) \tag{6.17}$$

Here $\hat{\psi}\left(\vec{q}\right)$ and $\hat{h}\left(\vec{q}\right)$ are the Fourier transforms of $\psi\left(\vec{x}\right)$ and $h\left(\vec{x}\right)$ respectively. A similar relationship holds for the expected Fourier spectrum in localization microscopy if all localizations are obtained with have the same localization precision σ [44]. The expected outcome of the application of the filter $\hat{\Phi}\left(\vec{q};\phi\right)$ to I is therefore equivalent to:

$$\left\langle \hat{I}\left(\vec{q}\right)\hat{\Phi}\left(\vec{q};\phi\right)\right\rangle = \hat{\psi}\left(\vec{q}\right)\exp\left(-2\pi^2\sigma^2q^2\right)\hat{\Phi}\left(\vec{q};\phi\right) \tag{6.18}$$

It can be shown that up to a multiplicative constant, $\exp\left(-2\pi^2\sigma^2q^2\right)\hat{\Phi}\left(\vec{q};\phi\right)$ can be described by the same expression as $\hat{\Phi}\left(\vec{q};\phi\right)$ if we make the following parameter substitution:

$$s_o \rightarrow s_o\sqrt{1+4\pi^2\sigma^2w_q^2} \tag{6.19}$$

$$w_q \rightarrow \frac{w_q}{\sqrt{1+4\pi^2\sigma^2w_q^2}} \tag{6.20}$$

Since $w_q s_o$ is typically chosen to be a fixed fraction, it follows that the net result is that nonzero σ increases the scale s_o at which the orientation is evaluated. In theory, the equations above also provide a means of correcting for this effect of increased scale.

The second consequence of the point spread function or localization error is the blurring of $c\left(\Delta\vec{x},\Delta\phi\right)$. If $\hat{h}\left(q=0\right)=1$, then the average image value $\langle I_l\rangle_{\vec{x}}$ remains unaffected. However, the numerator in the expression for $c\left(\Delta\vec{x},\Delta\phi\right)$ can be seen as a convolution between $\tilde{I}_1\left(\vec{x},\phi\right)$ and $\tilde{I}_2\left(-\vec{x},-\phi\right)$ over both $\vec{x}$ and ϕ. The effect of convolving these with the point spread functions is therefore:

$$\begin{aligned} c\left(\vec{x},\phi\right) &\rightarrow c\left(\vec{x},\phi\right) * \left(h_1\left(\vec{x}\right)\delta\left(\phi\right)\right) * \left(h_2\left(-\vec{x}\right)\delta\left(-\phi\right)\right) &(6.21)\\ &= c\left(\vec{x},\phi\right) * \left(h_1\left(\vec{x}\right) * h_2\left(-\vec{x}\right)\right)\delta\left(\phi\right), &(6.22)\end{aligned}$$

where $*$ denotes the convolution operator and $\delta\left(\phi\right)$ is the Dirac delta function. Note that if $h_1\left(\vec{x}\right)$ and $h_2\left(-\vec{x}\right)$ are known, then it might be possible to correct for their effects using deconvolution methods based on this insight.

The significance of these effects depends on the ratio between s_o and σ. For localization microscopy σ can be quite small, on the order of 5 to 10 nm, which means that the the localization error should not affect the co-orientation measurement very substantially. For deterministic microscopy techniques, these effects will often be much more significant, because the PSF is typically much wider.

CHANNEL CROSS-TALK

Channel cross-talk occurs when part of the intensity or localizations from molecules belonging in one color channel appears in the other channel. Typically, this fraction is quite homogeneous over the field of view, as the level of cross-talk is determined by the emission filters. If we neglect the influence of noise for now, then the intensity in channel l can be represented as:

$$I_l(\vec{x}) \rightarrow \left(1 - f_{l,m}\right) I_l(\vec{x}) + f_{m,l} I_m(\vec{x}) \tag{6.23}$$

where $f_{l,m}$ is the fraction of the intensity or localizations from molecules that are imaged with channel l ending up in channel $m \neq l$. Assuming for convenience that the minimal values of $I_l(\vec{x},\phi)$ and $I_m(\vec{x},\phi)$ are negligible, we find that:

$$\tilde{I}_l(\vec{x},\phi) \rightarrow \left(\frac{\left|\left(1 - f_{l,m}\right) I_l(\vec{x},\phi) + f_{m,l} I_m(\vec{x},\phi)\right|}{\int_{-\pi/2}^{\pi/2} \left|\left(1 - f_{l,m}\right) I_l(\vec{x},\phi') + f_{m,l} I_m(\vec{x},\phi')\right| d\phi'} \right) \left(\left(1 - f_{l,m}\right) I_l(\vec{x}) + f_{m,l} I_m(\vec{x})\right). \tag{6.24}$$

This shows that the impact of channel cross-talk on $\tilde{I}_l(\vec{x},\phi)$ is nonlinear, due to the nonlinearity in the operation of taking the absolute value. Therefore it is difficult to predict the impact of cross-talk on the co-orientation measurement. However, if the overlap of $I_1(\vec{x})$ and $I_2(\vec{x})$ after convolution with the filters $\Phi(\vec{x},\phi)$ is small, then the cross-talk will approximately result in:

$$\tilde{I}_l(\vec{x},\phi) \rightarrow \left(1 - f_{l,m}\right) \tilde{I}_l(\vec{x},\phi) + f_{m,l} \tilde{I}_m(\vec{x},\phi). \tag{6.25}$$

This implies that $c(\Delta\vec{x},\Delta\phi)$ will be corrupted by contributions due to the autocorrelation of $\tilde{I}_1(\vec{x},\phi)$ and $\tilde{I}_2(\vec{x},\phi)$ with respect to both $\vec{x}$ and ϕ.

In practice, effects of channel cross-talk should not be very substantial given that many fluorophores are now available for large parts of the visible spectrum.

NOISE

Noise sources will usually not affect the expected value of $c(\Delta\vec{x},\Delta\phi)$ for deterministic microscopy techniques, provided that they are uncorrelated between color channels and that they do not affect the expect value of I_1 and I_2 These are reasonable assumptions for most types of high resolution microscopy, where dominant noise sources are usually photon counting shot noise and additive readout noise.

For localization microscopy, the stochasticity in the number of acquired localizations per fluorescent emitter plays a similar role as the noise sources above. There are factors that influence these variations for both color channels and may thus lead to correlated errors, such as variations in local chemical environment, illumination

power, and missed localizations due to overlapping emissions in high density regions. In practice, the latter will usually have the largest impact, whereas the other factors are usually not very substantial. However, all these effects would only lead increase the apparent colocalization of both color channels, because they affect the density of localization in space. The orientation estimation would not be affected much, so no spurious co-orientation observations would be produced.

STOCHASTICITY IN LABELING

The process of fluorescently labeling a sample is another process that introduces stochasticity in the image formation. Firstly, there is stochasticity in the number of molecules that are labeled. For example, when fluorescent proteins are used then some of the proteins of interest will be of the wildtype variety without the fluorescent fusion protein. When antibody labeling is used, not all epitopes for the antibody will actually be bound by an antibody. Secondly, there is also stochasticity in the number of emitters associated with each of these markers such as antibodies: if secondary antibody labeling is used then the primary antibodies may have a varying number of secondary antibodies associated with them, and the number of emitters per secondary antibody may also vary.

If we make the reasonable assumption that these sources of stochasticity are uncorrelated between the molecules imaged in the different channels, then $c\left(\Delta\vec{x}, \Delta\phi\right)$ remains unaffected: although the expected values of I_1 and I_2 are affected by these sources of stochasticity, they have a more or less equal effect on the numerator and denominator of $c\left(\Delta\vec{x}, \Delta\phi\right)$ and therefore do not affect its expected value. The variance in the measurement of $c\left(\Delta\vec{x}, \Delta\phi\right)$ may be substantially altered by these noise sources though.

7

Conclusion

7.1. CONCLUSION

Below we present the conclusions with respect to the main topics of this thesis. However, before we turn to the conclusions per topic, we will first reflect on the motivation behind this thesis from chapter 1.

In chapter 1 we noted that new quantitative image analysis methods are needed to fully capture all the information in an image. The methods to quantify molecule numbers and measure co-orientation report quantities that characterize the structures in the images: the former by characterizing the molecular composition of the structures and the latter by characterizing the relation between these structures.

In chapter 1 we also noted that new methods are needed to prevent overinterpretation from visual inspection of images, which can lead to unsound biological conclusions. The co-orientation measurement was accompanied by a significance test to prevent undue interpretation of an effect where insufficient evidence is available. The FRC resolution is also primarily aimed at avoiding overinterpretation, by providing a lower bound on the size of details that can be interpreted in the images.

Finally we noted that these methods need to be suited to the nature of localization microscopy data. Although the presented methods in this thesis all make use of pixelated images in their software implementation, this pixelation in the images does not substantially affect the measurements. We showed this in chapter 2 pixelation does not reduce the image resolution more than 10% when the pixel size is smaller than a quarter of the resolution.

7.1.1. RESOLUTION MEASUREMENT

Chapter 2 introduced Fourier Ring Correlation (FRC) as a practical resolution measure for localization microscopy. We showed that it is sensitive to both the localization precision and density of localizations, but also other factors that affect the resolution such as the sample's spatial structure or specimen drift. The FRC can be computed directly from the localization data, even in the presence of multiple localizations per fluorophore, unlike alternative approaches based on the information transfer function [56] or kernel density estimation [157]. Moreover, the FRC provides an objective measurement for the full image, unlike the common alternative approach of measuring the full-width-at-half-maximum of manually selected structures in images.

In chapter 2 we showed that the FRC can be practically used to provide a stopping criterion for data acquisition, to compare the performance of three localization algorithms, to quantify the benefit of drift correction and to assess whether labeling density or localization precision limits the image quality. Since the publication of the FRC method for resolution measurement[44], the FRC has been similarly used to benchmark the performance of localization algorithms[158], to assess the impact of adaptive optics to reduce aberrations while imaging[159], and to compare drift correction algorithms[160]. This demonstrates the utility of FRC resolution for the development and assessment of novel techniques because of its holistic consideration of the factors affecting image quality. Many more applications can therefore be expected where the FRC is used to compare the performance of different techniques.

7.1.2. VISUALIZATION

In chapter 3 we considered which visualization method is most appropriate for localization microscopy. On the one hand this consideration was based on an objective quantitative comparison of the FRC resolution obtained by different visualization methods. The resolution of the Gaussian blob rendering method was found to be optimal in our simulations, although the histogram binning method provides a good alternative with a slightly worse resolution in a shorter computation time. On the other hand, we also considered how different methods conform to users' expectations of the relation between the image and the sample which have been formed for other fluorescence microscopy methods. We concluded that Gaussian blob rendering performs comparatively well on this aspect as well.

7.1.3. QUANTIFYING MOLECULE NUMBERS

Chapters 4 and 5 were dedicated to the problem of counting molecules using localization microscopy with reversibly switchable fluorophores. Quantification methods such as these are of great use in addressing important questions relating for example to the composition of macromolecular structures or to the abundance and oligomerization of signaling proteins. Already in chapter 2 we showed that spurious correlations in the FRC contain information on how often the same molecule is localized. In chapter 4 we developed a three-state model to relate the magnitude of the spurious correlations to the switching kinetics of the fluorophores and the stoichiometry of the number of fluorophores per marker. We used this model to derive a method to estimate the number of localizations per marker with a precision of 10 to 20%, which requires only a simple one-time stoichiometry calibration.

The method in chapter 4 was demonstrated on Alexa Fluor 647 dyes, which is the most common dye used for localization microscopy. We found that it could be effectively described by a three-state switching model with a single long-lived dark state, even though the existence of multiple long-lived dark states has been suggested for this fluorophore[161–163]. Other fluorophores that can also be effectively described by this model could similarly be used with our method.

A second assumption in the model is that each emitter on a multiple-labeled marker either behaves independent of all other emitters or goes entirely unobserved in an experiment due to quenching. This binary description of the behavior of the emitters is necessarily incomplete. However, in practice this description enabled accurate quantification of the number of localizations per Neutravidin tetramer.

An important limitation in chapter 4 is that only labeled molecules were quantified, which can lead to undercounting errors. In chapter 5 we proposed that this issue may be overcome if data is available of many identical structures, labeled with markers that have a single emitter. We showed how the number of protein copies in a subunit of a macromolecular complex could be inferred by including the labeling statistics of the binding sites in the analysis.

In chapter 5 nanobodies were used as markers with effectively just a single fluorophore. As nanobodies are increasingly used for localization microscopy due to their small sizes (~ 15 kDa or 2 nm)[164], the relevance and applicability of our analy-

sis method will increase as well. Moreover, rapid developments in labeling technologies are leading to additional methods for labeling molecules with single organic dye molecules, such as SNAP, CLIP or HALO tags[165–168].

There are also major ongoing developments of fluorescent proteins and better genome editing methods for introducing fluorescent proteins into cells, such as the CRISPR-Cas system[169, 170]. This will benefit competing counting methods that employ irreversibly switching fluorescent proteins. These methods are otherwise susceptible to undercounting because not all wildtype proteins of interested are replaced by fluorescent fusion proteins, or to overcounting when the fusion protein is overexpressed to reduce the fraction of wildtype proteins.

7.1.4. CO-ORIENTATION ANALYSIS

In chapter 6 we turned to the analysis of functional interactions between molecules in multicolor images. We extended the widely used co-localization analysis, by including the orientations of the structures on which the molecules reside. The term co-orientation was coined for the combination of co-localization and orientational alignment. This analysis can be applied directly to any kind of fluorescence microscopy. Additionally, other geometric features of structures could be considered in the analysis instead of orientational alignment, such as the curvature or size of objects. Measurements such as these will be crucial in characterizing how functional molecular interactions relate to the architecture of the extended structures to which they belong.

To test the statistical significance of the co-orientation in experimental data, we devised a data driven test based on the rotation of one color channel with respect to the other. This allowed us to demonstrate significant co-orientation between tubulin and vimentin filaments in a cell-type specific manner. The comparison between cell-types was further supported with our method to visualize the local co-orientation.

7.2. RECOMMENDATIONS

The following list provides a number of recommendations for what should be done to follow up the work in this thesis.

- A robust ImageJ plugin must be developed for the methods presented in this thesis, particularly for resolution measurement. This will results in better dissemination in the biological community.

- The Fourier Plane Correlation (FPC) analysis is currently only semi-quantitative. Schemes for weighting spatial frequencies in the FPC are needed to use the FPC to accurately quantify the resolution in three-dimensional imaging. If attempts to improve of the FPC prove unsuccessful, another option is to use the spectral signal-to-noise ratio (SSNR) instead.

- The algorithm to correct for spurious correlations needs to be adapted for use with the FPC or SSNR for three-dimensional resolution quantification.

- The algorithm to measure the magnitude of spurious correlations should be improved in two ways: firstly by automatically establishing the regime where spurious correlations dominate the FRC; secondly by simultaneous estimation at multiple time points in the acquisition, rather than independent estimation at each time point.

- Further refinement of Gaussian blob rendering should be pursued. Firstly, the amplitude of each blob can be varied with the likelihood that it indeed corresponds to a single molecule[11]. Secondly, the rendering method may account for the statistical dependence between clustered localizations when they derive from the same molecule.

- The visualization of local co-orientation needs to be improved to deal with regions with crossing filaments. Possible directions to address this issue are the automatic detection of these regions, or the incorporation of higher order moments of the generalized cross-correlation in the analysis.

- The presumed quenching mechanism that leaves emitters on multiple-labeled markers unobserved during an acquisition should be further investigated. This would resolve the duality between observed and unobserved emitters in our experiments in chapter 4. Possible approaches for investigation include spectroscopy or analysis of photon antibunching[115] in controlled samples such as DNA origami structures[171, 172].

- A standardized quality assessment procedure should be developed for localization microscopy data. FRC resolution measurement should be an integral part in this. Additionally, this assessment should report several raw camera frames from an acquisition, combined with overlays indicating segmented ROIs and PSF model fits to assess false positive and false negative localization rates.

- The stoichiometry inference method in chapter 5 should be improved by including timing information of the localizations in the analysis as well[40, 135].

7.3. OUTLOOK

In this final section, we provide a brief outlook on future developments relating to image processing and analysis for localization microscopy. To put these developments in context we will first consider the key requirements for localization microscopy from the point of view of the application to biological problems.

Most applications of localization microscopy so far have depended critically on its high resolution. In several important applications this enabled important new insights of the architecture of cellular structures. Prominent examples include investigations of the spatial organization of integrin-based focal adhesions[53], the nuclear pore complex[127], periodic cytoskeletal structures in axons[173], and endosomal sorting complexes required for transport at HIV assembly sites[132]. Similar investigations of the architecture of cellular structures consisting of many molecules

in small volumes will require even higher resolutions to investigate the most intricate details of their organization. In part this will require new labeling approaches and fluorophores to enhance the labeling density and localization precision. Below we will discuss several developments in image processing and analysis that benefit the resolution of localization microscopy.

In addition to the critical need for a higher spatial resolution, further improvement of the temporal resolution is also needed to enable live cell imaging. Until now the application of localization microscopy to live cell imaging has been limited. However, super-resolution imaging in live cells would be extremely useful to image processes in cells where the dynamics or order of events is crucial to their understanding. Examples include the dynamics of lipid domains and heterogeneous protein organization in membranes as well as the dynamic assembly of structures such as signaling complexes or virus particles[174]. Additionally, live cell imaging has the benefit that it is less sensitive to imaging artifacts due to fixation, and can be used to monitor for morphological changes due to cell stress from the imaging. Therefore we will discuss the prospects for live cell localization microscopy below as well.

Finally, localization microscopy is not only useful for generating high resolution images or movies that allow for visual interpretation of cellular structures and processes. Instead, quantitative analysis methods can be used to directly characterize these structures and processes from the localization microscopy data. The methods in this thesis for determining molecule numbers and quantifying co-orientation are examples of such applications of localization microscopy. Quantitative measurements such as these are highly useful for condensing the information in the data into a comprehensible form and for revealing subtle but functionally important differences between cells under different environmental conditions or in different stages of development or between different cell types. In addition, quantitative measurements are also necessary for crafting or testing biological models of cellular processes or structures. Below we will further discuss the need for new quantitative analysis methods, as well as the possible use of high throughput imaging for obtaining high data volumes.

7.3.1. MORE PRECISE LOCALIZATION

The basic image processing pipeline for single color two-dimensional localization microscopy is currently well established. Theoretically optimal algorithms have been published for segmenting and localizing single molecules in an acquisition with sparse activation under typical imaging conditions[11, 15]. In addition, an approach was proposed for three-dimensional imaging to obtain the lowest Cramer-Rao lower bound (CRLB) with a single emission path in the optical system[175]. The utility of algorithms for high density localization algorithms seems limited, as will be discussed below in the paragraph on live cell imaging. Therefore, further advances in the performance of localization algorithms will come from more accurate modeling of the physical image formation.

Improvements in localization precision will require that higher photon counts are obtained from fluorophores. However, the simplified PSF models that are commonly

used now will no longer suffice as the photon count from single fluorophores increases. Misspecification of the PSF model may become a dominant source of localization error rather than the limited photon count, particularly for axial localization. Very high localization precisions will therefore require the use of efficient localization algorithms that account for aberrations in the optical system, vectorial effects and possibly also imperfect rotational mobility of the fluorophores[14, 176, 177]. In addition, hardware demands on setups for high precision imaging will increase. For high performance setups, the use of active feedback systems to prevent specimen drift[26] and adaptive optics to correct for aberrations[159] will become obligatory. Aberration correction will benefit from approaches to quantify aberrations during an acquisition by PSF fitting on the imaged fluorophores.

The finite size of the marker molecule and the fluorophore becomes the limiting factor to the localization accuracy when photon counts on the order of many thousands have been obtained and an algorithm is available that accurately models the PSF[14]. Further gains in localization accuracy may then be improved by using fluorophores with limited rotational mobility. Polarization sensitive detection could then be used to estimate the fluorophore's orientation, which combined with a structural model of the fluorophore and marker molecule could enable estimation of the point where the marker binds to the structure of interest.

7.3.2. SUPER-RESOLUTION SENSING

Fitting a PSF model to a single fluorophore's emission is not only useful to estimate its position. For example, the PSF can also be modified to accurately measure the emission spectrum of the dye by inserting a diffractive grating or dispersive prism in the emission path[33, 34]. This allows for the simultaneous imaging of a number of different fluorophore species, although efficient photoswitching of all fluorophores is complicated by their conflicting requirements on the imaging buffer.

Other properties of a fluorophore other than information about its emission spectrum could be extracted from the PSF as well, such as the fluorophores' brightness, photoswitching rates, emission dipole orientation, rotational diffusion, or fluorescence lifetime. Each of these parameters could be used to encode information about fluorophores' surroundings, allowing them to function as densely sampled and precisely located sensors of their environment. This will require novel fluorescent probes that enable accurate sensing but also provide high photon counts and good photoswitching kinetics for localization. Also novel image sensors with very high frame rates, such as SPAD sensors, may be useful for accurately measuring photoswitching kinetics of fluorophores[178].

7.3.3. DATA FUSION FOR IDENTICAL PARTICLES

An intriguing application of localization microscopy can be found in the structural biology of macromolecular complexes. Localization microscopy has a large potential in this domain as a complementary technique to typically used X-Ray crystallography and cryo electron microscopy (EM) techniques: it can obtain nanoscale localization precision relatively deep inside intact cells with molecular labeling specificity.

Therefore it can be applied to macromolecular complexes which are difficult to image with these techniques, for example because they cannot be purified or crystallized well. Moreover, localization microscopy images can be correlated with high resolution reconstructions of components of complexes obtained from X-ray or cryo EM data. Also, the images can be correlated with cryo EM images of the entire complex to confirm the accuracy of the localizations and to determine molecular positions within the reconstructed electron densities. Together these techniques can therefore be used to obtain molecular models of complex structures.

The application of localization microscopy to structural biology suffers both from a limited localization precision and from finite labeling efficiency. In part these issues may be resolved by the developments described in the previous paragraphs. However, data fusion with identical structures presents a complementary approach to address these problems.

Data fusion with identical structures relies on the prior information that some macromolecular complexes, such as the NPC, are always identical in composition and geometry[52, 127]. We will refer to these complexes as particles. Different instances of these particles can be registered to each other or to a template. Because each site is labeled in some of the instances, this overcomes the problem of underlabeling. In chapter 5 we applied this principle to estimate the number of Nup160 and Seh1 copies per subunit in the NPC. However, significant challenges still remain in aligning these particles in an accurate and computationally efficient manner[134].

An additional challenge is how to combine the aligned localizations to accurately estimate the true molecular positions, based on their number, positions and timing. In principle, if N localizations per molecule are available in total, this could provide up to $\sqrt{N}$ times more precise position estimates. With possible numbers of particle of several thousands, the resulting precision could be extremely high indeed. In such an analysis the incomplete labeling of particles may actually prove beneficial: the labeling stochasticity may perform a similar role as the on-off switching of fluorophores, by providing instances where only one of several nearby molecules is imaged in a localization precision limited area. The method in chapter 5 may be of use in such an analysis, by indicating the number of positions to be extracted from the localizations.

In addition to data fusion for the reconstruction of an image, localizations from registered particles could also be employed to identify if nearly identical particles can actually be subdivided into homogeneous subgroups, or to identify the principal structural variations between particles. This type of analysis is commonly applied in single particle analysis in electron microscopy (see e.g. chapter 4 in reference [128]).

Interestingly, data fusion with identical particles could also be used with STED or RESOLFT microscopy. At very high depletion levels, the signal-to-noise-ratio will eventually also limit their resolution. Averaging identical particles may then lead to a single reconstruction with a vastly improved signal-to-noise-ratio. Moreover, with the use of an accurate model for the PSF of the optical system, it may be possible to use deconvolution as well to enhance the resolution of the averaged particle. However, specific alignment algorithms would need to be developed, as incomplete fluorescent labeling prohibits direct application of algorithms from electron microscopy.

7.3.4. STRUCTURAL MODELING

In the absence of identical structures, an alternative image analysis approach to overcome underlabeling is to model the structure. Often prior ideas exist for how an imaged structure should look. For example, cytoskeletal filaments should appear as linelike structures in images. This prior knowledge could be expressed in a mathematical model, which can then be used to estimate the positions of the filaments in the image. Even a limited number of localized molecules could then suffice to reconstruct an image of each filament.

The idea of using mathematical models of the structures for reconstructing localization microscopy images was first applied in Maji et al.[179], where filaments were modeled as straight line segments. However, straight line segments provide a relatively crude model of curved filaments, which limited the quality of the reconstructed images. This demonstrates the necessity of accurate models to enable such reconstructions.

An additional challenge for this approach is posed by the complex image formation in localization microscopy: molecules are typically labeled with multiple fluorophores, which are localized an unknown number of times, and each time with a different precision. This results in statistical dependencies between the localizations. These dependencies complicate tests for the goodness-of-fit of different models, which will be required for selecting the right model to describe the data.

7.3.5. LIVE CELL IMAGING

One of the reasons for the widespread use of fluorescence microscopy in biology is its use for live cell microscopy. So far applications of localization microscopy in this area have been limited. Contributing factors include toxicity of the buffers typically used for imaging, (toxically) high illumination intensities required for photoswitching, and low frame rates of the commonly used EMCCD cameras. Although phototoxicity can sometimes be reduced with selective plane illumination[180, 181] and acquisition speeds can be considerably increased by using sCMOS cameras[21, 163], video rate nanoscopy will likely remain infeasible in the coming years.

To achieve video rate localization microscopy with high spatial resolution, say 50 nm, a super-resolution image needs to be acquired every 20 ms. Chapter 2 recommends that a resolution of 50 nm is most efficiently obtained for a localization precision of 8 nm. For the structure in figure 2.1 this would entail a density of localizations of about 2000 per μm^2, although different structures may require perhaps an order of magnitude fewer localizations. Simulation results by Mukamel and Schnitzer[182] suggest that for spatial frequencies $q < \sigma_g^{-1}$ information about the sample is most efficiently collected if the density of active emitters is lower than $0.02\sigma_g^{-2}$, where $\sigma_g \sim$ 100 nm is the standard deviation of the Gaussian approximation of the PSF. This actually constitutes a regime in which spots from different emitters typically do not overlap, indicating a limited utility for high density localization algorithms. Together this implies a frame rate of 50 kHz of raw camera images, which is far beyond the current state-of-the-art. Moreover, the illumination intensities required at this frame rate will almost certainly be very stressful and eventually lethal for cells, which limits the maxi-

mum duration of the acquisition. Instead, the highest achievable temporal resolution in the near future will be on the order of a few seconds per super-resolution image.

Intelligent image analysis algorithms could be used to circumvent these requirements. Firstly, localization microscopy offers the unique possibility to not only estimate the position but also the velocity of molecules in live cells. This allows for improved interpolation of fluorophore positions between frames and thus reduced camera frame rates. Such an approach would thus combine elements of static localization microscopy and single-particle tracking PALM[183]. The latter will remain very useful for quantifying single molecules' diffusive motion, rather than imaging the motion of an underlying structure. Secondly, the use of structural models could reduce the density of localizations required to sample a structure, as discussed above.

For less demanding resolutions, localization microscopy is not the only fluorescence microscopy technique that could be considered for live cell imaging; possible alternatives include confocal microscopy or structured illumination microscopy (SIM) or superresolution techniques such as stimulated emission depletion (STED). The suitability of each method depends on a tradeoff between spatial resolution, temporal resolution, total acquisition time and (photo)toxicity.

A recent publication on nonlinear structured illumination microscopy [184] by Betzig and co-workers argues that SIM is generally preferable because it is the most photon-efficient technique for obtaining reasonably high resolutions. However, this conclusion relies on an unequal theoretical comparison between STED, RESOLFT, SIM, and localization microscopy. The image quality of STED, RESOLFT, and SIM was quantified by comparing their effective optical transfer functions (OTF) to the noise. The image quality of localization microscopy was determined instead by considering arbitrary standards for the fraction of molecules that should be localized in periodic structures. Further theoretical and experimental work is therefore required to provide a fair comparison between these techniques, to determine under which conditions there may be a place for localization microscopy in live cell imaging.

If live cell localization microscopy does indeed prove to be infeasible, an alternative approach for time resolved imaging is simply to image multiple fixed cells sequentially. This can then provide snapshots of different stages in a biological process.

7.3.6. HIGH THROUGHPUT IMAGING

Imaging multiple fixed cells is not only useful for observing snapshots of dynamic processes. The availability of data from large numbers of cells also provides new opportunities for statistical analyses to quantify variations among cells. This would for example enable the profiling of cellular phenotypes and provide inputs for systems biology approaches to study cellular processes[185]. However, these sorts of analyses require images of many hundreds or thousands of cells. Therefore, high throughput systems would need to be developed to enable for the automated super-resolution imaging to enable such an approach. Such a system could obtain on the order of 300 to 400 super-resolution images in 24 hours, assuming each acquisition requires 20,000 raw frames acquired with an sCMOS camera at 100 frames per second and an overhead per acquisition on the order of a minute. High throughput data acquisition

may therefore take several days but should not be infeasible.

High throughput imaging with localization microscopy will benefit from automation of tasks that are currently manually executed, such as: searching for suitable cells for imaging, controlling illumination powers, identifying fiducial markers for drift correction, controlling acquisition times per cell, and selecting images with a high image quality. The latter two tasks could benefit from the FRC resolution measurement as detailed in chapter 2. In addition, automatic interpretation of images will require measurements of quantities such as the number of imaged molecules or the co-orientation strength as described in this thesis, but also for example degrees of clustering or co-localization[65]. Quantitative measurements such as these could then provide the inputs needed for systems biology approaches.

7.3.7. IMAGE PROCESSING TOOLS

In this thesis several image analysis methods were discussed that were specifically developed for localization microscopy. As was mentioned in chapter 1, a practical necessity for the development of such methods is that common image analysis tools are not suited to localization microscopy data. They typically assume that structures appear continuous in images and that noise sources operate independently in each pixel. Therefore new algorithms for common image processing tasks - such as edge detection, segmentation, or size measurements - will need to be developed that are specifically adapted to localization data. This requires a departure from standard image processing ways of thinking about data in terms of pixels.

REFERENCES

[1] Rieger, B., Nieuwenhuizen, R. & Stallinga, S. Image processing and analysis for single molecule localization microscopy. *IEEE Signal Process Mag.* **32**, 49–57 (2015).

[2] Betzig, E. *et al.* Imaging intracellular fluorescent proteins at nanometer resolution. *Science* **313**, 1643–1645 (2006).

[3] Rust, M., Bates, M. & Zhuang, X. Sub-diffraction-limit imaging by stochastic optical reconstruction microscopy (STORM). *Nat. Methods* **3**, 793–795 (2006).

[4] Hess, S., Girirajan, T. & Mason, M. Ultra-high resolution imaging by fluorescence photoactivation localization microscopy. *Biophys. J.* **91**, 4258–4272 (2006).

[5] Klein, T., Proppert, S. & Sauer, M. Eight years of single-molecule localization microscopy. *Histochem. Cell Biol.* **141**, 561–575 (2014).

[6] Saxton, M. Single-particle tracking: the distribution of diffusion coefficients. *Biophys. J.* **72**, 1744–1753 (1997).

[7] Olivo-Marin, J.-C. Extraction of spots in biological images using multiscale products. *Pattern Recognit.* **35**, 1989–1996 (2002).

[8] Izeddin, I. *et al.* Wavelet analysis for single molecule localization microscopy. *Opt. Express* **20**, 2081–2095 (2012).

[9] Li, Y., Ishitsuka, Y., Hedde, P. & Nienhaus, G. Fast and efficient molecule detection in localization-based super-resolution microscopy by parallel adaptive histogram equalization. *ACS Nano* **7**, 5207–5214 (2013).

[10] Serge, A., Bertaux, N., Rigneault, H. & Marguet, D. Dynamic multiple-target tracing to probe spatiotemporal cartography of cell membranes. *Nat. Methods* **5**, 687–694 (2008).

[11] Smith, C., Rieger, B., Stallinga, S. & Grünwald, D. Robust detection of single molecules in fluorescence microscopy. *Mol. Biol. Cell* mbc.E15–06–0448 (2015).

[12] Hoogendoorn, E. *et al.* The fidelity of stochastic single-molecule super-resolution reconstructions critically depends upon robust background estimation. *Sci. Rep.* **4**, 3854 (2014).

[13] Zhang, B., Zerubia, J. & Olivio-Marin, J.-C. Gaussian approximations of fluorescence microscope point-spread function models. *Appl. Opt.* **46**, 1819–1829 (2007).

[14] Stallinga, S. & Rieger, B. Accuracy of the Gaussian point spread function model in 2D localization microscopy. *Opt. Express* **18**, 24461–24476 (2010).

[15] Smith, C., Joseph, N., Rieger, B. & Lidke, K. Fast, single-molecule localization that achieves theoretically minimum uncertainty. *Nat. Methods* **7**, 373–375 (2010).

[16] Thompson, R., Larson, D. & Webb, W. Precise nanometer localization analysis for individual fluorescent probes. *Biophys. J.* **82**, 2775–2783 (2002).

[17] Gordon, M., Ha, T. & Selvin, P. Single-molecule high-resolution imaging with photobleaching. *Proc. Natl. Acad. Sci. USA* **101**, 6462–6465 (2004).

[18] Deschout, H. *et al.* Precisely and accurately localizing single emitters in fluorescence microscopy. *Nat. Methods* **11**, 253–266 (2014).

[19] Ober, R., Ram, S. & Ward, S. Localization accuracy in single-molecule microscopy. *Biophys. J.* **86**, 1185–1200 (2004).

[20] Rieger, B. & Stallinga, S. The lateral and axial localization uncertainty in superresolution light microscopy. *ChemPhysChem* **15**, 664–670 (2014).

[21] Huang, F. *et al.* Video-rate nanoscopy using sCMOS camera-specific single-molecule localization algorithms. *Nat. Methods* **10**, 653–658 (2013).

[22] Chao, J., Ram, S., Ward, E. & Ober, R. Ultrahigh accuracy imaging modality for super-localization microscopy. *Nat. Methods* **10**, 335–338 (2013).

[23] Krizek, P., Raska, I. & Hagen, G. Minimizing detection errors in single molecule localization microscopy. *Opt. Express* **19**, 3226–3235 (2011).

[24] Annibale, P., Vanni, S., Scarselli, M., Rothlisberger, U. & Radenovic, A. Quantitative photo activated localization microscopy: Unraveling the effects of photoblinking. *PLoS ONE* **6**, e22678 (2011).

[25] Huang, B., Wang, W., Bates, M. & Zhuang, X. Three-dimensional superresolution imaging by stochastic optical reconstruction microscopy. *Science* **319**, 810–813 (2008).

[26] Pertsinidis, A., Zhang, Y. & Chu, S. Subnanometre single-molecule localization, registration and distance measurements. *Nature* **466**, 647–651 (2010).

[27] Mlodzianoski, M. *et al.* Sample drift correction in 3d fluorescence photoactivation localization microscopy. *Opt. Express* **19**, 15009–15019 (2011).

[28] Geisler, C. *et al.* Drift estimation for single marker switching based imaging schemes. *Opt. Express* **20**, 7274–7289 (2012).

[29] Juette, M. *et al.* Three-dimensional sub 100 nm resolution fluorescence microscopy of thick samples. *Nat. Methods* **5**, 527–529 (2008).

[30] Pavani, S. *et al.* Three-dimensional, single-molecule fluorescence imaging beyond the diffraction limit by using a double-helix point spread function. *Proc. Natl. Acad. Sci. USA* **106**, 2995–2999 (2009).

[31] Bates, M., Huang, B., Dempsey, G. & Zhuang, X. Multicolor super-resolution imaging with photo-switchable fluorescent probes. *Science* **317**, 1749–53 (2007).

[32] Churchman, L., Öktem, Z., Rock, R., Dawson, J. & Spudich, J. Single molecule high-resolution colocalization of Cy3 and Cy5 attached to macromolecules measures intramolecular distances through time. *Proc. Natl. Acad. Sci. USA* **102**, 1419–1423 (2005).

[33] Broeken, J., Rieger, B. & Stallinga, S. Simultaneous measurement of position and color of single fluorescent emitters using diffractive optics. *Opt. Lett.* **39**, 3352–3355 (2014).

[34] Zhang, Z., Kenny, S., Hauser, M., Li, W. & Xu, K. Ultrahigh-throughput single-molecule spectroscopy and spectrally resolved super-resolution microscopy. *Nat. Methods* (2015).

[35] Holden, S., Uphoff, S. & Kapanidis, A. DAOSTORM: an algorithm for high-density super-resolution microscopy. *Nat. Methods* **8**, 279–280 (2011).

[36] Huang, F., Schwartz, S., Byars, J. & Lidke, K. Simultaneous multiple-emitter fitting for single molecule super-resolution imaging. *Biomedical Opt. Express* **2**, 1377–1393 (2011).

[37] Mukamel, E., Babcock, H. & Zhuang, X. Statistical deconvolution for superresolution fluorescence microscopy. *Biophys. J.* **102**, 2391–2400 (2012).

[38] Zhu, L., Zhang, W., Elnatan, D. & Huang, B. Faster STORM using compressed sensing. *Nat. Methods* **9**, 721–726 (2012).

[39] Candes, E. & Fernandez-Grandam, C. Towards a mathematical theory of super-resolution. *Communications on Pure and Applied Mathematics* **67**, 906–956 (2014).

[40] Cox, S. *et al.* Bayesian localization microscopy reveals nanoscale podosome dynamics. *Nat. Methods* **9**, 195–200 (2012).

[41] Saxton, W. & Baumeister, W. The correlation averaging of a regularly arranged bacterial cell envelope protein. *Journal of Microscopy* **127**, 127–138 (1982).

[42] Van Heel, M. Similarity measures between images. *Ultramicroscopy* **21**, 95–100 (1987).

[43] Unser, M., Trus, B. & Steven, A. A new resolution criterion based on spectral signal-to-noise ratio. *Ultramicroscopy* **23**, 39–52 (1987).

[44] Nieuwenhuizen, R. *et al.* Measuring image resolution in optical nanoscopy. *Nat. Methods* **10**, 557–562 (2013).

[45] Hell, S. & Wichmann, J. Breaking the diffraction limit resolution by stimulated emission: stimulated-emission-depletion microscopy. *Opt. Lett.* **19**, 780–783 (1994).

[46] Hofmann, M., Eggeling, C., Jakobs, S. & Hell, S. Breaking the diffraction barrier in fluorescence microscopy at low light intensities by using reversibly photoswitchable proteins. *Proc. Natl. Acad. Sci. USA* **102**, 17565–17569 (2005).

[47] Fölling, J. *et al.* Fluorescence nanoscopy by ground-state depletion and single-molecule return. *Nat. Methods* **5**, 943–945 (2008).

[48] Heilemann, M. *et al.* Subdiffraction-resolution fluorescence imaging with conventional fluorescent probes. *Angew. Chem. Int. Ed. Engl.* **47**, 6172–6176 (2008).

[49] Lidke, K., Rieger, B., Jovin, T. & Heintzmann, R. Superresolution by localization of quantum dots using blinking statistics. *Opt. Express* **13**, 7052–7062 (2005).

[50] Dertinger, T., Colyer, R., Iyer, G., Weiss, S. & Enderlein, J. Fast, background-free, 3D super-resolution optical fluctuation imaging (SOFI). *Proc. Natl. Acad. Sci. USA* **106**, 22287–22292 (2009).

[51] Ram, S., Ward, E. & Ober, R. Beyond Rayleighs criterion: A resolution measure with application to single-molecule microscopy. *Proc. Natl. Acad. Sci. USA* **103**, 4457–4462 (2006).

[52] Löschberger, A. *et al.* Super-resolution imaging visualizes the eightfold symmetry of gp210 proteins around the nuclear pore complex and resolves the central channel with nanometer resolution. *J. Cell Sci.* **125**, 570–575 (2012).

[53] Kanchanawong, P. *et al.* Nanoscale architecture of integrin-based cell adhesions. *Nature* **468**, 580–584 (2010).

[54] Van de Linde, S., Wolter, S., Heilemann, M. & Sauer, M. The effect of photoswitching kinetics and labeling densities on super-resolution fluorescence imaging. *J. Biotechnol.* **149**, 260–266 (2010).

[55] Cordes, T. *et al.* Resolving single-molecule assembled patterns with superresolution blink-microscopy. *Nano Lett.* **10**, 645–651 (2010).

[56] Fitzgerald, J., Lu, J. & Schnitzer, M. Estimation theoretic measure of resolution for stochastic localization microscopy. *Phys. Rev. Lett.* **109**, 048102 (2012).

[57] Beckmann, R. *et al.* Alignment of conduits for the nascent polypeptide chain in the ribosome-sec61 complex. *Science* **278**, 213–2126 (1997).

[58] Böttcher, B., Wynne, S. & Crowther, R. Determination of the fold of the core protein of hepatitis B virus by electron cryomicroscopy. *Nature* **386**, 88–91 (1997).

[59] Rosenthal, P. & Henderson, R. Optimal determination of particle orientation, absolute hand, and contrast loss in single-particle electron cryomicroscopy. *J. Mol. Biol.* **333**, 721–745 (2003).

[60] Barry, D. *et al.* Analytical approximations for real values of the Lambert W-function. *Math. Comput. Simul.* **53**, 95–103 (2000).

[61] Small, A. Theoretical limits on errors and acquisition rates in localizing switchable fluorophores. *Biophys. J.* **92**, L16–L18 (2009).

[62] Wolter, S. *et al.* rapidSTORM: accurate, fast open-source software for localization microscopy. *Nat. Methods* **9**, 1040–1041 (2012).

[63] Bates, M., Dempsey, G., Chen, K. & Zhuang, X. Multicolor super-resolution fluorescence imaging via multi-parameter fluorophore detection. *ChemPhysChem* **13**, 99–107 (2012).

[64] Lando, D. *et al.* Quantitative single-molecule microscopy reveals that cenpacnp1 deposition occurs during g2 in fission yeast. *Open Biol.* **2**, 120078 (2012).

[65] Sengupta, P. *et al.* Probing protein heterogeneity in the plasma membrane using PALM and pair correlation analysis. *Nat. Methods* **8**, 969–975 (2011).

[66] Veatch, S. *et al.* Correlation functions quantify super-resolution images and estimate apparent clustering due to over-counting. *Plos ONE* **7**, e31457 (2012).

[67] Annibale, P., Vanni, S., Scarselli, M., Rothlisberger, U. & Radenovic, A. Identification of clustering artifacts in photoactivated localization microscopy. *Nat. Methods* **8**, 527–528 (2011).

[68] Dempsey, G., Vaughan, J., Chen, K., Bates, M. & Zhuang, X. Evaluation of fluorophores for optimal performance in localization-based super-resolution imaging. *Nat. Methods* **8**, 1027–1031 (2011).

[69] von Middendorff, C., Egner, A., Geisler, C., Hell, S. & Schönle, A. Isotropic 3D nanoscopy based on single emitter switching. *Opt. Express* **16**, 20774–20788 (2008).

[70] Toprak, E. *et al.* Defocused orientation and position imaging (DOPI) of myosin V. *Proc. Natl. Acad. Sci. USA* **103**, 6495–6499 (2006).

[71] Gustafsson, M. Surpassing the lateral resolution limit by a factor of two using structured illumination microscopy. *J. Microsc.* **198**, 82–87 (2000).

[72] Hell, S. Towards fluorescence nanoscopy. *Nat. Biotechnology* **21**, 1347–1355 (2003).

[73] Scheres, S. & Chen, S. Prevention of overfitting in cryo-EM structure determination. *Nat. Methods* **9**, 853–854 (2012).

[74] Tukey, J. *Analysis of time series*, chap. An introduction to the calculations of numerical spectrum analysis, 25–46 (Wiley, New York, 1967).

[75] Cleveland, W. Robust locally weighted regression and smoothing scatterplots. *J. Am. Stat. Assoc.* **74**, 829–836 (1979).

[76] Wolter, S., Endesfelder, U., van de Linde, S., Heilemann, M. & Sauer, M. Measuring localization performance of super-resolution algorithms on very active samples. *Opt. Express* **19**, 7020–7033 (2011).

[77] Xu, K., Babcock, H. & Zhuang, X. Dual-objective STORM reveals three-dimensional filament organization in the actin cytoskeleton. *Nat. Methods* **9**, 185–190 (2012).

[78] Ghosh, R. & Webb, W. Automated detection and tracking of individual and clustered cell surface low density lipoprotein receptor molecules. *Biophys. J.* **66**, 1301–1318 (1994).

[79] Lee, G., Ishihara, A. & Jacobson, K. Direct observation of brownian motion of lipids in a membrane. *Proc. Natl. Acad. Sci. USA* **88**, 6274–6278 (1991).

[80] Bates, M., Jones, S. & Zhuang, X. *Imaging: A Laboratory Manual*, chap. Stochastic Optical Reconstruction Microscopy (STORM): a method for super-resolution fluorescence imaging (Cold Spring Harbor Laboratory Press, 2011).

[81] Hanser, B., Gustafsson, M., Agard, D. & Sedat, J. Phase-retrieved pupil functions in wide-field fluorescence microscopy. *J. Microsc.* **216**, 32–48 (2004).

[82] Oppenheim, A., Willsky, A. & Young, I. *Signals and Systems* (Prentice-Hall International, London, 1983).

[83] Orlova, E. *et al.* Structure of keyhole limpet hemocyanin type 1 (klh1) at 15 a resolution by electron cryomicroscopy and angular reconstitution. *J. Mol. Biol.* **271**, 417–437 (1997).

[84] Van Heel, M. & Schatz, M. Fourier shell correlation threshold criteria. *J. Struct. Biol.* **151**, 250–262 (2005).

[85] Liao, H. & Frank, J. Definition and estimation of resolution in single-particle reconstructions. *Structure* **18**, 768–775 (2010).

[86] Fitzhugh, R. Statistical properties of the asymmetric random telegraph signal, with applications to single-channel analysis. *Math. Biosci.* **64**, 75–89 (1983).

[87] Saxton, W. *Computer Techniques for Image Processing of Electron Microscopy* (Academic Press, New York, 1978).

[88] Corless, R., Gonnet, G., Hare, D., Jeffrey, D. & Knuth, D. On the lambert-w function. *Adv. Comput. Math.* **5**, 329–359 (1996).

[89] Berro, A., Berglund, A., Carmichael, P., Kim, J. & Liddle, J. Super-resolution optical measurement of nanoscale photoacid distribution in lithographic materials. *ACS Nano* **11**, 9496–9502 (2012).

[90] Vogelsang, J., Cordes, T., Forthmann, C., Steinhauer, C. & Tinnefeld, P. Controlling the fluorescence of ordinary oxazine dyes for single-molecule switching and superresolution microscopy. *Proc. Natl. Acad. Sci. USA* **106**, 8107–8112 (2009).

[91] Donnert, G. *et al.* Macromolecular-scale resolution in biological fluorescence microscopy. *Proc. Natl. Acad. Sci. USA* **103**, 11440–11445 (2006).

[92] Nieuwenhuizen, R., Stallinga, S. & Rieger, B. *Cell Membrane Nanodomains: from Biochemistry to Nanoscopy*, chap. Visualization and Resolution in Localization Microscopy, 409–430 (Taylor and Francis, 2014).

[93] Hoebe, R. *et al.* Controlled light-exposure microscopy reduces photobleaching and phototoxicity in fluorescence live-cell imaging. *Nat. Biotechnology* **25**, 249–253 (2007).

[94] Caarls, W., Rieger, B., de Vries, A., Arndt-Jovin, D. & Jovin, T. Minimizing light exposure with the programmable array microscope. *J. Microsc.* **241**, 101–110 (2011).

[95] Abraham, A., Ram, S., Chao, J., Ward, E. & Ober, R. Quantitative study of single molecule location estimation techniques. *Opt. Express* **17**, 23352–23373 (2009).

[96] Egner, A. *et al.* Fluorescence nanoscopy in whole cells by asynchronous localization of photoswitching emitters. *Biophys. J.* **93**, 3285–3290 (2007).

[97] Baddeley, D., Cannell, M. & Soeller, C. Visualization of localization microscopy data. *Microsc. Microanal.* **16**, 64–72 (2010).

[98] Hell, S. Far-field optical nanoscopy. *Science* **316**, 1153–1158 (2007).

[99] Heintzmann, R. & Gustafsson, M. Subdiffraction resolution in continuous samples. *Nat. Photonics* **3**, 362–364 (2009).

[100] Sheppard, C. Super-resolution in confocal microscopy. *Optik* **80**, 53–54 (1988).

[101] Müller, C. & Enderlein, J. Image scanning microscopy. *Phys. Rev. Lett.* **104**, 198101 (2010).

[102] Kratky, O. & Porod, G. Röntgenuntersuchungen gelöster Fadenmoleküle. *Rec. Trav. Chim. Pays-Bas Belg* **68**, 1106–1124 (1949).

[103] Landau, L. & Lifshitz, E. *Statistical Physics, Part 1* (Pergamon Press, 1969), second edn.

[104] Faas, F., Rieger, B., van Vliet, L. & Cherny, D. DNA deformations near charged surfaces: electron and atomic force microscopy views. *Biophys. J.* **97**, 1148–1157 (2009).

[105] Gittes, F., Mickey, J., B. Nettleton & Howard, J. Flexural rigidity of microtubules and actin filaments measured from thermal fluctuations in shape. *J. Cell Biol.* **120**, 923–934 (1993).

[106] Pengo, T., Holden, S. & Manley, S. Palmsiever: a tool to turn raw data into results for single-molecule localization microscopy. *Bioinformatics* btu720 (2014).

[107] Holtzer, L., Meckel, T. & Schmidt, T. Nanometric three-dimensional tracking of individual quantum dots in cells. *Appl. Phys. Lett.* **90**, 053902 (2007).

[108] Pavani, S. & Piestun, R. Three dimensional tracking of fluorescent microparticles using a photon-limited double-helix response system. *Opt. Express* **16**, 22048–22057 (2008).

[109] Shtengel, G. *et al.* Interferometric fluorescent super-resolution microscopy resolves 3d cellular ultrastructure. *Proc. Natl Acad. Sci. USA* **106**, 3125–3130 (2009).

[110] Wang, S., Moffitt, J., Dempsey, G., Xie, S. & Zhuang, X. Characterization and development of photoactivatable fluorescent proteins for single-molecule-based superresolution imaging. *Proc. Natl. Acad. Sci. USA* **111**, 8452 – 8457 (2014).

[111] Lee, S.-H., Shin, J., Lee, A. & Bustamante, C. Counting single photoactivatable fluorescent molecules by photoactivated localization microscopy (PALM). *Proc. Natl. Acad. Sci. USA* **109**, 17436–17441 (2012).

[112] Puchner, E., Walter, J., Kasper, R., Huang, B. & Lim, W. Counting molecules in single organelles with superresolution microscopy allows tracking of the endosome maturation trajectory. *Proc. Natl. Acad. Sci. USA* **110**, 16015–16020 (2013).

[113] Nan, X. *et al.* Single-molecule superresolution imaging allows quantitative analysis of raf multimer formation and signaling. *Proc. Natl. Acad. Sci. USA* **110**, 18519–18524 (2013).

[114] Durisic, N., Laparra-Cuervo, L., Sandoval-Álvarez, A., Borbely, J. & Lakadamyali, M. Single-molecule evaluation of fluorescent protein photoactivation efficiency using an in vivo nanotemplate. *Nat. Methods* **11**, 156–162 (2014).

[115] Grussmayer, K., Kurz, A. & Herten, D.-P. Single-molecule studies on the label number distribution of fluorescent markers. *ChemPhysChem* **15**, 734–742 (2014).

[116] Ehmann, N. *et al.* Quantitative super-resolution imaging of Bruchpilot distinguishes active zone states. *Nat. Commun.* **5** (2014).

[117] Bates, M., Blosser, T. & Zhuang, X. Short-range spectroscopic ruler based on a single-molecule optical switch. *Phys. Rev. Lett.* **94**, 108101 (2005).

[118] Vogelsang, J. *et al.* A reducing and oxidizing system minimizes photobleaching and blinking of fluorescent dyes. *Angew. Chem. Int. Ed. Engl.* **47**, 5465–5469 (2008).

[119] Cronshaw, J., Krutchinsky, A., Zhang, W., Chait, B. & Matunis, M. Proteomic analysis of the mammalian nuclear pore complex. *J. Cell Biol.* **158**, 915–927 (2002).

[120] Ori, A. *et al.* Cell type-specific nuclear pores: a case in point for context-dependent stoichiometry of molecular machines. *Mol. Syst. Biol.* **9**, 648 (2013).

[121] Bui, K. *et al.* Integrated structural analysis of the human nuclear pore complex scaffold. *Cell* **155**, 1233–1243 (2013).

[122] Kasha, M., Rawls, H. & El-Bayoumi, M. The exciton model in molecular spectroscopy. *Pure Appl. Chem.* **11**, 371–392 (1965).

[123] Rösch, U., Yao, S., Wortmann, R. & Würthner, F. Fluorescent h-aggregates of merocyanine dyes. *Angew. Chem. Int. Ed. Engl.* **118**, 7184–7188 (2006).

[124] Bollmann, S., Löllmann, M., Sauer, M. & Doose, S. Dimer formation of organic fluorophores reports on biomolecular dynamics under denaturing conditions. *Phys. Chem. Chem. Phys.* **13**, 12874–12882 (2011).

[125] Espinoza, F., Oliver, J., Wilson, B. & Steinberg, S. Using hierarchical clustering and dendrograms to quantify the clustering of membrane proteins. *Bull. Math. Biol.* **74**, 190–211 (2012).

[126] Kask, P. *et al.* Two-dimensional fluorescence intensity distribution analysis: Theory and applications. *Biophys. J.* **78**, 1703–1713 (2000).

[127] Szymborska, A., Marco, N., A de. Daigle, Cordes, V., Briggs, J. & Ellenberg, J. Nuclear pore scaffold structure analyzed by super-resolution microscopy and particle averaging. *Science* **341**, 655–658 (2013).

[128] Frank, J. *Three-Dimensional Electron Microscopy of Macromolecular Assemblies* (Oxford University Press, 2006), 2 edn.

[129] Frank, J. Single-particle reconstructionof biological macromolecules in electron microscopy - 30 years. *Q. Rev. Biophys.* **42**, 139–158 (2009).

[130] Van Heel, M. *et al.* Single-particle electron cryo-microscopy: towards atomic resolution. *Q. Rev. Biophys.* **33**, 307–369 (2000).

[131] Laine, R. *et al.* Structural analysis of herpes simplex virus by optical super-resolution imaging. *Nat. Commun.* **6**, 5980 (2015).

[132] van Engelenburg, S. *et al.* Distribution of ESCRT machinery at HIV assembly sites reveals virus scaffolding of ESCRT subunits. *Science* **343**, 653–656 (2014).

[133] Stallinga, S. & Rieger, B. The effect of background on localization uncertainty in single emitter imaging. In *Proc. of the 2012 IEEE 9th International Symposium on Biomedical Imaging* 2012).

[134] Broeken, J. *et al.* Resolution improvement by 3D particle averaging in localization microscopy. *Methods Appl. Fluoresc.* **3**, 014003 (2015).

[135] Rollins, G., Shin, J., Bustamante, C. & Pressé, S. Stochastic approach to the molecular counting problem in superresolution microscopy. *Proc. Natl. Acad. Sci. USA* **112**, E110–E118 (2015).

[136] Förster, F., Medalia, O., Zauberman, N., Baumeiser, W. & Fass, D. Retrovirus envelope protein complex structure in situ studied by cryo-electron tomography. *Proc. Natl. Acad. Sci. USA* **102**, 4729–4734 (2005).

[137] Alberts, B. *et al. Essential cell biology* (Garland Science, New York, 2013), 4 edn.

[138] Klar, T., Jakobs, S., Dyba, S., Egner, A. & Hell, S. Fluorescence microscopy with diffraction resolution barrier broken by stimulated emission. *Proc. Natl. Acad. Sci. USA* **97**, 8206–8210 (2000).

[139] Manders, E., Stap, J., Brakenhoff, G., van Driel, R. & Aten, J. Dynamics of three-dimensional replication patterns during the s-phase, analysed by double labelling of dna and confocal microscopy. *J. Cell Sci.* **103**, 857–862 (1992).

[140] Manders, E., Verbeek, F. & Aten, J. Measurement of co-localization of objects in dual-colour confocal images. *J. Microsc.* **169**, 375–382 (1993).

[141] Lachmanovich, E. *et al.* Co-localization analysis of complex formation among membrane proteins by computerized fluorescence microscopy: application to immunofluorescence co-patching studies. *J. Microsc.* **212**, 122–131 (2003).

[142] Shivanandan, A., Radenovic, A. & Sbalzarini, I. Mosaicia: an imagej/fiji plugin for spatial pattern and interaction analysis. *BMC Bioinformatics* **14**, 349 (2013).

[143] Malkusch, S. *et al.* Coordinate-based colocalization analysis of single-molecule localization microscopy data. *Histochem. Cell Biol.* **137**, 1–10 (2012).

[144] Walters, D. Selection of image primitives for general-purpose visual processing. *Comput. Vis. Graph. Image Process.* **37**, 261–298 (1987).

[145] van Ginkel, M. *Image Analysis using Orientation Space based on Steerable Filters*. Ph.D. thesis, Delft University of Technology, Delft, The Netherlands (2002).

[146] Faas, F. & van Vliet, L. 3d-orientation space; filters and sampling. In *Proceedings of the 13th Scandinavian Conference on Image Analysis (Göteborg, Sweden)*, LNCS 2749, 36–42 (2003).

[147] Lagache, T., Meas-Yedid, V. & Olivo-Marin, J. A statistical analysis of spatial colocalization using Ripley's K function. In *Proc. of the 2013 IEEE 10th International Symposium on Biomedical Imaging*, 896–901 (2013).

[148] van Steensel, B. *et al.* Partial colocalization of glucocorticoid and mineralocorticoid receptors in discrete compartments in nuclei of rat hippocampus neurons. *J. Cell Sci.* **109**, 787–792 (1996).

[149] Mann, H. & Whitney, D. On a test of whether one of two random variables is stochastically larger than the other. *Ann. Math. Stat.* **18**, 50–60 (1947).

[150] Fontijn, R. *et al.* Maintenance of vascular endothelial cell-specific properties after immortalization with an amphotrophic replication-deficient retrovirus containing human papilloma virus 16 e6/e7 dna. *Exp. Cell Res.* **216**, 199–207 (1995).

[151] Goldman, A., Moir, R., Montag-Lowy, M., Stewart, M. & Goldman, R. Pathway of incorporation of microinjected lamin a into the nuclear envelope. *J. Cell Biol.* **119**, 725–735 (1992).

[152] Ketema, M. *et al.* The rod domain is not essential for the function of plectin in maintaining tissue integrity. *Mol. Biol. Cell*, mbc–E15 (2015).

[153] Sibson, R. Studies in the robustness of multidimensional scaling: Perturbational analysis of classical scaling. *J. R. Stat. Soc. Series B* **41**, 217–229 (1979).

[154] Sakamoto, Y., Boëda, B. & Etienne-Manneville, S. Apc binds intermediate filaments and is required for their reorganization during cell migration. *J. Cell Biol.* **200**, 249–258 (2013).

[155] Hookway, J. *et al.* Microtubule-dependent transport and dynamics of vimentin intermediate filaments. *Mol. Biol. Cell* **26**, 1675–1686 (2015).

[156] Heintzmann, R. & Cremer, C. Laterally modulated excitation microscopy: improvement of resolution by using a diffraction grating. *Proc. SPIE, Optical Biopsies and Microscopic Techniques III* **3568**, 185-196 (1999).

[157] Rees, E. *et al.* Blind assessment of localisation microscope image resolution. *Opt. Nanoscopy* **1**, 12 (2012).

[158] Sage, D. *et al.* Quantitative evaluation of software packages for single-molecule localization microscopy. *Nat. Methods* (2015).

[159] Burke, D., Patton, B., Huang, F., Bewersdorf, J. & Booth, M. Adaptive optics correction of specimen-induced aberrations in single-molecule switching microscopy. *Optica* **2**, 177–175 (2015).

[160] Wang, Y. *et al.* Localization events-based sample drift correction for localization microscopy with redundant cross-correlation algorithm. *Opt. Express* **22**, 15982–15991 (2014).

[161] Vogelsang, J. *et al.* Make them blink: Probes for super-resolution microscopy. *ChemPhysChem* **11**, 2475–2490 (2010).

[162] van de Linde, S. *et al.* Direct stochastic optical reconstruction microscopy with standard fluorescent probes. *Nat. Protocols* **6**, 991–1009 (2011).

[163] Lin, Y. *et al.* Quantifying and optimizing single-molecule switching nanoscopy at high speeds. *PLoS ONE* **10**, e0128135 (2015).

[164] Ries, J., Kaplan, C., Platonova, E., Eghlidi, H. & Ewers, H. A simple, versatile method for GFP-based super-resolution microscopy via nanobodies. *Nat. Methods* **9**, 582–587 (2012).

[165] Wormbacher, R. *et al.* Live-cell super-resolution imaging with trimethoprim conjugates. *Nat. Methods* **7**, 717–722 (2010).

[166] Lee, S. *et al.* Superresolution imaging of targeted proteins in fixed and living cells using photoactivatable organic fluorophores. *J. Am. Chem. Soc.* **132**, 15099–15101 (2010).

[167] Klein, T. *et al.* Live-cell dstorm with snap-tag fusion proteins. *Nat. Methods* **8**, 7–9 (2011).

[168] Jones, S., Shim, S.-H., He, J. & Zhuang, X. Fast, three-dimensional super-resolution imaging of live cells. *Nat. Methods* **8**, 499–505 (2011).

[169] Cong, L. *et al.* Genome engineering using CRISPR/Cas systems *Science* **339**, 819–823 (2013).

[170] Mali, P. *et al.* Rna-guided human genome engineering via cas9. *Science* **339**, 823–826 (2013).

[171] Rothemund, P. Folding dna to create nanoscale shapes and patterns. *Nature* **440**, 297–302 (2006).

[172] Schmied, J. *et al.* Fluorescence and super-resolution standards based on dna origami. *Nat. Methods* **9**, 1133–1134 (2012).

[173] Xu, K., Zhong, G. & Zhuang, X. Actin, spectrin, and associated proteins form a periodic cytoskeletal structure in axons. *Science* **339**, 452–456 (2013).

[174] Lippincott-Schwartz, J. & Manley, S. Putting super-resolution fluorescence microscopy to work. *Nat. Methods* **6**, 21 (2009).

[175] Shechtman, Y., Sahl, S., Backer, A. & Moerner, W. Optimal point spread function design for 3d imaging. *Phys. Rev. Lett.* **113**, 133902 (2014).

[176] Liu, S., Kromann, E., Krueger, W., Bewersdorf, J. & Lidke, K. Three dimensional single molecule localization using a phase retrieved pupil function. *Opt. Express* **21**, 29462–29487 (2013).

[177] Stallinga, S. Effect of rotational diffusion in an orientational potential well on the point spread function of electric dipole emitters. *J. Opt. Soc. Am. A* **32**, 213–223 (2015).

[178] Krishnaswami, V., Noorden, C., Manders, E. & Hoebe, R. Towards digital photon counting cameras for single-molecule Opt. Nanoscopy. *Opt. Nanoscopy* **3** (2014).

[179] Maji, S. & Bruchez, M. Inferring biological structures from superresolution single molecule images using generative models. *PLoS ONE* **7**, e36973 (2012).

[180] Huisken, J., Swoger, J., Del Bene, F., Wittbrodt, J. & Stelzer, E. H. K. Optical Sectioning Deep Inside Live Embryos by Selective Plane Illumination Microscopy. *Science* **305**, 1007–1009 (2004).

[181] Chen, B.-C. *et al.* Lattice light-sheet microscopy: Imaging molecules to embryos at high spatiotemporal resolution. *Science* **346**, 1257998 (2014).

[182] Mukamel, E. & Schnitzer, M. Unified resolution bounds for conventional and stochastic localization fluorescence microscopy. *Phys. Rev. Lett.* **109**, 168102 (2012).

[183] Manley, S. *et al.* High-density mapping of single-molecule trajectories with photoactivated localization microscopy. *Nat. Methods* **5**, 155–157 (2008).

[184] Li, D. *et al.* Extended-resolution structured illumination imaging of endocytic and cytoskeletal dynamics. *Science* **349** (2015).

[185] Pepperkok, R. & Ellenberg, J. High-throughput fluorescence microscopy for systems biology. *Nat. Rev. Mol. Cell Biol.* **7**, 690–696 (2006).

SUMMARY

Localization microscopy is a powerful tool for circumventing the diffraction limit in fluorescence microscopy. In this technique sparse subsets of the fluorophores labeling a sample are switched on and off, and subsequently localized with a precision on the order of several nanometers. A high resolution image can then be built up from the estimated positions. However, localization microscopy fundamentally produces a list of localizations rather than an image. This introduces a critical need for new quantitative image analysis methods that suit these data. This thesis describes several of these methods, which we have developed.

The resolution in localization microscopy is not limited by diffraction. Instead we propose an image based resolution measure based on Fourier ring correlation (FRC). The FRC is both sensitive to the localization precision and the density of single fluorescent labels in a sample, as well as other factors such as the sample's spatial structure. We show how the FRC can be corrected for spurious correlations for acquisitions where the same molecules are localized several times. The FRC resolution provides a quantitative guide for the smallest details that can be reliably interpreted in images, thus enabling sound biological conclusions.

Localization microscopy lacks a natural way of visualizing the data that are produced. Therefore we compare several proposed visualization methods, and show that the best FRC resolution is obtained by rendering localizations as Gaussian blobs whose widths are proportional to the corresponding localization precisions. Histogram binning provides a good alternative though, with only a slightly resolution in a shorter computation time.

A major application of localization microscopy is the quantification of numbers of molecules in biological structures. However, the reversibly switchable fluorophores which are commonly used for imaging suffer from overcounting due to multiple localizations of the same molecule. Here we provide a method to estimate how often a marker such as an antibody is localized on average. The method makes use of the build-up of spurious correlations in the FRC during acquisition, and draws upon a model for the statistics of activation, bleaching, and labeling stoichiometry. Our method achieves a counting error of less than 20% with single fluorophore labeled DNA oligomers and multiple-labeled Neutravidin tetramers, without any calibration of transition rates.

When overcounting problems are resolved, incomplete labeling of the sample may result in undercounting problems instead. We address this issue for well-defined macromolecular complexes such as the nuclear pore complex (NPC). We show how the number of protein copies per subunit can be inferred by combining the localizations from multiple underlabeled complexes in a single statistical analysis.

Co-localization analysis is a standard tool to probe multicolor fluorescence images for functional interactions between molecules in different channels. We extend this into the analysis of co-orientation: the combination of co-localization and orientational alignment of the structures on which the molecules reside. We employ this analysis to show that microtubuli exhibit statistically significant co-orientation with the intermediate filament vimentin in a cell-type specific manner.

Together these methods substantially advance our ability to reliably and quantitatively interpret localization microscopy data and thereby enhances their utility for biological research.

SAMENVATTING

Lokalisatiemicroscopie is een krachtige techniek om de diffractielimiet in lichtmicroscopie te omzeilen. Met deze techniek worden kleine subgroepen van de fluoroforen die een voorwerp markeren aan- en uitgeschakeld en vervolgens gelokaliseerd met een precisie in de orde van enkele nanometers. Een afbeelding met hoge resolutie kan dan worden opgebouwd uit de geschatte posities. Lokalisatiemicroscopie produceert echter fundamenteel een lijst met lokalisaties in plaats van een afbeelding. Dit introduceert een essentiële noodzaak om nieuwe kwantitatieve beeldanalysemethoden te ontwikkelen die geschikt zijn voor dit soort data. Dit proefschrift beschrijft een aantal van zulke methoden, die wij hebben ontwikkeld.

De resolutie in lokalisatiemicroscopie is niet beperkt door diffractie. Daarom introduceren wij een resolutiemaat voor lokalisatiemicroscopie die uitgaat van de gereconstrueerde afbeelding en gebaseerd is op Fourier ring correlatie (FRC). FRC is zowel gevoelig voor de lokalisatieprecisie als de dichtheid van fluorescente moleculen in een voorwerp, maar ook voor andere factoren zoals de spatiële structuur van het voorwerp. Wij laten zien dat de FRC gecorrigeerd kan worden voor de valse correlaties die ontstaan in acquisities waarin dezelfde moleculen meerdere keren worden gelokaliseerd. De FRC-resolutie levert een kwantitatieve maatstaf op voor de kleinste details die nog betrouwbaar kunnen worden geïnterpreteerd in beelden, wat gedegen biologische conclusies mogelijk maakt.

Lokalisatiemicroscopie mist een natuurlijke manier om de data die geproduceerd worden te visualiseren. Daarom vergelijken wij verschillende voorgestelde visualisatiemethoden, en laten zien dat de beste FRC-resolutie behaald wordt door lokalisaties weer te geven als Gaussische functies met een breedte die proportioneel is aan de bijbehorende lokalisatieprecisies. Een tweedimensionaal histogram biedt echter een goed alternatief, dat een enigszins slechtere resolutie oplevert maar minder rekentijd kost.

Een belangrijke toepassing van lokalisatiemicroscopie is de kwantificering van aantallen moleculen in biologische structuren. De reversibel schakelbare fluoroforen die vaak gebruikt worden lijden echter onder overschatting als gevolg van herhaalde lokalisatie van hetzelfde molecuul. Wij hebben een methode ontwikkeld om te schatten hoe vaak een markeerstof zoals een antilichaam gemiddeld gelokaliseerd wordt. De methode maakt gebruik van de opbouw van valse correlaties in de FRC tijdens een acquisitie en is gebaseerd op een model voor de statistiek van activatie, bleking, en stoichiometrie van fluoroforen per markeermolecuul. Onze methode behaalt een schattingsfout van minder dan 20% met DNA oligomeren voorzien van een enkel fluorofoor en Neutravidinetetrameren voorzien van meerdere fluoroforen, zonder dat er een kalibratie van de reactiesnelheden in het model nodig is.

Als problemen met overschatting van aantallen moleculen zijn opgelost, dan wordt onderschatting als gevolg van het onvolledig markeren van een voorwerp een probleem. Wij bieden een oplossing voor dit probleem voor welgedefinieerde macromoleculaire complexen zoals het kernporiecomplex. We laten zien hoe het aantal eiwitkopieën per onderdeel van een complex kan worden bepaald door lokalisaties van verschillende onvolledig gemarkeerde complexen te combineren in een enkele statistische analyse.

Colokalisatie-analyse is een standaardmethode om meerkleurenfluorescentie afbeeldingen te analyseren voor functionele interacties tussen moleculen in verschillende kanalen. Wij breiden deze analyse uit naar de analyse van co-oriëntatie: de combinatie van colokalisatie en uitlijning van de structuren waarop de moleculen zich bevinden. We passen deze analyse toe om te laten zien dat microtubuli statistisch significante co-oriëntatie vertonen met vimentinefilamenten op een manier die afhangt van het celtype.

Samen bieden de hier beschreven methoden een substantiële vooruitgang in de mogelijkheden om lokalisatiemicroscopiedata op een betrouwbare en kwantitatieve manier te interpreteren. Dit vergroot het nut van die data voor biologisch onderzoek.

CURRICULUM VITÆ

Robert Pieter Joachim Nieuwenhuizen was born in The Hague, The Netherlands on August 4, 1987. He obtained his high school diploma from the Interconfessionele Scholengemeenschap het Westland in 's-Gravenzande in 2005. In that same year he enrolled for the BSc program in Applied Physics at Delft University of Technology. In 2008 obtained his BSc degree in Applied Physics (cum laude) and subsequently he enrolled in a double degree MSc program in Applied Physics and Management of Technology. He graduated and obtained MSc degrees in both subjects in 2011 (both cum laude). For his MSc thesis project in Applied Physics he worked in the Quantitative Imaging group at Delft University of Technology on resolution measurement for localization microscopy, which is described elsewhere in this thesis. During this project he went on a two month internship with dr. Keith Lidke lab at the University of New Mexico, Albuquerque, USA. His MSc thesis project in Management of Technology was carried out at the IBM Benelux Center for Advanced Studies in Amsterdam on the development of a quantitative tool for measuring innovation capacity and performance of companies.

In 2012 he started as a PhD student in the Quantitative Imaging group. His project was part of the Nanoscopy program of the Dutch technology foundation STW, which is part of the Netherlands Organisation for Scientific Research (NWO). In his research on this project he focused on the quantitation of localization microscopy.

LIST OF PUBLICATIONS

7. Nieuwenhuizen, R.P.J., Nahidiazar, L., Manders, E.M.M., Jalink, K., Stallinga, S. & Rieger, B. Co-orientation: Quantifying simultaneous co-localization and orientational alignment of filaments in light microscopy. *PLoS ONE* **10**, e0131756 (2015).

6. Nieuwenhuizen, R.P.J., Bates, M., Szymborska, A., Lidke, K.A., Rieger, B. & Stallinga, S. Quantitative localization microscopy: Effects of photophysics and labeling stoichiometry. *PLoS ONE* **10**, e0127989 (2015).

5. Broeken, J., Johnsson, H., Lidke, D.S., Nieuwenhuizen, R.P.J., Stallinga, S., Lidke, K.A. & Rieger, B. Resolution improvement by 3D particle averaging in localization microscopy. *Methods Appl. Fluoresc.* **3**, 014003 (2015).

4. Rieger, B., Nieuwenhuizen, R.P.J. & Stallinga, S. Image processing and analysis for single molecule localization microscopy. *IEEE Signal Process. Mag.* **32**, 49–57 (2015).

3. Nieuwenhuizen, R.P.J., Stallinga, S. & Rieger, B. *Cell Membrane Nanodomains: from Biochemistry to Nanoscopy*, chap. Visualization and Resolution in Localization Microscopy, 409–430 (Taylor and Francis, 2014).

2. Nieuwenhuizen, R.P.J., Stallinga, S. & Rieger, B. Image resolution in optical nanoscopy. *Proc. SPIE* **8815**, 881508 (2013).

1. Nieuwenhuizen, R.P.J., Lidke, K.A., Bates, M., Leyton Puig, D., Grünwald, D., Stallinga, S. & Rieger, B. Measuring image resolution in optical nanoscopy. *Nat. Methods* **10**, 557–562 (2013).

ACKNOWLEDGEMENTS

A careful search of this thesis would reveal that the grammatical person is always plural: the word we is used rather than the word I. This reflects that this work was not produced in a solo effort, and could not have been produced without the help of many others. Therefore I owe a debt of gratitude to all those who have helped me during the project that led to this thesis.

Bernd and Sjoerd, thank you for providing me with so much freedom in my work, for all of our invigorating discussions, for all the fun we had on conferences close to home and far away, and for forming a perfectly complementary supervisory pair. Lucas, thank you for persuading me to take on this project.

Keith, thank you for making my conference visits and experimental work in Albuquerque possible. My development as a PhD student would not have been complete without the invaluable practical experience I gained in your lab. A special thanks also to Diane, Sam, Fang, Jason, Chris, Hannah, and the other members of the Lidke labs for your assistance with my experiments.

Mark, thank you for the close collaboration on working out our methods for quantitative localization microscopy. We would not have been able to develop the Q analysis without your infinite patience in obtaining new datasets and trying out new approaches. Also a special thanks for arranging my lab visit in the fall of 2015.

Daniela, thank you for the beautiful cellular data you provided for demonstrating the FRC resolution measure.

Leila, thank you for the fruitful interaction on developing our co-orientational analysis and for the gorgeous picture on the cover of this thesis.

Kees, thank you for your constructively critical attitude in our discussions.

Erik, thank you for your efforts in connecting all the separate STW Nanoscopy project with each other.

Annelies and Mandy, thank you for your friendly help in dealing with the big bad bureaucracy in the university.

Ronald, thank you for helping me with all my embarrassingly basic computer related problems.

I would also like to thank all the members of the QI group in general for all the good times we had. For the coffee breaks, dagjes uit, PhD dinners, ad hoc traditions, and great atmosphere.

Finally, thanks to my family and friends for supporting me throughout my PhD project, particularly in the difficult final stages of writing my thesis, and for helping me to keep the balance between work and life.